Evidence for a narrow state decaying to $K^0_S p$ and $K^0_S \bar{p}$ in deep inelastic scattering

Dissertation
zur Erlangung des Doktorgrades
des Fachbereichs Physik
der Universität Hamburg

vorgelegt von

Amita Raval

aus Canberra

Hamburg
2005

Gutachter der Dissertation:	Dr. A. Geiser Prof. Dr. R. Klanner
Gutachter der Disputation:	Prof. Dr. E. Lohrmann Prof. Dr. B. Naroska
Datum der Disputation:	
Vorsitzender des Prüfungsausschusses:	Prof. Dr. G. Heinzelmann
Vorsitzender des Promotionsausschusses:	Prof. Dr. G. Huber
Dekan des Fachbereichs Physik:	Prof. Dr. G. Huber

Abstract

Recent results from fixed-target experiments give evidence for a narrow baryonic resonance decaying to K^+n and K^0_Sp, interpreted as a pentaquark (Θ^+). This thesis presents a search for such a resonant state in the $K^0_Sp(\bar{p})$ invariant-mass spectrum. The data was collected with the ZEUS detector at HERA and corresponds to an integrated luminosity of 121 pb^{-1}. The analysis was performed in the central rapidity region of inclusive deep inelastic scattering at an *ep* center-of-mass energy of 300-318 GeV for exchanged photon virtuality, $Q^2 > 2$ GeV^2.

The results presented here support the existence of the Θ^+ state. A narrow resonance is seen in the $K^0_Sp(\bar{p})$ invariant-mass spectrum in the kinematic region of $Q^2 > 20$ GeV^2. The peak position, determined from a fit to the mass distribution, is 1521.5 ± 1.6(stat.) $^{+2.1}_{-2.6}$(syst.) MeV, and the measured Gaussian width of $\sigma = 6.9 \pm 1.4$(stat.) $^{+2.4}_{-2.0}$(syst.) MeV is slightly above, but consistent with the experimental resolution. The number of events ascribed to the signal by this fit is 217 ± 45. The statistical significance, estimated from the number of events assigned to the signal by the fit, varies between 3.5σ and 4.8σ, depending on the assumption of the background shape. Several cross checks were made in order to validate the particle identification, to study possible reflections from known states and to verify the robustness of the peak. The 1522 MeV peak passes all checks.

In high-energy experiments, where hadron production is dominated by fragmentation, hadrons and their antiparticles should be produced in equal numbers. Hence the invariant-mass spectra of K^0_Sp and $K^0_S\bar{p}$ were searched independently. An enhancement is also seen in the $K^0_S\bar{p}$ channel. The number of events ascribed to the signal by the same fit is 75 ± 40. If the K^0_Sp signal is interpreted as a pentaquark, then the enhancement in the $K^0_S\bar{p}$ channel may correspond to its antiparticle, the $\bar{\Theta}^-$. This would be the first evidence for $\bar{\Theta}^-$.

If an isotensor state is responsible for the Θ^+ signal, its isotensor partner, the Θ^{++}, might be expected in the K^+p spectrum. Furthermore, one advantage of reconstructing the Kp invariant mass is that it allows the usage of the well established $\Lambda(1520)D_{03}$-meson in this decay mode to check the efficiencies and resolutions. A clean peak is seen in the $K^-p(K^+\bar{p})$ channel at 1518.5 ± 0.6(stat.) MeV, however no peak is seen in the like-sign spectrum, thereby disfavoring the isotensor interpretation of the Θ^+ state.

The Θ^+ signal is observed to come predominantly from protons in the forward region, which does not support the assumption that the production is via fragmentation. Instead it raises the question whether Θ^+ production might have some connection with the proton-remnant. However, higher statistical precision is necessary in order to draw a stronger conclusion.

Also reported in this thesis are cross-section measurements for Θ^+ production and decay, assuming the signal is real. The cross section for $\Theta^+(\bar{\Theta}^-) \to K^0p(\bar{p})$ is measured in the kinematic region, defined by $0.04 < y < 0.95$, $p_T > 0.5$ GeV and

$|\eta| < 1.5$. The total and differential cross sections, $d\sigma/dQ^2$, for $Q^2 > 20$ GeV^2 are presented. The total cross section is 130.0 ± 26.9(stat.) pb.

Furthermore, the Θ^+ cross section is compared to that of $\Lambda \to p\pi$, produced in the same kinematic region. The Λ-baryons were reconstructed via both the dE/dx and the secondary vertexing information. The latter method provides a cross check on the detector acceptance with the dE/dx method and a measure of the uncertainty on the K^0_S reconstruction. The two methods yield cross-section results that are within 6% of each other. The ratio of Θ^+/Λ production cross section varies between 4% and 15% as a function of Q^2 for $Q^2 > 20$ GeV^2. For $Q^2 < 20$ GeV^2, the same ratio is $7 \pm 7\%$, which is consistent with zero.

Finally, the detector acceptance for Θ^+ for $Q^2 < 20$ GeV^2 is $0.5 \pm .03\%$, compared to 4% for $Q^2 > 20$ GeV^2. This rather low acceptance means that there is low sensitivity in the low Q^2 region. Hence a Θ^+ signal cannot be excluded in this region. However, it is possible that the suppression of the signal may also be related to its unknown production mechanism.

Kurzfassung

In der jüngeren Vergangenheit wurden von mehreren *fixed-target* Experimenten Hinweise auf die Existenz einer schmalen, baryonischen Resonanz in den Zerfallskanälen K^+n und K^0_Sp beobachtet, die als Pentaquark (Θ^+) interpretiert werden kann. In der vorliegenden Arbeit wird die Suche nach einer solchen Resonanz in der invarianten $K^0_Sp(\bar{p})$ Masse vorgestellt. Die verwendeten Daten wurden mit dem ZEUS Detektor bei HERA aufgenommen und entsprechen einer integrierten Luminosität von 121 pb^{-1}. Es wurde der Bereich zentraler Pseudorapiditäten in tiefinelastischer ep Streuung bei Schwerpunktsenergien von 300-318 GeV untersucht. Der kinematische Bereich ist auf Werte der Virtualität des ausgetauschten Photons von $Q^2 > 2$ GeV^2 beschränkt.

Die Ergebnisse der vorliegenden Arbeit unterstützen die Annahme der Existenz eines Θ^+-Zustandes. Für Photonvirtualitäten oberhalb von 20 GeV^2 wurde eine schmale Resonanz in der Verteilung der invarianten $K^0_Sp(\bar{p})$ Masse beobachtet. Die Anpassung der Parameter einer Gaußfunktion an die Daten ergaben eine Masse von $1521.5 \pm 1.6(\text{stat.}) \,^{+2.1}_{-2.6}(\text{syst.})$ MeV und eine Breite des Signals von $\sigma = 6.9 \pm 1.4(\text{stat.}) \,^{+2.4}_{-2.0}(\text{syst.})$ MeV, die etwas oberhalb der experimentellen Auflösung liegt, mit dieser aber verträglich ist. Es wurden 217$\pm$45 Signalereignisse beobachtet. Unter Verwendung verschiedener Annahmen über die Abhängigkeit des Untergrundes ergibt sich eine statistische Signifikanz des Signals von 3.5σ bis 4.8σ.

Es wurden mehrere Tests durchgeführt, anhand derer die Teilchenidentifikation, die mögliche Existenz von Reflektionen bekannter Zustände sowie die Stabilität des Signals bei 1522 MeV überprüft wurden, das in allen Tests bestand.

In Teilchenkollisionen bei hohen Energien werden Hadronen vorwiegend im Fragmentationsprozess erzeugt, wobei Teilchen und Antiteilchen in vergleichbaren Raten produziert werden. Daher wurden die K^0_Sp- und $K^0_S\bar{p}$-Massenspektren gesondert betrachtet. Auch im $K^0_S\bar{p}$-Kanal wurde eine Anreicherung beobachtet, zu der 75 ± 40 Signalereignisse beitragen. Interpretiert man das Signal in der K^0_Sp Massenverteilung als Pentaquark, könnte dies die erste Beobachtung des Antipentaquarks, $\bar{\Theta}^-$, darstellen.

Falls es sich bei dem Θ^+-Signal um einen Isotensorzustand handelt, erwartet man im invarianten K^+p Massenspektrum ein Signal des Isospinpartners Θ^{++}. Darüber hinaus können mittels des $\Lambda(1520)D_{03}$ Mesons, das ebenfalls im Zerfallskanal Kp rekonstruiert werden kann, Effizienzen und Auflösungen überprüft werden. Es wurde ein deutliches Signal im $K^-p(K^+\bar{p})$ Kanal bei $1518.5 \pm 0.6(\text{stat.})$ MeV beobachtet. Im Spektrum gleichgeladener Spuren konnte dagegen kein Signal beobachtet werden, welches man ausgehend von der Interpretation des Θ^+als Isotensor jedoch erwarten würde.

Das Θ^+-Signal wird vorwiegend bei positiven Pseudorapiditäten, im Vorwärtsbereich des Detektors, und im K^0_Sp-Kanal beobachtet, was die Frage aufwirft, ob

die Θ^+-Produktion in Verbindung mit der Fragmentation des Protonrestes stattfindet. Die vorliegenden Daten reichen jedoch nicht aus, um eine eindeutige Aussage zu treffen.

das Θ^+beobachtet wurde. Geht man davon aus, dass tatsächlich das Θ^+beobachtet wurde, können die Wirkungsquerschnitte für die Θ^+-Produktion bestimmt werden. Der totale Wirkungsquerschnitt für die Reaktion $\Theta^+(\bar{\Theta}^-) \rightarrow K^0 p(\bar{p})$ und der differentielle Wirkungsquerschnitt in Abhängigkeit von Q^2 wurden im kinematischen Bereich $0.04 < y < 0.95$, $p_T > 0.5$ GeV und $|\eta| < 1.5$ und für Photonvirtualitäten $Q^2 > 20$ GeV^2 gemessen. Der totale Wikrungsquerschnitt beträgt 130.0 ± 26.9(stat.) pb.

Des Weiteren werden die Θ^+-Wirkungsquerschnitte mit denen der Λ Baryonproduktion im gleichen kinematischen Bereich verglichen. Dabei werden zwei alternative Methoden zur Rekonstruktion der Λ Baryonen verwendet, einerseits unter Verwendung der dE/dx-Messung, andererseits anhand der Rekonstruktion des Sekundärvertex. Letztere wird dazu herangezogen, die Detektorakzeptanzen der dE/dx-Methode zu überprüfen und die Unsicherheit der K^0_S-Rekonstruktion zu bestimmen. Die mittels der beiden Methoden erhaltenen Wirkungsquerschnitte stimmen innerhalb von 6% miteinander überein. Für $Q^2 > 20$ GeV^2 variiert das Verhältnis der Θ^+/Λ Produktion von 4% bis 15% für verschiedene Q^2-Bereiche, während sich für $Q^2 < 20$ GeV^2 ein Verhältnis von 7 ± 7% ergibt, das mit null verträglich ist.

Die Detekorakzeptanz für das Θ^+ beträgt für $Q^2 < 20$ GeV^2 nur $0.5 \pm .03$%, im Vergleich zu 4% für $Q^2 > 20$ GeV^2. Diese recht niedrige Akzeptanz bedeutet, dass die Sensitivität bei kleinem Q^2 gering ist. Deshalb kann ein Θ^+ -Signal in dieeem Bereich nicht ausgeschlossen werden. Es ist jedoch auch möglich, dass die Unterdrückung des Signals mit dessen unbekanntem Produktionsmechanismus in Zusammenhang steht.

Two quarks, three quarks . . .

How about five quarks for Muster Mark?

Strange? Indeed!

Contents

Contents **i**

List of Figures **vii**

List of Tables **xi**

Introduction **1**

1 Theoretical overview **9**
1.1 Quantum Chromodynamics 10
1.2 High-energy *ep* collisions 10
1.2.1 Event kinematics 11
1.2.2 *ep* cross section and structure functions 12
1.3 Quark Parton Model 15
1.4 QCD corrections to Quark Parton Model 16
1.5 QCD factorization and parton densities 18
1.6 Strange particle production 19
1.6.1 Strange quark production in DIS 19
1.6.2 Hadron production in DIS 20
1.7 Pentaquark phenomenology 24
1.7.1 Chiral soliton model 24
1.7.2 The narrow width puzzle 25

2 The ZEUS detector at HERA **29**
2.1 HERA accelerator 30
2.2 ZEUS detector 31
2.3 Intermezzo: particle interactions in matter 36
2.4 Calorimetry and the Uranium Calorimeter (CAL) 37
2.5 Central Tracking Detector (CTD) 42

2.6 Small-angle Rear Tracking Detector (SRTD) 44
2.7 Luminosity Monitor (LUMI) 45
2.8 Background rejection 46
2.9 Data Acquisition (DAQ) 47
2.9.1 First Level Trigger (FLT) 48
2.9.2 Second Level Trigger (SLT) 48
2.9.3 Event Builder (EVB) 50
2.9.4 Third Level Trigger (TLT) 50
2.10 Offline reconstruction 50

3 Event simulation **53**
3.1 Physics simulation 54
3.2 Detector simulation 56
3.3 MC used in this analysis 58
3.3.1 NC DIS background 58
3.3.2 Pentaquarks 59

4 Event reconstruction **61**
4.1 Track reconstruction 61
4.1.1 Track finding 62
4.1.2 Track fitting 62
4.1.3 Vertex finding 63
4.2 CTD B-field correction 64
4.3 Ionization energy loss 65
4.3.1 Bethe - Bloch equation 65
4.3.2 Reconstruction of dE/dx 66
4.4 Global calorimeter quantities 68
4.4.1 Calorimeter noise supression 69
4.4.2 Calorimeter energy corrections 70
4.5 Energy Flow Objects (EFOS) 70
4.6 Electron reconstruction 71
4.7 Kinematic reconstruction 72

5 Event selection **75**
5.1 Data-set . . . 75
5.2 Online selection . . . 76
5.2.1 First Level Trigger . . . 77
5.2.2 Second Level Trigger . . . 78
5.2.3 Third Level Trigger . . . 78
5.3 Offline selection . . . 79
5.3.1 Electron identification . . . 79
5.3.2 Kinematic cuts . . . 80
5.3.3 Global cuts . . . 81
5.4 V0 requirement . . . 81
5.5 Control plots . . . 82

6 Particle identification **87**
6.1 Strange particle reconstruction . . . 88
6.2 K^0_S reconstruction . . . 88
6.2.1 Armenteros-Podolanski plots . . . 89
6.2.2 Extraction of the K^0_S signal . . . 90
6.2.3 K^0_S lifetime . . . 92
6.3 Λ reconstruction . . . 92
6.3.1 Extraction of the Λ signal . . . 93
6.3.2 Λ lifetime . . . 95
6.3.3 $\Lambda(\bar{\Lambda})$ asymmetry: background study . . . 95
6.4 K^0_S revisited with collinearity cut . . . 101
6.5 Proton identification . . . 103
6.5.1 Track requirements . . . 103
6.5.2 dE/dx requirements . . . 103
6.5.3 Momentum requirement . . . 107
6.5.4 dE/dx cut revisited . . . 108
6.6 Summary . . . 108

7 $K^0_S p(\bar{p})$ invariant mass **111**
7.1 $K^0_S p(\bar{p})$ reconstruction . . . 112
7.1.1 Detector resolution . . . 112
7.2 $K^0_S p(\bar{p})$ invariant-mass spectrum . . . 113
7.2.1 Extraction of signal parameters and significance . . . 113
7.2.2 Narrow width . . . 120

7.3 $\bar{\Theta}^-$: antipentaquark? . . . 120
7.4 Checks: pion contamination . . . 123
7.4.1 K^* cut . . . 123
7.4.2 Energy imbalance cut . . . 125
7.4.3 Energy imbalance and K^* cuts combined . . . 126
7.4.4 Pion enhancement . . . 127
7.5 Checks: kaon contamination . . . 129
7.6 More checks... . . . 129
7.7 Θ^+ production properties . . . 131
7.7.1 η dependence of Θ^+ production . . . 132
7.7.2 Θ^+: isotensor? . . . 132
7.8 Systematic uncertainties . . . 135
7.9 Summary . . . 136

8 Θ^+ cross section **139**
8.1 Cross-section definition . . . 140
8.2 Reminder: data sample and selection cuts . . . 140
8.2.1 DIS event selection . . . 140
8.2.2 Track selection . . . 141
8.2.3 Electron selection . . . 141
8.2.4 Θ^+ reconstruction . . . 141
8.2.5 Λ reconstruction . . . 142
8.3 Monte Carlo revisited . . . 143
8.4 Trigger revisited . . . 144
8.5 Θ^+ acceptance and cross section . . . 144
8.5.1 Low Θ^+ acceptance . . . 145
8.6 Λ acceptance and cross section . . . 147
8.7 Θ^+/Λ cross-section ratio . . . 150
8.8 Systematic uncertainties . . . 153
8.9 Summary . . . 155

Summary and discussion **159**

A ZEUS vertex reconstruction **167**
A.1 Primary vertex reconstruction 167
A.1.1 Simple vertex fit 167
A.1.2 Full vertex fit 167
A.2 Secondary vertex reconstruction 167
A.2.1 VFIND 168
A.2.2 VCTRAK multivertex mode 170

List of Figures

1 PDFs from the ZEUS NLO QCD fit 3
2 World average for Θ^+ mass 6

1.1 Kinematic variables of *ep* scattering 11
1.2 NC and CC cross sections as functions of Q^2 14
1.3 Illustration of scaling violation 16
1.4 F_2^{em} as a function of Q^2 for fixed values of x 17
1.5 Schematic illustration of string fragmentation in the Lund model . 21
1.6 Schematic illustration of diquark and popcorn models 22
1.7 Schematic illustration of cluster fragmentation model 23
1.8 Antidecuplet of pentaquark baryons 27

2.1 Aerial view of the DESY laboratory 29
2.2 Schematic view of the HERA accelerator 31
2.3 Integrated luminosity delivered by HERA 32
2.4 ZEUS coordinate system 33
2.5 Cross section of ZEUS detector along the beam axis 34
2.6 Cross section of ZEUS detector perpendicular to the beam axis . . 35
2.7 Showers in the calorimeter 37
2.8 Layout of an FCAL module 39
2.9 View of a CTD octant 42
2.10 Layout of a drift cell in the CTD 43
2.11 SRTD layout 44
2.12 Schematic illustration of ZEUS luminosity-measurement system . 45
2.13 ZEUS trigger and data acquisition system 49

3.1 Diagram of ZEUS data and MC reconstruction chain 54
3.2 Illustration of DIS process generation using DJANGOH 56
3.3 Diagram of ZEUS data and MC reconstruction chain 57

3.4 Feynman diagrams of Born level and LO QED corrections for NC DIS 58

4.1 Schematic illustration of the five-helix-parameter model 63
4.2 dE/dx versus momentum of well reconstructed tracks in the CTD 66
4.3 Typical dE/dx pulse for a low momentum pion exhibiting the Landau shape and saturation at high dE/dx. 67

5.1 Control Plots for DIS event selection: $Q^2, E_{el}, E - p_z$ 84
5.2 Control Plots for DIS event selection: Y_{el}, Y_{JB}, Z_{vtx} 85

6.1 Armenteros-Podolanski Plots 90
6.2 $\pi^+\pi^-$ invariant-mass distribution 91
6.3 Proper lifetime distribution, $c\tau$, for K^0_S 92
6.4 $p\pi$ versus $\pi\pi$ invariant mass for data and ARIADNE 94
6.5 $p\pi$ invariant-mass distribution 94
6.6 Proper lifetime distribution, $c\tau$, for Λ 96
6.7 $\mathrm{p}\pi^-$ and $\bar{\mathrm{p}}\pi^+$ invariant mass for data 97
6.8 Secondary vertex position y versus x of Λ and $\bar{\Lambda}$ candidates . . . 98
6.9 Secondary vertex radius of Λ and $\bar{\Lambda}$ candidates before and after collinearity cut 99
6.10 Secondary vertex position y versus x of Λ and $\bar{\Lambda}$ candidates after collinearity cut 99
6.11 Proper lifetime distribution, $c\tau$, for Λ after collinearity cut 100
6.12 $\mathrm{p}\pi^-$ and $\bar{\mathrm{p}}\pi^+$ invariant mass after collinearity cut 101
6.13 Secondary vertex radius of K^0_S candidates before and after collinearity cut 102
6.14 $\pi^+\pi^-$ invariant mass after collinearity cut 102
6.15 dE/dx distribution for tracks from primary vertex - Data 104
6.16 dE/dx distribution for tracks from primary vertex - ARIADNE . . 104
6.17 Distributions of proton and antiproton candidates' momenta after $f < dE/dx < F$ cuts 105
6.18 dE/dx distribution for tracks from Λ decays 106
6.19 ARIADNE predictions for number of p and $\bar{p}$ candidates after $f < dE/dx < F$ cuts 107

7.1 Schematic illustration of $K^0_S p$ reconstruction 112
7.2 $K^0_S p(\bar{p})$ invariant-mass spectra as functions of minimum Q^2 . . . 114

7.3 $K^0_S p(\bar{p})$ invariant-mass spectra in uncorrelated bins of Q^2 115
7.4 $K^0_S p(\bar{p})$ invariant-mass spectra with different fits: $Q^2 > 20$ GeV^2 117
7.5 $K^0_S p(\bar{p})$ invariant-mass spectra as functions of minimum Q^2 with fit 119
7.6 $K^0_S p(\bar{p})$ invariant-mass spectra in uncorrelated bins of Q^2 with fit 121
7.7 $K^0_S p(\bar{p})$ invariant-mass spectrum: natural width extraction 122
7.8 $K^0_S p$ and $K^0_S \bar{p}$ invariant-mass spectra 123
7.9 MC study of K^* cut 124
7.10 $K^0_S p(\bar{p})$ invariant-mass spectrum with K^* cut 125
7.11 $K^0_S p(\bar{p})$ invariant-mass spectrum with $E(p) > E(K^0_S)$ cut 126
7.12 Events rejected by $E(p) > E(K^0_S)$ and K^*-rejection cuts 127
7.13 $K^0_S p(\bar{p})$ invariant-mass spectrum with $E(p) > E(K^0_S)$ and K^*-rejection cuts 128
7.14 K^0_S $\pi^\pm$ invariant-mass spectra 128
7.15 K^0_S $K^\pm$ invariant-mass spectra 129
7.16 Comparison between ARIADNE, random-event selection and pion background 130
7.17 $K^0_S p$ and $K^0_S \bar{p}$ invariant-mass spectra and dependence on η 133
7.18 Proton and kaon selection with dE/dx 134
7.19 $K^\pm p(K^\pm \bar{p})$ invariant-mass spectra 135

8.1 $K^0_S p(\bar{p})$ invariant-mass spectra in data and RAPGAP MC in bins of Q^2 146
8.2 $\Theta^+(\bar{\Theta}^-) \to K^0 p(\bar{p})$ acceptance and cross section in bins of Q^2 . . 147
8.3 pπ invariant-mass spectra in data and ARIADNE MC in bins of Q^2 (dE/dx method) 148
8.4 pπ invariant-mass spectra in data and ARIADNE MC in bins of Q^2 (V0 method) 149
8.5 Acceptance and cross-section comparison for V0 and dE/dx Λ-baryons in bins of Q^2 151
8.6 Cross-section ratio for $\Theta^+ \to K^0 p$ to $\Lambda \to p\pi$ in bins of Q^2 152
8.7 $\Theta^+(\bar{\Theta}^-) \to K^0 p(\bar{p})$ cross section and associated uncertainty 155
8.8 Cross-section ratio for $\Theta^+ \to K^0 p$ to $\Lambda \to p\pi$ and associated uncertainty 156

A.1 Intersecting helical tracks in $x - y$ plane 169

List of Tables

1 Summary of experiments that see evidence for Θ^+ 5
2 Summary of experiments that do not see evidence for Θ^+ 5

2.1 Angular acceptance and longitudinal depth of the Calorimeter . . 40

3.1 MC samples for the simulation of NC DIS events and pentaquarks 60

5.1 HERA running conditions and ZEUS gated luminosities 76
5.2 Summary of DIS01 and DIS03 prescales and box cuts 80

6.1 Properties of K^0_S and Λ-hadrons 88

7.1 Results of the different fits to the $K^0_S p(\bar{p})$ invariant-mass spectrum for $Q^2 > 20$ GeV^2 118
7.2 Sensitivity of the $K^0_S p(\bar{p})$ mass and width measurements to changes in selection criteria 136

8.1 Cross sections for Λ-baryons 152
8.2 Cross sections for Θ^+-baryons and associated uncertainties 154

Introduction

The fundamental constituents of matter are quarks and leptons and the forces that bind them are electromagnetic, weak, strong and gravity. While the first three govern the microscopic world of atoms and the particles within, gravity governs the motions of cricket balls and galaxies. These forces are mediated via an exchange of field quanta which determine the properties of these interactions and are called bosons. There is the photon, γ, mediating the electromagnetic interaction, the three vector bosons, Z^0 and $W^{\pm}$, mediating the weak interaction, and eight gluons, g, mediating the strong interaction. The unified description of electromagnetism, described by Quantum Electrodynamics (QED), and the weak force is called the Electroweak Theory. The theory describing the strong force is called Quantum Chromodynamics (QCD). And the combined suite of theories is called the Standard Model (SM). See for example, [1].

The way to the establishment of QCD was paved by Doctors Gross, Politzer and Wilczek for their hypothesis of asymptotic freedom, according to which the gluon-mediated interaction between quarks inside particles gets weaker the closer the quarks are to each other and stronger the farther apart they are. The reason for this strange behavior, the three physicists clarified, was that unlike photons, gluons carried their own "color" charge and, as a result, could interact with each other such that at high probing energies the interaction became weak. The consequence of asymptotic freedom is that quark interactions at high energies can be interpreted as interactions amongst "free" constiquents. This is why "free" quarks are only observed in high-energy collisions or, conversely, never seen in nature. For their role in explaining the strong force, Gross, Politzer and Wilczek were awarded the Nobel prize in physics in 2004.

According to the constituent quark model, hadrons are classified as composites of $q\bar{q}$ (meson) or qqq (baryon) states. Both contain the minimal quark content required to produce an overall color singlet, compatible with the

experimental data on color confinement. However QCD does not exclude the existence of other color-neutral quark configurations such as tetraquarks ($qq\bar{q}\bar{q}$), pentaquarks ($qqqq\bar{q}$), etc., or states including gluons, such as glueballs (gg) or hybrids ($q\bar{q}g$).

For example, one can always add extra color-singlet $q\bar{q}$-pairs or qqq-triplets to any color-singlet combination and rearrange the internal color structure to obtain a new and allowed color-singlet state. However these new multi-quark states will decay rapidly to $q\bar{q}$ and qqq states and be sufficiently broad as to go undetected in experiment. This is a result of the trivial requirement on the internal color rearrangement to convert a state into two or more color-singlet states which are then free to separate (unless prevented by some other symmetry or kinematics). The problem with the above requirement is that in hadronic QCD - a strongly interacting regime - internal color rearrangement is not expected to be suppressed.

Actually the concept of a baryon composed of three constituent quarks is certainly oversimplified and the hadronic properties of baryons cannot be understood or, at least, are not yet fully understood in terms of quarks and their interactions. Deep Inelastic Scattering (DIS) experiments such as ZEUS examine the proton at small momentum fractions, x, or high photon virtuality, Q^2, with far-off-mass-shell photons and find there to be a much richer quark and antiquark structure. This is because a color and flavor singlet $q\bar{q}$-pair can always be added to a baryon without changing its overall quantum numbers, such that it can be considered to have a schematic quark Fock state expansion,

$$|B\rangle \;\approx\; |qqq\rangle\,(1 \;+\; a_1|q\bar{q}\rangle \;+\; a_2|q\bar{q}q\bar{q}\rangle \;+\; \ldots)\,. \qquad (1)$$

Hence the reason baryons are thought to be composed of qqq only is because this is the minimal (valence) quark content that is required to make up the quantum numbers. This dominance of the tri-quark state is seen when protons are examined at low Q^2 or with near on-shell (quasi-real) photons. Figure 1 shows the parton distribution functions (PDFs) extracted from ZEUS and H1 next-to-leading order (NLO) QCD analyses of DIS data. As can be seen from the figure, the u and d quarks are roughly peaked near to a momentum fraction of $1/3$ and the peak amplitude for u is close to twice that of d. What is also clear is that sea-quarks, which signal the extra $q\bar{q}$-pairs, are non-zero only for small

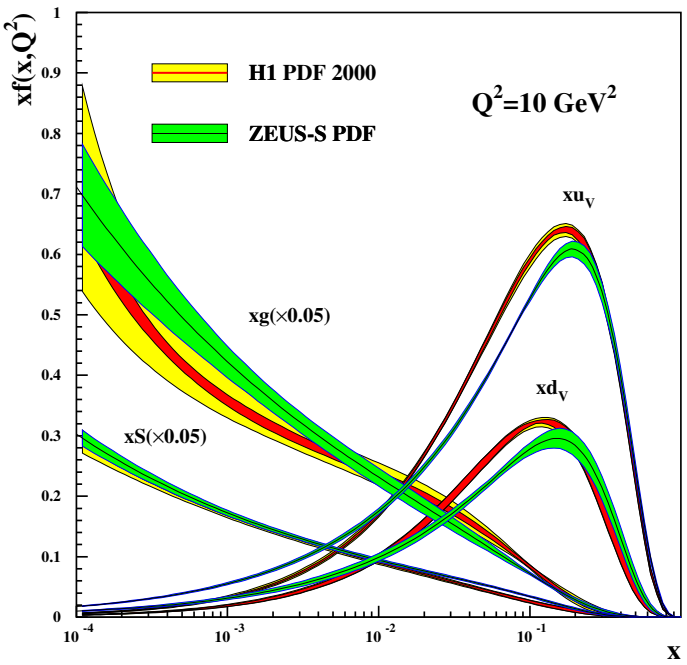

Figure 1: The gluon, sea, u and d valence distributions extracted from the ZEUS and H1 NLO QCD fits at $Q^2 = 10$ GeV^2 (from [2]).

momentum fractions and, at high x, have much smaller amplitudes than do the quark distributions.

Constituent quark models, which give best description of scattering data, treat mesons and baryons only in terms of their minimal quark content and give the valence quarks large masses (for $u, d \approx 350$ MeV), as a result of which, additional on-shell (real) $q\bar{q}$-pairs are suppressed. Furthermore, while these models have been successful in predicting properties of hadrons which might be described as on-shell, such as masses, decay rates and magnetic moments, they do not describe the high-Q^2 or very small-x DIS observations.

But what happens if a non-flavor-singlet $q\bar{q}$-pair is added to a qqq-triplet? For example, consider adding $s\bar{u}$ to udd. Since QCD allows annihilation of the $u\bar{u}$-pair, a state with quark content of sdd will remain. This is equivalent to adding a flavor singlet ($u\bar{u}$) to a $\Sigma^-(sdd)$ state. On the other hand, what if a $u\bar{s}$ state is added to udd? The $q\bar{q}$-pair can no longer be annhilated and the resulting state has a minimal five quark content, $uudd\bar{s}$.

Such a baryon cannot be composed of qqq as it has strangeness of $+1$, and therefore it is a flavor-exotic pentaquark. Hence the observation of such a state requires no model-dependent analysis of its properties to determine its pentaquark nature as it is manifestly exotic in its flavor quantum numbers.

However, as discussed earlier, the general problem with multi-quark hadrons still remains: by a simple internal color rearrangement a $uudu\bar{s}(uudd\bar{s})$ state can become an $nK^+(pK^0)$ state. In the constituent quark model, this pentaquark would have a mass of around 1750 MeV and hence considerable phase space for the unsuppressed decay to $nK^+(pK^0)$. Hence this state would be unobservable due to its large width [3].

In spite of the arguments presented above, the years 2003 and 2004 have seen a renaissance of hadron spectroscopy. There were many reports of discoveries of exotic narrow resonances including those of the celebrated strange pentaquarks, Θ^+ [4–14] and $\Xi^{--}(1862)$ [15], the charmed pentaquark, $\Theta_c(3099)$ [16], a charmonium state $X(3872)$ [17] and a new $D_S(2632)$-meson [18]. While the signal for $X(3872)$ has been seen by several experiments, no experiment has been able to validate $\Xi^{--}(1862)$ and $\Theta_c(3099)$. For example, the negative ZEUS results can be found in [30, 31].

Amongst the observations mentioned above, Θ^+ ($\rightarrow nK^+(pK^0_S)$[1]), with quark content $uudd\bar{s}$, was the most striking event. It was discovered in a seminal experiment performed by the LEPS group at the SPring-8 facility in Harima, Japan [4]. LEPS investigated the reaction $\gamma n \rightarrow K^- + \Theta^+ \rightarrow K^- + K^+ + n$ with the neutron from a ^{12}C nucleus. In the missing mass spectrum they found a peak at 1540 ± 10 MeV with a width below 25 MeV at a statistical significance of 4.6 σ. This search was motivated by the theoretical prediction of a narrow $S = +1$ baryon, by Diakonov, Petrov and Polyakov (DPP) [46], in which the narrow width arises from constraints by symmetries of the coupling constants and the phase space of the decay to a KN final state. This is discussed in more detail in chapter 1.

The observation of Θ^+ by LEPS has generated a flurry of experiments. To date, there are 10 experiments that claim to see a Θ^+ signal in both the $K^0_S p$ and $K^+ n$ channels and 10 experiments which do not. See Tables 1 and 2 below.

One puzzle is that, with the exception of the ZEUS result, most observations of Θ^+ are at relatively low energies suggesting that exotic baryons may have

[1] $|K_S\rangle \sim (|K^0\rangle + |\bar{K^0}\rangle)/\sqrt{2}$

Ref.	Group	Reaction	Mass (MeV)	Width (MeV)	σ	S
[4]	LEPS	$\gamma n \to K^-(K^+n)$	1540 ± 10	< 25	4.6	K^+n $(S=+1)$
[5]	CLAS	$\gamma d \to pK^-(K^+n)$	1542 ± 5	< 21	5.2	K^+n $(S=+1)$
[6]	CLAS	$\gamma p \to \pi^+K^-(K^+n)$	1555 ± 10	< 26	7.8	K^+n $(S=+1)$
[7]	SAPHIR	$\gamma p \to K^0_S\ (K^+n)$	1540 ± 6	< 25	4.8	K^+n $(S=+1)$
[8]	DIANA	$K^+Xe \to Xe'(K^0_S\ p)$	1539 ± 2	< 9	4.4	K^0_Sp $(\lvert S\rvert=1)$
[9]	ITEP	$\nu A^* \to X(K^0_S\ p)$	1533 ± 5	< 20	6.7	K^0_Sp $(\lvert S\rvert=1)$
[10]	SVD	$pA^{**} \to X(K^0_S\ p)$	1526 ± 5	< 24	5.6	K^0_Sp $(\lvert S\rvert=1)$
[11]	HERMES	$e^+d \to X(K^0_S\ p)$	1526 ± 3	13 ± 9	~ 5	K^0_Sp $(\lvert S\rvert=1)$
[12]	COSY-TOF	$pp \to \Sigma^+(K^0_S\ p)$	1530 ± 5	< 18	4-6	K^0_Sp $(\lvert S\rvert=1)$
[13]	YEREVAN	$pC_3H_8 \to Xp(K^0_S\ p)$	1545 ± 12	< 34	5.5	K^0_Sp $(\lvert S\rvert=1)$
[14]	ZEUS	$e^\pm p \to e^\pm X(K^0_S\ p(\bar{p}))$	1522 ± 2	8 ± 4	~ 5	K^0_Sp $(\lvert S\rvert=1)$

Table 1:
Summary of experiments that see evidence for Θ^+.
$^*A: H,\ d,\ NH-\text{mix},\ NH_2-\text{mix}$ $\quad$ $^{**}A: C,\ Si,\ Pb$

Ref.	Group	Reaction	Limit
[19]	BES	$e^+e^- \to J/\Psi(\Psi(2S)) \to K^0_Sp K^-\bar{n}$ & $K^0_S\bar{p}K^+n$	$< 1.1 \times 10^{-5}$ B.R.
[20]	Belle	$e^+e^- \to \Psi(2S) \to B^0\bar{B}^0 \to \bar{p}(K^0_S\ p)$	$< 2.3 \times 10^{-7}$ B.R.
[21]	BaBar	$e^+e^- \to \Upsilon(4S) \to B\bar{B} \to X(K^0_S\ p)$	$< 1.0 \times 10^{-4}$ B.R.
[22]	ALEPH	$e^+e^- \to Z \to (K^0_S\ p)$	$< 6.2 \times 10^{-4}$ B.R.
[23]	CDF	$p\bar{p} \to X(K^0_S\ p)$	$< 0.03 \times \Lambda^*$
[24]	E871	$pCu \to X(K^0_S\ p)$	$< 2.5 \times 10^{-3}$ B.R.
[25]	HERA-B	$pA^* \to X(K^0_S\ p)$	$< 0.02 \times \Lambda^*$
[26]	PHENIX	$AuAu \to X(K^-\bar{n})$	(not given)
[27]	CLAS	$\gamma p \to K^0_S(K^+n)$	(not given)
[28]	H1	$e^\pm p \to e^\pm X(K^0_S\ p(\bar{p}))$	< 120 pb**

Table 2:
Summary of experiments that do not see evidence for Θ^+.
$^*A: C,\ Ti,\ W$ $\quad$ ** depending on $K^0_Sp(\bar{p})$ invariant mass

production mechanisms that are different from those of conventional baryons. Furthermore, for the experiments with positive results, the masses and decay widths vary but are compatible between experiments. It seems that observations of the Θ^+ in the K^+n final state tend to yield higher masses than do observations in the K^0_Sp final state, as seen in figure 2. One thing to bear in mind is that while, the K^+n channel fixes strangeness, K^0_Sp does not unless an additional K or Σ is

found. Also, for these experiments, the reaction mechanisms, which are listed in the table above, vary. While a kinematic reflection or a cusp effect could affect one reaction channel, it would be difficult to find a mechanism that could create a false peak in all cases. However, it should be noted that some experiments require harsh cuts which, in combination with detector acceptance, could create unexpected structures in the mass spectra. Also in some cases, the shape of the background under the peak is not well known, which could affect the statistical significance and the value of the measured mass.

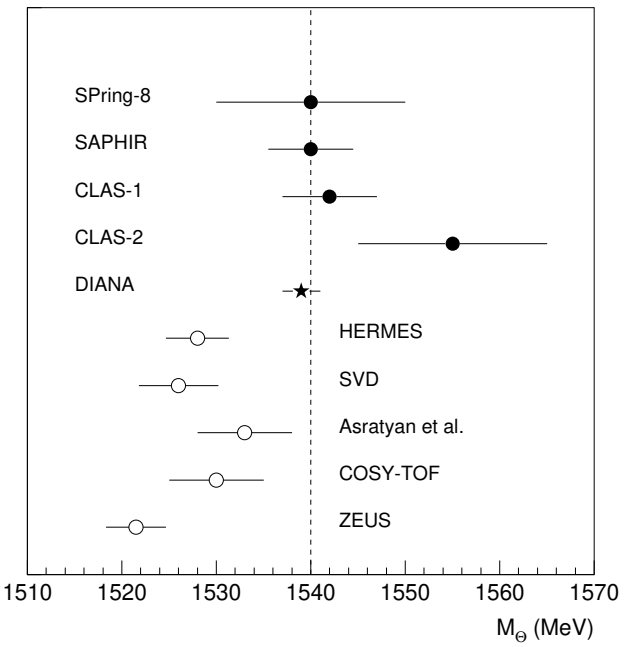

Figure 2: The mass of the Θ^+ measured in K^+n final states (solid circles) tends to be larger than in $K^0_s p$ final states (open circles). DIANA is an experiment that connects $K^+n \to K^0_S p$ [29].

The experiments that do not make observations of Θ^+, can be separated into two categories: e^+e^- production, where there are no quarks and gluons in the initial state, and high-energy $p\bar{p}$ or pA collisions, where the multiplicity of particles in the final state is typically large. In the case of e^+e^- annihilation, baryon-antibaryon production has a lower probability than meson pair production.

If the Θ^+ exists, no reasonable theoretical prediction is available for the

probability of its production. None of the models are able to convincingly explain, simultaneously, its low mass, narrow width and its production mechanism. Hence the proof of its existence is an experimental issue, requiring high-statistics experiments. And if the Θ^+ is confirmed, then a new landscape of multi-quark hadrons will have emerged. Then it will be imperative to answer the above questions.

The main purpose of this thesis is to describe the Θ^+ search carried out by ZEUS. The thesis is organized as follows: The first chapter lays out the theoretical background relevant to this analysis, including a brief description of hadronization models and pentaquark phenomenology. The second chapter describes the HERA collider and the ZEUS-detector components used in this analysis. The Monte Carlo simulations of the signal and background processes are explained in chapter three, while chapter four describes the reconstructed variables used in this analysis. Chapter five details the dataset and event selection and chapter six, the identification and reconstruction of K^0_S and Λ-hadrons and protons. The search for Θ^+ and its presumed observation is presented in chapter seven. The Θ^+ cross section and its ratio to that of the $\Lambda(1116)$ are presented in chapter eight. This thesis concludes with a summary and discussion section, which also provides a brief outlook for the on-going high-luminosity HERA II data-taking period and the improved tracking capabilities of a new Silicon Microvertex Detector (MVD) installed in the ZEUS detector.

Chapter 1

Theoretical overview

The fundamental properties of pentaquarks, described in the introduction, and the way in which they form are not known. In fact, their existence is still debated. Regardless of whether this picture of a baryon composed of four quarks and one antiquark turns out to be correct, the possibility of such states is offering exciting new insights into the subtleties of the strong interaction, described by the theory of Quantum Chromodynamics (QCD).

QCD is a "colorful", well-defined theory with a small number of parameters. It has survived rigorous experimental tests and independent measurements, but it has limitations. The problem is that the equations of the theory are very difficult to solve. And their most interesting consequence is that neither quarks nor gluons can appear in isolation. This property of QCD involves complex and nonlinear dynamics. While there are circumstances in which quantitative predictions can be made directly from the fundamental theory, there are also many physically important questions that cannot be answered quantitatively.

In other words, QCD does a good job of predicting, at the high energy scale, the properties of quarks and gluons, and of the "jets" of hadrons that they leave behind. However, it is not able to describe the way that quarks and gluons bind together to form hadrons. QCD does not provide a quantitative means of calculating the masses and properties of familiar particles such as protons, neutrons and pions from first principles, not to mention their many baryon and meson relatives. Neither does it provide analytical means to understand, for example, the production of particles containing strangeness. To address these questions, theorists have to turn to lattice calculations or phenomenological models, which can only be confirmed or dismissed by high-energy scattering experiments.

To this end, the first portion of this chapter provides a brief theoretical introduction to QCD. The portion that follows concentrates on the physics being conducted at HERA, whereby physics of lepton-proton scattering is described. This is followed by a description of the specific physics processes relevant to this thesis, such as the phenomenology of strange particle production and the strange pentaquark, Θ^+.

1.1 Quantum Chromodynamics

The theory of Quantum Chromodynamics describes the interactions of colored particles, i.e. quarks and gluons. QCD has a unique feature, which is that it is a non-Abelian gauge theory based on the $SU(3)$ color symmetry group. Simply put, the gluons are not color neutral, hence they couple to each other, a consequence of which is that the coupling of these strong interactions, α_s, gets stronger as the distance increases. It is this "running" of α_s that explains why quarks are permanently confined within hadrons, yet behave like free particles when probed at high momentum in deep inelastic scattering (DIS) experiments. This means that at very small distances (large momentum transfer), quarks behave as if they were essentially free, non-interacting fermions. Consequently, in the high-energy limit, as α_s becomes small, leading to asymptotic freedom, quantities which do not depend on the long distance behavior of the theory are calculable as a perturbative expansion in the coupling.

1.2 High-energy ep collisions

The justification for the use of perturbative QCD rests to a large extent directly on experiment. High-energy scattering experiments provide a good test of QCD. The Hadron Elektron Ring Anlage (HERA) collides highly energetic beams of protons, known to be composite particles, with constituents held together by the strong force, with beams of electrons or positrons[1]. In these collisions, the electron interacts with the proton via the exchange of an electroweak gauge boson. If the boson is highly virtual, it can be seen as a point-like object probing the inner structure of the proton and the forces that bind it. This exchanged boson can be

[1]The term 'electron' denotes both electrons (e^-) and positrons (e^+), unless stated otherwise.

an electrically neutral particle, such as a γ or a Z^0, in which case the interaction is termed Neutral Current (NC). The exchange can also be via an electrically charged $W^{\pm}$ particle, in which case the interaction is termed Carged Current (CC). In Neutral Current events, the resulting final-state lepton is an electron, while in Charged Current events it is a neutrino, which can only be detected via missing energy and momenta.

1.2.1 Event kinematics

The event kinematics, as seen in figure 1.1, are described by the incoming and scattered lepton 4-momenta, k and k', respectively, and the 4-momenta of the incoming proton and the final hadronic state, p and p', respectively. Thus the

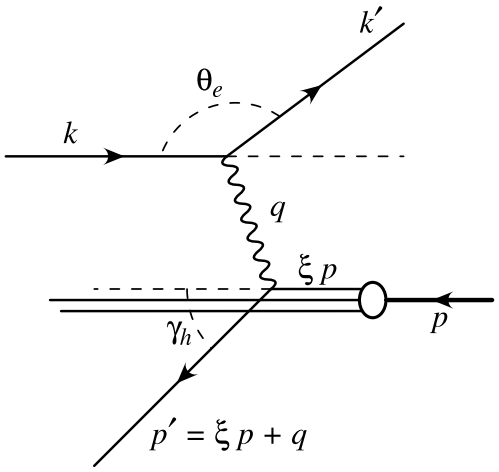

Figure 1.1: Generic diagram of ep scattering, showing the scattered lepton at an angle θ_e and the struck quark of the proton at an angle γ_h to the proton beam direction.

event kinematics can be described in terms of the following Lorentz invariant variables:

- $s = (k + p)^2$, center-of-mass energy squared of the electron-proton system
- $Q^2 \equiv -q^2 = -(k - k')^2$, virtuality of the exchanged boson, where, $0 \leq Q^2 \leq s$

- $x \equiv \frac{Q^2}{2p.q}$, Bjorken scaling variable, where $0 \leq x \leq 1$ (ξ in figure 1.1)
- $y \equiv \frac{p.q}{p.k}$, inelasticity or the relative energy transfer from the electron to the proton in the proton's rest frame where $0 \leq y \leq 1$
- $W^2 = (q + p)^2$, center-of-mass energy squared of the outgoing hadronic system.

When the masses of the particles can be neglected, four of the variables are related by the equation $s = Q^2/xy$. The center-of-mass energy, $\sqrt{s}$, is fixed at HERA to a value of 318 (300) GeV by the beam energies of 27.5 GeV and 920 (820) GeV from 1998-2000 (1994-1997) for electrons and protons, respectively. Consequently, only two of the three invariants x, y or Q^2 are actually independent. Thus, at any given value of s, the kinematic variables x, y and Q^2 can be reconstructed from any two of the four measured quantities: the angles and the measured energies of the scattered electron and struck quark. The Q^2 of the interaction characterizes how energetic the reaction is, and therefore at what scale the structure of the proton is probed. High Q^2 means that the proton structure is probed at a very small distance scale.

Deep inelastic scattering processes are characterized by values of Q^2 that are larger than 1 GeV^2. Here *deep* means "virtual enough to probe the contents of the nucleon" ($Q^2 \gg M_p^2$), and *inelastic* means "to probe some internal process" ($W^2 \gg M_p^2$), in contrast with *elastic*, whereby the colliding particles only exchange some share of their energies and momenta. In this scheme, photoproduction is defined to be the region where $Q^2 \approx 0$ and the photon is quasi-real. Thus far, HERA data cover a Q^2 region of up to 40 000 GeV^2, corresponding to a resolvable distance scale of $\lambda \approx \hbar c/\sqrt{Q^2} = 10^{-18}$ m, which is 1/1000 of the proton radius.

1.2.2 ep cross section and structure functions

The general form of the inclusive DIS cross section can be factorized into a leptonic tensor $L_{\mu\nu}$ and a hadronic tensor $W^{\mu\nu}$ (for instance see [34]):

$$d\sigma \propto L_{\mu\nu} W^{\mu\nu} \, . \tag{1.1}$$

The leptonic tensor, which is symmetric in μ and ν and can be calculated using QED, can be written as:

$$L_{\mu\nu} = \frac{1}{2}\sum_{e\ spins}[\bar{u}(k')\gamma^{\mu}u(k)][\bar{u}(k')\gamma^{\nu}u(k)]^{\star}\ , \tag{1.2}$$

where $u(k)$ and $\bar{u}(k')$ are the incoming and outgoing four-momenta of the electron, respectively and γ^{μ} and γ^{ν} are the Dirac matrices. The hadronic tensor can be parameterized using a combination of tensors as

$$\begin{aligned} W^{\mu\nu} &= -W_1 g^{\mu\nu} + \frac{W_2}{M^2}p^{\mu}p^{\nu} - i\frac{W_3}{M^2}\varepsilon^{\mu\nu\lambda\rho}p^{\lambda}q^{\rho} \\ &\quad + \frac{W_4}{M^2}q^{\mu}q^{\nu} + \frac{W_5}{M^2}(p^{\mu}q^{\nu} + p^{\nu}q^{\mu})\ , \end{aligned} \tag{1.3}$$

where p and q are the momenta, M is the mass of the proton and W_i are functions of the two independent scalars q^2 and $p\cdot q$. The antisymmetric terms have been left out as they drop out after insertion into 1.1. Current-conservation argument ($\partial_{\mu}J^{u}=0$) requires $q_{\mu}W^{\mu\nu}=q_{\nu}W^{\mu\nu}=0$, yielding the following constraints on the Lorentz scalars:

$$W_5 = -\frac{p\cdot q}{q^2}W_2 \quad \text{and} \quad W_4 = \left(\frac{p\cdot q}{q^2}\right)^2 W_2 + \frac{M^2}{q^2}W_1\ . \tag{1.4}$$

Their more common definitions are:

$$F_1(x,Q^2) = M\cdot W_1(x,Q^2) \tag{1.5}$$

$$F_2(x,Q^2) = \frac{Q^2}{2Mx}\cdot W_2(x,Q^2) \tag{1.6}$$

$$F_3(x,Q^2) = \frac{Q^2}{2Mx}\cdot W_3(x,Q^2)\ . \tag{1.7}$$

Now the inclusive differential cross section for inelastic electron-proton scattering, $ep\rightarrow eX$ can be written as:

$$\frac{d\sigma}{dE'_e d\Omega} = \frac{\alpha^2}{q^4}\frac{E'_e}{E_e}L_{\mu\nu}W^{\mu\nu}\ , \tag{1.8}$$

where E_e and E'_e are the incoming and outgoing electron energies, respectively. Substituting the above calculated tensor terms in equations 1.5 - 1.7 into Eq. 1.8 one obtains the NC ep cross section:

$$\frac{d^2\sigma^{NC}(e^{\pm}p)}{dxdQ^2} = \frac{4\pi\alpha^2}{xQ^4}\left[(Y_+F_2(x,Q^2) - y^2F_L(x,Q^2) \mp Y_-xF_3(x,Q^2)\right]\ , \tag{1.9}$$

where $F_L = F_2 - 2xF_1$ and $Y_\pm = 1 \pm (1-y)^2$.

In the above cross section, F_2 provides the main contribution to the NC cross section. F_L is the contribution from the absorption of a longitudinally polarized photon ($= 0$ in the Quark Parton Model). F_3 is the parity-violating contribution coming from both, the pure exchange of the massive propagator Z^0 and from the quantum mechanical interference between $\gamma - Z$, and is small for $Q^2 \ll M_Z^2$. It is important at large x and Q^2, where it substantially reduces (increases) the e^+p (e^-p) cross section.

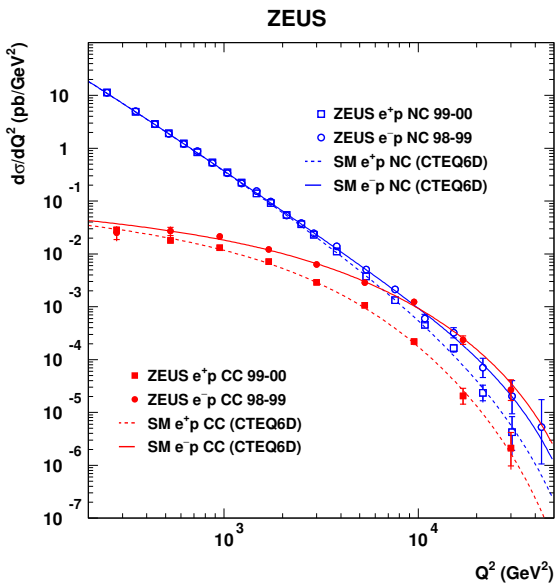

Figure 1.2: NC and CC cross sections as functions of Q^2 (from [2]).

Figure 1.2 shows the differential NC and CC cross sections measured by the ZEUS collaboration as a function of Q^2 for $e^\pm p$ scattering. In the kinematic range of $Q^2 \ll M_Z^2$ GeV^2, photon exchange is the dominant process because the cross section for the exchange of massive $W^\pm$ and Z bosons is suppressed with respect to that of photon exchange by the ratio of the propagators squared, i.e.:

$$\frac{\sigma(Z, W^\pm)}{\sigma(\gamma)} \approx \left(\frac{Q^2}{Q^2 + M_{Z,W}^2}\right)^2 . \tag{1.10}$$

Consequently, the CC cross section is suppressed with respect to the NC cross section until Q^2 reaches values close to the vector boson masses ($\mathcal{O}(10^4 \text{GeV}^2)$). In

this region, $\gamma - Z^0$-interference becomes important and leads to sizeable deviations from a pure QED prediction.

1.3 Quark Parton Model

The Quark Parton Model (QPM) describes DIS as the incoherent sum of elastic scattering processes of the lepton from an effectively point-like constituent within the proton. In this model, the DIS process is described as the quasi-elastic scattering of the exchanged gauge boson off a single quark in the proton. In QPM, the Bjorken scaling variable, x, represents the fraction of the proton's momentum carried by the struck quark. If the quarks are assumed to be non-interacting, static particles confined within the proton, then the structure functions can be expected to be a function of x but not of Q^2, since changes in Q^2 correspond to changes in the scale probed by the exchanged boson, which will be irrelevant for point-like constituents; i.e. $F_i(x, Q^2) = F_i(x)$. This behavior, originally proposed by Bjorken in the limit $Q^2 \to \infty$ and finite x, is known as *scale invariance*.

In QPM, the structure function F_2 can be expressed in terms of the parton density functions f_i as

$$F_2(x) = x \sum_i e_i^2 f_i(x) \; , \tag{1.11}$$

where e_i is the charge of parton i and $f_i(x)dx$ is the probability of finding a parton of type i in the momentum range between x and $x + dx$. For spin-$\frac{1}{2}$ partons the Callan-Gross relation [35],

$$F_2(x) = 2xF_1(x) \quad \Rightarrow \quad F_L = 0 \; , \tag{1.12}$$

holds since, in head-on collisions, longitudinally polarized photons only couple to spin-0 particles while transverse photons only couple to spin-$\frac{1}{2}$ particles. Furthermore, experiments show that [36]

$$\sum_i \int_0^1 x f_i(x) dx \approx 0.5 \; , \tag{1.13}$$

implying that only half of the proton's momentum is carried by charged quarks. The other half is carried by neutral partons which are identified with gluons. Direct experimental evidence for the existence of gluons was found in 1979 at DESY via the observation of three-jet events in e^+e^- annihilation [37].

1.4 QCD corrections to Quark Parton Model

The QPM, as described in the previous section, has been quite successful in kinematic regions where the effects of gluons can be neglected. However, the QPM is not enough to describe the effects observed at HERA. In this kinematic region, the QPM needs to be modified in order to include coupling of quarks to gluons - as required by QCD. This means that quarks can radiate gluons which in turn can split into $q\bar{q}$-pairs. (Such quarks are called "sea" quarks). In such a case, the number of partons increases while the average momentum per parton decreases. With increasing Q^2, more and more of these fluctuations can be resolved as illustrated in figure 1.3.

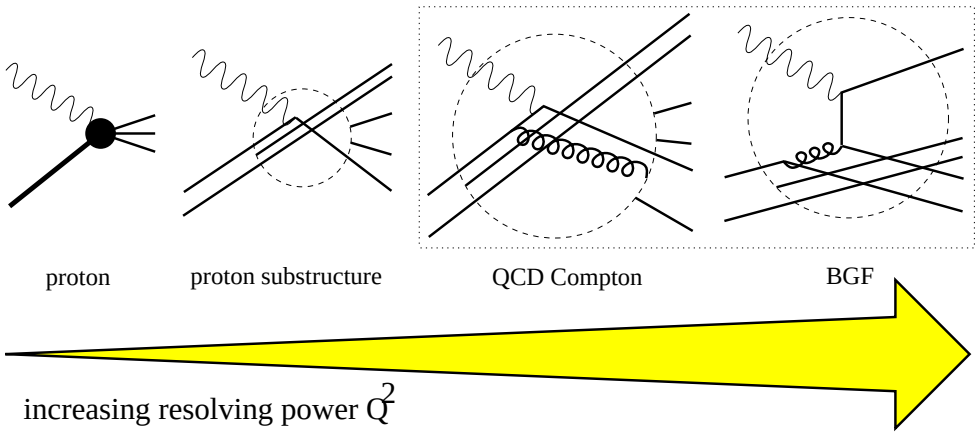

Figure 1.3: Illustration of scaling violation. Processes such as gluon radiation (QCD Compton) or quark-antiquark splitting (Boson Gluon Fusion) can be resolved with increasing Q^2.

At high x, the cross section is sensitive mainly to the valence quarks. The energy and momentum of the valence quarks will fall with increasing Q^2 due to gluon radiation, resulting in *scaling violation* and a decrease in the cross sections. At low x, gluon radiation leads to more gluons and quark-antiquark pairs in the proton, so this scaling behavior is not obeyed and the cross sections will rise with increasing Q^2. This can clearly be seen in figure 1.4 which shows the structure function F_2^{em} measured as a function of Q^2 for fixed values of x [2]. F_2^{em} is the purely electromagnetic part of the F_2^{NC} structure function. For x of ~ 0.1, F_2^{em} is approximately independent of Q^2.

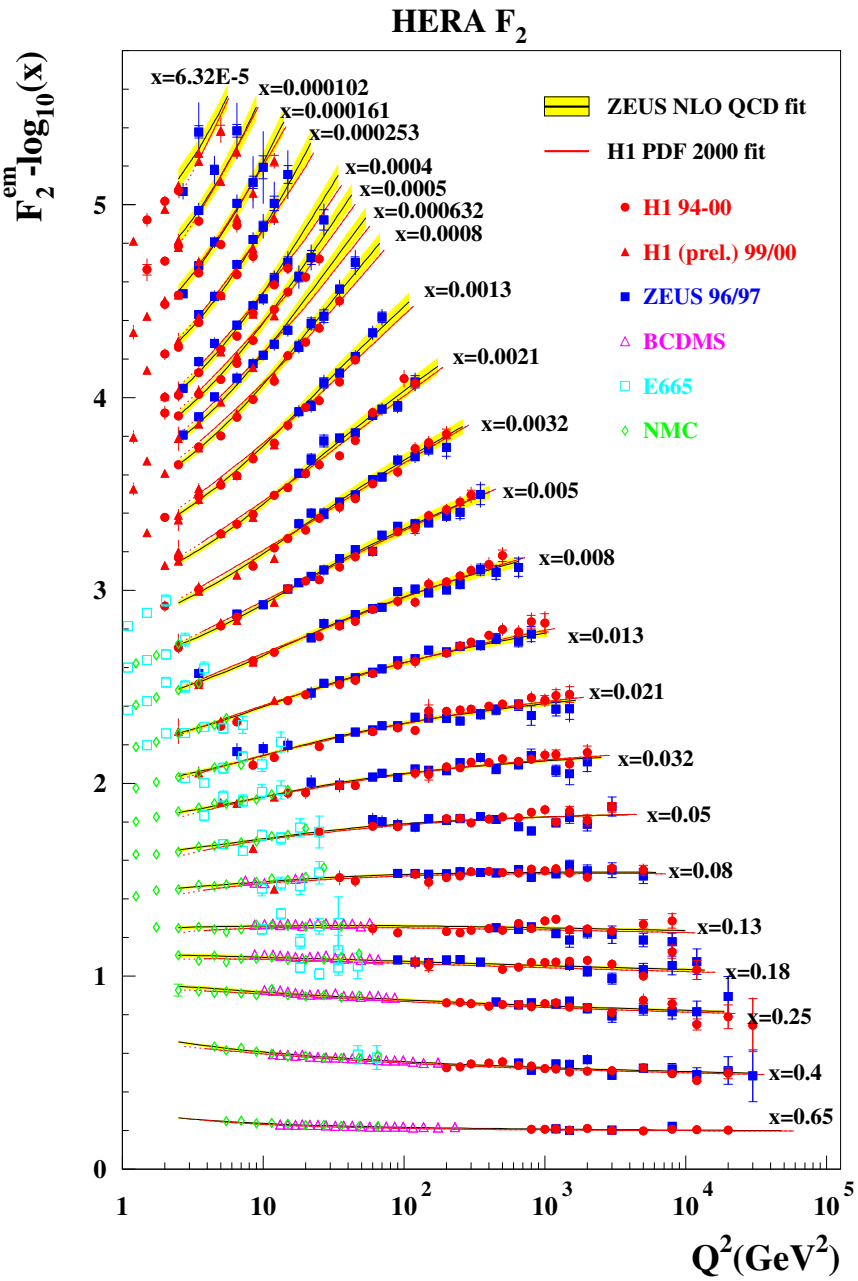

Figure 1.4: The structure function F_2^{em} as a function of Q^2 for fixed values of x. Results from ZEUS are shown together with fixed target results and NLO QCD fits. For $x \approx 0.1$, F_2^{em} is constant as Q^2 changes by 4 orders of magnitude. For smaller x values, F_2^{em} is observed to increase logarithmically with Q^2.

Gluon radiation also results in a transverse momentum component of the quarks which can consequently couple to longitudinally polarized photons. The Callan-Gross relation is thus no longer satisfied exactly and F_L is different from zero.

1.5 QCD factorization and parton densities

The distribution of partons in hadrons cannot be calculated from first principles within perturbation theory. However, the *factorization* theorem of QCD allows the separation of the non-perturbative long-range contribution (soft process) from the short-range contribution (hard process) which is calculable in perturbative QCD:

$$\sigma_{ep}(x, Q^2) = \sum_{i \in partons} f_{i/p}(x, \mu_F^2) \otimes \sigma_{ei}(x, Q^2, \mu_F^2) \; . \tag{1.14}$$

The parton density functions (PDFs), $f_{i/p}$, give the probability of finding a quark, q, with momentum fraction x at a given Q^2, and the σ_{ei} are the hard-scattering cross sections describing the short-range interactions. The PDFs have to be determined by global fits to measured experimental data sets. The factorization scale, μ_F, defines the scale at which the gluon radiation is absorbed into the PDFs or into the hard scattering cross section, hence it determines the line of separation between what is considered to be the long-range inner dynamics of the proton ($f_{i/p}$) and the dynamics of the hard lepton-parton interaction (σ_{ei}).

The PDFs are parameterized in x at a fixed starting value of Q^2 and can then be evolved using the DGLAP equations [38] to all points in Q^2 where perturbative QCD is applicable. These equations use the measured values of the PDFs at a given scale to predict their evolution to some new scale and the knowledge of the evolution of the PDFs can be exploited to determine them experimentally. If the perturbative part is calculated and the cross section of a certain process is measured, the PDF can be extracted from the data. The factorization theorem of QCD states that the PDFs are process independent. Once determined for a given process, they can be used to make a prediction for another process. For the small-x regime with a finite Q^2, another scheme called BFKL [39] is used for parton evolution. Figure 1 in the introduction shows the PDFs extracted from ZEUS and H1 NLO QCD analyses of DIS data [2]. As can be seen from the figure, the u and d valence-quark densities dominate at large values of $x \gtrsim 0.3$, while sea-quarks and gluons become important only at lower values of x.

1.6 Strange particle production

So far the discussion has been focused on the initial state and the hard scatter and no mention has been made of baryon and meson production in the final state. As mentioned before, while perturbative QCD is very successful in describing the strong interaction involving large momentum transfers, it breaks down at low momentum transfer where partons combine to form observable hadrons.

Furthermore, information on QCD can also be obtained from measurements of the hadronic final state generated after the hard scatter. As one example, such measurements can address the issue of the suppression of strange quark production.

This analysis requires the reconstruction of particles with strangeness, such as K^0_S, Λ and Θ^+. Hence there are at least two questions that arise: what is the origin of strangeness in NC DIS events and how do quarks combine to become hadrons?

1.6.1 Strange quark production in DIS

There are several ways in which an s quark might be produced in NC DIS events, the first two of which describe the same process but in two different kinematic ranges.

- Flavor excitation: Following a gluon fluctuation within the proton, $g \rightarrow s\bar{s}$, if one of the strange quarks receives a large momentum transfer by the exchanged virtual photon then a recombination of the pair is not possible. As a result, the struck quark leaves the proton while the other quark remains roughly collinear with the proton remnant.

- Boson gluon fusion: The virtual photon couples with a gluon of the proton via a virtual $s\bar{s}$ quark pair.

- Decays of heavier quarks: Strange quarks in the final state can result from decays of charm quarks, which in turn can come from decays of beauty quarks. Due to their larger masses, and hence the limited phase space, charm and beauty quarks are produced less frequently. Recent inclusive measurements of $F_2^{c\bar{c}}$ and $F_2^{b\bar{b}}$, at low Q^2, yield a contribution to the total ep cross section of 22% and 0.8%, respectively [40]. (The c and b fractions

depend on x and Q^2. In the limit $Q^2 \gg M_{Quark}$ and $x \ll 1$, simple charge counting yields: $F_2^{c\bar{c}}/F_2 = 4/11$, and $F_2^{b\bar{b}}/F_2 = 1/11$. Furthermore, if the Cabibbo-suppressed decays are neglected, then every charm decays to one strange and every b decays to at least one charm. The latter decay, in turn, yields 1.66 strange per every b decay.)

- Fragmentation: This is the dominant process by which hadrons containing strangeness are produced and is described below.

1.6.2 Hadron production in DIS

Hadronization refers to the mechanism by which quarks and gluons produced in the hard processes form the hadrons that are observed in the final state. This is an intrinsically non-pertubative process and therefore not calculable in perturbative QCD. At present, the description of this transition of quarks and gluons to hadrons is done via phenomenological models only. Hence the measurement of strange mesons and baryons in high-energy scattering experiments represents a test of the hadronization models. Two such models are the *Lund string* model and the *cluster* fragmentation model as implemented in the Monte Carlo (MC) programs JETSET [83] and HERWIG [84], respectively. HERWIG is not used in this analysis and is described only briefly.

Lund string model

The more salient points of the Lund model [41] are described here. The starting assumption of the string model is the linear confinement potential between two color charges at large separations. In the simplest case, when two quarks ($q\bar{q}$) move apart, on a common axis, from their common production point, a gluon field conveys color between the quarks. This field between the quarks, called *color flux tube* or *string*, stores energy in the same way that a stretched spring does. After its production, the $q\bar{q}$-pair separates, hence the tube joining it stretches. The more it stretches, the more work is done against the recoil force of the string, thereby adding energy to the system. At some point, as it becomes energetically possible, the string will break creating another $q\bar{q}$-pair at the break-point, resulting in two $q\bar{q}$-pairs. (See figure 1.5). The breaking of strings continues as long as the invariant mass of either of the two segments of the string is large enough. Finally,

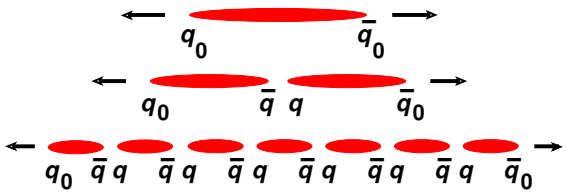

Figure 1.5: Schematic illustration of string fragmentation in the Lund model. The blobs represent color strings which connect two quarks.

when the splitting ceases, several such $q\bar{q}$-pairs, or mesons, will have been created. For charge, color and flavor convservation, the $q\bar{q}$-pairs are produced at the same point in space-time. If the quarks have mass and/or transverse momentum, then the q and $\bar{q}$ are produced with a finite separation in order to transform the field energy between them into the sum of the two quarks' transverse masses m_{T}. For quantum number conservation, the Lund string model assumes that the quarks are produced at the same space-time point after which they are allowed to quantum mechanically tunnel into the classically allowed region. The tunneling probability is given by

$$\exp(-\frac{\pi m_{\mathrm{T}}^2}{k}) = \exp(-\frac{\pi m^2}{k}) \exp(-\frac{\pi p_{\mathrm{T}}^2}{k}) \ , \tag{1.15}$$

where m_{T} is the transverse mass, m the quark mass, p_{T} is the transverse momentum and k the string constant. The factorization of transverse mass and momentum terms in equation 1.15 implies a Gaussian spectrum in p_{T} for the quark pairs formed from the string splitting. Equation 1.15 also implies a suppression of heavier quark production from fragmentation with different quark flavors produced in the ratio $P(u) : P(d) : P(s) : P(c) \approx 1 : 1 : 0.3 : 10^{-11}$[2], where $P(q)$ is the probability of producing a $q\bar{q}$-pair in the color field. For this reason, charm and heavier quarks are not expected to be produced in soft

[2]A suppression factor of 10^{-11} means that $c\bar{c}$ pairs are almost never produced in string fragmentation. Since charm mass is about six times Λ_{QCD}, charm production is described by perturbative QCD and not by fragmentation models. Therefore, MC programs like JETSET produce charm quarks in the perturbative part -hard interaction or parton shower- and not in the fragmentation part, thus measurements of charm production are not translated into fragmentation parameters. The reason the charm suppression factor is not exactly zero is because there is a tiny tunneling probability that, from mass considerations, is of the order of 10^{-11}. Clearly even if it were zero, the resulting charm cross section would be the same.

fragmentation but only from the hard interaction or parton shower. The ratio of the probability $P(s)$ to $P(u) \approx P(d)$ is parameterized by a phenomenological parameter $\lambda_s = P(s)/P(u)$, called the *strangeness suppression factor*. The default value of strangeness suppression in JETSET is $\lambda_s = 0.3$ and was tuned with LEP data.

Once the flavors have been selected, a choice needs to be made as to which meson or baryon state is produced. The non-relativistic classification is that the meson is assigned a valence-quark spin, S, and internal angular momentum, L, so that the spin of the meson, J, is given by $J = L + S$. Radially excited states are expected to make a negligible contribution, hence only $L = 0$ is allowed. This means $J = 0, 1$, therefore only pseudoscalar or vector mesons can be produced.

For baryon production, there exist two different mechanisms in the Lund string model: the *diquark* and the *popcorn* models . Figure 1.6 (a) illustrates the diquark

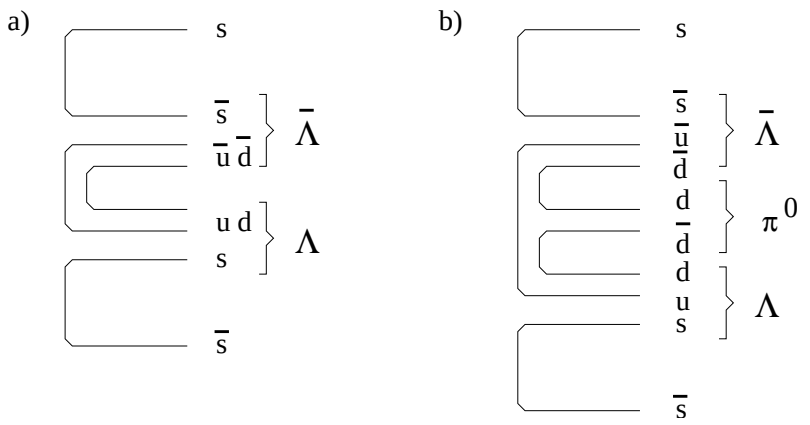

Figure 1.6: Illustration of meson and baryon production in the (a) diquark (b) popcorn mechanisms in the Lund model as implemented in JETSET.

model in which the spring-breaking produces not one $q\bar{q}$-pair but a $(qq)(\bar{q}\bar{q})$-pair, that is a qq on one end of the break and a $\bar{q}\bar{q}$ at the other, thereby producing a baryon at one end and an anti-baryon at the other. There are extra parameters associated with the formation of baryons compared with mesons. The main ones are listed below along with their default value settings in JETSET.

- the relative probability of producing a diquark pair compared with that of $q\bar{q}$-pair, $P((qq)(\bar{q}\bar{q}))/P(q\bar{q}) = 0.1$,

- the extra suppression for a diquark containing strange in addition to λ_s, $(P(us)/P(ud))/(P(s)/(P(u) \approx P(d))) = 0.4$,
- the suppression of spin-1 diquarks relative to spin-0, $1P(ud_1)/3P(ud_0) = 0.05$.

A more complete description of baryon production is implemented in JETSET via the popcorn model, in which baryons are formed not by diquark production but by multiple $q\bar{q}$ production. The usual string splitting occurs via

$$q_i\bar{q}_i \rightarrow (q_i\bar{q})(q\bar{q}_i) \ , \tag{1.16}$$

where the brackets delimit color singlet objects. In the popcorn model it is possible for two successive splittings to occur and form baryons as shown in figure 1.6 (b):

$$q_i\bar{q}_i \rightarrow q_iq_1\bar{q}_1\bar{q}_i \rightarrow (q_iq_1q_2)(\bar{q}_2\bar{q}_1\bar{q}_i) \ or \ (q_iq_1q_2)(\bar{q}_2q_3)(\bar{q}_3\bar{q}_1\bar{q}_i) \ . \tag{1.17}$$

The popcorn parameter $(P(BMB)/P(BB))$ sets the relative production of BMB compared to that of BB, where B and M represent baryon and meson, respectively. The default value for this in JETSET is 0.5.

Cluster fragmentation model

A schematic of the cluster model [42] is shown in figure 1.7. This model starts by non-perturbatively splitting the outgoing gluons into light quarks, $g \rightarrow q\bar{q}$, once the parton shower has terminated. Each final-state color line can be followed from

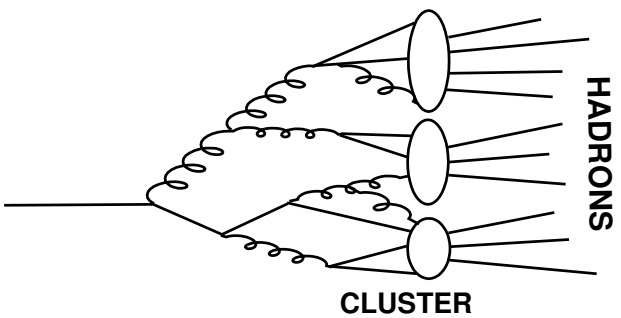

Figure 1.7: Illustration of meson and baryon production in the cluster fragmentation model as implemented in HERWIG.

a quark to an antiquark, which, in turn, can form a color-singlet combination. These color-singlet combinations are assumed to form clusters, which mostly undergo simple isotropic decay into pairs of observable hadrons, chosen according to the density of states with appropriate quantum numbers. For example a cluster of flavor $f_1\bar{f}_2$ decays to hadrons of flavor $f_1\bar{f}$ and $f\bar{f}_2$, where f is chosen at random from u, d, s. For a given cluster $(f_i\bar{f}_j)$, hadrons are then chosen with the same flavor from the $J^P = 0^-$, $1^\pm$ or 2^+ mesons and $1/2^+$ or $3/2^+$ baryons.

The preconfinement property of the QCD parton shower allows the cluster masses to peak at low values. A cluster which is too light for two-body decay is taken to be the lightest hadron of its flavor and its mass is shifted to the correct values via momentum exchange with the neighboring cluster. The high-mass tail of the cluster distribution has masses too high for two-body decays to be a reasonable assumption and such clusters are fragmented using an iterative fission model.

1.7 Pentaquark phenomenology

Exotic hadrons with manifestly more complex quark structures, in particular, pentaquarks (see Introduction), were first proposed on the basis of quark and bag models [45] in the early days of QCD. However, in the eighteen months since the first report from Spring-8 [4], theoretical responses have sprouted on the preprint server like mushrooms after an autumn rain - well over one hundred preprints have been submitted to the arXiv on pentaquarks and related topics. Most of these theoretical models can be roughly divided into two sets based on their assumption of Θ^+ parity. Those advocating positive parity include the chiral soliton model [46], the diquark model [47], some quark models [48] such as the diquark-triquark model [49], and one lattice calculation [50]. On the other hand, those that side with negative parity include QCD sum rule approaches [51] and two lattice calculations [52], amongst others. The most prominent of these models, the chiral soliton model, is discussed briefly here. For more on some of the above theoretical descriptions see [3, 29, 53–56] and the references therein.

1.7.1 Chiral soliton model

As has already been discussed above, the most fundamental and experimentally proven description of strong interactions available today is QCD in which quarks

and gluons, the constituents of nucleons, interact via the strong force mediated by the gluons. However, an effective theory that describes many aspects of nuclear physics well enough is the chiral quark soliton model (CSM) [57]. This model uses the same description of quarks as before, however the quarks are no longer coupled via gluons. Instead, they are bound together by a self-consistent field called "soliton".

In the early 60's, Tony Skyrme studied the pion field equation and discovered that by adding a non-linear "σ" term to the classical equations of the pion field, stable solutions could result [58]. These non-trivial, non-dissipative solutions with half-integer spin were called soliton solutions and baryons were viewed as solitons of CSM. (With the advent of quarks two years later, the Skyrme model lay largely dormant until 1983, when Edward Witten showed that its efficacy for low-energy strong interactions could be understood in terms of QCD).

In this model, since baryons are considered to be topological clouds, effectively composed of very many (light) quarks, higher multiplets are expected in addition to the octet and decuplet baryons. As can be seen in figure 1.8, this model predicts other exotic states in addition to Θ^+ and $\Xi^{--}(1862)$, filling out an antidecuplet of SU(3). The Θ^+-baryon is the lightest exotic baryon lying at the apex of this spin-1/2 antidecuplet. Treating the known $N(1710)$ resonance as a member of the antidecuplet, Diakonov and his collaborators derived a mass of about 1530 MeV and a width of less than 15 MeV for Θ^+ and quantum numbers, $B = 1$, $J^P = 1/2^+$, $I = 0$ [46].

It should be noted that the existence of a relatively light, exotic antidecuplet of baryons was first pointed out in the context of the Skyrme model by Manohar in 1984 [59]. Furthermore, the mass of the lightest member of this antidecuplet was first computed by Praszalowicz in 1987 [60]. His mass prediction was approximately 1530 MeV as well.

1.7.2 The narrow width puzzle

According to Quantum Mechanics, the width, Γ, or the natural spread in energy of a decaying state is given by:

$$\Gamma = \frac{\hbar}{\tau} = \hbar R \,, \tag{1.18}$$

where $\hbar$ is Planck's constant and τ is the mean lifetime of the decaying state. Additionally, R, given by Fermi's Golden Rule, is the transition rate for a given

process in terms of its Feynman amplitude (or *dynamical* information) and the available phase space (or *kinematical* information). The phase space factor depends on the masses, energies, and the momenta of the participants, and reflects the fact that a given process is more likely to occur the more "room to maneuver" there is in the final state. Hence decays which have small phase space are those which have little extra mass to spare and are tightly constrained. This means their decay rate is small which, in turn, means their width is small.

Apart from this, in their derivation of the Θ^+ width, DPP use two parameters, $(G_0 + 1/2G_1)$ and G_1/G_0, where G_0 and G_1 are Yukawa coupling constants. For the first parameter, they obtain a value of ≈ 19 from the equation of the decay width of $\Delta(1232)$. The value of the second parameter, 0.4, they take from chiral quark soliton models. Finally, they substitute these values into the equation for the decay width of Θ^+ to obtain ≈ 15 MeV.

This value has been contested by R. Jaffe [61], who asserts that DPP have made a simple arithmatic error in their calculation. According to Jaffe, $(G_0 + 1/2G_1)$ should equal 25, which in turn would yield a Θ^+ width of 30 MeV. This error, which was originally acknowledged by one of the authors, is now refuted by DPP. Their response can be found in [62].

Recently the CSM was updated by Ellis *et.al* [63]. In their model, the Θ^+ mass falls somewhere between 1430 MeV and 1660 MeV. They also attempt to explain the narrow width puzzle, for which there are many other models on the market [64].

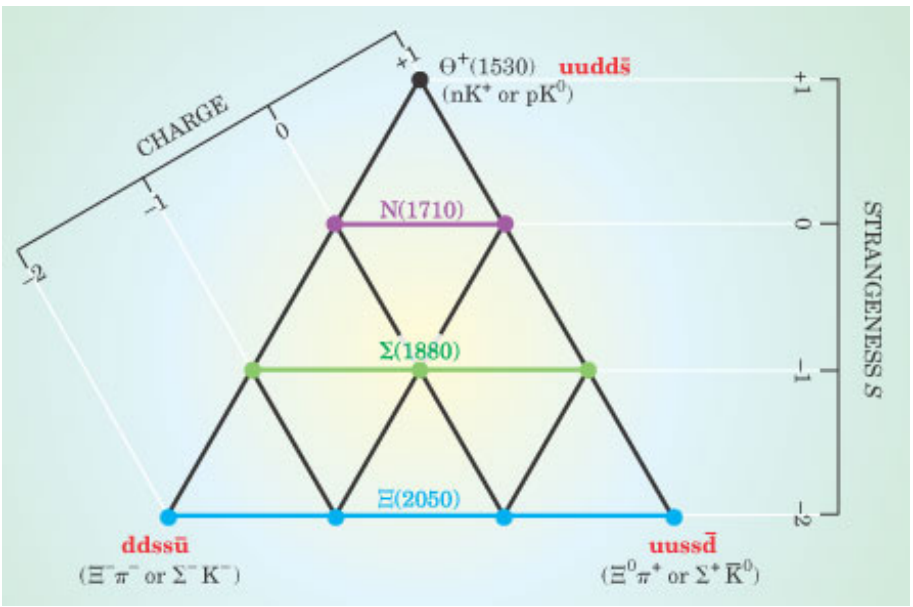

Figure 1.8: The antidecuplet of pentaquark baryons and its quark decomposition. The states at the corners of the triangle manifest exotic quantum numbers and cannot be made of three quarks. In parantheses are their decay modes. The recently discovered Θ^+, with flavor content $uudd\bar{s}$, sits at the apex of this spin-1/2 antidecuplet. The numbers in parentheses are the predicted masses (MeV) in the chiral soliton model of the charge multiplets for each value of the strangeness. The increase in mass per unit of strangeness is 170-180 MeV (instead of 100-120 MeV when going from ρ or ω mass to K^* mass).

Chapter 2

The ZEUS detector at HERA

Figure 2.1: Aerial view of the DESY site in Hamburg. The location of the HERA and PETRA accelerators is indicated by dashed lines. S and N indicate the locations of the two colliding-beam experiments, ZEUS and H1, respectively.

The HERA collider provides an ideal laboratory for testing and advancing the understanding of QCD via measurements of lepton-proton scattering. This chapter provides a brief overview of the HERA collider and the ZEUS[1] detector

[1] $ZE\Upsilon\Sigma$: *Ζήτησις καθ' Ευρετής Υποκειμένης Συμμετρίας* (*Search to Elucidate Underlying Symmetry*)

with a somewhat more detailed description of the components important to this analysis.

2.1 HERA accelerator

HERA [65], the only lepton-proton collider in the world, is located at the Deutsches Elektronen Synchrotron (DESY) laboratory in Hamburg, Germany. An aerial view of the HERA ring is shown in figure 2.1. Built between 1984 and 1990, in a tunnel 15 – 25 meters underground, HERA consists of two separate rings for electrons and protons and is 6.3 km long. Upon injection into HERA, the electrons and protons are accelerated in two separate rings via super-conducting and conventional cavities, respectively. However, for beam-focusing, the situation is reversed: the electrons and protons are focused with conventional and super-conducting magnets, respectively. The two beams are brought to collision in the north and south experimental areas where the two colliding-beam experiments, H1 and ZEUS are located. See figure 2.2. These two experiments, which started taking data in 1992, complement and (frequently) validate each other as they have independent detector designs which were optimized differently.

Two fixed-target experiments, HERMES, located in the east hall and HERA-B in the west, make use of the electron and proton beams, respectively. HERMES studies the spin contribution of the constituents of the nucleon to its total spin by scattering longitudinally-polarized electrons off polarized gas jet targets such as hydrogen, deuterium or ^{3}He. The polarization of the electrons is switched using spin rotators. The HERA-B experiment is designed to measure $\mathcal{CP}$-violation in the $B^0\overline{B^0}$-system. The B-mesons are produced by collisions of the proton beam halo with a wire target.

HERA was originally designed to accelerate electrons up to 30 GeV and protons up to 820 GeV in energy. For the data-taking period of 1996-2000 considered in this thesis, the electron-beam energy was 27.5 GeV. The proton-beam energy was 820 GeV until 1998 when it was increased to 920 GeV, yielding a center of mass energy of $\sqrt{s} = 314$ GeV before 1998 and 318 GeV after.

The beams consist of up to 220 bunches of electrons and protons with approximately 10^{10} particles and cross each other at a rate of 10.4 MHz. Each bunch of electrons is set up to collide with a specific bunch of protons, but not all bunches are actually filled. Unpaired or non-colliding bunches are used to

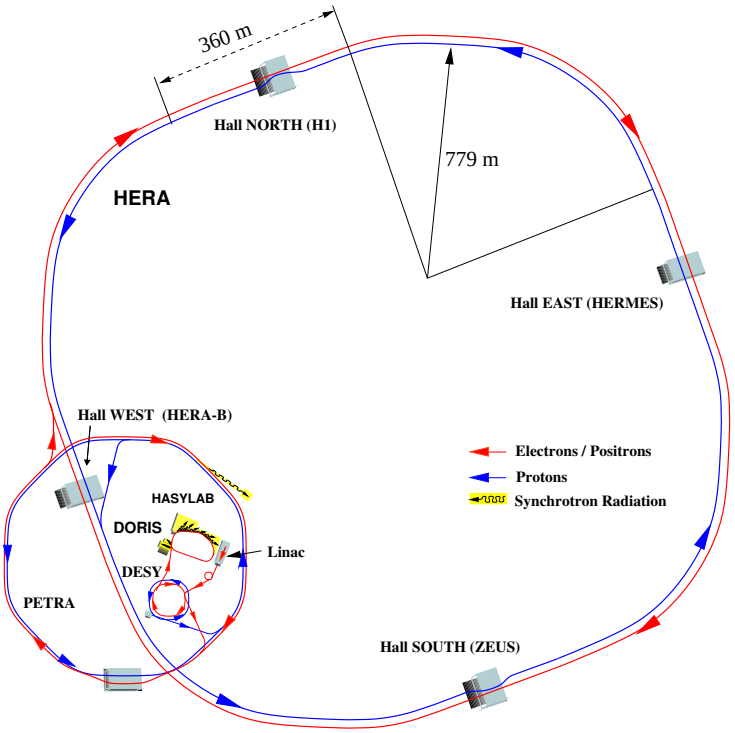

Figure 2.2: Schematic view of the HERA accelerator.

estimate the beam-related background noise and empty bunches are used for calibration purposes and to measure cosmic-ray background.

Since more integrated luminosity opens the possibility for new and interesting measurements, HERA was shut down for an upgrade from the end of 2000 to 2001, the goal of which was to increase the integrated luminosity to 1 fb^{-1}. As of the writing of this thesis, HERA has provided about 77(83) pb^{-1} of $e^+p(e^-p)$ data between 2003 and 2005. [66]. The integrated luminosities for the three different running periods of 1994-2000 are shown in figure 2.3. The ratio of the luminosity delivered by HERA to that gated by ZEUS is about 75%. (Similar figures for 2003-2005 are not shown here as this data was not used for this analysis.)

2.2 ZEUS detector

The ZEUS detector is situated about 30 meters underground and has a size and weight of $12 \times 11 \times 20$ m^3 and 3600 tons, respectively. It has been built and is being operated by a collaboration of about 318 physicists and about the same

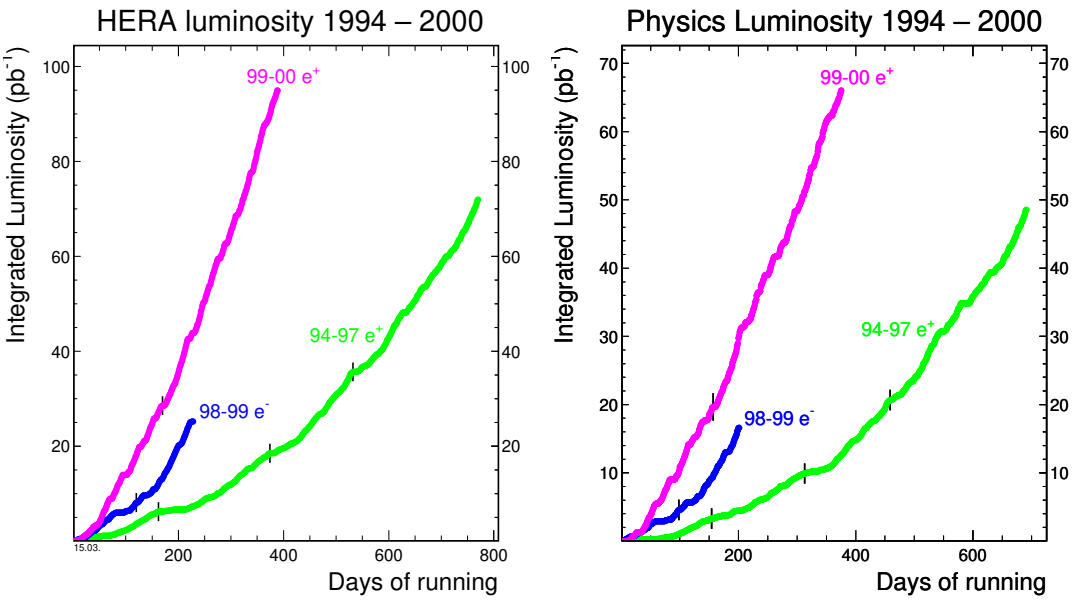

Figure 2.3: Integrated luminosity delivered by HERA (left) and luminosity recorded by ZEUS (right) for data analysis.

number of engineers from 51 institutes in 12 different nations. ZEUS is a multi-purpose magnetic detector designed to study a wide range of physics involving electron-proton scattering at HERA. It is a quasi-hermetic detector as it covers most of the 4π solid angle with the exception of small regions around the beam-pipe. Its design reflects the forward-backward asymmetry of the ep final state resulting from the difference in the energies of the electron and proton beams. Since its comissioning in 1992, several detector upgrades have been carried out as a consequence of the physics and technical understanding gained during the first years of data taking.

The detector design is inspired by the various physics processes that can be observed at HERA. While in Neutral Current (NC) DIS events, the scattered lepton has to be identified and measured with high precision, in Charged Current (CC) DIS processes, the missing transverse momentum carried by the outgoing neutrino has to be reconstructed. Also particle identification is needed for a wide momentum range. ZEUS can measure energies from a few MeV's to hundreds of GeV's in the forward region. Low-momentum particles are better measured via tracking since the tracking resolution behaves as $\sigma(p_{\mathrm{T}})/p_{\mathrm{T}} \sim p_{\mathrm{T}}$, while high-

energy particles are well measured with calorimetry where the resolution behaves as $\sigma(E)/E \sim \sqrt{E}/E$.

The ZEUS coordinate system is defined as a right-handed orthogonal system with the origin at the nominal interaction point (IP). The positive(negative) z-axis points in the proton(electron) beam-direction and is called the forward(rear) region. As can be seen in figure 2.4, the y-axis points upwards and the x-axis points horizontally towards the center of HERA. The polar angle of the proton(electron)-beam, θ, measured with respect to the z-axis, is $0°(180°)$. The azimuthal angle ϕ is measured with respect to the x-axis. Often the pseudorapidity, η = -ln tan($\theta/2$), is used instead of θ.

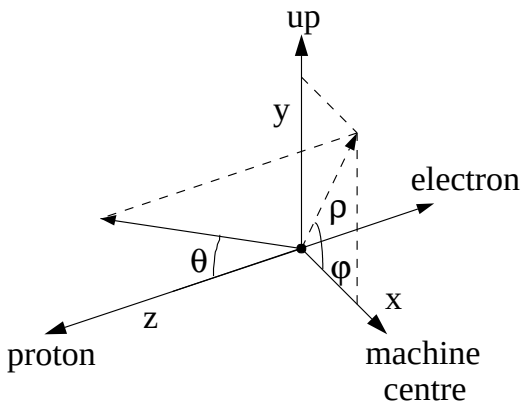

Figure 2.4: The ZEUS coordinate system.

Cross sections of the ZEUS detector can be seen in figures 2.5 and 2.6. A brief overview of the main components is given below followed by a more detailed description of some components essential to this analysis. For a more complete description, see [67]. Directly around the interaction region is the tracking system which detects charged particles. The innermost part of ZEUS used to be a vertex detector (VXD). It was removed during the shutdown in 1995/96 and, in 2001, a silicon micro-vertex detector (MVD) was installed in its place. For the data considered in this analysis, the innermost detector was the central tracking detector (CTD) which is a cylindrical drift chamber, surrounding the beam-pipe at the interaction point. The CTD is supplemented in the forward region with three sets of planar drift chambers (FTD) with transition radiation detectors (TRD) sandwiched between them (labelled as FDET in figure 2.5) and

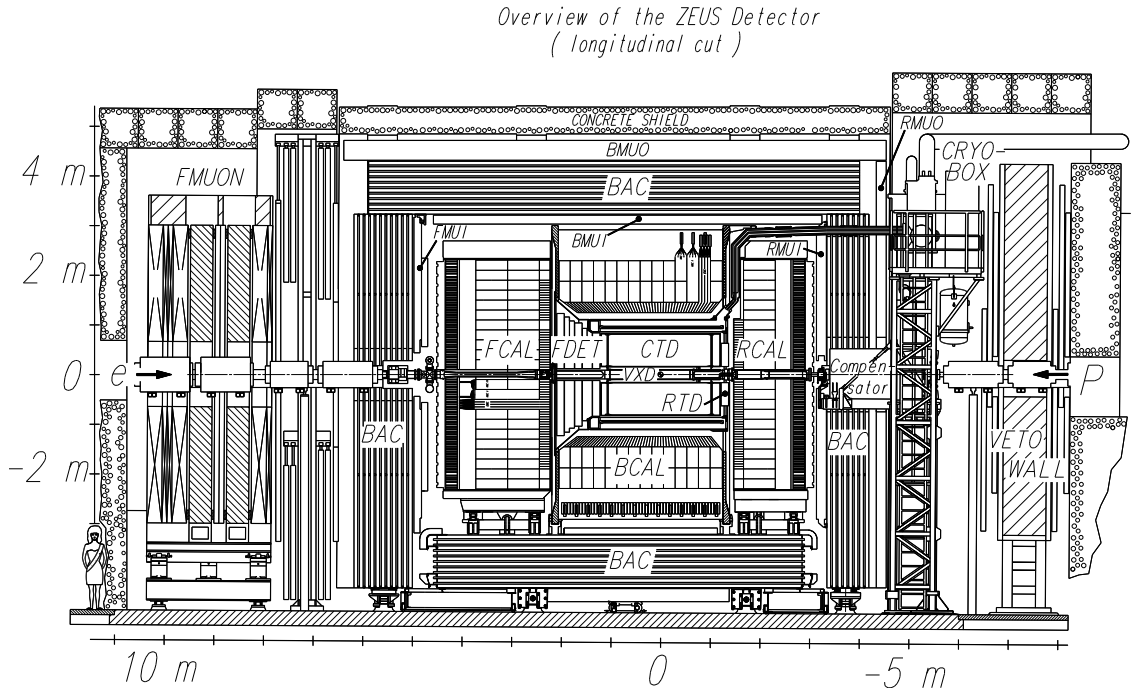

Figure 2.5: Cross section of the ZEUS detector along the beam axis.

in the rear region, with one planar drift chamber consisting of three layers (RTD). Enclosing the tracking system is a super-conducting solenoid providing a magnetic field of 1.43 T. Its purpose is to bend the particles' tracks, thereby providing a measurement of their charges and momenta.

Surrounding the tracking system is a high-precision, compensating uranium calorimeter (UCAL), which is divided into forward (FCAL), barrel (BCAL) and rear (RCAL) sections. Its purpose is to measure the energy of the scattered particles. In addition, presampler detectors (FPRES, BPRES, RPRES) are mounted on the front of the calorimeter modules to help correct the energy of particles that start showering before reaching the calorimeter. The hadron-electron separator (HES) is installed after three radiation lengths inside the forward and rear part of the calorimeter. It consists of a plane of 3×3.3 cm^2 silicon diodes and is designed to improve the separation between hadronic and electromagnetic showers. The CAL is surrounded by an iron yoke which provides a return path for the magnetic-field flux. In order to measure particles which have not been absorbed into the CAL, muon identification chambers are placed inside (FMUI, BMUI, RMUI) and outside (FMUON, BMUON, RMUON) the yoke. Attached to the front face of the RCAL, is the small angle rear tracking

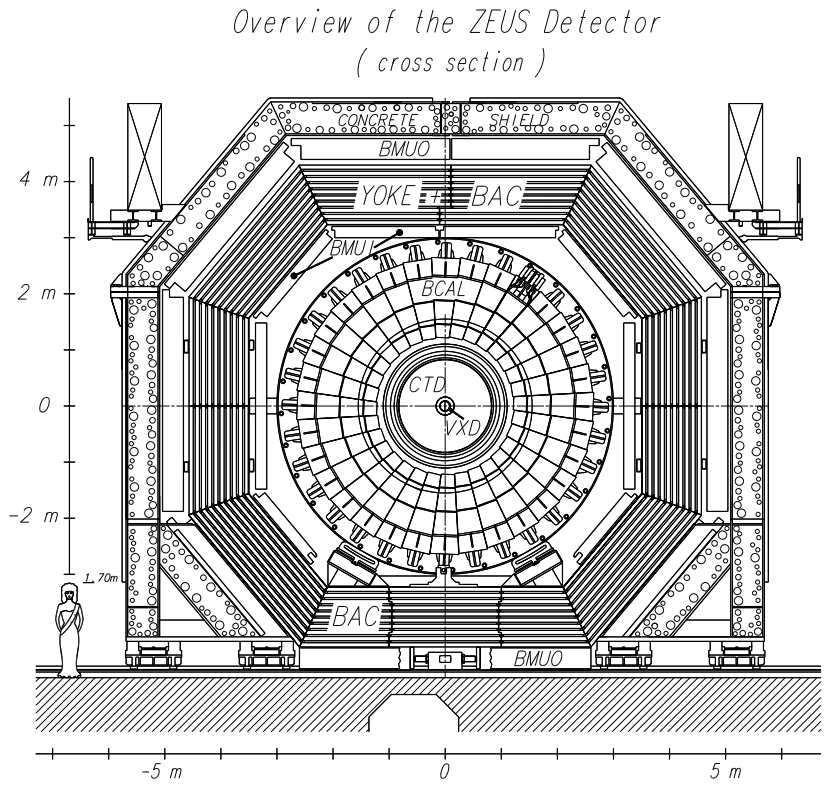

Figure 2.6: Cross section of the ZEUS detector perpendicular to the beam axis.

detector (SRTD). This scintillator-strip detector covers an area of 68 x 68 cm^2 minus the beam-hole (20 x 20 cm^2) and is used to measure the impact point of the scattered electrons with high accuracy.

In the rear, the VETO wall, an iron-scintillator detector, is used to reject background from proton beam-gas interactions. The C5 counter, located at the rear end of the calorimeter, consists of two planes of scintillators, one above and one below the beam-pipe. The timing information given by these two sub-detectors is also used to reject proton-beam gas events.

The luminosity measurement is done by the LUMI detector, which consists of a photon calorimeter at $z = 104$ m and an electron calorimeter at -34 m. Both are lead-scintillator calorimeters that detect electrons and photons from bremsstrahlung events for the luminosity measurement. They are also used for tagging photoproduction events in which the scattered electron escapes the electron beam through the beam-pipe. Because of the reduced energy of the electron, it is driven by the magnetic field of the beam magnets.

2.3 Intermezzo: particle interactions in matter

When a charged particle traverses matter such as CO_2 or Uranium, it loses energy as it interacts with the atoms in that matter. The measurement of this energy loss or ionization provides, amongst other things, the path and identity of the particle. Additionally, if the same charged particle is subjected to a magnetic field, it will bend depending on its charge and mass, thereby allowing charge and momentum measurements, respectively. Furthermore, the amount of ionization depends on the particle's charge and velocity. Most particles can be assumed to ionize minimally, which means that their energy loss depends only on their charge. For such particles, the energy loss effectively provides the number of particles traversing the medium.

As a result of this 'particle-matter' interaction, the particle is absorbed or deflected and, in the process, several new particles are created, all possessing a fraction of the parent particle's energy and momentum. Hence an avalanche or 'shower' of particles is created, becoming wider as it penetrates deeper into the material. However, because of conservation of momentum and energy, as more particles are created, they become less energetic. As a result, the rate of generation of new particles slows down and the shower starts to become smaller and eventually disappears.

It is the nature of the interacting particle that dictates the nature of the interaction. The simplest examples are electrons and photons, both of which produce a cascade of electrons and photons, called electromagnetic showers. At high particle energies, the electrons will emit bremsstrahlung photons and the photoelectrons will mostly produce pairs of oppositely-charged electrons. At lower energies, the predominant processes are Compton scattering for photons and ionization losses for electrons. On the other hand, if the shower starts from a hadron, it is dominated by inelastic hadronic interactions. At high energies these interactions include multi-particle production and particle emission from nuclear decay and excited nuclei. Additionally, since most of the π^0's that are produced decay electromagnetically by emitting two photons, the hadronic showers also have an electromagnetic component.

Of the other leptons, there are two of special interest, muons and neutrinos. Muons move through matter depositing minimum ionizing energy and neutrinos are ghost-like particles because they generally don't interact with matter at all, leaving no signature behind. See figure 2.7.

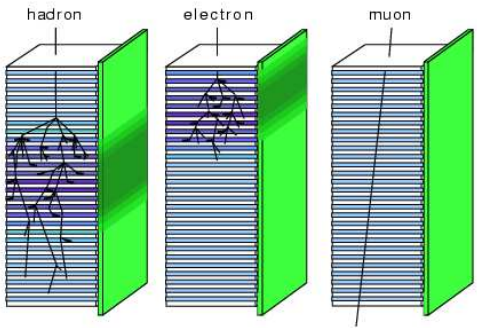

Figure 2.7: Typical shower profiles in the calorimeter for different types of particles.

The two main detectors used for particle detection in this and most ZEUS analyses are the CAL and the CTD, which are discussed in detail next.

2.4 Calorimetry and the Uranium Calorimeter (CAL)

Devices that measure particle energies are called calorimeters. The standard design for a calorimeter includes a massive chunk of high-Z matter, which when hit by a particle, produces a shower. The resulting energy loss, deposited into the calorimeter, is then measured. A way to measure this energy is via scintillators, which comprise of any material that turns a fraction of the energy deposited into it to light. The light can then be measured with photodiodes or photomultipliers. However, as most scintillators have long radiation lengths, the resulting calorimeter would be gargantuan. Hence, to reduce the size and cost, scintillators are mixed with materials with short radiation length, called absorbers.

Calorimeters that use scintillators and absorbers are called sampling calorimeters because they measure only a fraction of the shower's energy that is deposited in the scintillator. Two popular designs for calorimeters are the 'sandwich' and the 'spaghetti' designs. In the former, the scintillator is sandwiched between the absorbers, while in the latter, scintillating fibers are placed lengthwise through the calorimeter.

The thickness of the scintillators and absorbers can be chosen to obtain compensation, which means that the detector response is the same for both

electrons and hadrons of the same energy (e/h = 1). As mentioned in the last section, electromagnetic and hadronic showers develop differently. The signal from hadronic showers is usually smaller since a fraction of the energy is lost due to nuclear processes that don't result in a measurable signal or due to muons, neutrinos and slow neutrons. Also since a fraction of the shower is electromagnetic, one has to guess the electromagnetic component afterwards (offline) in order to make a correction. Alternatively one can compensate for these losses by lowering the ratio of the electron to hadron signal. One way to achieve this is to make the absorber out of U^{238} (or a high-Z material such as Pb). The spallation neutrons from the Uranium can be detected with plastic scintillators in which the neutrons create recoil protons upon scattering on hydrogen nuclei. Compensation can then be achieved by the the right tuning of the uranium to scintillator ratio.

The most important property of a calorimeter is its energy resolution. While the resolution for sampling calorimeters is influenced mostly by its sampling fluctuations, there exist several other effects which vary in how they scale with the energy:

- statistical effects ($\Delta E_{\mathrm{stat}}/E \sim 1/\sqrt{E}$): mostly from sampling fluctuations; sometimes from photostatistics;
- noise ($\Delta E_{\mathrm{noise}}/E \sim 1/E$): noise from the electronics;
- constant ($\Delta E_{\mathrm{const}}/E \sim 1$): from mis-calibrations of individual channels and non-uniformities;
- leakage ($\Delta E_{\mathrm{leak}}/E \sim lnE$): from longitudinal leakage of the shower out of the detector.

Apart from the energy resolution, there are a number of other properties that characterize a calorimeter, some of which are:

- calibration uncertainty: If the calibration is off by a factor, there will be a systematic shift in the energy reconstruction which is very hard to detect using the calorimeter signals alone;
- non-uniformity of the energy reconstruction: Due to manufacturing and calibration tolerances, there might be position-dependent variations in the signal response. This can create a serious bias in data-selection or may degrade the resolution;

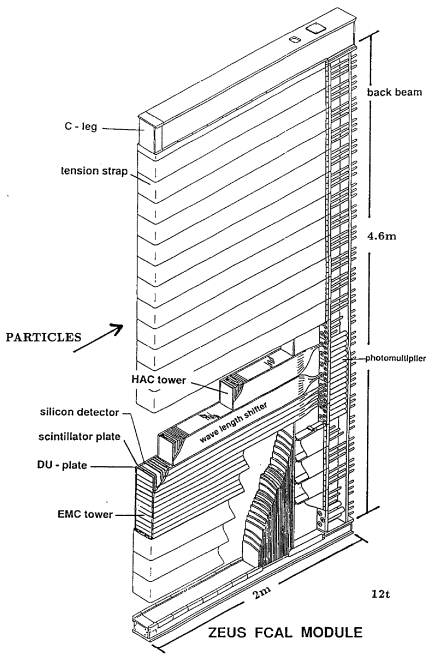

Figure 2.8: Layout of one FCAL module.

- non-linearity of the energy reconstruction: Reasons for non-linearity can be nonlinear photomultiplier responses or leakage;
- angular coverage: angular coverage provided by the calorimeter.

The goals of the ZEUS calorimeter (CAL) design were to achieve (almost) a full solid-angle coverage, a good energy resolution, good calibration of the absolute energy scale and of the individual calorimeter sections with respect to each other and a good angular resolution.

The ZEUS CAL is a sandwich calorimeter composed of depleted uranium (98.1% $U^{238}, 1.7\%$ Nb, 0.2% U^{235}) and plastic scintillator (SCSN38). The thicknesses of the uranium layers, 3.3 mm, and that of the organic scintillators, 2.6 mm, have been optimized to achieve compensation. Hence the detector response is the same for both electrons and hadrons of the same energy (e/h=1.00 ± 0.02). The energy resolution measured under test-beam conditions for electrons and hadrons is:

$$\frac{\sigma_e}{E} = \frac{18\,\%}{\sqrt{E}} \oplus 2\,\% \quad \text{and} \quad \frac{\sigma_{\mathrm{had}}}{\mathrm{E}} = \frac{35\,\%}{\sqrt{\mathrm{E}}} \oplus 1\,\% \,. \tag{2.1}$$

	FCAL	BCAL	RCAL
η-range	3.8 - 1.0	1.1 - (-0.74)	(-0.72) - (-4.2)
θ-range	2.5° - 39.9°	36.7° - 129.1°	128.1° - 178.4°
EMC rad. length X_0	25.9	22.7	25.9
total abs. length λ	7.14	4.92	3.99

Table 2.1: Angular acceptance and longitudinal depth of the Calorimeter

with E in GeV.

The calorimeter consists of three parts: the hollow cylindrical section called the barrel (BCAL) and the flat forward and rear sections (FCAL, RCAL), situated at the two ends of the barrel [68–70]. All three sections are sub-divided into modules which are groups of towers containing stacks of absorber and scintillator material. See figure 2.8. FCAL and RCAL consist of 23 calorimeter modules which consist of up to 23 towers near the middle and fewer on the side so that almost a circular shape is achieved. (The middle tower of the middle module was omitted to leave space for the beam-pipe). The BCAL has 32 modules. For electron-hadron separation, the towers are segmented longitudinally into an electromagnetic (EMC) hadronic (HAC) sections. In the FCAL, each tower consists of one EMC (5×20 cm^2) and two HAC (20×20 cm^2) sections. The RCAL consists of one EMC and one HAC sections. The EMC sections are stacked on top of each other, while the HAC sections are lined up behind them. The reason for the asymmetry in design between the RCAL and FCAL is that the energy absorbed by the CAL is a strong function of θ. As a result, the depth of the CAL sections have been designed to be deeper in the forward region than in the rear. The BCAL again consists of four EMC sections and two HAC sections, but the towers are wedge-shaped due to BCAL's cylindrical geometry. The outermost towers have fewer EMC cells which are slightly tilted toward the interaction point. Some of the basic properties of the three CAL sections are summarized in table 2.4.

The scintillator light of each cell (6,000 in total) is transported to two opposite sides of the cell. There wavelength shifters convert the light to a longer wavelength and transport it to the back of the tower, where it is read out by two photomultiplier tubes (PMT). There are several reasons why two PMTs are used for each cell:

- The left to right signal ratio gives an approximation of the transverse

location of the shower in the cell;

- The measurement becomes less dependent on the impact point of the particle;
- The average of the signals from both sides gives a more uniform detector response then a signal from one side alone;
- PMTs can often generate noise pulses. These can be reduced by comparing signals from both sides;
- Hardware failures rarely occur simultaneously on both sides. Hence with two PMTs there will rarely be a dead spot in the detector.

The excellent time resolution of the CAL - of the order of 1-2 ns - allows it to be used to reject background events. Since the timing of each channel is adjusted to produce a signal for an interaction at the nominal vertex with t=0, a global offset or a timing difference between the CAL sections will characterize a background event. (For example, if the expected signal arrival time is 0 seconds, then a large negative time in the RCAL indicates proton-beam gas interaction upstream in the beam-pipe. Also a time difference in the upper and lower parts of the CAL indicates a cosmic-ray event.)

The constant signal resulting from the radioactive decay of ^{238}U (half-life $4.5{\cdot}10^9$ years) is used as a reference to calibrate the calorimeter to better than 2 %. The PMTs and the readout electronics are additionally calibrated using charge, LED, LASER and test pulses. A full calibration, which includes calibration of the front-end electronics, trimming of the high-voltage settings for the PMTs and generation of a list of read-out channels to be excluded for physics analyses is done when there is no beam in the HERA machine - approximately, weekly, with daily updates.

This author was a member of the ZEUS calorimeter group and as such performed data quality monitoring (DQM) shifts on a monthly basis. DQM duties involved the calibrating of the CAL, monitoring or replacement of damaged or suspicious detector hardware, monitoring of online and offline data quality, and giving periodic reports to the group on the status of the calorimeter.

2.5 Central Tracking Detector (CTD)

The CTD, the main detector used in this analysis, [71] is a cylindrical drift chamber which measures the direction and momentum of charged particles and the energy loss dE/dx, which is used for particle identification. Its active volume ranges from z = -100 cm to z = -104 cm with an inner radius of 18.2 cm and an outer radius of 79.4 cm. It covers polar angles of $15° < \theta < 164°$ and has a complete azimuthal angular coverage. The CTD is filled with a mixture of argon, ethane and carbon dioxide in proportions of 82:13:5.

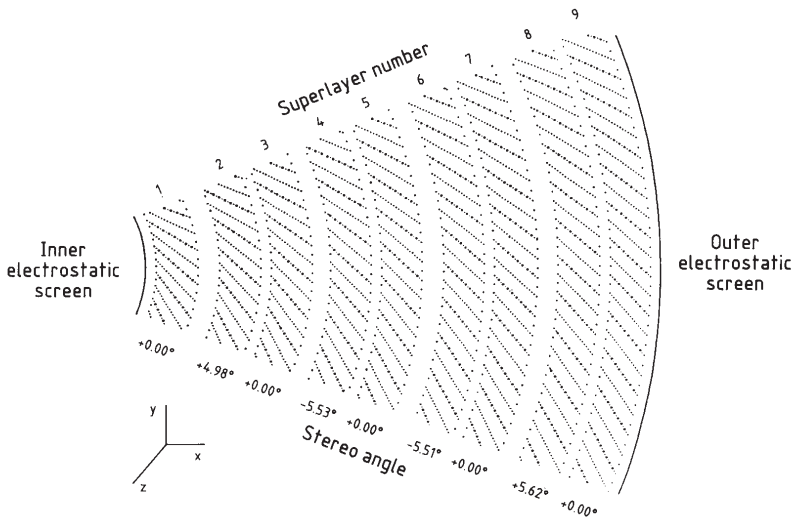

Figure 2.9: A xy-cross section of one octant of the CTD. The dots indicate sense wires.

When a charged particle passes through gas, it leaves a track where it has ionized that gas. If a high voltage is applied on the wires, the electrons will move to the positive sense wires and the positive ions will drift towards the negative field wires. In the field of the sense wires, the electrons ionize more atoms producing a multiplication of the electrons by about a factor of 10^5. This results in a signal pulse, which is measured via electronic read-out. The distance that the electrons travel can be estimated from the time it takes the electrons to reach the sense wire. An octant of the CTD is shown in figure 2.9.

The CTD wires are arranged in 9 superlayers (SL), with each SL containing cells made up of 8 wires. See figure 2.10. The drift field is oriented at a Lorentz

angle of 45° to the radial axis so that the drift electrons travel along radially transverse paths in the $r\phi$-plane. This is important in left-right ambiguity breaking. The drift wires of the odd numbered SLs are parallel to the beam axis, whereas those of the even numbered layers are inclined by a "stereo" angle of $\sim \pm 5°$. This allows an accurate determination of the z-position of the hit. The achieved hit resolution for full length tracks is $\sim .18$ mm in the $r\phi$-plane and ~ 2 mm in z. The measured event vertex is accurate to about 1 mm in xy and 4 mm in z [72].

Additionally layers 1, 3 and 5 are equipped with a 'z-by-timing' system which determines the z-coordinate of a hit by the difference in arrival times at both ends of the CTD. Although the resolution achieved (~ 4 cm) is somewhat crude, it is a fast method and is used predominantly for trigger purposes since it allows tracks to be reconstructed already at the first level trigger.

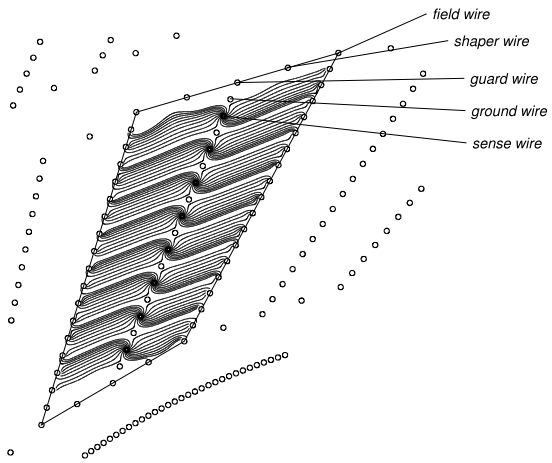

Figure 2.10: Layout of a drift cell in the CTD.

For tracks fitted to the interaction vertex and passing at least three CTD layers with $p_{\mathrm{T}} > 150$ MeV, the position resolution given above results in a transverse momentum resolution [73] of:

$$\frac{\sigma(p_{\mathrm{T}})}{p_{\mathrm{T}}} = 0.0058 \cdot p_T \oplus 0.0065 \oplus 0.0014/p_{\mathrm{T}} \,, \tag{2.2}$$

where p_{T} is in GeV and the symbol $\oplus$ indicates that the three terms are added in quadrature. The first term is due to the position resolution, whereas the second

and third are due to multiple scattering before and inside the CTD, respectively. ($p_{\mathrm{T}} \propto BQR$, where B is the magnetic field in the CTD, Q is the particle charge and R is the curvature of the particle's path.)

2.6 Small-angle Rear Tracking Detector (SRTD)

The SRTD [74] is specifically designed to measure electrons scattered at small angles relative to the incident lepton-beam direction and to improve the measurement of their position and energy. The SRTD consists of a vertical and horizontal layer of finely segmented scintillator strips which are arranged in two planes of four 24 cm $\times$ 44 cm quadrants each. See figure 2.11.

Electrons which lose energy through showers in the inactive material in front of the calorimeter in general deposit more energy in the SRTD than non-showering electrons. The measured energy deposit in the SRTD can therefore be used to correct for this energy loss. The position of the scattered lepton can be measured with a resolution of 3 mm. The SRTD also provides a fast time measurement (resolution $\sim$ 2 ns), which is used to reject background events at the trigger level.

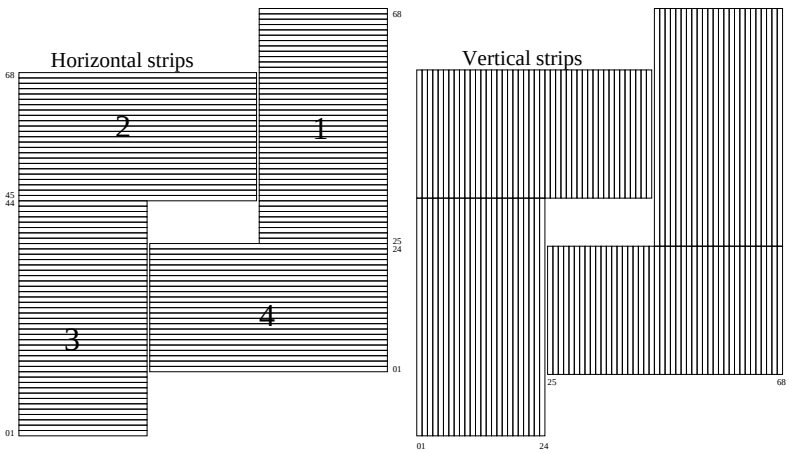

Figure 2.11: Orientation and numbering scheme of the strips of the two SRTD planes. The strip size is 0.98 $\times$ 24 $\times$44 cm^2.

2.7 Luminosity Monitor (LUMI)

Since the event rate $\dot{R}$ is related to the luminosity $\mathcal{L}$ and the cross section σ by $\dot{R} = \mathcal{L} \cdot \sigma$, an accurate knowledge of $\mathcal{L}$ is crucial for cross section measurements. In ZEUS, $\mathcal{L}$ is determined by measuring the rate of bremsstrahlung events produced by the Bethe-Heitler process $ep \rightarrow e\gamma p$ [76], where the photon and the lepton are scattered at small angles. The cross section for this process has been calculated with an accuracy of 0.5 %.

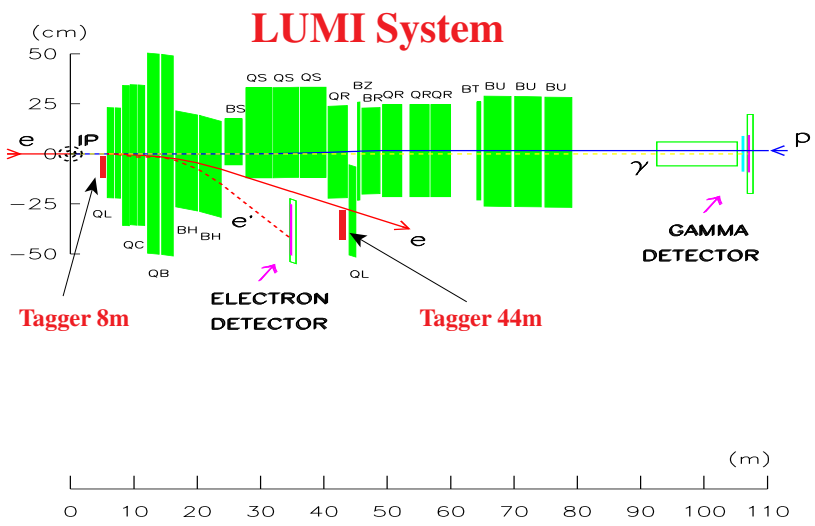

Figure 2.12: Illustration of the ZEUS luminosity-measurement system. Shown are the gamma (LUMIG) and electron detectors (LUMIE) used for the luminosity measurement together with the electron taggers at $z = -44\,\mathrm{m}$ and $z = -8\,\mathrm{m}$.

The LUMI, a schematic illustration of which is seen in figure 2.12, consists of two separate sampling lead-scintillator calorimeters for the measurement of the small angle lepton and photon. Both detectors are positioned downstream of the lepton beam, with the electron calorimeter located at z = -34 m and the photon calorimeter at z = -104 m. Leptons with scattering angles of $\theta_e < 6$ mrad and energies $0.2E_{e-\mathrm{beam}} < E'_e < 0.8E_{e-\mathrm{beam}}$ are deflected out of the beam orbit by the HERA magnetic field from the bending dipoles (BH in figure 2.12). They leave the beam-pipe via an exit window located at z = -27 m to be subsequently detected by the electron calorimeter. In contrast, photons radiated within a cone of 0.5 mrad around the beam axis will leave the beam-pipe via a window at z = -92 m

to be then detected by the photon calorimeter. For photons with energy greater than 5 GeV, the acceptance is 98%. The energy resolution of both calorimeters is $\sigma(E)/E = 23\%/\sqrt{E}$. The bremsstrahlung event rate is determined by counting the number of photons above a fixed energy threshold. (The reason it is not determined by the simultaneous identification of the lepton and the photon is because of the dependence of the lepton calorimeter acceptance on the beam position and angle.) The luminosity is then extracted by dividing the evaluated rate by the bremsstrahlung cross section, corrected for the detector acceptance.

The main contribution to the background is given by the bremsstrahlung of leptons in the residual gas in the beam-pipe. This can be estimated by evaluating the rate of bremsstrahlung events in pilot bunches. These are lepton bunches with no paired proton bunches.

The achieved precision on the luminosity measurement is 1.5-2.2%. The largest uncertainty comes from the acceptance of the photon calorimeter. A more detailed description of the LUMI can be found in [77].

2.8 Background rejection

Background events are those that do not originate from genuine *ep* interactions but arise from other sources. The ZEUS detector utilizes several specialized sub-detectors and uses a variety of other techniques designed specifically for the identification and/or reduction of background. There are three main types of non-physics background that can occur in the ZEUS detector.

- Beam-gas: these are interactions between beam-particles and residual gas in the beam-pipe (or with the beam-pipe wall) and can occur in either of the beams. If such events occur close to or inside the detector, they may produce a signal;

- Halo muons: these are muons resulting from decays of particles produced in beam-gas interactions (e.g. $\pi^{\pm}$, $K^{\pm}$). They pass the ZEUS detector mainly parallel to the beam-line;

- Cosmics: these are muons arising from cosmic-ray interactions. They mostly pass through the detector in straight lines from top to bottom and deposit energy into the detector giving rise to a signal.

In order to reduce the background, ZEUS employs a two-fold strategy, the first of which is to shield the detector. The ZEUS detector is located 25 m below ground level and is surrounded by a ∼1 m thick layer of concrete and an iron yoke. This shielding considerably reduces background from cosmic-ray muons. The detector is also shielded against particles produced by the beams in the HERA tunnel. The iron VETO wall, which lies at $z = -7.5$ m, has a thickness of 0.87 m provides shielding from the proton-beam halo.

The second strategy for background reduction is employed at the trigger level. For example, the VETO wall is instrumented with scintillation counters on both sides. When it absorbs particles in the proton-beam halo and from hadronic showers, it produces a signal. The coincidence in these counters is used to reject halo muons at the trigger level. In addition, ZEUS has a series of collimators (C1-C6 counting from the forward to the rear). These are instrumented in order to provide an estimate of background rates. Of particular importance is the C5 counter, attached to HERA collimator number 5, located at $z = -3.15$ m. It measures synchrotron radiation and timing of bunches.

For the rejection of background events at the trigger level, the timing information from the CAL, SRTD and C5 counter is of most importance. In ZEUS, the timing measurement of different components is calibrated in such a way that particles from a true lepton-proton collision at the nominal IP are assigned t = 0. Beam-gas events have a flat vertex distribution and so will usually arrive at components at one end of the detector before the other. Such events can be identified using timing information from the RCAL, SRTD and C5 counter. The difference in arrival time in the FCAL and RCAL can also be used to reject these events. In the case of muons from cosmic ray interactions, there will be a difference in the time of arrival at the upper and lower halves of the BCAL.

2.9 Data Acquisition (DAQ)

As previously mentioned, the interval between bunch crossings in the HERA accelerator is 96 ns. This corresponds to a nominal bunch crossing rate of ∼10 MHz of which only a small fraction are interesting *ep* events. This poses challenges for the DAQ and trigger systems. The interaction rate is dominated by beam-gas interactions, which contribute about ∼10 - 100 kHz. In contrast, the

rate of interesting *ep* events written to tape is of the order of 1-10 Hz. In order to achieve the necessary rate reduction while efficiently selecting genuine *ep* events, the ZEUS experiment employs a three-level, pipe-lined read-out trigger system [137]. A schematic diagram of the trigger and DAQ chain is shown in figure 2.13.

2.9.1 First Level Trigger (FLT)

The FLT is a hardware trigger which is designed to reduce the signal to below 1 KHz. (The actual value is about 400 Hz!). Each ZEUS subcomponent has its own FLT electronics, which operate locally and have available to them a subset of the full data comprising of very coarsely measured quantities. Furthermore, each subcomponent has $\sim$2 μs after the bunch crossing to complete its internal trigger calculations. It then passes information for that particular crossing to the Global First Level Trigger (GFLT), where an overall decision is made within a 4.4 μs timescale.

Since most detector components cannot contribute a useful trigger decision in the 96 ns beam-crossing interval, data is stored in a 4.4 μs pipeline (corresponding to exactly 46 bunch crossings) while a trigger decision is formed regarding a particular bunch crossing. The use of pipelines means that the whole process has zero dead-time.

At the FLT, decisions are made based on limited tracking information and global or regional energy sums in the ZEUS CAL. The FLT is the fastest but also the least pure of the triggers.

2.9.2 Second Level Trigger (SLT)

Following acceptance by the GFLT, the data is transferred to the SLT. This is a software trigger which uses parallel processing on transputer networks in order to reduce the $\sim$1 kHz (actually $\sim$400 Hz) output rate from the FLT to below 100 Hz. The component SLTs provide information on charged particle tracks and on the interaction vertex (CTD-SLT) and on calorimeter timing and global energy sums such as the transverse energy (E_T) or $E - p_z$ (CAL-SLT). Analogously to the FLT, the outputs of the local subtriggers are passed to the Global SLT (GSLT), where a decision for the whole event is made in a few milliseconds. Since the time allowed for the decision to be made is much longer than for the FLT, more complete sub-component data is available for the decision and more sophisticated process algorithms are possible. The maximum output rate of the SLT is 60 Hz.

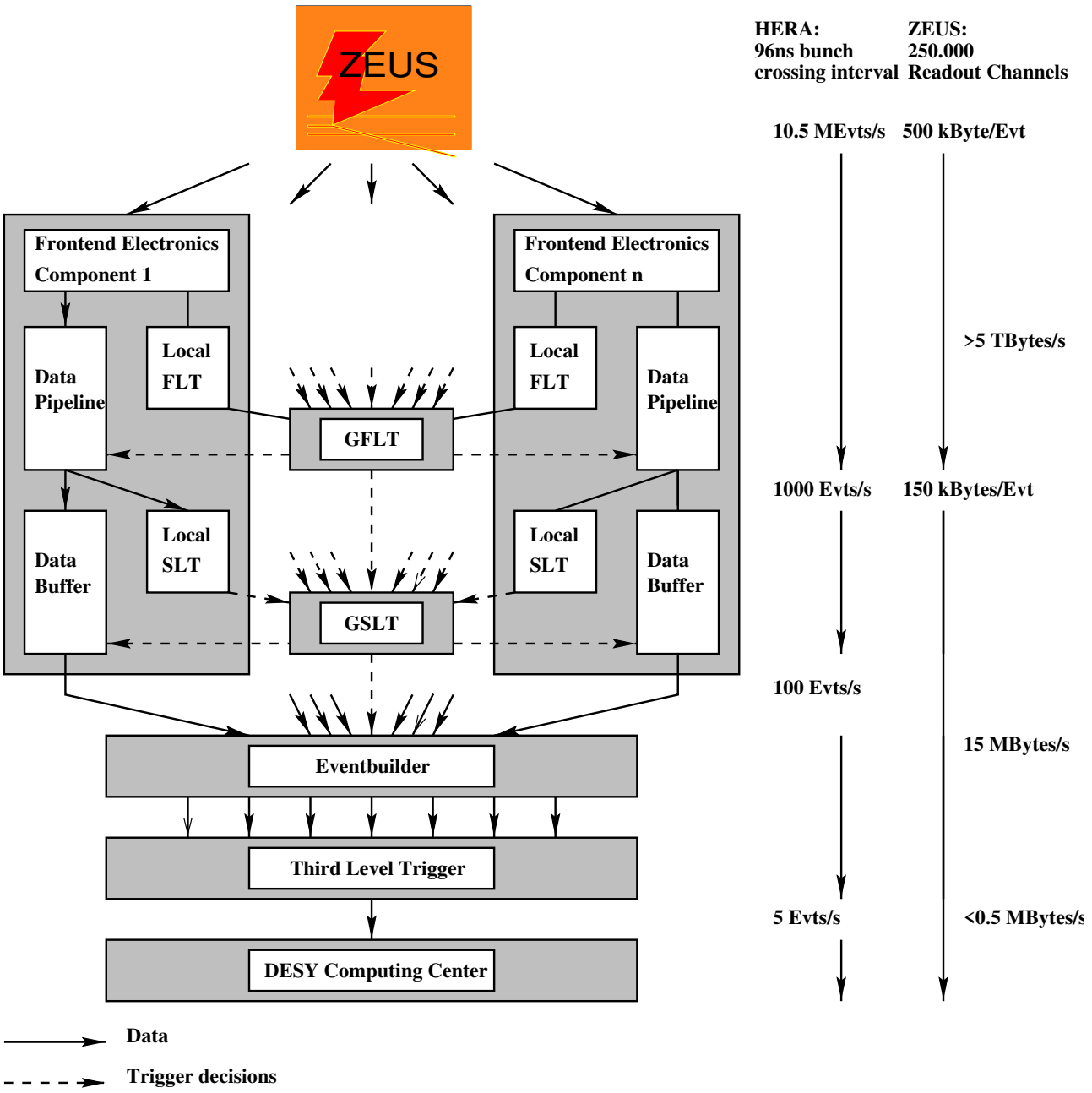

Figure 2.13: Data flow through the ZEUS trigger and DAQ systems.

2.9.3 Event Builder (EVB)

Following acceptance by the GSLT, each component passes the accepted events to the EVB. This stores the data from the components and combines it into one consistent record -the event- ready to be used by the Third Level Trigger (TLT). The EVB will build up to 75 events in parallel and has buffers which are able to store up to 72 further events.

2.9.4 Third Level Trigger (TLT)

The TLT is a software trigger running on a farm of personal computers and is able to view the event as a whole. It uses a version of the offline reconstruction software in order to calculate the kinematics of the event. The TLT is able to make decisions concerning kinematic properties and is able to perform more refined vertex-finding and jet-finding. After this reconstruction, the TLT classifies *ep* events into physics categories according to various filters set by the physics working groups. The final output rate of the TLT is ∼1-10 Hz. Events which have triggered a TLT slot are written to disk and later to tape via a tape robot, over a dedicated connection to the DESY computing center (FLINK). Each event is typically 0.3 MB.

2.10 Offline reconstruction

Following the trigger selection, the data is processed using offline reconstruction software in order to more precisely reconstruct the kinematics of each event. All procedures which are too slow to be available at the TLT, such as the implementation of complete calibration constants, are implemented in the offline reconstruction. The data is also passed through additional filters, which makes selections based on physics criteria. The events selected by each filter are allocated a code, called a Data Summary Tape (DST) bit.

TLTzgana[2] is the offline TLT physics simulation software that mimics the online TLT. It is an extensive piece of Fortran code, a large portion of which consists of physics filters, electron finders, jet finders, muon finders, amongst many other things. There are 125 filter slots classified into five major groups,

[2]Third Level Trigger ZEUS Geant ANAlysis

defined by the class of physics events selected. The physics filters make use of all the reconstructed data, which takes place at the TLT prior to the events being passed through the physics triggers. Each physics group is responsible for its own filter code. TLTzgana, which is accessible to everyone on ZEUS, is used to develop or upgrade filter code and to verify online trigger decisions.

For a period of eight months, this author was the manager of TLTzgana.

Chapter 3

Event simulation

The use of simulation programs is essential in physics analyses for it allows a comparison between measurements and theoretical predictions and it allows a determination of the detector's response to physics events. This chapter gives a somewhat detailed description of the detector simulation and simulation of all physics processes that were considered in this analysis.

High-energy particle detectors are highly complex devices, so the measurement of cross sections and other observables require corrections to account for finite detector efficiency, resolutions and acceptances. Although the performance of the detector should be independent of the physics process being investigated, this is rarely the case and will depend on the details of event topology and the cuts imposed. The simulation of physics events at ZEUS is performed in three stages:

1. Physics process: The *ep* scattering process (see figure 3.2) is simulated with the use of an event generator program which simulates the perturbative leading order (LO) matrix element and leading logarithm initial- and final-state parton showers. The non-perturbative hadronization and parton density functions are also included via phenomenological models and parameterizations;

2. Detector simulation: In order to simulate the response of the detector to the *ep* scattering process, the events from the physics generator are passed to a full simulation of the ZEUS detector. The passage of particles through all sub-detectors is simulated using detailed knowledge of the detector's material composition and geometry;

3. Trigger simulation: The data acquisition chain and trigger response are simulated.

The full event simulation is referred to as Monte Carlo simulation (MC). Figure 3.1 illustrates components of the ZEUS MC simulation, reconstruction, and analysis chain. The paths followed by MC simulated events on the right and data on the left are indicated with arrows. This chapter, describes the general structure of an event generator and the MC used for this analysis.

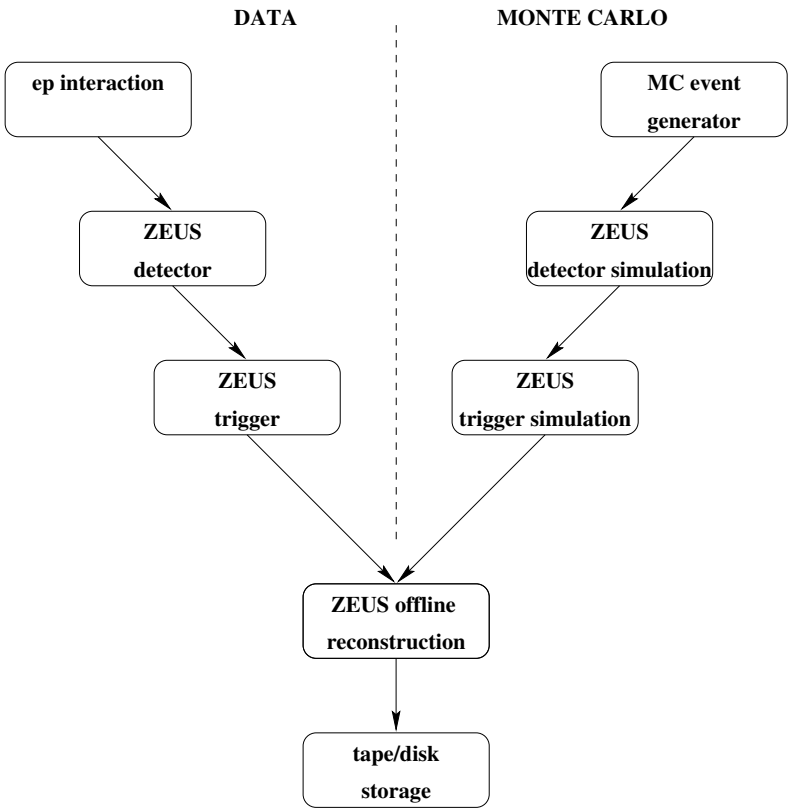

Figure 3.1: Schematic diagram of the ZEUS analysis and MC reconstruction chain.

3.1 Physics simulation

The factorization theorem for hard processes is the main theoretical justification for QCD Monte Carlo event generators. As illustrated in figure 3.2 and described

below, it allows the separation of hard scattering processes from the subsequent soft QCD cascades and hadronization as follows:

- Hard sub-process: the main feature of the event. It is the interaction between a parton in the proton and the exchanged photon, or a photon constituent in resolved photon events. This process can be calculated in a fixed order perturbative expansion since it involves a hard scale μ;

- Initial- and final-state radiation: in processes involving charged and colored objects, the topology of an event can be strongly influenced by the emission of gluons and photons in the initial or final state. These perturbative corrections are usually modelled by the so-called *parton shower method* in which the radiation is simulated by an arbitrary number of branchings of one parton into two, for example, $e \to e\gamma$, $q \to qg$, $q \to q\gamma$, $g \to q\bar{q}$. One of the two final partons keeps a fraction z of the parent parton energy, the other, a fraction $(1-z)$. The probability distribution of the shared energy between the two partons is given by $P_{a\to b\ c}(z)$. The two daughters may branch, in turn, producing other partons, and so on. Via *initial-state radiation*, a parton, constituent of the incident hadron (photon), having low space-like virtuality, radiates time-like partons, increasing its space-like virtual mass. On the other hand, via *final-state radiation*, an outgoing virtual parton with large time-like mass generates a shower of partons having lower virtuality. The shower evolution stops at some fixed scale μ_0, typically of the order of 1 GeV;

- Hadronization: process in which colorless hadrons are formed starting from colored partons. It is a non-perturbative phenomenon and is yet to be understood. Therefore simulation programs model the hadronization process using phenomenological inputs. As described in the previous chapter, the main hadronization models on the market are the cluster model and the string model;

- Beam-remnant: in *ep* interactions, the simulation programs reconstruct the particles that have gone through initial-state radiation and have then generated the partons involved in the hard sub-process. These initial particles, one from each beam, include a parton in the proton and the

exchanged photon or, in resolved photon processes, a parton from the photon. They carry only a fraction of the initial beam energy, the rest is taken by the beam-remnant. If the shower initiator is colored, the beam-remnant will be as well. It is therefore connected to the rest of the event and has to be fragmented and reconstructed coherently.

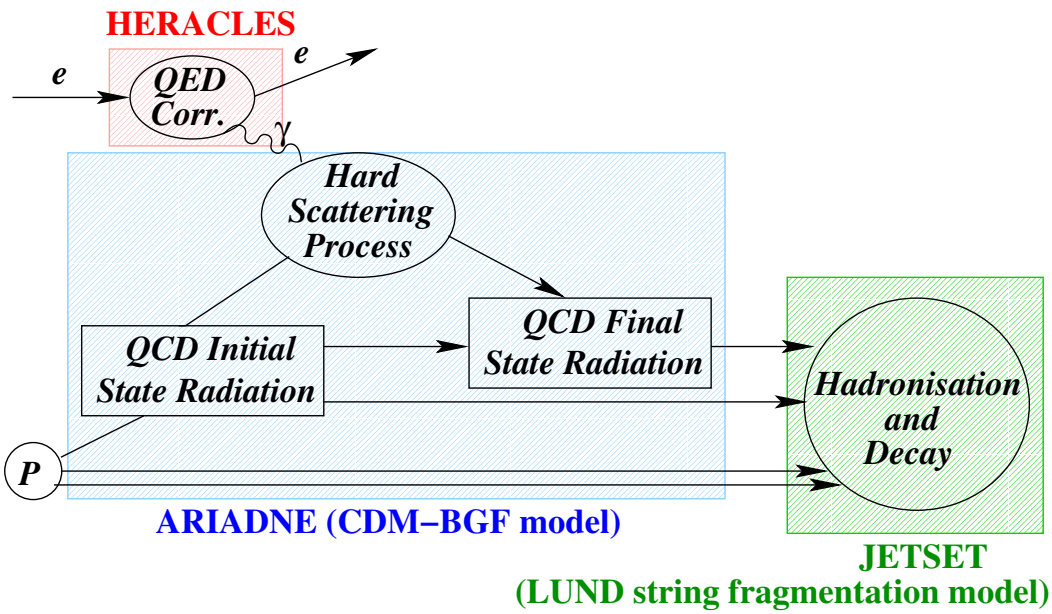

Figure 3.2: Schematic diagram of processes involved in hard QCD interactions and event generation using the DJANGOH framework

3.2 Detector simulation

Event generators, such as ARIADNE [82] and HERWIG [84], which are supported in the ZEUS framework, are gathered in a software program called AMADEUS. The output of the chosen event generator, such as the four-momenta of the particles produced in the hard scatter and all the relevant kinematic variables, are the input to MOZART[1], the ZEUS detector simulation program. MOZART is based on the GEANT [78] package which contains a description of all the relevant physics processes for electromagnetic and hadronic interactions in arbitrary geometries of any element or compound. GEANT tracks particles through the detector,

[1]MOnte Carlo for Zeus Analysis Reconstruction and Triggering.

simulating its response accounting for energy loss, multiple scattering and particle decays in flight. The output of MOZART has the same format as the data output, enabling identical event reconstruction for data and simulated events. The events then pass through CZAR[2], which simulates the trigger logic used for data taking. Both MC-simulated events and ZEUS raw data are then processed by the offline reconstruction package ZEPHYR[3]. While the input for ZEPHYR is all the detector information, its output are event variables such as particle momenta and energies.

The ZEUS data is organized with the ADAMO[4] [85] data management system, which is used for the storage of data, either in memory or on external media. The LAZE[5] program generates bi-dimensional graphical representation of the real or simulated events. Finally users gain access to this data with the EAZE[6] program or the ORANGE[7], a more inclusive EAZE job, where both MC events and data are analyzed in identical fashion. A diagram of the ZEUS reconstruction scheme for data and Monte Carlo is shown in figure 3.3.

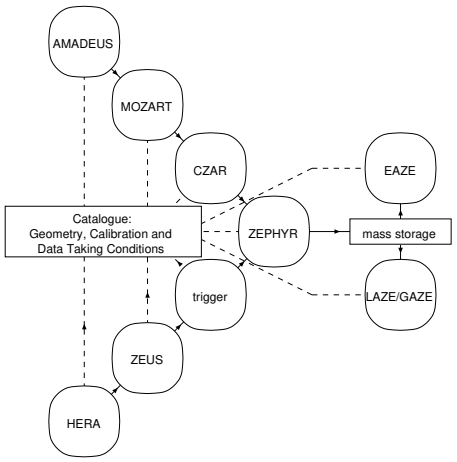

Figure 3.3:
Schematic diagram of ZEUS data and Monte Carlo reconstruction chain.

[2]Complete Zgana Analysis Routine
[3]ZEus PHYsics Reconstruction
[4]Aleph DAta MOdel
[5]Logical Access to ZEUS Events
[6]Effortless Analysis of ZEUS Events
[7]Overlying routine for analysis ntuple generation

3.3 MC used in this analysis

In this analysis, the inclusive DIS background was simulated with ARIADNE. For Θ^+ acceptance and cross section extraction, RAPGAP MC was used. Both are described here.

3.3.1 NC DIS background

Figure 3.2 illustrates the generation scheme and MC packages used for inclusive DIS $ep \to eX$ events for this analysis. The events were generated with DJANGOH 1.1 [79], which is an interface between the LEPTO 6.5.1 [81] and HERACLES 4.6.1 [80] generators. LEPTO simulates the hard-scatter between the lepton and the parton, and HERACLES simulates electroweak corrections of $O(\alpha)$, i.e. corrections for initial- and final-state radiation from the incoming and outgoing electron, respectively, vertex and propagator corrections, and two boson exchange processes as shown in figure 3.4.

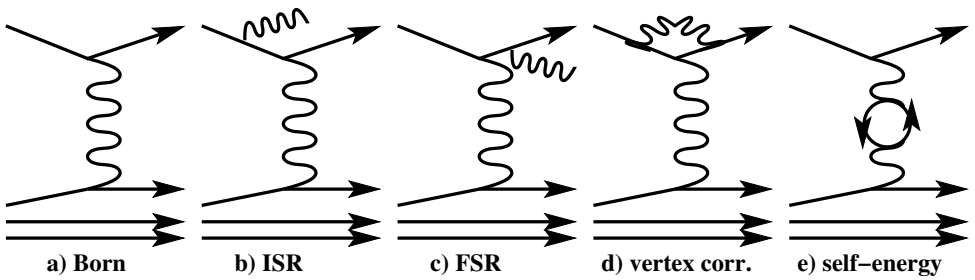

Figure 3.4:
Feynman diagrams of the Born level and LO QED corrections for NC DIS.

The ARIADNE 4.08 program was used to simulate higher order QCD corrections. In ARIADNE, the QCD cascade is simulated by the color dipole model (CDM) [43], including boson-gluon fusion (BGF). (The BGF process is particularly important at low x where there is a strong rise in the gluon density). In the CDM, the color dipole, which is formed by the struck quark and the proton remnant, radiates gluons which can in turn emit softer gluons or split into quark-antiquark pairs. These processes continue until all the dipoles have reached some

minimum energy. This CDM-BGF model provides the best description of the characteristics of the DIS hadronic final state and includes all leading order QCD diagrams.

Neutral current DIS events were generated using electroweak parameters from the particle data group (PDG) [44] and the next-to-leading order (NLO) parton density function parameterization used was CTEQ5D. (See section 1.5 for more on PDF's.)

To form the colored partons produced in the QCD cascades into colorless hadrons, the ARIADNE program uses the Lund string model for hadronization, as implemented in JETSET 7.410 [83]. Finally the weak decays of light hadrons are simulated by JETSET according to the known particle decay properties.

The generated events were then passed through a full simulation of the detector using GEANT 3.13 [78] and processed with the same reconstruction program as used for the data. The detector-level MC samples were then selected in the same way as the data. The generated MC luminosity was twice that of data. See table 3.1 at the end of this chapter.

Several samples of charged current DIS MC were used with different minimum Q^2 cuts at the generator level. Using separate samples in this way eliminates the need to generate large numbers of low Q^2 events in order to cover the HERA Q^2 (and x) range. The samples are then combined using weighting appropriate to the luminosity of each sample. The Q^2 thresholds and luminosities of the samples used are detailed in table 3.1.

3.3.2 Pentaquarks

The acceptance and cross-section extraction for Θ^+ was calculated using the RAPGAP 3.00 MC event generator [88], whereby Σ^+-baryons were assumed to have the same production and decay characteristics as the Θ^+-baryons. The modified Σ^+-baryons were assumed to have a natural width of zero and a mass of 1522 MeV and were forced to decay, with 100% branching ratio, to the $K^0 p(\bar{p})$ final state.

RAPGAP implements all features except NLO matrix elements, which is conceptually difficult in event generators. RAPGAP consists of LEPTO 6.5, which simulates the hard scatter between the lepton and the parton. The parton showers comprise of gluon radiation from charmed quarks and approximate the NLO

MC Samples	Collisions	Q^2 (GeV^2)	σ (pb)	Events	$\int \mathcal{L}$ (pb^{-1})
Background					
ARIADNE	300 GeV				
	e^+p	> 0.8	730480	2 M	2.74
	e^+p	> 2	407860	8 M	19.61
ARIADNE	318 GeV				
	e^-p	> 0.8	744200	7 M	9.40
	e^+p	> 2	417210	23 M	55.04
	e^+p	> 3	434204	10 M	23.03
	e^+p	> 10	128383	14 M	109.05
Signal					
RAPGAP (Σ^+)	318 GeV				
	e^+p	> 1	487555	1M	

Table 3.1: MC samples for the simulation of NC DIS events and pentaquarks.

corrections for charm production. HERACLES 4.6.1 [80] is used for the simulation of initial and final state radiation from the DIS electron and JETSET 7.4 is used for the fragmentation and decay of the partons. RAPGAP events are passed through the standard ZEUS detector and trigger simulation packages to simulate the detector response as described above. Approximately 1 million such events were generated.

Chapter 4

Event reconstruction

Following the trigger selection, only partial event information is available. Hence a full reconstruction of events and event properties must be performed offline in order to extract information on the properties of a particular event.

The detector components that are necessary to select NC DIS events are the CTD, SRTD and CAL. The CTD provides the particle tracks and their momenta and also the position of the primary and secondary vertices. In addition, it provides the energy loss of the particles due to ionization, dE/dx. The SRTD is used to determine the impact position of the scattered electron. And the CAL measures the hadronic final state and the energy of the scattered electron as well as its impact position if outside the fiducial volume of the SRTD.

This chapter describes the techniques used to convert the information from these detector components into a fully reconstructed data-set.

4.1 Track reconstruction

The analysis presented in this thesis relies heavily on track and vertex information for the precise measurement of particle positions and momenta.

The track and vertex finding for ZEUS is performed by a pattern recognition software package called VCTRAK [89]. Hits made by charged particles as they fly through the CTD are fitted with VCTRAK, which if run in the "regular" mode uses information from CTD, FTD, RTD and SRTD. However for this analysis, the "CTD-only" mode was used, i.e. only CTD information was required.

In a nutshell, the VCTRAK software groups the individual hits into track candidates, which are then fit with a five-parameter curve. The tracks can be

connected to the primary (interaction) vertex or a secondary vertex originating from particle decays or nuclear collisions in material such as the beam-pipe. The connection to a vertex adds additional constraints on the track and at the same time constrains the position of the vertex.

4.1.1 Track finding

The VCTRAK algorithm first considers hits in the axial superlayers only. Each track candidate begins as a track seed consisting of three adjacent hits in the outer superlayers, where the hit densities are lower. The software then connects the hits found in each superlayer to form complete tracks. The reconstruction begins from the outermost superlayer and is extrapolated inwards, guided by an additional "virtual hit" at $x = y = 0$. A circular arc is formed in the xy-plane as additional axial hits are gathered as the process of extrapolation continues and the trajectory parameters are updated.

In order to reconstruct the z-coordinate of the trajectory, information from both the axial and stereo superlayers is needed. Initially z-by-Timing (zbT) measurement is used, yielding a coarse first estimation of the trajectory in 3D (resolution of $\sigma_{z\mathrm{bT}} \approx 4.4$ cm [91]). This limits the region which has to be searched for stereo hits, which are also used to provide more accurate information on the z-position. With this configuration, the z-position of a track can be reconstructed with an accuracy of approximately 2 mm.

The entire procedure is repeated until all track seeds in the outermost superlayer are used, at which point it continues with the next inner superlayer. So the longest tracks are found first, and the shortest tracks last.

4.1.2 Track fitting

Since the magnetic field provided by the solenoid is almost parallel to the axis of the CTD, a track path can be well represented by an axial helix. Hence each track candidate is fitted to a five-parameter helix model with the fit beginning from the innermost tracks. This parameterization is given in terms of the following variables and is illustrated in figure 4.1.

- ϕ_H, the azimuthal angle of the helix tangent at its point of closest approach to the line $x = y = 0$;

- Q/R, where Q is the track charge and R the local radius of curvature. "Local" refers to the radius of curvature of the helix closest to the reference point (0,0);
- QD_H, where D_H is the distance of closest approach of the line $x = y = 0$;
- Z_H, the z-coordinate of the track at its closest approach to $x = y = 0$;
- $\cot\theta_H$, where θ_H is the polar angle of the track.

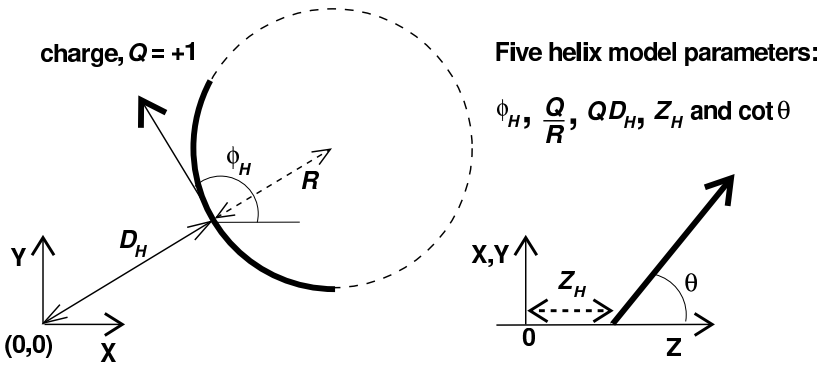

Figure 4.1: Schematic illustration of the five-helix-parameter model.

The trajectory fit commences by first estimating a momentum, which is based on the slope and curvature provided by the pattern recognition. A trajectory is established by "swimming" through the magnetic field, starting from the vicinity of the innermost measured hit, and proceeding outward as far as necessary. Finally, the trajectory is transported inward, from the region of the innermost measured hit to perigee with the z axis at $x = y = 0$.

In order to absorb the effect on the resolution of variations in the drift velocity and Lorentz angle, a drift velocity fit has also been implemented. In addition to this, allowance is also made for Coloumb scattering inside the beam-pipe and the inner wall of the CTD. The information is then ready to be used for vertex reconstruction.

4.1.3 Vertex finding

Once the tracks are reconstructed via the procedure described above, they are used for fitting primary and secondary vertices, which is done in the following steps:

- Tracks that are incompatible with the intersecting beam-line are removed from the fit;
- Vertex "simple fit": for the surviving tracks, the weighted center of gravity, $(x, y, z)^{simple}$ is found. Tracks that contribute too much to the overall χ^2_{simple} are discarded, one at a time, until the fit quality is acceptable. This vertex is the starting point for the full vertex fit.
- Vertex "full fit": with the vertex from the simple fit, the final vertex position is resolved. The remaining trajectories are constrained to this vertex, while at the same time, the direction and curvature are refitted. Tracks which extend into the innermost superlayer are candidates for primary-vertex tracks.
- Secondary-vertex finding: secondary vertices are identified by pairing all reconstructed tracks which are not already refitted to the primary vertex. Candidates for secondary-vertex tracks, originating from long-lived particle decays, constitute tracks which have hits in at least two axial superlayers and the intervening stereo layer, but which have no information in the innermost superlayer. Bad tracks yielding a high vertex χ^2 are filtered out with a vertex fit and at least two tracks have to survive in one cluster for it to be accepted. Furthermore, if intersections in the transverse $r\phi$-plane are found, then the distance between the tracks in δz is calculated, with true secondary vertices having low values of δz.

Appendix A provides a more detailed description of how primary and secondary vertices are reconstructed. This analysis requires tracks originating from both. While the primary-vertex tracks are required for the identificaton of protons, the secondary vertices and tracks are used to reconstruct K^0_S-mesons and Λ-baryons .

4.2 CTD B-field correction

High statistics studies of mass peaks of particles such as J/ψ, D^*, K^0_S, for example, suggest that the magnetic field used by VCTRAK is low by about 0.3%. Hence the p_{T} of all tracks, which is proportional to B (cf. section 2.5), is scaled by a factor of 1.003 to correct for this effect.

4.3 Ionization energy loss

Section 2.3 provided a description of how a particle loses energy via ionization as it interacts with matter. The measurement of this ionization, yet another means of particle identification, is achieved by first measuring a raw-pulse size, which then has to be converted into a more meaningful and useful quantity like dE/dx or the amount of energy loss of the particle. Before moving on to a description of how this is done, a brief introduction to the theory of ionization-energy loss is given.

4.3.1 Bethe - Bloch equation

For all charged particles, except for electrons, due to their small mass, ionization losses dominate over radiation losses at all but the highest attainable energies. These ionization losses are dominated by Coulomb scattering off atomic electrons. There is some scattering from the nucleus however this is a negligible effect since the recoil energy of the nucleus is much smaller due to its greater mass. The ionization-energy loss can be parametrized by the Bethe-Bloch equation, which is presented here. For a particle with charge z equal to plus or minus the electron charge, the energy loss of a particle, dE/dx (in MeV/cm), is:

$$-dE/dx = 4\pi N_A r_e^2 m_e c^2 z^2 \frac{Z}{A}\frac{1}{\beta^2}[\ \log(\frac{2\mathrm{m_e c^2}\beta^2\gamma^2}{\mathrm{I}}) - \beta^2 - \frac{\delta(\gamma)}{2}]\ , \qquad (4.1)$$

where x is the traversed distance, N_A is Avogadro's number, r_e and m_e are the electron's classical radius and mass, respectively and c, β and γ have their standard relativistic definitions. The properties of the medium are Z and A, the atomic number and weight of the medium, respectively, $\delta(\gamma)$, the dielectric screening correction which is important for highly relativistic particles and I which is the mean ionization potential of the atoms averaged over all electrons and is given approximately by $I = 10Z$ eV for $Z > 20$.

Figure 4.2 shows the variation of dE/dx with momentum for well reconstructed particles in the CTD. The superimposed curves distinguish the different classes of particles. The energy loss is a function of the velocity, $c\beta$, of the particle: for low β, the ionization loss decreases steeply, down to a minimum for $\gamma = (1-\beta^2)^{-0.5} \approxeq 3$, and then rises logarithmically up to a plateau at very high γ. At low momenta, $p = \beta\gamma m$, the energy loss is different for different particle

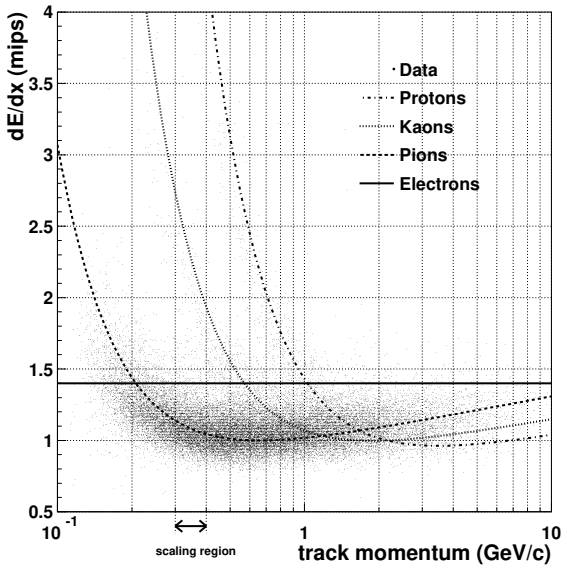

Figure 4.2: dE/dx versus momentum of well reconstructed tracks in the CTD with curves illustrating the particle classes.

masses. For hadrons, there is a rapid fall in dE/dx as the momentum increases from zero due to the $1/\beta^2$ factor.

Hence, since the value of dE/dx depends on the velocity of the charged particle, it is possible to distinguish different particles with the same momentum but different masses by a careful measurement of dE/dx.

4.3.2 Reconstruction of dE/dx

The raw pulse sizes from ionized electrons are recorded in order to provide the dE/dx information. All sense wires in the CTD are read out with 8-bit flash analog-to-digital converters (FADC). For a given wire, the data is packed into an array of digitized signals in FADC counts in time-bins of 9.6 ns. These are called pulse trains. The FADC output is further analyzed by digital signal processors (DSPs), which search the pulse train for groups of time-bins having a characteristic pulse shape. The DSPs then determine the height of the pulse for a given wire in FADC counts as displayed in figure 4.3. And it is the height that provides the relevant information on the energy loss. The large spike at about 235 counts is due to saturation, which occurs when, for very high energy losses, the value of FADC counts exceeds 200. This behavior is a result of limitations of

the read-out with 8 bits.

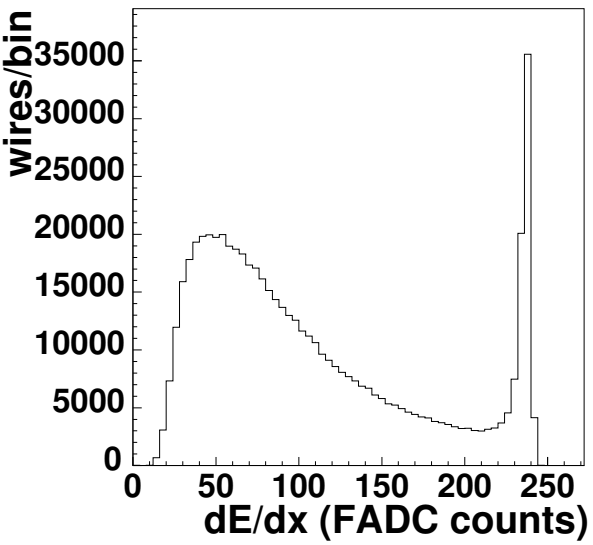

Figure 4.3: Typical dE/dx pulse for a low momentum pion exhibiting the Landau shape and saturation at high dE/dx.

The FADC pulse heights can be associated with track trajectories once the tracks have been reconstructed. The energy loss, and thus the pulse height in FADC counts, is influenced by the trajectory of the track and detector effects. Hence the path length, dx, which depends on the the polar angle, θ, of the track, is corrected. In addition, the different gains of the sense wires, the z-position of the hit, the drift distance, differences between positive and negative tracks and the Lorentz angle are taken into account. Furthermore, pulses are rejected if a track is parallel to the drift direction, if the drift distance is near a cell boundary or if the pulse height is distorted by an earlier hit (within 100 ns) on the same sense wire.

The hits that pass the corrections described above are ordered by size and form a Landau-like FADC distribution shown in the figure. In order to reject the large asymmetric tail of the distribution, a truncated mean is performed, whereby the lowest 10% and the highest 30% of the hits are discarded. If at least four hits remain, the mean energy loss is then defined as the sum over the remaining pulse heights divided by the remaining number of hits. If the remaining 60% of the pulse heights still contain saturated hits, they are further removed, thus resulting in a number of hits below 60%. To recover the normalization of the remaining hits

after discarding all saturated hits, a fitted polynomial correction is applied to the calculation for the mean energy loss [89]. A reconstructed dE/dx value in FADC counts is thus obtained for use in particle identification, however more offline corrections are needed to further refine the ionization energy-loss measurement.

The value of dE/dx for a given particle type in a certain momentum and angular range changes as a function of time due to changes in the composition of the gas and the pressure (equal to the atmospheric pressure). A variation in the pressure changes the gas density, which has an impact on the number of ions produced, which in turn has a direct effect on the average pulse size. So the dE/dx has to be scaled for the average pressure change over different runs and *within* one run if it is of a long duration ($\sim$ 8 hours) in order to enable comparisons between runs. Hence in order to account for any such variation of dE/dx between different runs, all measured dE/dx values in one run are normalized to the average dE/dx for pions around the minimum ionization, i.e. in the momenta range, 0.3 to 0.4 GeV, where they are most easily distinguishable from other particles. As can be seen in figure 4.2, in this narrow momentum region, the pion band is far from bands of the other hadrons. It is close to its minimum, hence well separated from electrons. So in this momentum range, a clear pion signal is obtained, which when fitted with a Gaussian for each run, yields an average value for the pions for that particular run. To account also for pressure variation within a run, the pressure is monitored every 10-20 minutes and a correction factor is applied to each measured dE/dx value. The normalized value of dE/dx has the units of mips or minimum ionizing pions. See [75] for a more detailed explanation on the corrections.

4.4 Global calorimeter quantities

The reconstruction of the hadronic final state relies on the precise knowledge of information from the CAL, one of the main components used in this and most ZEUS analyses. The calorimeter measurement consists of a list of energies in the different calorimeter cells. The total energy deposition in the CAL, $E_{\rm tot}$, and its

projections, p_x, p_y, p_z, along the space coordinates are defined as:

$$E_{\text{tot}} = \sum_i E_i, \tag{4.2}$$

$$p_x = \sum_i E_i \sin\theta_i \cos\phi_i, \tag{4.3}$$

$$p_y = \sum_i E_i \sin\theta_i \sin\phi_i, \tag{4.4}$$

$$p_z = \sum_i E_i \cos\theta_i. \tag{4.5}$$

The summation index i runs over all CAL cells. E_i, θ_i and ϕ_i are the energy, polar and azimuthal angles of the i-th CAL cell, respectively. The angles are calculated using the z-position of the reconstructed event vertex and the center of each cell.

Four-momentum is assumed to be conserved in all processes, which means that also the difference between the energy and the longitudinal component of the momentum, $E - p_z$, is conserved, where $E - p_z$ is defined as:

$$(E - p_z)_{beam} = E_{\text{tot}} - p_z = \sum_i E_i(1 - \cos\theta_i) \ . \tag{4.6}$$

As a result, due to the definition of the ZEUS coordinate system, the energy and momentum of the proton cancel, however they add up to twice the beam energy or 55 GeV for the electron. The only energy and momentum assumed to escape undetected is associated with the proton-remnant going down the beam-pipe. It carries energy and longitudinal momentum, however little $E - p_z$.

4.4.1 Calorimeter noise supression

There are events which may contain low levels of hadronic activity or those for which the hadronic mass must be precisely determined. Such events are sensitive to the effects of noise in the cells. Hence the cells that are affected by noise are excluded from further reconstruction [92]. Cells are assumed to be noisy if they:

- are of low energy: $E_{\text{cell}}(\text{EMC}) < 0.06$ GeV, $E_{\text{cell}}(\text{HAC0}) < 0.10$ GeV and $E_{\text{cell}}(\text{HAC}) < 0.11$ GeV;

- have one PMT with much higher signal than the other: if $E_{\text{cell}} < 1$ GeV, then a cut of $|I_{\text{cell}}| < 0.49{*}E_{\text{cell}} + 0.03$ GeV is applied, where I_{cell} is the difference in energy recorded by the two PMTs. This cut removes noise which arises predominantly from small sparks in the PMTs, which is usually lower than 0.7 GeV;

- are isolated and of low energy: $E_{\text{emc}} < 0.08\,\text{GeV}$ or $E_{\text{hac}} < 0.14\,\text{GeV}$. This cut is effective in removing noise stemming from the natural radioactivity of the uranium material;

- are already known to be "hot" due to bad PMTs or electronic read-out. A list of these noisy cells is maintained for each data-taking period.

While the first three effects are corrected in the same manner in Monte Carlo simulation, the last effect is not.

4.4.2 Calorimeter energy corrections

The calorimeter energy response needs to be corrected for energy loss in inactive material between the interaction point and the CAL, for back-splash from the CAL and for non-uniformity in the energy response of the CAL cells. The correction takes into account the difference in the CAL response between data and MC events. The hadronic system and identified electrons are treated separately for this correction and added after the correction to form the total corrected CAL four-momentrum vector. If there is no SRTD or PRES information, the correction is applied to all cells in the calorimeter. Otherwise, it is applied only to those cells which are not identified with the electron candidate. The energies in the FCAL and BCAL are scaled by global factors of 1.000 and 1.005 respectively, while the energies in the RCAL are scaled by cell-by-cell factors of between 1.000-1.0025, depending on the energy and position of the islands [93]. Islands are clusters of CAL cells.

4.5 Energy Flow Objects (EFOS)

CAL information would be sufficient for the measurement of energy deposits, however the tracking system has a much better angular resolution and a

better momentum resolution at low energies. Hence if calorimeter and tracking information is combined, an improved measurement of the energy deposits can be made.

All good primary vertex tracks and cells, except those belonging to the scattered electron, are used. Tracks are matched to calorimeter information by combining cells belonging to one shower into one island. These energy-flow objects or matches of tracks and islands are called EFOs or ZUFOs[1]. A ZUFO can have more than one track or island and is not required to have both a track and an island. In this analysis, ZUFOs are used to calculate the $E - p_z$ of the event and the kinematic variables for the double angle and the Jacquet-Blondel methods described below. For more details on ZUFOs, see [94].

4.6 Electron reconstruction

The primary signature of neutral current DIS events is the scattered electron found in the calorimeter, hence a reliable method of electron-identification is required. For this analysis, electrons are identified offline using the SINISTRA95 [95] electron-finder. SINISTRA is a neural network which has been trained on low-Q^2 NC DIS and Monte Carlo data to produce the best separation between electromagnetic and hadronic energy deposits by using the properties of shower profiles to establish the nature of the originating particle.

SINISTRA uses calorimeter islands without noise as input for the neural net, where each island is a potential electron candidate. The output is a number between 0 and 1, with 0 being hadron-like and 1 being electron-like. Hence this value is interpreted as the probability that the energy deposit is of electromagnetic origin. If the candidate with the highest probability has a probability greater than 0.9, it is assumed to be an electron. For this analysis, if there are several candidates with a probability greater than 0.9, only the one with the highest probability is considered.

For the surviving electron candidate, the energy is the sum of all the cell energies in the island. This energy is then corrected for energy loss in inactive material according to test-beam measurements. Only isolated electrons with a corrected energy, $E_{el'} > 4$ GeV, have been used in this analysis. The direction of the electron is calculated from the CTD track pointing in the direction of the electron candidate.

[1] ZEUS Unidentified Flow Objects

4.7 Kinematic reconstruction

Once the electron has been detected, the kinematic properties of the event can be reconstructed, for which an exact reconstruction of the four-momentum of the exchanged photon is necessary. Any combination of the following can be used for the reconstruction: the electron beam energy, E_{ebeam}, the polar angle, $\theta_{el'}$, and energy, $E_{el'}$, of the scattered electron, the transverse momentum and the difference of energy and longitudinal momentum of the hadronic system.

For the reconstruction of the exchanged photon, the azimuthal angle needs to be reconstructed, for which the electron's azimuthal angle is used as it has a higher precision than the one obtained from the hadronic system. Three methods exist by which the kinematic variables Q^2, x and y can be reconstructed:

- Electron method: conceptually the simplest method, it uses the scattered electron for the kinematic reconstruction. The three quantities are given as:

$$x_{el} = \frac{E_{ebeam}}{E_p} \quad \frac{E_{el'}(1+\cos\theta)}{2E_{ebeam} - E_{el'}(1-\cos\theta)} \ , \tag{4.7}$$

$$y_{el} = 1 - \frac{E_{el'}}{2E_{ebeam}}(1-\cos\theta) \quad \text{and} \tag{4.8}$$

$$Q^2_{el} = 2E_{ebeam}E_{el'}(1+\cos\theta) \ . \tag{4.9}$$

  The reason this is the simplest method is that it requires only the measurement of the energy and polar angle of the scattered electron.

- Double Angle Method [96]: this method uses the scattering angles of the electron and the struck quark and yields the following kinematical relationships:

$$x_{da} = \frac{E_{ebeam}}{E_p}\frac{\sin\gamma_h + \sin\theta + \sin(\theta+\gamma_h)}{\sin\gamma_h + \sin\theta - \sin(\theta+\gamma_h)} \ , \tag{4.10}$$

$$y_{da} = \frac{\sin\theta(1-cos\gamma_h)}{\sin\gamma_h + \sin\theta - \sin(\theta+\gamma_h)} \quad \text{and} \tag{4.11}$$

$$Q^2_{da} = 4E^2_{ebeam}\frac{\sin\gamma_h(1+\cos\theta)}{\sin\gamma_h + \sin\theta - \sin(\theta+\gamma_h)} \ . \tag{4.12}$$

  Since the angle, γ_h, of the struck quark can't be measured directly, it is calculated from hadronic variables using the Jaquet-Blondel Method

described below:

$$\cos\gamma_h = \frac{(\sum_h p_{xh})^2 + (\sum_h p_{yh})^2 - (\sum_h E_h - p_{zh})^2}{(\sum_h p_{xh})^2 + (\sum_h p_{yh})^2 + (\sum_h E_h - p_{zh})^2} \,. \tag{4.13}$$

The advantage of using angles is that angular resolution is normally better than energy resolution, giving a more precise measurement.

- Jaquet-Blondel Method [97]: this method reconstructs the kinematics using only the hadronic system, hence it is independent of the electron. The hadronic final state consists of many particles of which some belong to the remnant and escape through the beam-pipe. In this method, the four-momenta of all these particles are summed up. To avoid biases from the particles lost through the beam-pipe, only the transverse momentum $p_{T,h}$ and the difference between energy and longitudinal momentum $(E_h - p_{zh})$ are used. Both of these variables are close to zero for the proton-remnant going down the beam-pipe. The resulting formulae are:

$$y_{JB} = \frac{(E_h - p_{zh})}{2E_{ebeam}} \,, \tag{4.14}$$

$$Q^2_{JB} = \frac{p^2_{T,h}}{1 - y_{JB}} \,. \tag{4.15}$$

Most analyses utilize several of the kinematic reconstruction methods presented above depending on the kinematic region examined. While the double angle method has a good resolution at high Q^2, the electron method has a better resolution at low Q^2. The double angle method is used if the electron has a track associated with it and $\gamma_h < \pi/2$, otherwise the electron method gives a better resolution. In this analysis, the default choice is the electron method, while the double angle method is used as a systematic check. For low $y_{JB}(y_{JB} < 0.05)$, Jaquet-Blondel method provides a better resolution than does the electron method. However the resolution of Q^2_{el} and x_{el} is always better than that of Q^2_{JB} and x_{JB}, respectively, thus the latter are not used in this analysis.

Chapter 5

Event selection

The ZEUS data is selected in two stages. First the data is filtered by the online trigger system, which was described in chapter 2. Next the events are filtered further once the full event reconstruction has been performed as described in chapter 4. This chapter outlines the events selected for this analysis and explains the trigger conditions and offline cuts. The chapter concludes with distributions of data and Monte Carlo comparisons for the selected events containing at least one K^0_S-meson. The same comparisons with events containg Λ-baryons is not shown as they are very similar.

5.1 Data-set

The analysis is performed with NC DIS events in the HERA-I data taken with the ZEUS detector between the years 1996 and 2000. Runs were selected using the EVTAKE routine [98], which is a code that selects runs if the following criteria are met:

- the LUMI monitor is fully functional;
- the magnetic field is on;
- the CTD is at full high voltage with no large dead regions;
- the CAL is operational without a significant number of dead channels;
- the interaction vertex is not shifted.

Following EVTAKE selection, the data corresponds to a total integrated luminosity of $\mathcal{L} \approx 121$ pb$^{-1} \pm 2\%$. The quoted systematic uncertainty for the combined data-taking period was obtained by averaging the luminosity-weighted uncertainties for the single years. This sample is summarized in table 5.1.

Year	Collision	cms energy	$\int \mathcal{L}$ (pb^{-1})	σ_{syst} (%)
1996	e^+p	300 GeV	10.77	1.1
1997	e^+p	300 GeV	27.85	1.8
1998	e^-p	318 GeV	4.61	1.8
1999	e^-p	318 GeV	12.10	1.8
1999	e^+p	318 GeV	19.62	2.25
2000	e^+p	318 GeV	45.69	2.25
Total			120.64	1.98

Table 5.1: HERA running conditions and integrated luminosities taken with ZEUS and considered in this analysis.

What follows is a description of all the requirements made to filter out the NC DIS events and a brief explanation as to why those cuts are made.

5.2 Online selection

As described in section 2.9, ZEUS uses a three level trigger system to preselect events and reduce the rate. The trigger at each level is decomposed into sets of requirements and associated logic which are grouped together into trigger "slots". The trigger slots provide a binary decision on whether a given event is preserved or rejected and these decisions for a trigger level are grouped into trigger words. This provides a rapid mechanism for filtering events based on very small trigger words stored with the event. In making the trigger selection, a few things need to be considered:

- The trigger does not only cut background, but also physics events, making certain regions of phase-space inaccessible and giving other regions an acceptance that is difficult to understand. Hence a few trigger slots should be used along with a region of phase-space where these slots have a good acceptance;

- Sometimes some Monte Carlo events survive all cuts even if they are not selected by the trigger. To avoid a discrepancy between data and Monte Carlo, exactly the same trigger bits should be used for both;
- Some slots are prescaled, i.e. they take only every n-th event of all those they trigger on. Here n is the prescale value. These events should be given a weight based on the effective luminosity for the prescaled slots. If a large fraction of events comes from prescaled slots, the statistical error becomes larger since it corresponds to the effective luminosity.

This analysis uses a trigger chain which is well understood and simulated for MC events. For the selection of DIS events, the two TLT slots used are the fully inclusive, but prescaled DIS trigger (DIS01) and the medium-Q^2 DIS trigger (DIS03). Both these triggers have their own configuration of logical ORs of FLT and SLT slots, which are described below.

5.2.1 First Level Trigger

The FLT slots can be vetoed by signals from the C5, Veto Wall, SRTD or CTD. The event is taken if there is no veto and at least one of the following requirements is fulfilled:

- the total electromagnetic energy in the calorimeter exceeding 15 GeV;
- an isolated electromagnetic deposit in the FCAL or BCAL and a track in the CTD;
- an isolated electromagnetic deposit in the RCAL with one of the following:
  - the total electromagnetic energy in the RCAL exceeding 2 GeV,
  - a signal in the SRTD and a track in the CTD or
  - a track in the CTD and total energy exceeding 18 GeV;
- the total transverse energy in the calorimeter exceeding 18 GeV;
- the total transverse energy in the calorimeter exceeding 11.5 GeV and a track in the CTD;

- an isolated electromagnetic deposit in the RCAL (BCAL) exceeding 3.4 GeV (4.8 GeV) and a track in the CTD.

The combination of these different triggers allows an efficient selection of NC DIS events over the full Q^2 range. The average trigger efficiency for events that pass the offline selection cuts, as described in section 5.3, is above 99% and is determined from independent triggers [99].

5.2.2 Second Level Trigger

At the second level trigger, the event is taken if $E - p_z + 2 \cdot E_\gamma^{(lumi)}$ exceeds 29 GeV, where $E_\gamma^{(lumi)}$ is the energy deposited in the photon calorimeter of the luminosity monitor system. This is done in order to eliminate background from photoproduction events. These are events in which the electron escapes down the beam-pipe and hence cannot be included in the $E - p_z$ calculation. As a result, $E - p_z$ peaks at much lower values. In addition, one of the following requirements is met:

- electromagnetic energy in RCAL or BCAL exceeding 2.5 GeV;
- electromagnetic or hadronic energy in FCAL exceeding 10 GeV.

5.2.3 Third Level Trigger

At the third trigger level, the event is taken if one of the two TLT slots, DIS01 or DIS03, takes the event. Below is a description of the two slots.

DIS01 - Inclusive DIS trigger for low-Q^2:

- requires an electron in the RCAL with $E_{el'} > 4$ GeV outside a region of $12 \times 6\,\mathrm{cm}^2$, centered around the beam-pipe;
- has a prescale of 1, 10 or 100 resulting in an integrated luminosity of $16.69\,\mathrm{pb}^{-1}$. This number is calculated by summing up the ratios of integrated luminosity and prescale for the individual runs.

DIS03 - Inclusive DIS trigger for medium-Q^2:

- requires an electron in the RCAL with $E_{el'} > 4\,\text{GeV}$ energy outside of a box or circle of varying values centered around the beam-pipe. The corresponding luminosities are:
  - 14×14 cm^2: ~ 7.39 pb^{-1}
  - R > 25 cm: ~ 47.95 pb^{-1}
  - R > 35 cm: ~ 65.31 pb^{-1}
- has a prescale of 1.

Throughout 1996-2000, while DIS01 was implemented with the same box cut, it was heavily prescaled due to its large contribution to the TLT output rate. DIS03, on the other hand, was never prescaled, however over the years, it was implemented with varying box/radius cuts. See table 5.2 for specific prescale and box/radius-cut values for the different run ranges and the corresponding luminosities.

Furthermore, DST (Data Summary Tape) bit 9 is required which means that an electron finder reconstructed a positron with an $E_{el'} > 4$ GeV.

5.3 Offline selection

Once the events have passed the trigger selection, they are reconstructed using the full ZEUS reconstruction and subjected to more stringent offline selection. The cuts made on various observables are motivated by comparing distributions in data with Monte Carlo and are shown at the end of this chapter.

5.3.1 Electron identification

SINISTRA was used to find the scattered electron, which distinguishes NC DIS processes from the rest.

- $P_{el'} \geq 0.9$: SINISTRA electron probability as explained in section 4.6;
- SRTD 'box' cut: cut on the electron position in the RCAL to remove events with electrons near the beam-pipe region, where a bad reconstruction of the electron may occur:

$$|x_{el'}| >= 13\,\text{cm} \quad \text{OR} \quad |y_{el'}| >= 7\,\text{cm}\,. \tag{5.1}$$

Year	Run Range	**DIS01**:Box Cut (12 x 6) cm^2		**DIS03**: PScale = 1	
		PScale	$\int \mathcal{L}_{eff}$ (nb^{-1})	Box Cut	$\int \mathcal{L}$ (nb^{-1})
COM Energy: **300 GeV**					
1996 e^+p	20718 - 21631	1	1620.750	14 x 14	
	21634 - 21853	OFF	0.0	14 x 14	7386.871
	21871 - 22447	100	44.402	14 x 14	
	22451 - 22462	1	148.240	R $>$ 25	
	22466 - 22662	100	8.057	R $>$ 25	3385.580
	22673 - 22954	1	2431.660	R $>$ 25	
1997 e^+p	25190 - 25336	1	749.670	R $>$ 25	27854.832
	25344 - 27889	100	270.956	R $>$ 25	
Total: 96 - 97 e^+p			5273.733		38627.283
COM Energy: **318 GeV**					
1998 e^-p	30758 - 31544	100	31.363	R $>$ 25	4610.111
	31557 - 31752	1	1473.810	R $>$ 25	
1999 e^-p	31784 - 32213	1	3220.840	R $>$ 25	12101.533
	32214 - 32906	100	88.778	R $>$ 25	
Total: 98 - 99 e^-p			4814.792		16711.644
1999 e^+p	33125 - 34486	10	1962.447	R $>$ 35	19624.475
2000 e^+p	35031 - 37584	10	4469.674	R $>$ 35	
	37588 - 37639*	1	(815.060)	R $>$ 35	45686.000
	37646 - 37715	10	98.927	R $>$ 35	
Total: 99 - 00 e^+p			6531.050		65310.475
Total: 96 - 00 $e^\pm p$			16619.602		120636.953

Table 5.2: Summary of DIS01 prescales and DIS03 box cuts for 96-00 data.
* Shifted vertex runs - not used in this analysis

5.3.2 Kinematic cuts

The kinematic cuts describe the kinematic range analyzed and can be directly reconstructed from the four-momentum of the virtual photon.

- $E_{el'} \geq 10$ GeV: a high corrected energy of the scattered electron in the calorimeter ensures a high purity and efficiency of the electron finder. (For lower electron energies the efficiency drops to 50%);

- $Q^2_{el} \geq 2$ GeV^2: the lower end of the kinematic region was set to eliminate photoproduction events. In order to gain more statistics, no upper cut was placed; the reason for not lowering this cut further is because most of the

MC is generated at $Q^2 > 2$ GeV^2, with the exception of 2 million events which were generated at $Q^2 > 0.8$ GeV^2 as indicated in table 3.1;

- $y_{el} \leq 0.95$: an upper cut on Bjorken y, reconstructed with the electron method, removes fake electron candidates (mostly highly energetic pions in the FCAL decaying into two photons). It also improves the electron finding efficiency for low energy electrons;

- $y_{\mathrm{JB}} \geq 0.04$: a lower cut on the Bjorken y, reconstructed with the Jaquet-Blondel method, ensures a sufficient energy in the hadronic system, which is necessary in order to use the double angle method. (Reconstructed with hadronic variables, it scales directly with the hadronic $E - p_z$).

5.3.3 Global cuts

- $38 \leq E - p_z \leq 60$ GeV: the lower cut removes photoproduction events which have a lower value of $E - p_z$ compared to that of DIS events because the scattered electron escapes in the beam-pipe hole of the rear calorimeter; the lower cut also removes proton beam-gas interactions. The upper cut removes cosmic events superimposed on normal ep events;

- $|Z_{\mathrm{vertex}}| \leq 50$ cm: the reconstructed z-position is restricted. The ZEUS coordinate system is set up so that the nominal interaction point (IP) is at its origin and the IP vertex should be close to it. If the interaction occurs upstream or downstream of the nominal IP, it is more likely to originate from an interaction of the beam with residual gas in the beam-pipe.

5.4 V0 requirement

Lastly, events are selected only if they contain at least one "V0" or reconstructed secondary vertex, the reconstruction of which was briefly described in section 4.1 and in more detail in Apprendix A. In order to limit the combinatorial background, to remove poorly measured secondary vertices and to restrict the study to a region where the CTD track acceptance and resolution are high, the V0 tracks are required to:

- start from the first CTD superlayer and pass more than three CTD superlayers. This requirement guarantees a minimum number of axial and stereo hits,
- have transverse momenta $p_{\mathrm{T}} \geq 0.15$ GeV,
- have pseudorapidity in the laboratory frame $|\eta| \leq 1.75$ and
- have opposite charge. Candidates for long-lived neutral strange hadrons decaying to two charged particles are identified by selecting pairs of oppositely charged tracks, fitted to a displaced secondary vertex.

After these selection cuts, a sample of about 1 300 000 events remained. The reconstructed secondary vertices are then used to identify K^0_S and Λ-hadrons.

5.5 Control plots

In this analysis, the NC DIS inclusive MC is only meant to describe the background to the pentaquark signal. It is not used to extract the cross section, hence the aim here is not to get an exact agreement between data and MC samples. Figures 5.1 and 5.2 serve mainly to demonstrate that the data sample does not contain a large photoproduction background.

Figures 5.1 and 5.2 compare data and ARIADNE Monte Carlo for events which have at least one K^0_S candidate, the reconstruction of which is described in the next chapter. The distributions of some kinematic variables are shown for the low- and medium-Q^2 triggers on the left and right, respectively, the definitions of which were described in section 5.2.3. The MC is scaled to the number of entries in the distribution of the data, thus the shape of the two distributions can be compared. Also the 820 GeV and 920 GeV MC events were mixed in a correct proportion to the luminosity.

As can be seen, in the figure, the description of the data by the MC is somewhat problematic for Q^2 between 2 and 20 GeV^2. This is mostly due to contamination from high-y photoproduction events. On the other hand, data above about Q^2 of 20 GeV^2 is reasonably described by the MC simulation because it is taken with the medium Q^2 trigger, DIS03, which becomes efficient at about $Q^2 > 20$ GeV^2. The reason the agreement between data and MC is not complete

is because of the changing definition of the medium-Q^2 trigger, which has not been simulated here. (It will be however, for the extraction of the Θ^+ cross section). The slight shift in $E - p_z$ is due to a bad reconstruction of the scattered electron's energy, which is not described well by MC. This could be due to an improper description of the inactive material in MC for electrons close to the beam-pipe.

The agreement between data and MC can be improved, however the analysis doesn't gain much in doing so. Furthermore, the remaining differences will be accounted for in the systematic uncertainty.

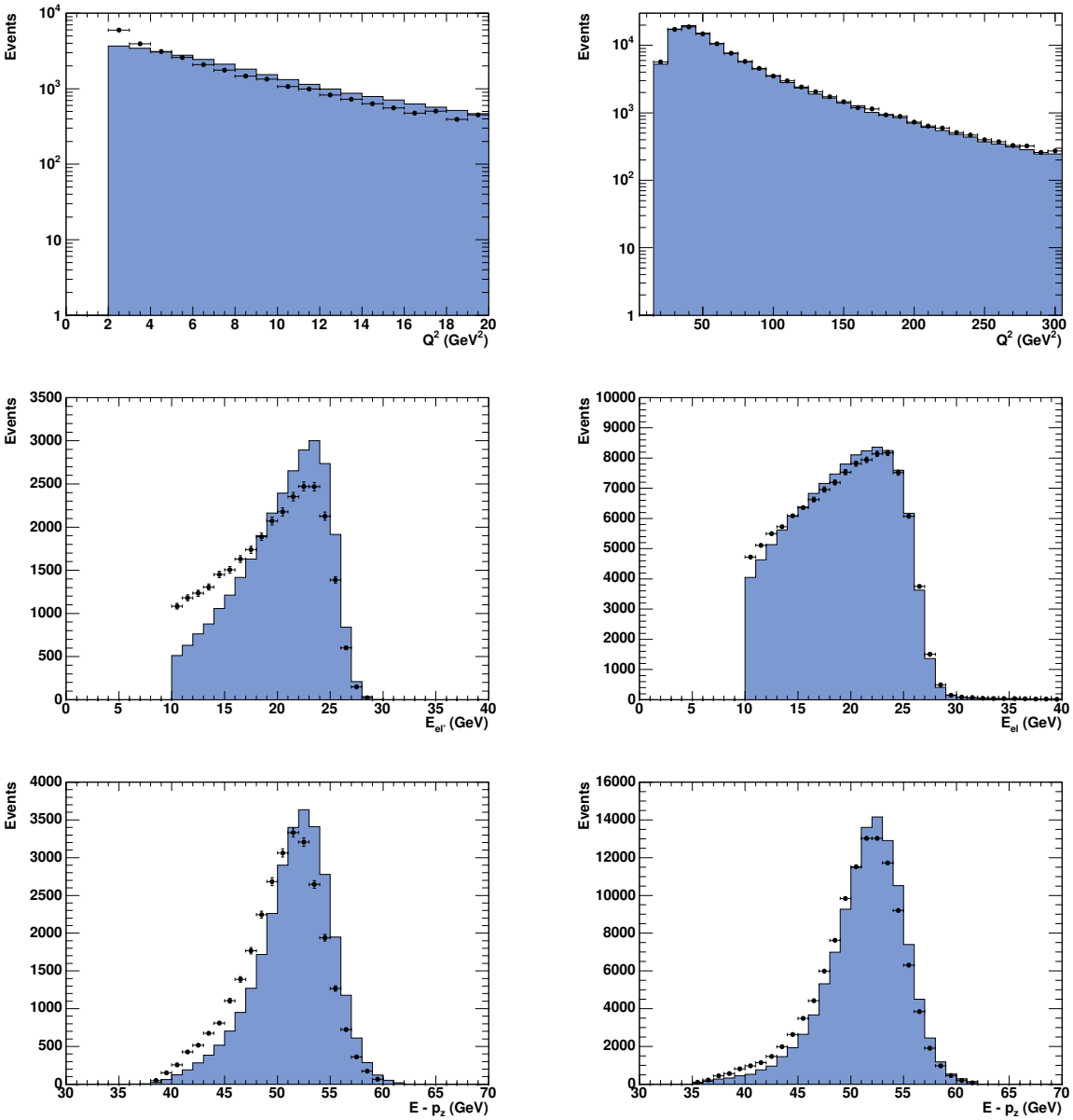

Figure 5.1: Comparison at detector level between data (solid circles) and ARIADNE Monte Carlo (solid line) for events which have at least one K^0_S candidate. Distributions of some kinematic variables are shown for $2 < Q^2 < 20$ GeV^2 (left) and $Q^2 > 20$ GeV^2 (right): the squared four-momentum transfer reconstructed with the electron method, Q^2_{el}, the corrected energy of the electron, $E_{el'}$ and the $E - P_z$ distribution. The MC distribution is scaled to the number of entries in the distribution of the data, thus the two shapes can be compared.

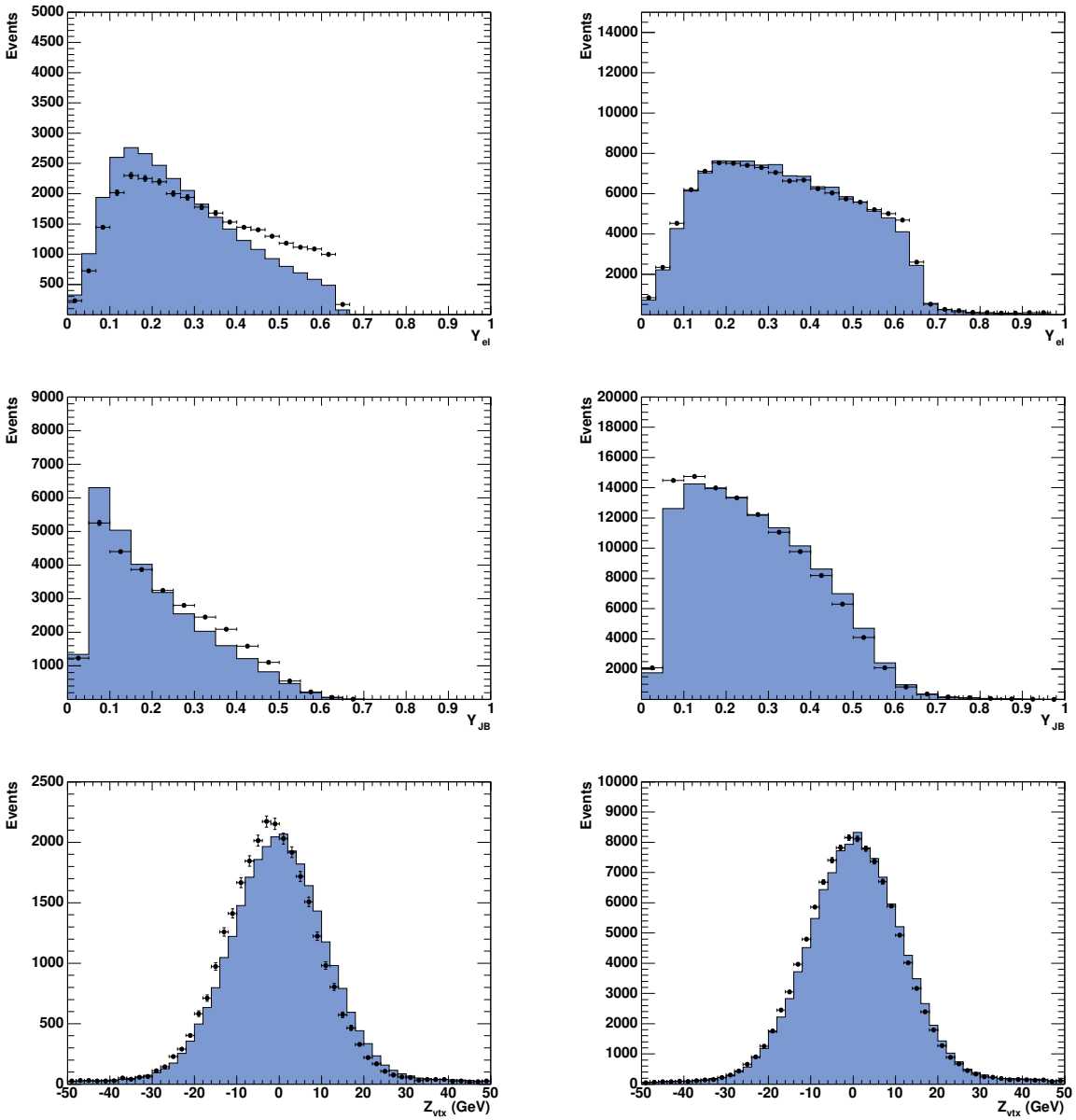

Figure 5.2: Comparison at detector level between data (solid circles) and ARIADNE Monte Carlo (solid line) for events which have at least one K^0_S candidate. Distributions of some kinematic variables are shown for $2 < Q^2 < 20$ GeV^2 (left) and $Q^2 > 20$ GeV^2 (right): the inelasticity reconstructed with the electron method, y_{el} and with the Jacquet-Blondel method, $y_{\rm JB}$ and the z-position of the primary vertex, z_{vtx}. The MC distribution is scaled to the number of entries in the distribution of the data, thus the two shapes can be compared.

Chapter 6

Particle identification

As has already been described in the introduction of this thesis, the quantum numbers of Θ^+ permit decays to $K^0_S p$ and $K^0_S \bar{p}$. Thus, the particles that have to be identified and reconstructed in this analysis are protons[1] and K^0_S. Furthermore, Λ-baryons[2] are also reconstructed. The reason for this is that if and when the Θ^+ signal is established (see chapter 7), the comparison of its production rate to that of a well-known baryon becomes of interest (see chapter 8).

There are several reasons as to why $\Lambda(1116)$ was chosen for this purpose, the most obvious one being that it is a baryon containing strangeness. Furthermore, its kinematics are well described by MC. Another advantage of using $\Lambda(1116)$ is that it can be reconstructed by two different means, one is with the dE/dx information, described in chapter 1.2.2, and the other is with the V0-method previously described in section 5.4. Λ's reconstructed with the dE/dx-method are used for the Θ^+ to Λ ratio calculation. This approach allows for a minimization of uncertainty in the reconstruction of the energy loss, dE/dx, since Θ^+'s are reconstructed with the same method. On the other hand, the Λ's reconstructed with the V0-method are used as a cross check on the detector acceptance with the dE/dx method. The V0 method also provides a measure of the uncertainty on the K^0_S reconstruction. There are several previous Λ cross-section measurements utilizing the V0-method [100–103].

This chapter provides a description of how these particles are identified and/or reconstructed.

[1] Henceforth the term protons is used to refer to both protons and anti-protons unless specified otherwise.

[2] Henceforth the term Λ is used to refer to both Lambdas and anti-Lambdas unless specified otherwise.

6.1 Strange particle reconstruction

Light, strange hadrons are produced in strong interactions and decay weakly. While strangeness is conserved in the production process, it is violated in the weak decays. The properties of K^0_S and Λ-particles along with their decay modes and branching ratios (BR) for $\pi^+\pi^-$/pπ are listed in table 6.1 and are obtained from [44].

Particle	Content	Mass (MeV)	$c\tau$ (cm)	$I(J^P)$	Decay	BR
K^0_S	$d\bar{s}/sd$	497.672	2.6786	1/2 (0^-)	$\pi^+\pi^-$	68.6%
$\Lambda/\bar{\Lambda}$	$uds/\bar{u}\bar{d}\bar{s}$	1115.683	7.89	0 ($1/2^+$)	$p\pi^-/\bar{p}\pi^+$	63.9%

Table 6.1: Properties of K^0_S and Λ-hadrons.

The mean decay length of these long-lived, neutral strange hadrons can be given by

$$L = \beta\gamma c\tau \tag{6.1}$$

where β is the ratio of the particle's velocity to the speed of light c (or $E/\vec{p}$), γ is the relativistic relation, $1/\sqrt{1-\beta^2}$, and τ is the particle's decay time.

Because of their long lifetimes, these particles are relatively easy to identify in the CTD. Since the decays or secondary vertices are well displaced from the primary interaction point, they can be clearly distinguished from the primary vertex. Furthermore, the pions and protons involved in the above decays leave tracks in the CTD, which are reconstructed as described in section 4.1. Hence the reconstruction of strange particles requires the identification of these tracks and the subsequent combination of those tracks to form secondary vertices. Appendix A provides a detailed description of how the secondary vertex reconstruction is done.

6.2 K^0_S reconstruction

For K^0_S selection, tracks originating from secondary vertices, having passed all the requirements described in section 5.4, were further required to satisfy selection cuts of:

$$p_{\mathrm{T}} > 0.3 \text{ GeV} \quad \text{and} \quad \text{-}1.5 \leq |\eta(K^0_S)| \leq 1.5.$$

K^0_S-mesons were identified by their charged-decay mode of $K^0_S \rightarrow \pi^+\pi^-$. Hence the two secondary-vertex tracks that passed the cuts above were assigned the mass of charged pion and the invariant mass, $M(\pi^+\pi^-)$, of each track-pair was calculated.

Futher cuts can be imposed in order to reduce the background. The main source of non-combinatorial background is from photon conversions to electron pairs ($\gamma \rightarrow e^+e^-$) and from mis-reconstructed Λ's. The latter is a result of protons being misidentified as pions. The following requirements were made in order to reduce contamination from these two effects:

- $M(e^+e^-) \geq 0.05$ GeV, where the electron mass was assigned to each track,
- $M(p\pi) \geq 1.121$ GeV, where the proton (pion) mass was assigned to each track with higher (lower) momentum and
- $0.483 \text{ GeV} \leq M(\pi^+\pi^-) \leq 0.513$ GeV.

6.2.1 Armenteros-Podolanski plots

One way of illustrating the removal of the non-combinatorial background from the sources described above is to plot the Armenteros-Podolanski variables $p_{T,rel}$ versus α, before and after the above cuts have been applied.

The Armenteros-Podolanski $p_{T,rel}$ is the projection of either one of the charged V0 daughters' momentum to a plane that is perpendicular to that of the total V0 momentum. The variable α is the ratio of the relative difference between the longitudinal momentum components, p_L, of the two daughters to their sum. See equations 6.2 and 6.3.

Figure 6.1 shows the Armenteros-Podolanski variables. To the left is a scatter plot before contamination from photon conversions and mis-reconstructed Λ's is removed and to the right, after. In the figure on the left, the horizontal band at about 0.01 GeV shows the contamination from photon conversions and the two smaller elliptical bands show contamination from Λ's. As can be seen from the figure on the right, both these regions are removed upon application of the cuts described above. An alternate way of achieving the same result, not used in this analysis, is to require $p_{T,rel}$ to be greater than about 0.11 GeV.

$$\alpha = \frac{p_L^+ - p_L^-}{p_L^+ + p_L^-} = \frac{p^+\cos\,\theta - \mathrm{p}^-\cos\,\theta}{p^+\cos\,\theta + \mathrm{p}^-\cos\,\theta} \tag{6.2}$$

$$p_{T,rel}^{\pm} = p^{\pm}\sin\,\theta \tag{6.3}$$

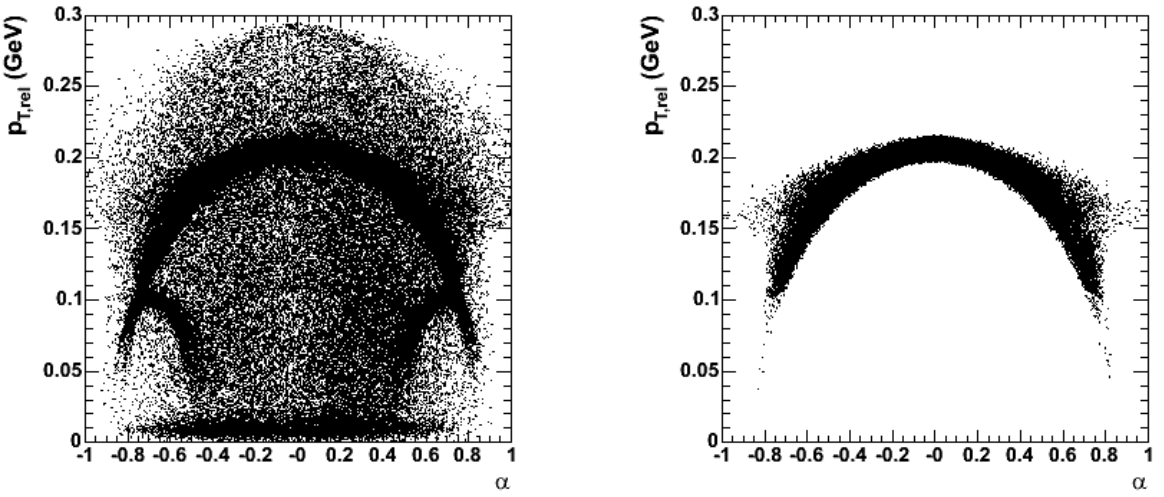

Figure 6.1: Armenteros-Podolanski variables before removal of contamination from photon conversions and mis-reconstructed Λ's (left) and after (right). In the figure on the left, the horizontal band at 0.01 GeV shows the contamination from photon conversions and the two smaller elliptical bands show contamination from Λ's.

6.2.2 Extraction of the K_S^0 signal

Figure 6.2 shows the $M(\pi^+\pi^-)$ invariant-mass distribution for data on the left and MC on the right for $Q^2 > 2$ GeV^2. The data, represented by solid circles, is fitted with a parametrization, which consists of a linear term to describe the background (dashed line in the figure) plus two Gaussian functions, normalized to one, for the K_S^0 signal (solid line in the figure):

$$P(m) = \underbrace{N \cdot \Big[\; r \;\cdot G_{1,m_{K_s^0},\sigma_1} + (1-r)\;\cdot G_{2,m_{K_s^0},\sigma_2}\Big]}_{Signal} + \underbrace{A \cdot \frac{B\cdot(m-0.45)+1}{\int_{0.483\ \mathrm{GeV}}^{0.513\ \mathrm{GeV}} [B\cdot(m-0.45)+1]\,dm}}_{Linear\,Background}. \tag{6.4}$$

The fit to the signal includes the two Gaussians, G_1 and G_2, the widths of which, σ_1 and σ_2, respectively, are fixed initially to 4 and 9 MeV and then released. The common parameter for mass, $m_{K^0_s}$, is also initially fixed to the PDG value of 497.67 MeV and then released. The normalization of the signal, N, and the parameter r are kept free. For the fit to the background, the parameters A and B are also left free.

Shown also in the figure is the resulting number of K^0_S-mesons, $N_{K^0_S}$, which is obtained as follows: First the total number of entries in the mass distribution is calculated by integrating over the mass region of interest, $0.483 \leq M(\pi^+\pi^-) \leq 0.513$ GeV. Next, the number of background events in the same mass window is determined by parameter A from the fit. This value is then subtracted from the result of the integral, thus yielding the total number of K^0_S-mesons, $N_{K^0_S}$.

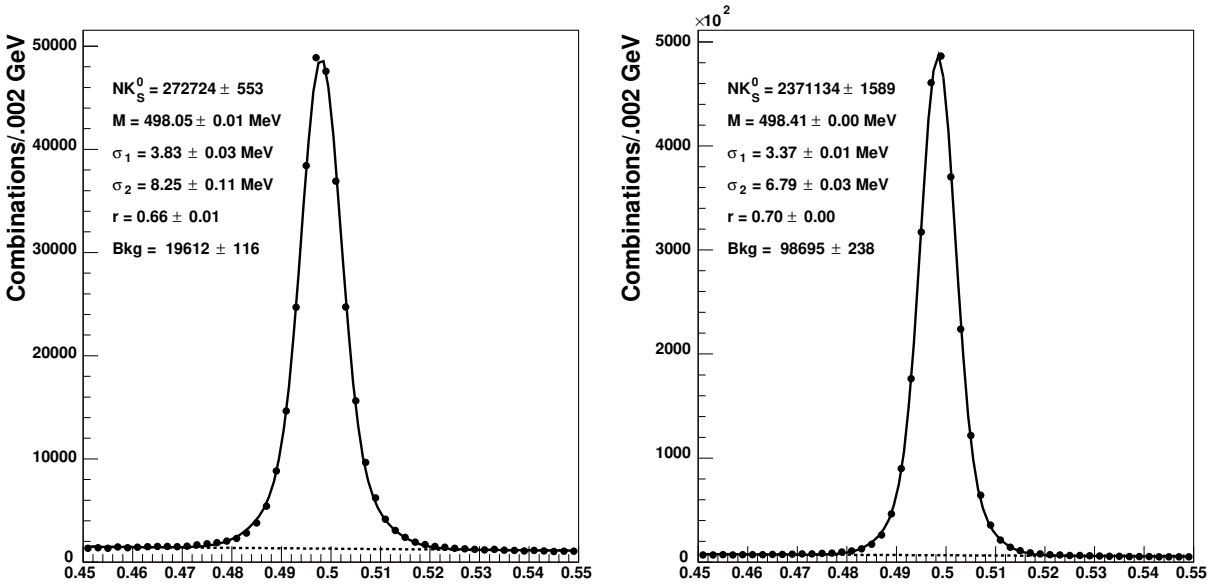

Figure 6.2: The $\pi^+\pi^-$ invariant-mass distribution for data (left) and MC (right) for $Q^2 > 2$ GeV^2. The solid line shows the fit result using a double Gaussian plus a linear background, while the dashed line shows the linear background.

The fitted mass, $m_{K^0_s}$, for the data is measured to be $m_{K^0_s} = 498.05 \pm 0.01$ (stat.) MeV, which agrees with the current world average quoted by the PDG [44] of $m_{K^0_s} = 497.67 \pm 0.03$ MeV within the calibration uncertainty of the CTD. The number of K^0_S-mesons after background subtraction is 272 724 $\pm$ 553 with a

background under the peak constituting approximately 7% of the total number of candidates.

6.2.3 K^0_S lifetime

As an additional check on K^0_S reconstruction, the K^0_S proper $c\tau$ distribution is measured and compared with the same in Monte Carlo. Figure 6.3 shows the comparison between data (solid circles) and ARIADNE (solid line) for events which have at least one K^0_S candidate within the mass range of $0.483 \leq M(\pi^+\pi^-) \leq 0.513$ GeV. The MC distribution is scaled to the number of entries in the distribution of the data, thus the two shapes can be compared. As can be seen

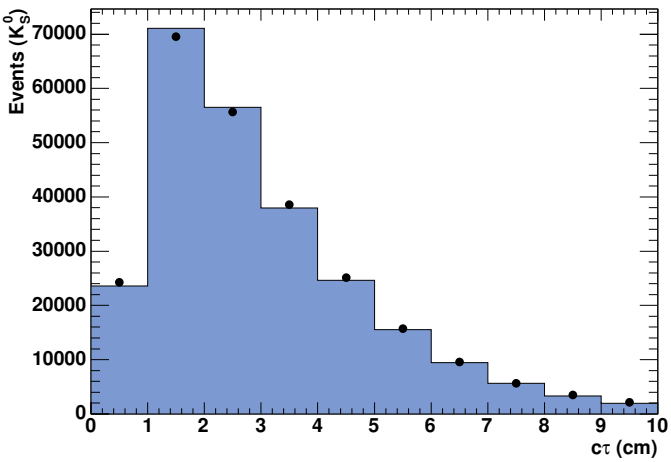

Figure 6.3:
Comparison at detector level between data (solid circles) and ARIADNE MC (solid line) for the proper lifetime, $c\tau$, distribution for K^0_S within the mass range of 0.483 to 0.513 GeV.

from the figure, there is an excellent agreement between data and MC. This gives further confidence in the K^0_S reconstruction and efficiency determination. It should be noted, however, that no cut on the $c\tau$ was made in this analysis.

6.3 Λ reconstruction

The same method used for K^0_S reconstruction can be used to reconstruct Λ-baryons. However for the latter, information on the loss of energy, dE/dx, in the

CTD can also be utilized. Both methods were used in this analysis. This section describes the reconstruction of Λ-baryons with the V0 method. Λ reconstruction with the dE/dx method will be discussed in chapter 8.

For Λ selection, tracks originating from secondary vertices, having passed all the requirements described in section 5.4, were further required to satisfy selection cuts of:

$$p_{\mathrm{T}} > 0.3 \text{ GeV} \quad \text{and} \quad \text{-1.5} \leq |\eta(K^0_S)| \leq 1.5.$$

Λ's were identified by their charged-decay mode, $\Lambda(\bar{\Lambda}) \rightarrow p\pi^-(\bar{p}\pi^+)$. To the two tracks that passed the above cuts, a mass of the proton (pion) was assigned to the track with the higher (lower) momentum and the invariant mass, $M(p\pi)$, of each track-pair was calculated.

As in the case of K^0_S-mesons, in order to eliminate contamination from non-combinatorial background from photon conversions and mis-reconstructed tracks, further cuts were applied:

- $M(e^+e^-) \geq 0.05$ GeV, where the electron mass was assigned to each track,
- $M(\pi^+\pi^-) \leq 0.483$ GeV, where a pion mass assigned to each track and
- 1.113 GeV $\leq M(p\pi) \leq$ 1.120 GeV.

Figure 6.4 shows plots of $p\pi$ versus $\pi\pi$ invariant masses for data on the left and ARIADNE on the right with the lines indicating the cuts for the K^0_S (vertical) and Λ (horizontal) resonances. The open symbols show the photon-conversion contribution, which was removed.

6.3.1 Extraction of the Λ signal

Figure 6.5 shows the invariant-mass distribution for Λ candidates for data on the left and MC on the right for $Q^2 > 2$ GeV^2. As before, the data, represented by solid circles, is fitted with a parametrization, which consists of a linear term to describe the background (dashed line in the figure) plus two Gaussian functions, normalized to one, for the Λ signal (solid line in the figure):

$$P(m) = \underbrace{N \cdot [\ r\ G_{1,m_\Lambda,\sigma_1}(m) + (1-r)\ G_{2,m_\Lambda,\sigma_2}(m)\ ]}_{Signal} + \underbrace{A \cdot \frac{[m-(m_p+m_{\pi^-})]^B}{\int_{1.113\text{ GeV}}^{1.120\text{ GeV}} [m-(m_p+m_{\pi^-})]^B\, dm}}_{LinearBackground}. \tag{6.5}$$

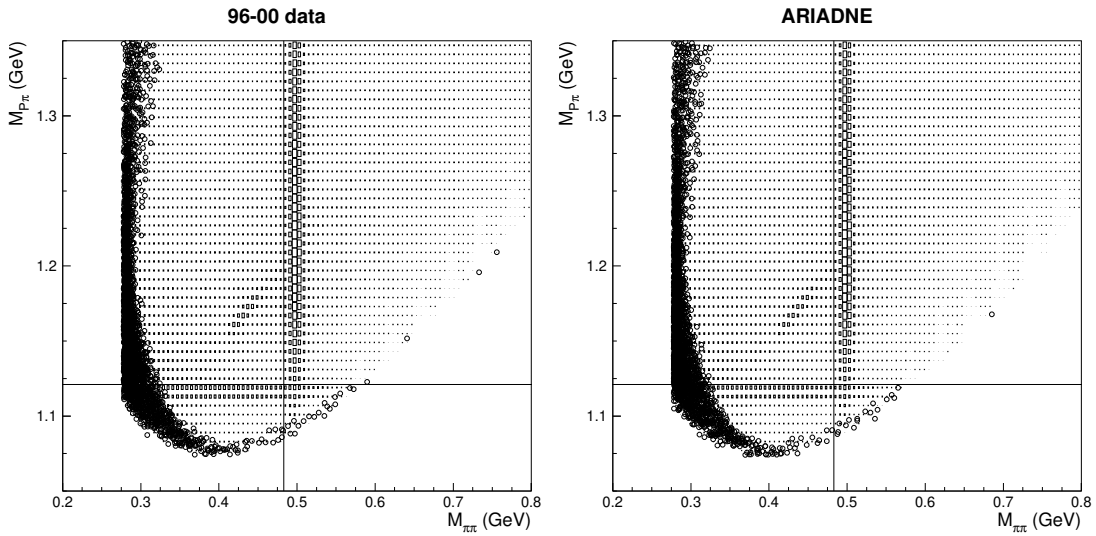

Figure 6.4: $p\pi$ versus $\pi\pi$ invariant mass for data (left) and ARIADNE (right). The open symbols show contribution from photon-conversion. The lines indicate the cuts for the K^0_S (vertical) and Λ (horizontal) resonances.

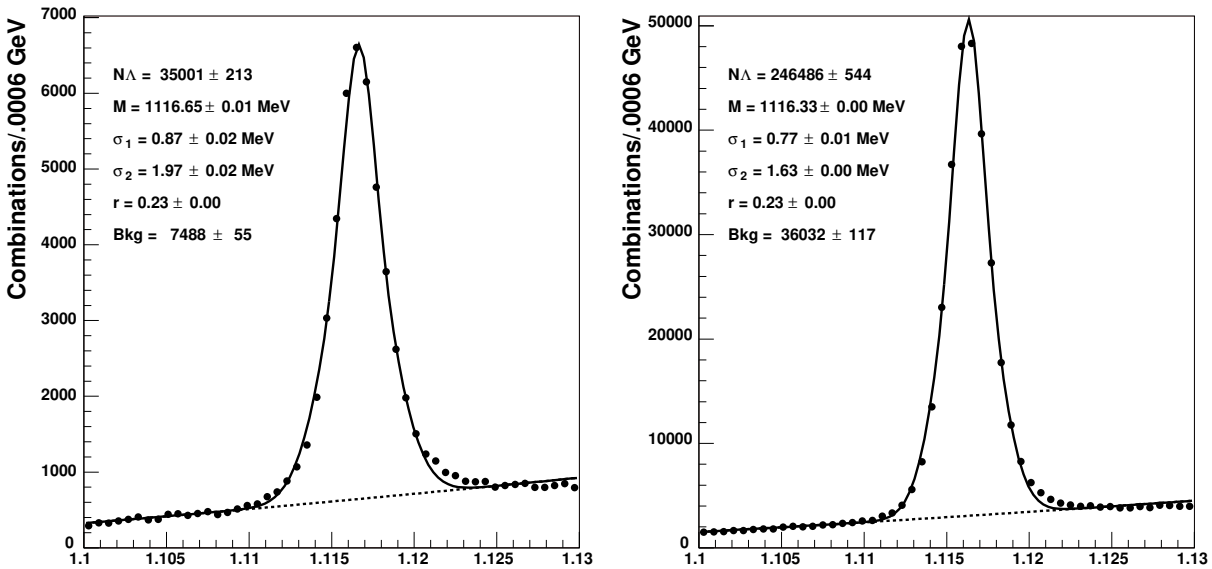

Figure 6.5: The $p\pi$ invariant-mass distribution for data (left) and MC (right) for $Q^2 > 2$ GeV^2. The solid line shows the fit result using a double Gaussian plus a linear background, while the dashed line shows the linear background.

Once again, for the fit to the signal, the two Gaussian widths, σ_1 and σ_2, are initially fixed to 0.9 and 2.2 MeV and then released. The common parameter for mass, m_Λ, is also initially fixed to the PDG value of 1116 MeV and then released. Furthermore, the normalization of the signal, N, and the parameter r are kept free. For the fit to the background, the parameters A and B are also left free.

Shown in the figure is the resulting number of Λ-baryons, N_Λ, which is obtained in the same manner as that for K^0_S-mesons, described in section 6.2.2. First the total number of entries in the mass distribution is calculated by integrating over the mass region of interest, $1.113 \leq M(p\pi) \leq 1.120$ GeV. Next, the number of background events in the same mass window is obtained by parameter A from the fit. This value is then subtracted from the result of the integral, thus yielding the total number of Λ baryons, N_Λ.

The fitted mass m_Λ for the data is measured to be $m_\Lambda = 1116.65 \pm 0.01$ (stat.) MeV, which agrees with the current world average quoted by the PDG [44] of $m_\Lambda = 1115.68 \pm 0.01$ MeV within the calibration uncertainty of the CTD. The number of Λ-baryons after background subtraction is $35\,001 \pm 213$ with a background under the peak constituting approximately 18% of the total number of candidates.

6.3.2 Λ lifetime

What was done for K^0_S-mesons earlier is repeated for Λ-baryons here. As an additional check on Λ reconstruction, the Λ proper $c\tau$ distribution is measured and compared with Monte Carlo. Figure 6.6 shows the comparison between data (solid circles) and ARIADNE (solid line) for events which have at least one Λ candidate. The MC distribution is scaled to the number of entries in the distribution of the data, thus the two shapes can be compared. As can be seen in the figure, there is reasonable agreement between data and MC, thereby giving confidence in Λ reconstruction. One thing to note however is that $c\tau$ for Λ candidates is not as well described by MC as it is for K^0_S candidates, probably due to the higher background under the peak for the Λ-baryons.

6.3.3 $\Lambda(\bar{\Lambda})$ asymmetry: background study

At high energies, hadron production is dominated by fragmentation, hence baryons and antibaryons should be produced in equal amounts. Figure 6.7 shows

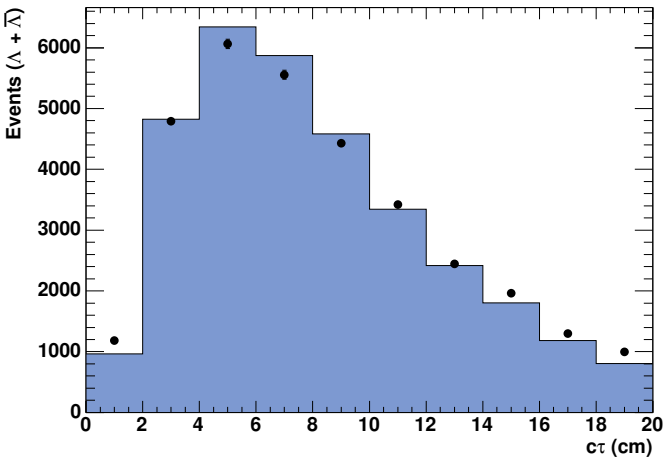

Figure 6.6:
Comparison at detector level between data (solid circles) and ARIADNE MC (solid line) for the proper lifetime, $c\tau$, distribution for Λ within the mass range of 1.113 to 1.120 GeV.

the Λ and $\bar{\Lambda}$ invariant-mass distributions separately for data. The number of Λ and $\bar{\Lambda}$-baryons after background subtraction, using the same method described in section 6.2.2, is 18 853 $\pm$ 151 and 16 267 $\pm$ 142, respectively, with the fits for both providing a mass of 1116.65 MeV. There exists an asymmetry of 14.7% between Λ-baryon and $\bar{\Lambda}$-baryon production. On the other hand, ARIADNE, not shown here, yields an asymmetry of 4.6%.

Secondary scatter and collinearity cut

In order to understand the origin of the asymmetry between baryon and anti-baryon production, the decay-vertex postion of Λ's and $\bar{\Lambda}$'s in the xy-plane is investigated. The *location* of the secondary vertices in the detector can shed light on the mechanism by which they are produced. Ideally, the secondary vertices sought in this analysis, are those that originate from decays of Λ-baryons originating from the IP, however, there are other means by which secondary vertices may arise. One possible way can be due to secondary interactions of charged particles with the nuclei in the detector material and another can be from decays of Λ's arising from such scatter and, therefore, *not* originating at the IP. While the secondary vertices from the first category are expected to

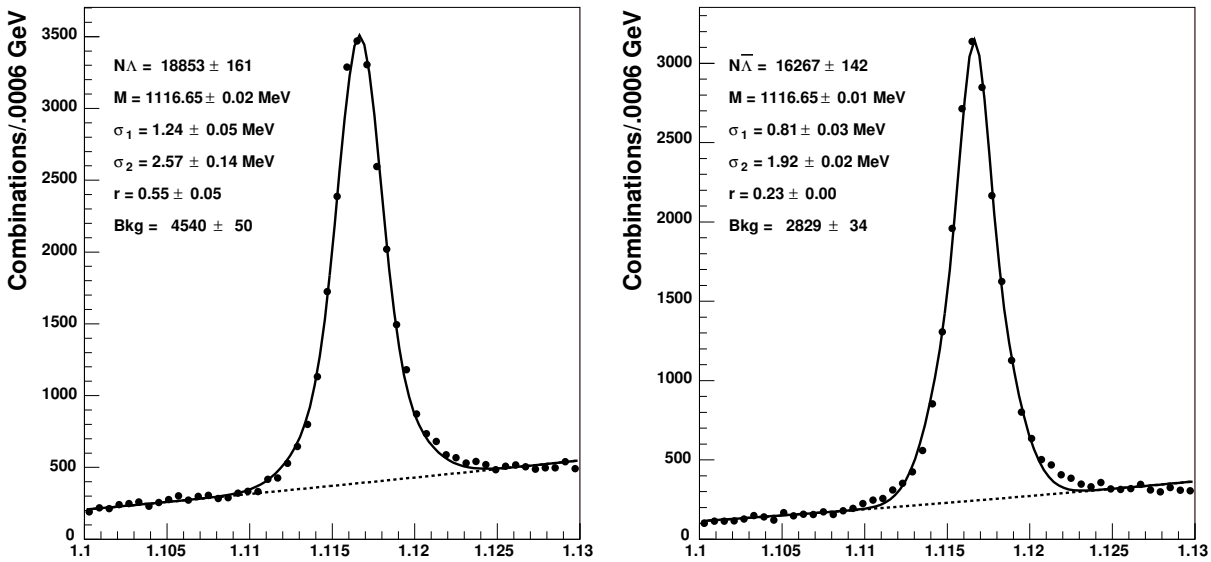

Figure 6.7: $p\pi^-$ (left) and $\bar{p}\pi^+$ (right) invariant mass for data.

be concentrated near detector material (such as the beam-pipe, for example), those from the latter group are not, since Λ-baryons have a long decay length as seen above. Furthermore, the vertices from secondary scatter are expected to contribute to the background and are not expected to create a peak. In contrast, those from Λ decays are expected to make a small contribution to the Λ signal itself. The contribution from both can be reduced significantly by requiring the vertices to "point" back to the IP. How this is done is described below.

But first, figure 6.8 shows secondary-vertex position y versus x of Λ candidates on the left and $\bar{\Lambda}$ candidates on the right. Two rings can be seen in both the scatter plots, although they are much more pronounced in the one for Λ's. The inner ring coincides with the location of the beam-pipe and the outer, the inner wall of the CTD. This feature, also present in MC (not shown here), indicates that there is considerable background due to secondary interactions with the nuclei of the detector material. This can further explain why the rings are much more pronounced for $\Lambda(\rightarrow p\pi^-)$ candidates than they are for their counterparts.

So how can the contribution from secondary interactions be reduced? As mentioned above, one way is to eliminate those secondary vertices which do not arise from the decays of Λ's originating at the IP. To this end, a cut can be made

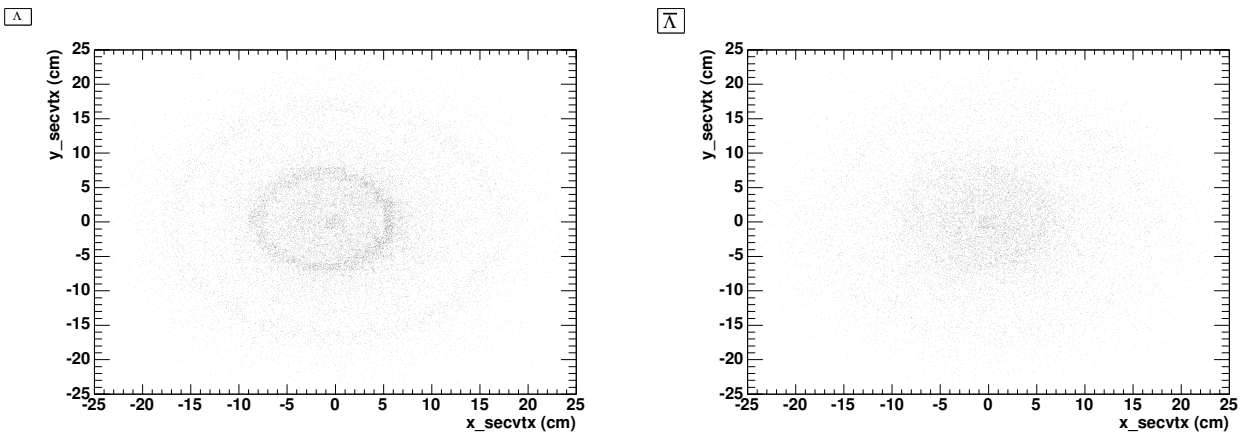

Figure 6.8: Secondary vertex position y versus x of Λ (left) and $\bar{\Lambda}$ (right) in the mass range, 1.113 to 1.120 GeV in data.

on θ_{xy}, where θ_{xy} is the angle (collinearity) between the Λ candidate's momentum vector and the vector defined by the interaction point and the Λ-decay vertex in the xy plane. If θ_{xy} is required to be less than 0.2, events from the beam-pipe and the inner wall of the CTD are greatly reduced. (The reason for choosing 0.2 is that there is a sharp drop in the θ_{xy} distribution at this value, such that 90% of the selected secondary vertices have θ_{xy} below 0.2).

Figure 6.9 shows the radius of the secondary vertex before (solid line) and after (dashed line) the collinearity cut for Λ on the left and $\bar{\Lambda}$ on the right. As can be seen, the cut reduces the number of events at about 5 cm and 16 cm, where the beam-pipe and the inner wall of the CTD are located. (The double peak at 16 to 17 cm is due to the two layers of the inner wall of the CTD.)

The secondary vertex position y versus x of $\Lambda(\bar{\Lambda})$ candidates is replotted, this time with the collinearity cut, and is shown in figure 6.10. The two rings seen in figure 6.8 have been removed.

Furthermore, figure 6.11 shows $c\tau$ distributions for data and MC with the collinearity cut. The agreement between the two has improved from before. Raising the collinearity cut to $< .25$ worsens the agreement. While lowering it to $< .15$ yields similar result but reduces the statistics.

The resulting Λ and $\bar{\Lambda}$ invariant-mass distributions, after the collinearity cut, can be seen in figure 6.12. Firstly, the figures show a considerable reduction in the combinatorial background. While the Λ background was reduced by 70% in both data and MC, the $\bar{\Lambda}$ background was reduced by about 57% in both.

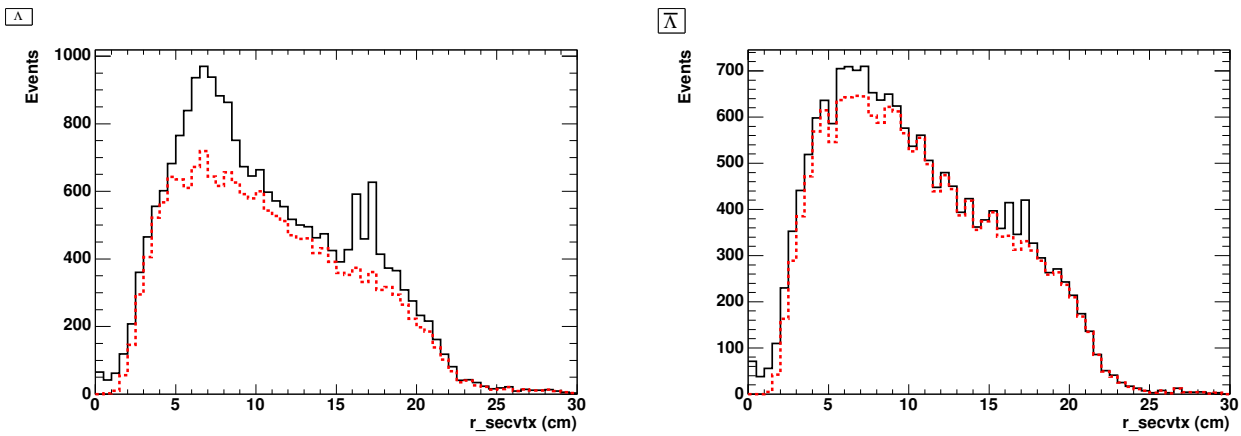

Figure 6.9: Secondary vertex radius before (solid line) and after (dashed line) the collinearity cut for Λ (left) and $\bar{\Lambda}$ (right).

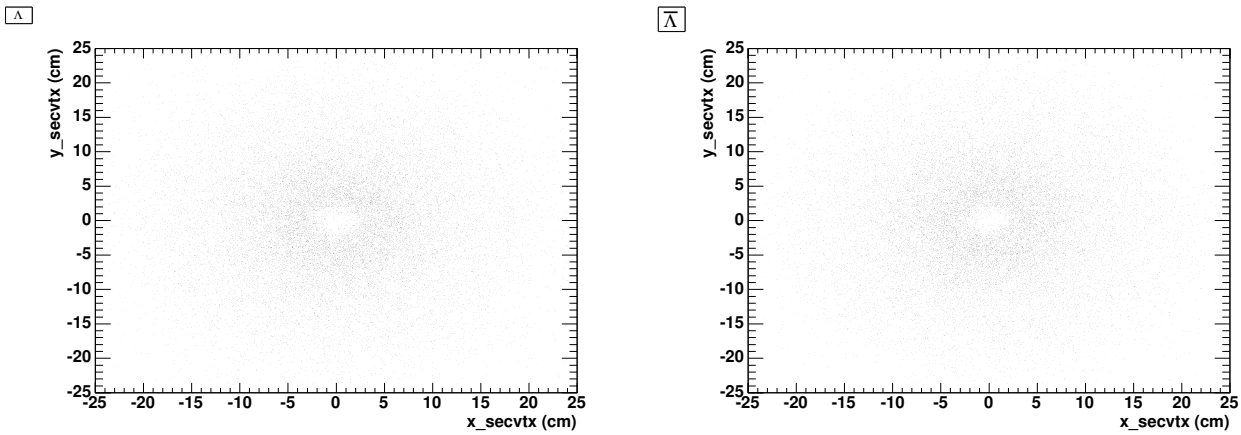

Figure 6.10: Secondary vertex position y versus x of Λ (left) and $\bar{\Lambda}$ (right) in data in the mass range 1.113 to 1.120 GeV after collinearity cut.

Secondly, the number of Λ's in the peak was reduced by 10% (3% in MC) by the collinearity cut and the number of $\bar{\Lambda}$'s was reduced by 1% (0.7% in MC) only. The Λ candidates eliminated by the collinearity cut are those which are produced via secondary interactions and do not originate from the IP. However because they decay in the CTD similarly to the Λ's which are produced at the IP, they make a contribution to the signal. The fact that more such Λ's are removed than are $\bar{\Lambda}$'s suggests that more Λ's than $\bar{\Lambda}$'s come from secondary scatter as expected. Furthermore, the reduction of Λ candidates is greater in data than in MC. A possible explanation for this could be that Λ's from secondary scatter are

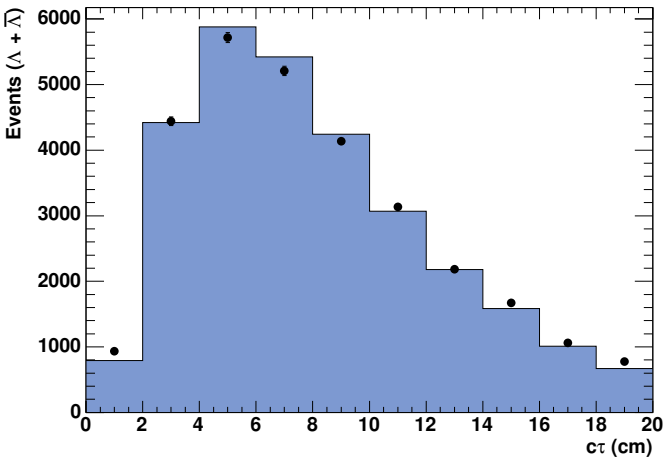

Figure 6.11:
Comparison at detector level between data (solid circles) and ARIADNE MC (solid line) for the proper lifetime, $c\tau$, distribution for Λ within the mass range of 1.113 to 1.120 GeV with collinearity cut.

not perfectly simulated. This also explains why there is reasonable agreement in the reduction of $\bar{\Lambda}$ candidates in both data as in MC.

The number of Λ and $\bar{\Lambda}$-baryons in data after background subtraction is 16 965 $\pm$ 138 and 16 074 $\pm$ 137, respectively, with the fits for both providing a mass of 1116.6 $\pm$ .01 MeV. The asymmetry still exists but now there is a 5.4% difference between Λ's and $\bar{\Lambda}$'s in data, as compared to 14.7% before the collinearity cut. The ARIADNE prediction yields an asymmetry of 1.8%, as compared to 4.6% from before. At generator level, it is 0.4%, which is compatible with zero. Once again, the reason for the higher asymmetry in data than in MC might be that Λ's from secondary scatter are not perfectly simulated.

Finally, according to figure 6.12, the resolution of the $\bar{\Lambda}$ signal is better than that of the Λ signal. This is probably due to the fact that the CTD has a better hit efficiency for positive, low-p_{T} tracks. At high p_{T}, the difference in hit efficiency between positive and negative tracks is less, since both trajectories are equally straight [104]. While these combined effects provide a similar resolution for the higher-momentum proton and antiproton tracks, they yield a better resolution for the lower-momentum π^+ tracks than for their counterparts. This can explain why there is a better resolution for $\bar{\Lambda}$-baryons.

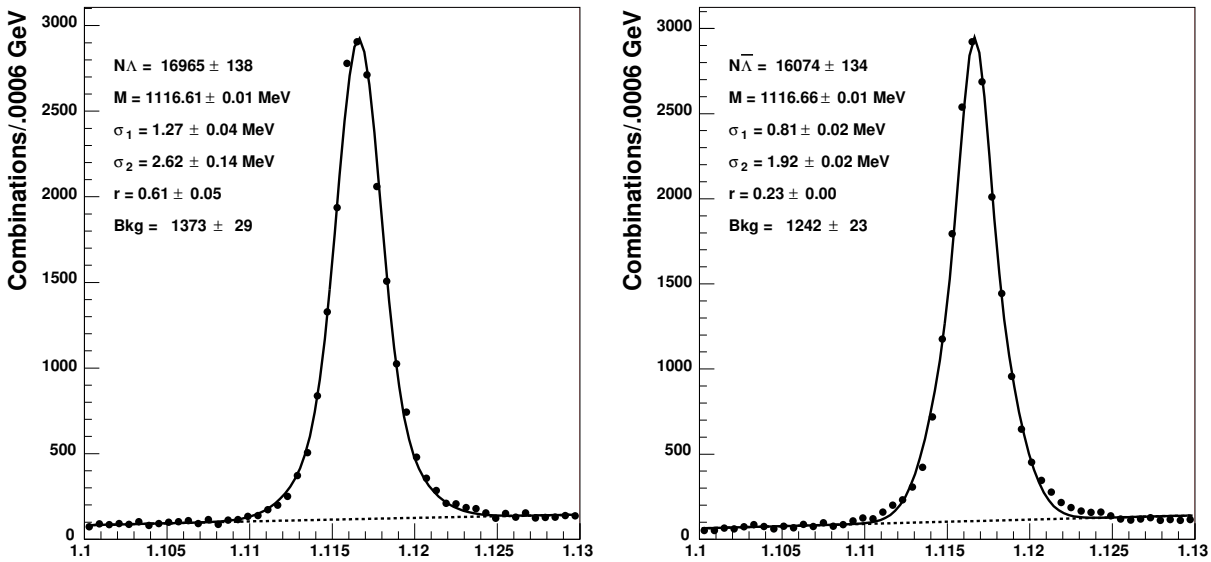

Figure 6.12: $\mathrm{p}\pi^-$ *(left) and* $\bar{\mathrm{p}}\pi^+$ *(right) invariant mass after the collinearity cut.*

6.4 K^0_S revisited with collinearity cut

The previous discussion on the effect on the $\Lambda(\bar{\Lambda})$ signal from secondary scatter raises the obvious question: Does secondary scatter have a similar impact on the K^0_S signal? A priori, the answer would be no since proton tracks are not required in K^0_S reconstruction.

Figure 6.13 shows the radius of the secondary vertex before (solid line) and after (dashed line) the collinearity cut for K^0_S candidates. The collinearity cut has the same effect on K^0_S's as it had on Λ's - it reduces the number of events at the beam-pipe and the inner wall of the CTD.

However, as expected, this effect is not as pronounced as it was for Λ's. Figure 6.14 shows the K^0_S invariant-mass distributions for data on the left and MC on the right after the collinearity cut. The reduction in signal in data is 4.5% (2.3% in MC). As before, the reason for the higher reduction in data than in MC could be that K^0_S's from secondary scatter are not perfectly simulated.

Finally, what is of paramount interest is that this cut has absolutely *no* effect on the $K^0_S p(\bar{p})$ invariant mass spectrum, the reconstruction of which is described in chapter 7. This means that the K^0_S candidates selected for

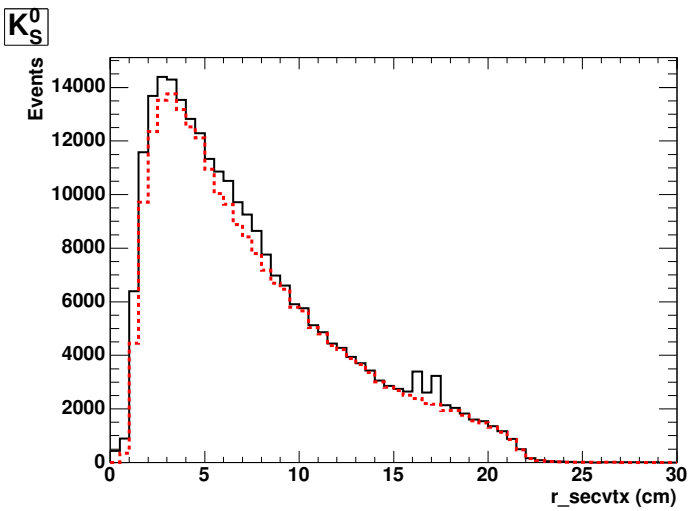

Figure 6.13: Secondary vertex radius before (solid line) and after (dashed line) the collinearity cut for K^0_S in the mass range 0.483 and 0.513 GeV.

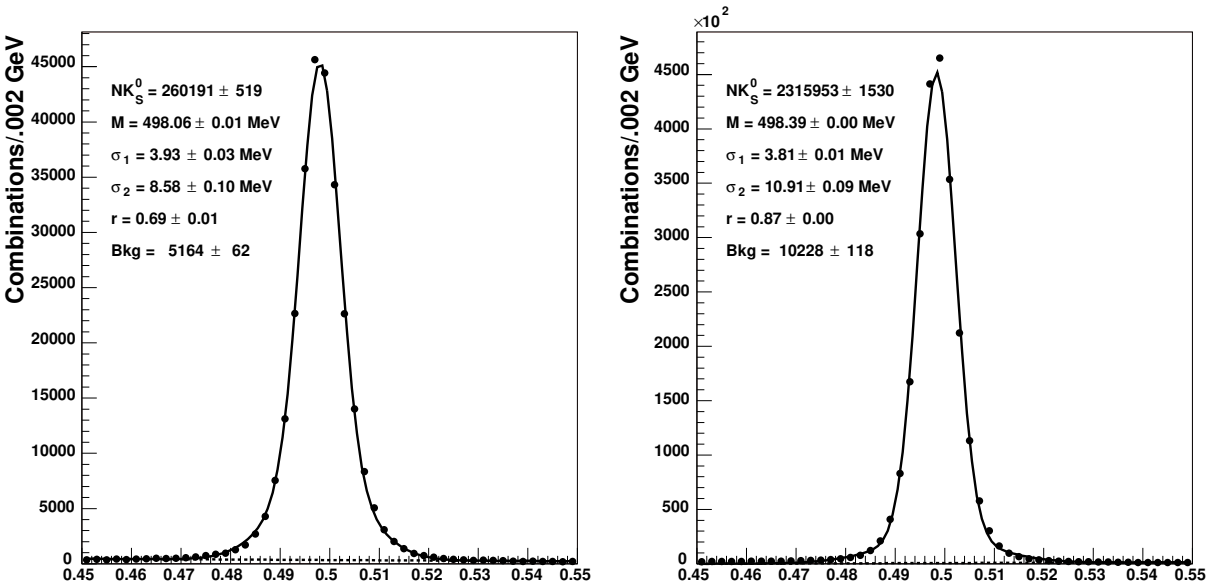

Figure 6.14: *$\pi^+\pi^-$ invariant mass for data (left) and MC (right) after the collinearity cut in the mass range 0.483 and 0.513 GeV.*

$K^0_S p(\bar{p})$ reconstruction are not coming from secondary scatter. Hence, it is for this reason, the collinearity cut is not used for $K^0_S p(\bar{p})$ reconstruction.

6.5 Proton identification

The last particle that needs to be identified is the (anti)proton. The selection of (anti)proton candidates was made using both the tracking information as before and the information on on the loss of energy dE/dx in the CTD as described in section 4.3.

6.5.1 Track requirements

Several requirements were placed on proton track candidates. Tracks were required to:

- originate from the primary vertex,
- have $p_T > 0.15$ GeV and $|\eta| < 1.75$,
- start from the first CTD superlayer and pass more than three CTD superlayers and
- contain more than 40 hits per track to ensure good quality of dE/dx reconstruction.

6.5.2 dE/dx requirements

Tracks were further selected by requiring dE/dx to be between f and F, where f and F are functions motivated by the Bethe-Bloch equation:

$$f = \frac{0.35}{p^2} + 0.8 \qquad F = \frac{1.0}{p^2} + 1.2 \qquad \text{for positive tracks,} \tag{6.6}$$

$$f = \frac{0.3}{p^2} + 0.8 \qquad F = \frac{0.75}{p^2} + 1.2 \qquad \text{for negative tracks ,} \tag{6.7}$$

where p is the total track momentum in GeV. Furthermore, in order to reduce pion contamination, the minimum dE/dx allowed was 1.15 mips, the reason for which is explained in section 6.5.4.

All the above cuts were found from an examination of dE/dx as a function of p and are illustrated in figures 6.15 and 6.16 for data and ARIADNE MC, respectively. On the left is the scatter plot for positive tracks and on the right,

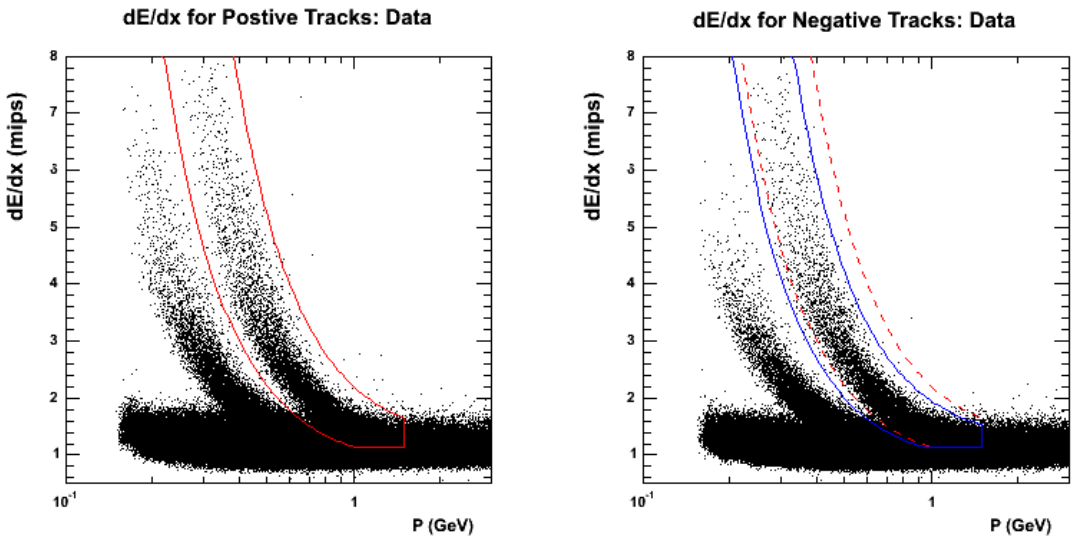

Figure 6.15:
dE/dx distribution for positive (left) and negative (right) tracks from the primary vertex for data. The dark lines show the applied cuts. The dashed line in the figure on the right indicates the cuts used for positive tracks.

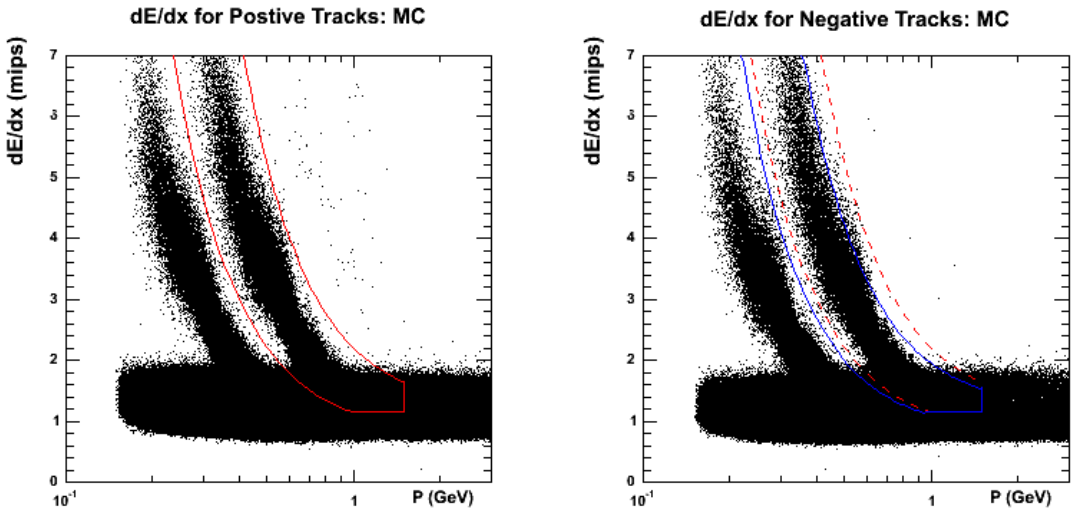

Figure 6.16:
dE/dx distribution for positive (left) and negative (right) tracks from the primary vertex for ARIADNE. The dark lines show the applied cuts. The dashed line in the figure on the right shows the cuts used for positive tracks.

the same for negative tracks. For MC, for the dE/dx correction, a value of 48 was used. This value was determined from the data. In all the figures, the horizontal band represents pions and the band next to it represents charged kaons. The third band, indicated by selection-cut lines is the proton band.

For positive tracks, there is a small number of deuterons to the right of the proton band, both in data and MC, which suggests that there is a small contribution from secondary interactions for positive tracks but not for negative. This is in line with the results of the Λ background study. (The density of the deuterons is difficult to judge from the figure because the binning of the scatter plots is not infinitesimally small, and as a result, one entry in the display does not correspond to one deuteron only).

Figure 6.17 shows the momentum distributions for the proton and antiproton candidates. There is almost an equal number of candidates for both. This

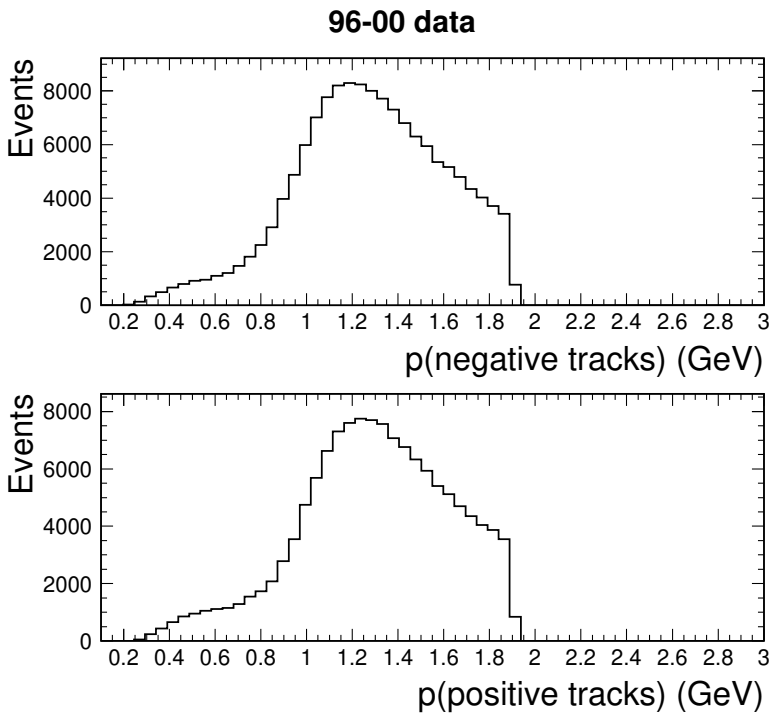

Figure 6.17:
Distributions of antiproton (top) and proton (bottom) candidate momenta after the $f < dE/dx < F$ cuts. The cut $p < 1.9$ was set to reduce the size of the ntuples.

means that the vertex association works and that secondary interactions, which are obviously very important for secondary vertices as illustrated in section 6.3.3, do not play a very important role for primary tracks.

Lastly, a small shift to higher values of dE/dx is observed for positively charged tracks compared to negatively charged tracks. Also both the proton band and the π^+ band, at low momentum, are slightly broader than the antiproton and π^- bands. This can be understood as a consequence of the higher CTD hit efficiency for low-momentum positively charged tracks, which gives a higher average dE/dx. In addition, the higher dE/dx values lead to fewer hits entering the truncated mean and therefore a larger spread in dE/dx values than for negatively charged tracks.

One can validate the cuts in equations 6.6 and 6.7 by reconstructing the dE/dx for the higher-momentum tracks in the $\Lambda(\bar{\Lambda})$ event sample, which are assumed to be protons(antiprotons). Figure 6.18 shows the dE/dx distribution of $\Lambda(\bar{\Lambda})$-baryons on the left(right) as a function of momentum for the higher-momentum tracks. Both the proton and antiproton bands fall within the drawn lines, which indicate the track selection cuts used for fully inclusive events. Once again, at low momentum, the proton band is slightly broader than the antiproton band and is slightly shifted to the right compared to the antiproton band.

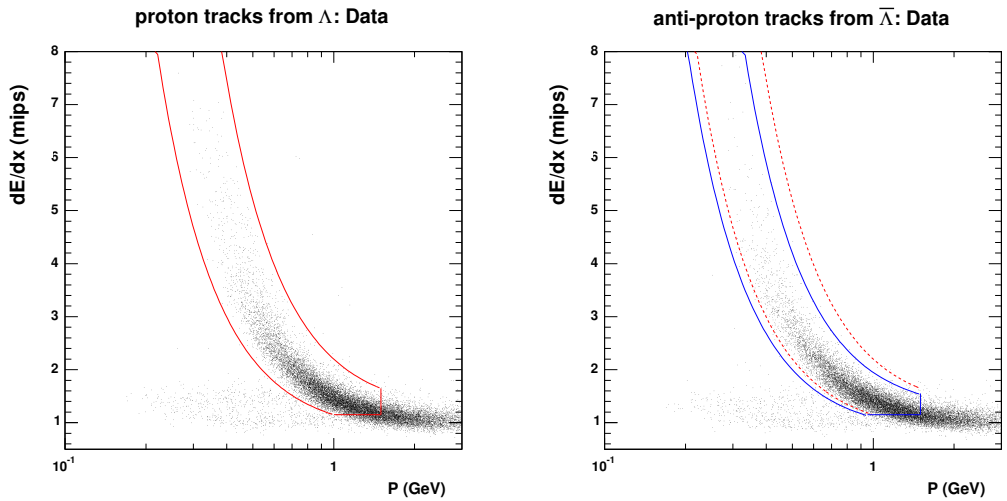

Figure 6.18: dE/dx distribution for tracks originating from Λ(left) and $\bar{\Lambda}$ (right) decays. The dark lines show the cuts used for track selection for fully inclusive events.

6.5.3 Momentum requirement

Even after the $f < dE/dx < F$ cut, there is significant background from pions in the region where the pion and proton bands completely overlap. Figure 6.19 shows the ARIADNE predictions for tracks selected as described in the previous section. It is clear that the cut on the total momentum cannot be high, as the purity of the proton sample would decrease dramatically. Hence, in order to reduce pion contamination from the overlapping region, the proton momentum was required to be less than 1.5 GeV. A tighter cut on the same reduces statistics. The momentum cut is indicated by the vertical line in figure 6.15.

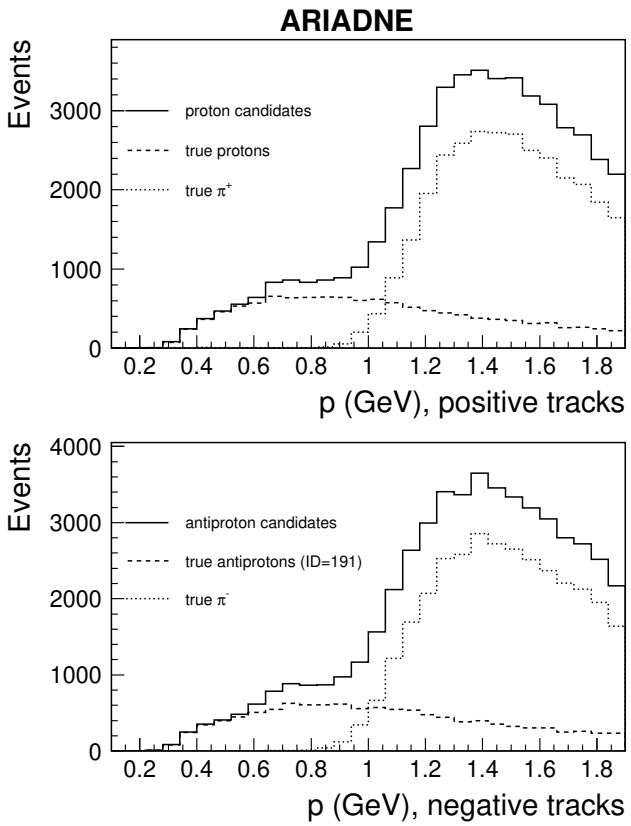

Figure 6.19:
ARIADNE predictions for the number of proton top and antiproton (bottom) candidates as a function of the total track momentum after the $f < dE/dx < F$ cut.

6.5.4 dE/dx cut revisited

The proton purity can be increased by raising the lower dE/dx cut, but in doing so, the acceptance for protons in the high-momentum region is reduced, which in turn, reduces the statistics. For example, figure 6.15 shows that a requirement of $dE/dx > 2$ corresponds to a cut of $p < 0.6 - 0.7$ GeV. According to MC prediction (figure 6.19), this cut leads to a very high purity of protons. However there is a significant number of protons below $dE/dx \sim 2$, hence the use of this harsher dE/dx cut would lead to a significant reduction of statistics (about 70%).

After all the cuts, which include kinematic and track selection cuts and the dE/dx and momentum cuts, the purity of the proton sample, estimated from the MC simulation, is around 60%, varying from 96% at low momentum to 17% at the highest accepted momenta.

6.6 Summary

To summarize, there is much confidence in K^0_S and Λ reconstruction, the efficiencies of which are 22% for K^0_S, and 8.7% for Λ and $\bar{\Lambda}$, combined, in the kinematic range defined by $Q^2 > 2.0$ GeV^2, $P_t > 0.30$ GeV and $|\eta| < 1.50$. Furthermore, the purity of the proton sample, selected using dE/dx, is around 60%, varying from 96% at low momentum to 17% at the highest accepted momenta.

There are several reasons for conducting the Λ-background studies described in this chapter, the main one being that the Θ^+ cross section is compared to that of Λ in chapter 8. (See the introduction of this chapter for the reasons for choosing $\Lambda(1116)$). The asymmetry seen between Λ and $\bar{\Lambda}$ reconstruction can be greatly reduced by imposing the collinearity cut described in this chapter. This cut serves two purposes. It reduces the background arising from the secondary scatter of particles with the nuclei in the detector material. It also removes Λ-baryons, which contribute to the signal, but are produced via secondary scatter and, as a result, do not originate from the IP. This study shows that the differences in the reconstruction of baryons and their counterparts arise mainly from misidentificaton of tracks, hence it sheds light on the differences in the reconstruction of protons and anti-protons as well.

The study also indicates that secondary scatter is not as much of a problem for K^0_S reconstruction and that it has *no* effect on the $K^0_S p(\bar{p})$ reconstruction described in the next chapter.

Chapter 7

$K^0_S p(\bar{p})$ invariant mass

The quantum numbers of $\Theta^+(\bar{\Theta}^-)$ permit decays to $K^0_S p(K^0_S \bar{p})$. Even though the evidence for a corresponding signal has been seen in this channel by many experiments [7–13], the jury is still out on whether the pentaquark exists since most of these experiments yield a statistical sensitivity that is relatively low. As a result, at present, the most immediate priority is to either prove or refute the existence of Θ^+, for which more analyses with high-statistics are needed. This was the primary motivation to perform a resonance search in the $K^0_S p(\bar{p})$ channel at the predicted Θ^+ mass of around 1530 MeV with the ZEUS detector.

Furthermore, in the event, that the Θ^+ does exist, its production mechanism becomes of interest. All the observations obtained thus far have been in fixed target experiments at low center-of-mass energies, where valence quarks from the target nucleons can easily become part of the pentaquark final state. The Θ^+ has never been observed in high-energy experiments, where hadron production is dominated by fragmentation and hadrons and their antiparticles should be produced in equal numbers. It is therefore an interesting question whether the pentaquarks observed in fixed target collisions should also be seen in high-energy experiments and, if so, whether collider experiments should also see its antiparticle, the antipentaquark. This was the second motivation to search for the $\Theta^+(\bar{\Theta}^-)$ in the ZEUS data.

The current chapter builds on the information provided by chapter 6, which describes K^0_S reconstruction and proton identification (see chapter summary). This chapter provides a description of the $K^0_S p(\bar{p})$ invariant-mass reconstruction and follows it up by a discussion of the results. It also outlines and describes the checks and studies conducted to test the robustness of the signal.

7.1 $K^0_S p(\bar{p})$ reconstruction

The $K^0_S p(\bar{p})$ invariant mass was obtained by combining K^0_S and (anti)proton candidates selected as described in chapter 6. The selected events were required to have at least one K^0_S originating from a secondary vertex that is well displaced from the primary vertex (see appendix A) and one proton track originating from the primary vertex as depicted in figure 7.1.

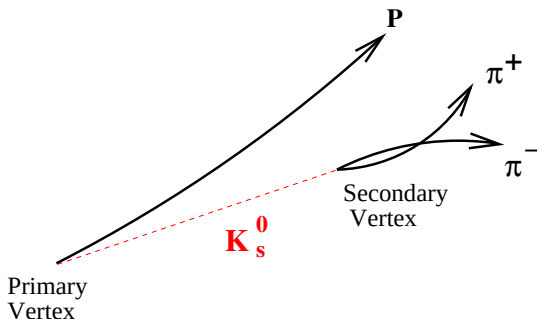

Figure 7.1: A schematic illustration of $K^0_S p$ reconstruction

The following additional requirements were made on the K^0_S candidates:

- $p_{\mathrm{T}}(K^0_S p(\bar{p})) > 0.5$ GeV,
- $|\eta(K^0_S p(\bar{p}))| \leq 1.5$ and
- the K^0_S candidate mass was fixed to the PDG value of .49767 GeV.

The proton candidate mass was fixed to the PDG value of .93827 GeV.

7.1.1 Detector resolution

The resolution of the $K^0_S p(\bar{p})$ invariant-mass measurement, estimated with MC simulations, was found to be 2.7 ± 0.1(stat.) MeV in the region near 1522 MeV, for the $K^0_S p(\bar{p})$ channel. See figure 7.9. Since the natural width of the Θ^+-baryons was assumed to be zero, the Gaussian width of 2.7 MeV, provided by the fit, gives the resolution of the detector. (See section 3.3.2 for more on the RAPGAP MC.)

7.2 $K^0_S p(\bar{p})$ invariant-mass spectrum

The $K^0_S p(\bar{p})$ mass spectrum, in the range from threshold to 1700 MeV, is shown in figure 7.2 for various regions of the DIS phase-space. Figures 7.2(a)-7.2(m) show the mass distribution integrated above a minimum Q^2 ranging from 2 GeV^2 to 50 GeV^2. The data shows signs of structure below about 1600 MeV.

For $Q^2 > 2$ GeV^2 , a structure is seen in the mass distribution at about 1522 MeV. As the cut on the minimum value of Q^2 is raised, the statistics decrease, as expected, however the peak remains visible.

Before detector simulation, the $K^0_S p(\bar{p})$ invariant-mass distribution was calculated from the true K^0_S and (anti)protons in the mass range up to 2000 MeV. Figure 7.2 also shows this expectation from the MC simulation, scaled to agree with the data in the mass region above 1650 MeV. If normalized to the luminosity, the simulation lies below the data by a factor of approximately two which is not shown here. Even after scaling, the data is not well described by the simulation for masses below 1600 MeV, and no structure is seen in the simulated data. The PDG reports a possible Σ resonance at 1480 MeV, and several states above 1550 MeV. None of these states are included in the simulation, as ARIADNE includes only well established resonances.

Figure 7.2 establishes that the peak at 1522 is visible for different minimum values of Q^2, however, in order to glean more information about the structure's evolution, the $K^0_S p(\bar{p})$ invariant mass spectrum was investigated in separate bins of Q^2. Figure 7.3 shows the same mass distribution in four uncorrelated bins of Q^2, the ranges of which are as follows: (a) $2 < Q^2 < 20$ GeV^2, (b) $20 < Q^2 < 40$ GeV^2, (c) $40 < Q^2 < 80$ GeV^2 and (d) $Q^2 > 80$ GeV^2.

In the first bin one can see a slight excess in data above MC in the mass region of interest, however it does not show a significant structure. On the other hand, the next three bins show a possible enhancement around 1522 MeV in spite of a decrease in statistics. A more quantitative statement will be made in the next section. Lastly, in all four bins, the data is not well described by the simulation for masses below 1600 MeV, and no structure is seen in the simulated data.

7.2.1 Extraction of signal parameters and significance

The next step is to estimate the significance of the peak, as well as its position and width. Since the peak at 1522 MeV seems to start emerging at $Q^2 > 20$

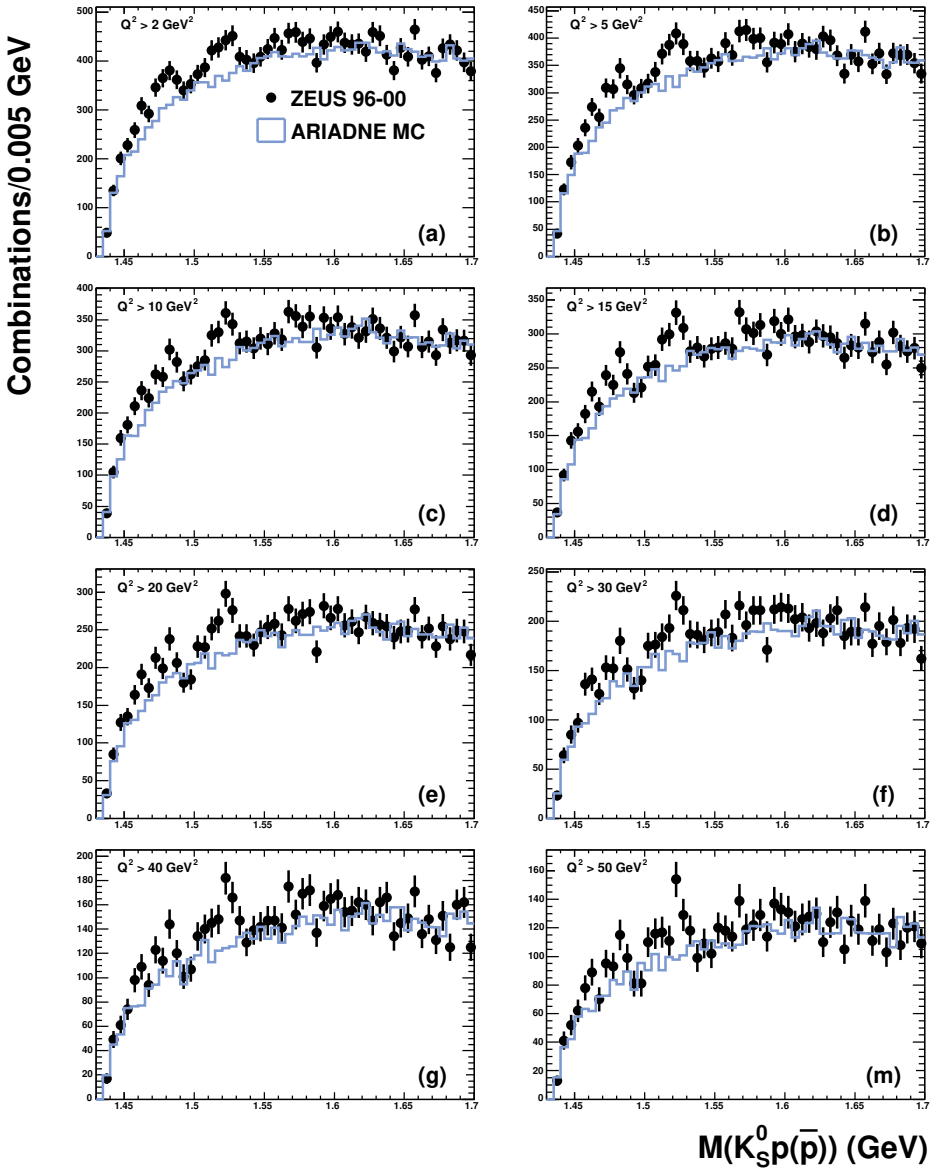

Figure 7.2: Invariant-mass spectra for the $K^0_S p(\bar{p})$ channel, after the cuts $f \leq dE/dx \leq F$, $dE/dx > 1.15$ mips and $p < 1.5$ GeV, integrated for (a) $Q^2 > 2$ GeV^2, (b) $Q^2 > 5$ GeV^2, (c) $Q^2 > 10$ GeV^2, (d) $Q^2 > 15$ GeV^2, (e) $Q^2 > 20$ GeV^2, (f) $Q^2 > 30$ GeV^2, (g) $Q^2 > 40$ GeV^2, (m) $Q^2 > 50$ GeV^2. The histogram shows the prediction of the ARIADNE MC simulation normalized to the data in the mass region above 1650 MeV.

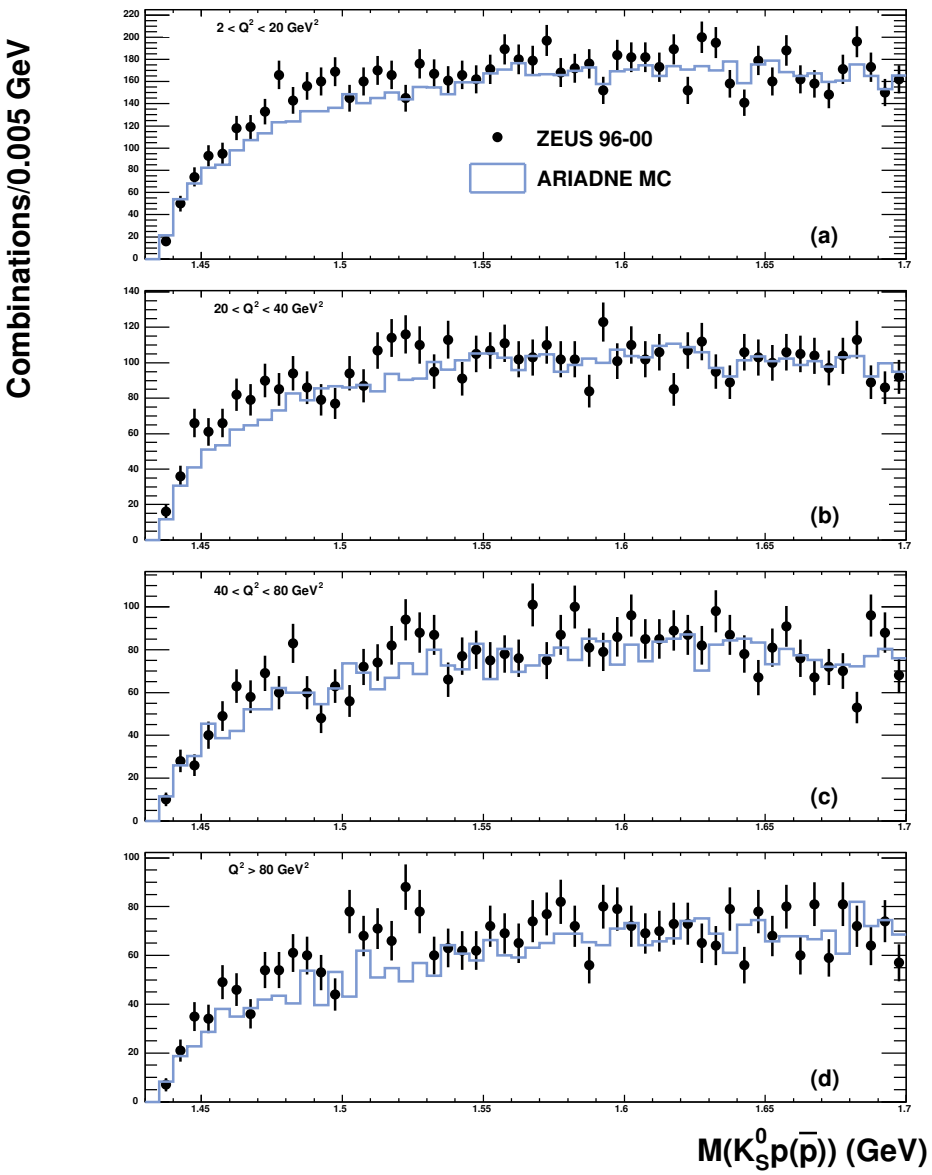

Figure 7.3: Invariant-mass spectra for the $K^0_S p(\bar{p})$ channel, after the cuts $f \leq dE/dx \leq F$, $dE/dx > 1.15$ mips and $p < 1.5$ GeV, in bins of (a) $2 < Q^2 < 20$ GeV^2, (b) $20 < Q^2 < 40$ GeV^2, (c) $40 < Q^2 < 80$ GeV^2, (d) $Q^2 > 80$ GeV^2. The histogram shows the prediction of the ARIADNE MC simulation normalized to the data in the mass region above 1650 MeV.

GeV^2, several functional forms were fit to the data over the mass range from threshold up to 1700 MeV for $Q^2 > 20$ GeV^2 to describe the signal at 1522 MeV as well as possible contributions from the bumps to the left and right of it. A background of the form

$$P_1(M - m_p - m_{K^0_S})^{P_2} \times (1 + P_3(M - m_p - m_{K^0_S})), \tag{7.1}$$

where M is the $K^0_S p(\bar{p})$ candidate mass, m_p and $m_{K^0_S}$ are the masses of the proton and the K^0_S, respectively, and P_1, P_2 and P_3 are parameters, was found to give a good description of the data when combined with a varying number of Gaussians.

Fit variation

Figures 7.4(a) - (d) show the mass spectrum fitted with the background function, described above, combined with zero to three Gaussians. In all the figures, the dashed lines show the Gaussian components and the dotted line, the background according to this fit. The parameters of the Gaussians and the background were left free and a bin-by-bin χ^2 minimization was used. For all the $K^0_S p(\bar{p})$ spectra, the total number of signal events was found by integrating the function over the mass region of interest and subtracting the background - obtained from the parametrization described above- in the same mass window.

As can be seen in the figure, the fit with no Gaussian yields a χ^2 per degree of freedom of 79/50, which is not a good fit. This value is dominated by contributions from the low-mass region.

The addition of one Gaussian to the background function, describing the signal at 1522 MeV, yields a mass of 1522.4 ± 1.5(stat.) MeV, a width of 5.0 ± 1.9(stat.) MeV and 134 ± 33 signal events above the background, which corresponds to a statistical significance of 4.1σ. However the χ^2 per degree of freedom of the fit of 63/47, although slightly better than before, can still use some improvement.

The addition of a second Gaussian significantly improves the fit in the low mass region. The χ^2 per degree of freedom for the fit with the two Gaussians over the entire fitted mass range is 44/44. For the second Gaussian, the fit yields a mass of 1464.9 ± 2.4(stat.) MeV and a width of 15.8 ± 2.4(stat.) MeV, which may correspond to a broader resonance such as the unestablished $\Sigma(1480)$ [44]. However it can also be interpreted as an empirical parametrization of a more

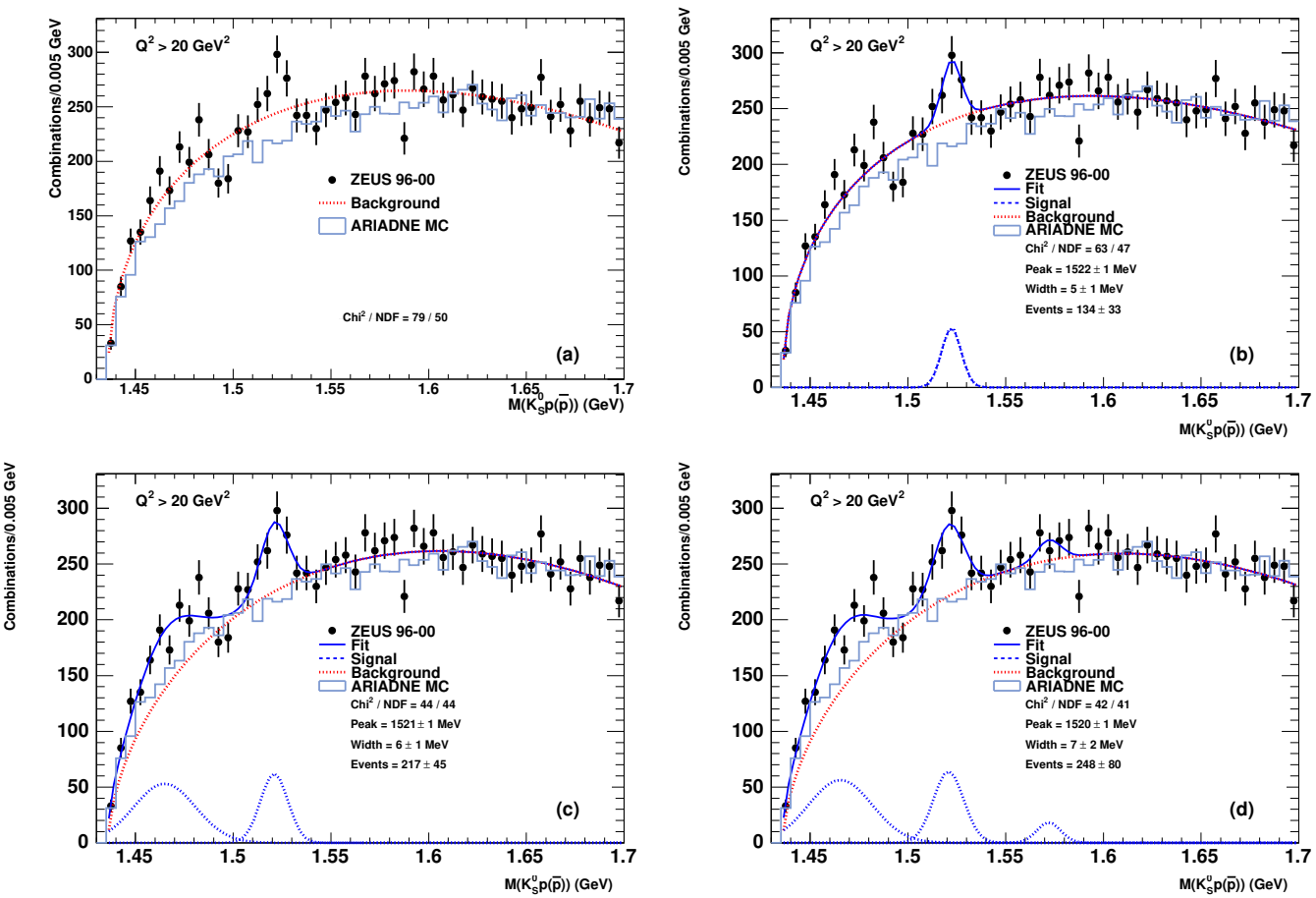

Figure 7.4: Invariant-mass spectra for the $K^0_S p(\bar{p})$ channel for the cuts as in fig. 7.2 integrated for $Q^2 > 20$ GeV^2. The solid line is the result of a fit to the data using a three-parameter background function plus (a) no Gaussians, (b) one Gaussian, (c) two Gaussians and (d) three Gaussians (see text). The dashed lines show the Gaussian components and the dotted line the background according to this fit. The histogram shows the prediction of the ARIADNE MC simulation normalized to the data in the mass region above 1650 MeV.

complicated background shape. Unfortunately, the parameters and significance of any state in this region are difficult to estimate due to the steeply falling background close to threshold. The signal peak position is 1521.5 ± 1.6(stat.) MeV, with a measured Gaussian width of 6.9 ± 1.4(stat.) MeV, which is slightly above the detector resolution. The fit yields 217 ± 45 signal events above the background, corresponding to 4.8σ.

Increasing the number of parameters by adding a third Gaussian, in an attempt to describe the higher mass region, does not particularly improve the χ^2 per degree of freedom of the fit. While this is not a bad fit, the third Gaussian has little physical significance as it does not converge to anything meaningful. The results of the fit using the background function plus the varying number of Gaussians are shown in Table 7.8. Finally, the background shape was fitted with several different polynomial functions (for example: $P_1 * x^{P_2} * exp\ (-x)$, where $x = M - m_p - m_{K^0_S}$). While none of them yielded good fits, they made little difference to the peak at 1522 MeV.

Fit		Bkg	Gaussian+Bkg.	2 Gaussians+Bkg.	3 Gaussians+Bkg.
χ^2/ndf		79/50	63/47	44/44	42/41
Peak 1	mass (MeV)	-	-	1464.9 ± 2.4	1465.5 ± 2.3
	width (MeV)	-	-	15.8 ± 2.4	16.2 ± 3.0
	events	-	-	408 ± 137	444 ± 215
Signal	mass (MeV)	-	1522.2 ± 1.5	1521.5 ± 1.6	1520.8 ± 1.8
	width (MeV)	-	5.0 ± 1.9	6.9 ± 1.4	7.7 ± 2.1
	events	-	134 ± 33	217 ± 45	248 ± 80
Peak 3	mass (MeV)	-	-	-	1572.1 ± 5.7
	width (MeV)	-	-	-	6.1 ± 3.7
	events	-	-	-	444 ± 364

Table 7.1: Results of the different fits to the $K^0_S p(\bar{p})$ invariant-mass spectrum for $Q^2 > 20$ GeV^2. Only statistical errors are given here.

It is clear that the fit with the two Gaussians provides the best results. Hence, in order to quantify what was seen "by eye" before (see discussion on figures 7.2 and 7.3), this fit was applied to the $K^0_S p(\bar{p})$ mass distribution. Figures 7.5(a) - (m) show the $K^0_S p(\bar{p})$ mass distribution integrated above a minimum Q^2 ranging from 2 GeV^2 to 50 GeV^2. As before, the statistics decrease as the cut on the mininmum value of Q^2 is raised, however, the fit results clearly show that the number of events in the signal remains the same up to about Q^2 of 20 GeV^2. Above this value, both the signal and background are consistent with having a $1/Q^4$ dependence, similar to the inclusive cross section. This, a somewhat surprising result, will be discussed in the next chapter.

To verify that the signal indeed emerges at about $Q^2 > 20$ GeV^2, the same fit was used to fit the $K^0_S p(\bar{p})$ invariant mass spectrum in separate bins of Q^2. Figure

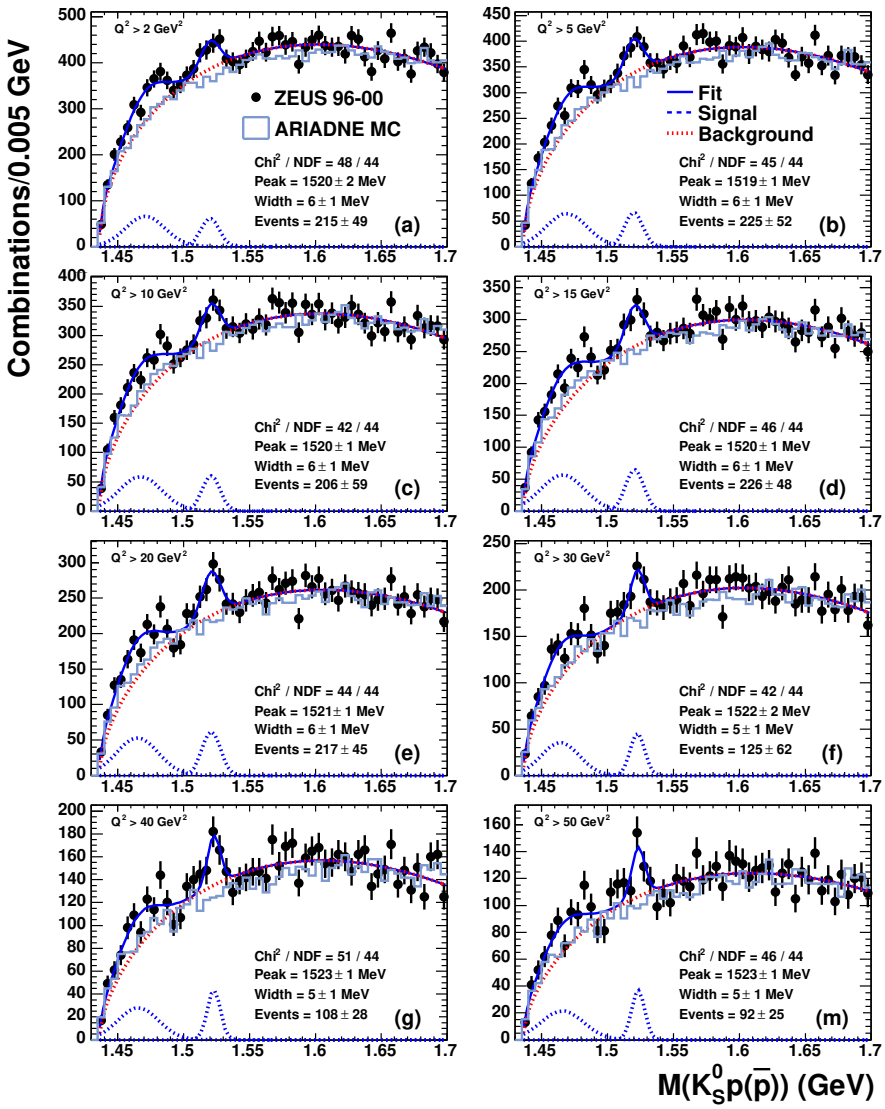

Figure 7.5: Invariant-mass spectra for the $K^0_S p(\bar{p})$ channel for the cuts as in fig. 7.2 for (a) $Q^2 > 2$ GeV^2, (b) $Q^2 > 5$ GeV^2, (c) $Q^2 > 10$ GeV^2, (d) $Q^2 > 15$ GeV^2, (e) $Q^2 > 20$ GeV^2, (f) $Q^2 > 30$ GeV^2, (g) $Q^2 > 40$ GeV^2, (m) $Q^2 > 50$ GeV^2. The solid line is the result of a fit to the data using a three-parameter background function plus two Gaussians (see text). The dashed lines show the Gaussian components and the dotted line the background according to this fit. The histogram shows the prediction of the ARIADNE MC simulation normalized to the data in the mass region above 1650 MeV.

7.6 shows the same mass distribution in four uncorrelated bins of Q^2, the ranges of which are the same as before: (a) $2 < Q^2 < 20$ GeV^2, (b) $20 < Q^2 < 40$ GeV^2, (c) $40 < Q^2 < 80$ GeV^2 and (d) $Q^2 > 80$ GeV^2. As observed by eye before, while there is a small excess in data above MC prediction in the mass region of interest in the first bin, it is not significant. However, in the following three bins, in spite of a decrease in statistics, there is an enhancement at 1522 MeV, the statistical significance of which ranges from 2.5σ to 3.6σ.

7.2.2 Narrow width

The chiral soliton model [46] predicts a width of less than 15 MeV for the Θ^+. While direct evidence limits the width to be less than about 10 MeV [8, 11], indirect evidence, based on analysis of KN scattering estimates widths of a few MeV or less [106, 107]. Such a narrow width for a resonance 85 - 100 MeV above its strong decay threshold would be exotic indeed. Hence the value of the Θ^+ width is an important measurement as it can rule out some theories, thereby allowing theorists to get a better handle on its production mechanism.

To this avail, in order to obtain an estimate of the intrinsic width of the peak near 1522 MeV, the Gaussian function was replaced by a Breit-Wigner function convoluted with a Gaussian. The width of the Gaussian distribution was fixed to the experimental resolution of 2.7 MeV. See figure 7.7. The extracted width, using the same threshold function to describe the background as before, was $\Gamma = 4.1 \pm 3.2$(stat.) MeV and is compatible with the proposed theories.

7.3 $\bar{\Theta}^-$: antipentaquark?

As has been mentioned before, in high-energy experiments, hadrons are mainly produced from the fragmentation of a sea (anti)quark in the proton struck by the photon, and do only faintly "remember" their proton parent, if at all [108]. Hence hadrons and their antiparticles are expected to be produced in approximately equal proportions. Recall the discussion on $\Lambda/\bar{\Lambda}$ production in chapter 6, where it was shown that $\Lambda(\rightarrow p\pi^-)$ and $\bar{\Lambda}(\rightarrow \bar{p}\pi^+)$ are produced in almost equal amounts within the ZEUS detector. This means that if the Θ^+ can be detected by ZEUS, so should be the $\bar{\Theta}^-$.

Figures 7.8(a) and (b) show the $K^0_S p$ and $K^0_S \bar{p}$ invariant-mass spectra, respectively, for $Q^2 > 20$ GeV^2. The results for the two decay channels

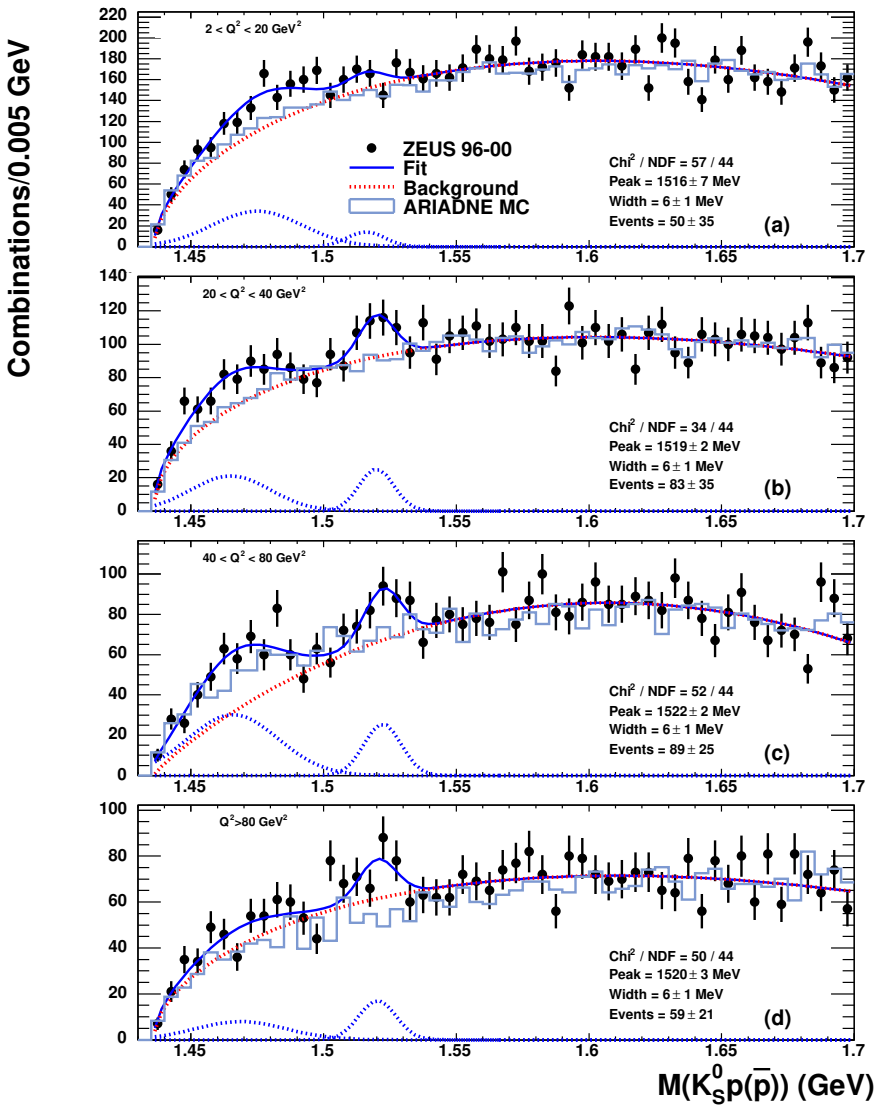

Figure 7.6: Invariant-mass spectra for the $K^0_S p(\bar{p})$ channel for the cuts as in fig. 7.3 in bins of (a) $2 < Q^2 < 20$ GeV^2, (b) $20 < Q^2 < 40$ GeV^2, (c) $40 < Q^2 < 80$ GeV^2, (d) $Q^2 > 80$ GeV^2. The solid line is the result of a fit to the data using a three-parameter background function plus two Gaussians (see text). The dashed lines show the Gaussian components and the dotted line the background according to this fit. The histogram shows the prediction of the ARIADNE MC simulation normalized to the data in the mass region above 1650 MeV.

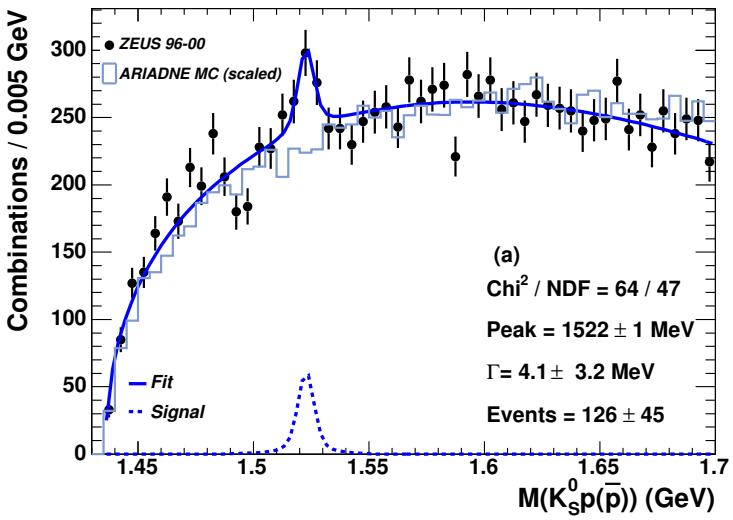

Figure 7.7: Invariant-mass spectrum for the $K^0_S p(\bar{p})$ channel for the cuts as in fig. 7.2 for $Q^2 > 20$ GeV^2. The solid line is the result of a fit to the data using one Gaussian convoluted with a Breit-Wigner function plus a three-parameter background function (see text). The dashed line shows the Gaussian component and the dotted line the background according to this fit. The histogram shows the prediction of the ARIADNE MC simulation normalized to the data in the mass region above 1650 MeV.

are compatible, though the number of $K^0_S \bar{p}$ candidates is lower. The mass distributions were fitted using the same function as for the combined sample and gave statistically consistent results for the peak position and width, which are shown in the figures. The number of signal events in the $K^0_S p$ channel is 149 ± 38 and in the $K^0_S \bar{p}$ channel, 75 ± 40. This result, while not completely decisive, suggests that if the $K^0_S p$ signal is interpreted as a pentaquark, then the enhancement in the $K^0_S \bar{p}$ channel might correspond to its antiparticle. This would be the first evidence of $\bar{\Theta}^-$.

In order to investigate the possibility of the signal being produced by selection cuts or from pion contamination in the proton selection, to study possible reflections from known states and to verify the robustness of the 1522 MeV peak, many checks have been carried out.

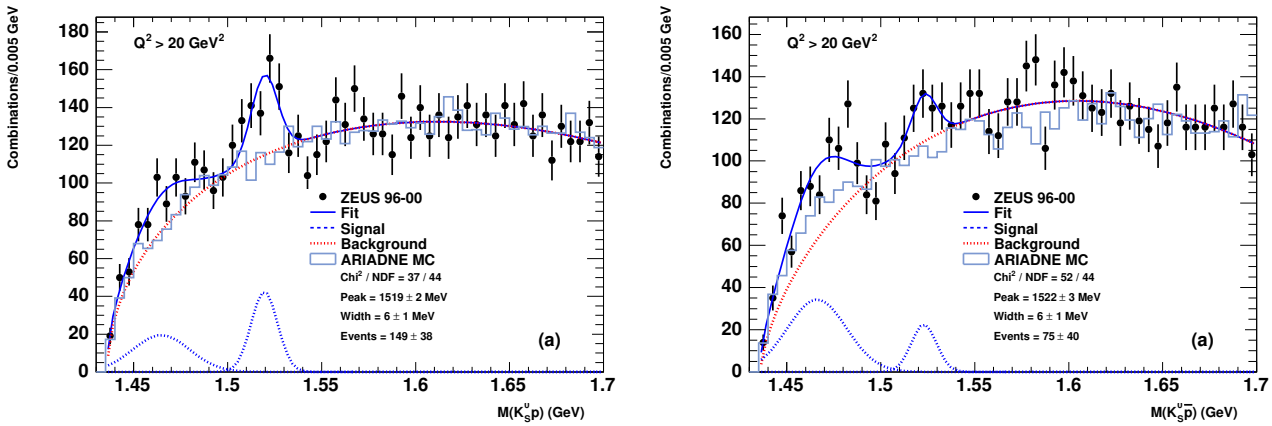

Figure 7.8: Invariant-mass spectra for the $K^0_S p$ (a) and $K^0_S \bar{p}$ (b) channels for the cuts as in fig. 7.2 for $Q^2 > 20$ GeV^2. The solid line is the result of a fit to the data using a three-parameter background function plus two Gaussians. The dashed lines show the Gaussian components and the dotted line the background according to this fit. Both histograms show the prediction of the ARIADNE MC simulation normalized to the data in the mass region above 1650 MeV.

7.4 Checks: pion contamination

As mentioned above, the confidence in K^0_S reconstruction is enhanced by the observation of a clear peak with low background with a mass value that is consistent with the PDG. See figure 6.2. However this is not the case for protons, which are identified solely with the dE/dx information. As can be seen in figure 6.15, even after the momentum and dE/dx cuts are applied, there is still some overlap between the proton- and pion-dE/dx bands. This means that there is some contamination from pions in the proton selection. (The purity of the proton sample is 60%. See section 6.5). Hence it is imperative to deplete pions and/or enhance protons in the selection. Furthermore it is necessary to check whether alternative methods of proton-pion separation, in lieu of the lower cut on dE/dx, yield the same results.

7.4.1 K^* cut

A reflection from $K^*(\rightarrow K^0_S \pi)$ can occur if pion tracks are misidentified as proton tracks. In order to eliminate such a reflection, tracks from the proton band within twice the width of the K^* peak were removed. The $dE/dx > 1.15$ mips

requirement was not made, however all other cuts were kept the same as before. According to a MC calculation, this cut increases the purity of the proton sample by 15% and reduces the number of signal events by about 32%. See figure 7.9, which shows the $K^0_S p(\bar{p})$ invariant-mass distribution obtained with the RAPGAP MC. Figure 7.9 (a) shows the distribution with the nominal cuts of the analysis, before the K^* cut is made, while figure 7.9 (b), after for $Q^2 > 20$ GeV^2.

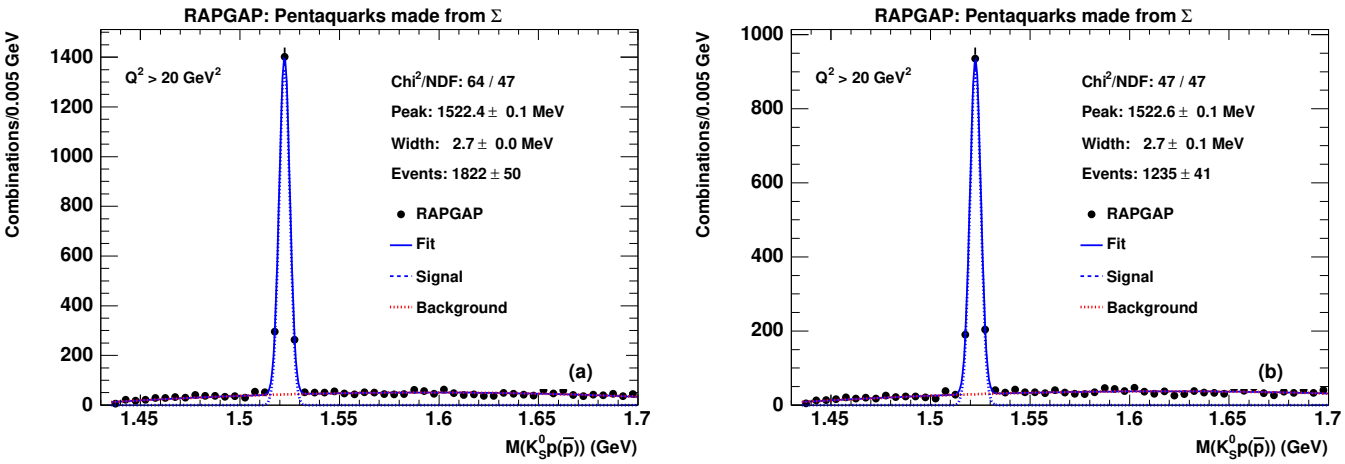

Figure 7.9: Invariant-mass spectra for the $K^0_S p(\bar{p})$ channels for cuts similar to those in fig. 7.2 minus the lower dE/dx cut before K^* removal (a) and after (b) for $Q^2 > 20$ GeV^2. The solid line is the result of a fit to the data using a second order polynomial for the background plus one Gaussian. The dashed line shows the Gaussian component and the dotted line, the background according to this fit.

The result of the K^* cut on data is shown in figures 7.10 (a) and (b), which show the $K^0_S p(\bar{p})$ invariant mass spectrum before and after K^* removal, respectively, for $Q^2 > 20$ GeV^2. The fits in figure 7.10 are done with two Gaussians and the same three-parameter background function as before. The removal of K^*'s enhances the significance of the peak at 1522 MeV. Furthermore the resulting peak position and width are unchanged, which is what one would expect from a signal. This check indicates that the signal is not a result of a reflection from K^*'s. (Curiously, the application of the K^* cut results in a much better agreement between data and MC in the low-mass region. This might suggest that the broad bump at 1465 MeV might be a reflection from K^*'s.)

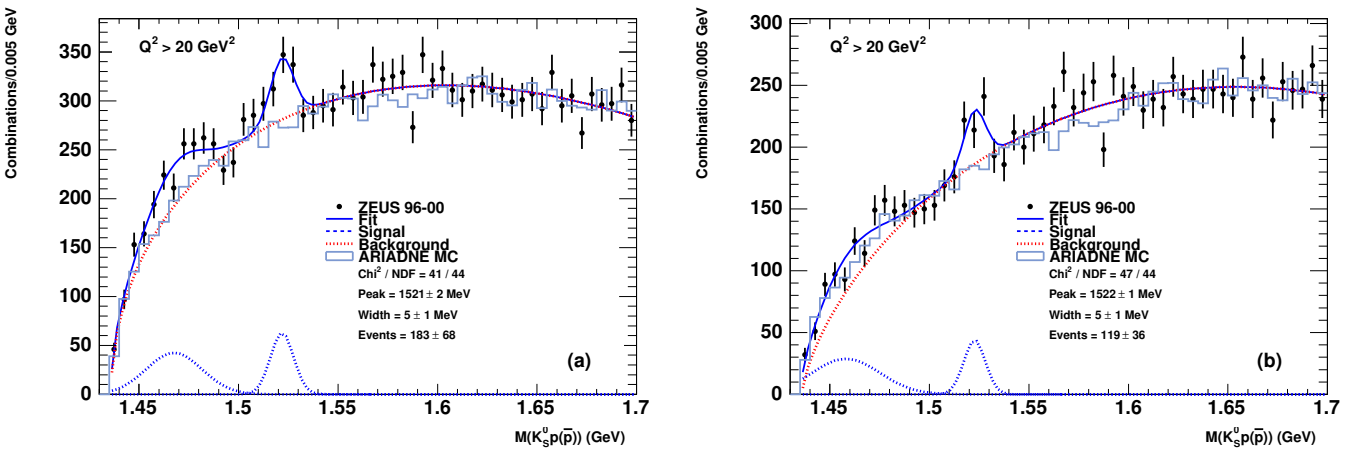

Figure 7.10: Invariant-mass spectra for the $K^0_S p(\bar{p})$ channels for cuts similar to those in fig. 7.2 minus the lower dE/dx cut before K^* removal (a) and after (b) for $Q^2 > 20$ GeV^2. The solid line is the result of a fit to the data using a three-parameter background function plus two Gaussians. The dashed lines show the Gaussian components and the dotted line, the background according to this fit.

7.4.2 Energy imbalance cut

With the K^* cut, described above, the pions were depleted. However, one can also enhance the number of protons. From Λ decays, it is known that, on average, the heavier particle, the proton, takes more momentum than the lighter particle, the pion. (See section 6.3). One can assume a similar asymmetry between protons and K^0_S's and can require the proton momentum or energy to be greater than that of the K^0_S. Furthermore, the mass difference between the Θ^+ daughters is not as large as that of the Λ daughters. As a result, a momentum or energy imbalance cut, in this case, should be 'softer' than in the case of Λ-baryons [110].

Figure 7.11 (b) shows the $K^0_S p(\bar{p})$ invariant mass spectrum for $Q^2 > 20$ GeV^2, obtained by requiring $E(p) > E(K^0_S)$ plus the nominal cuts, with the exception of the $dE/dx > 1.15$ mips requirement. Figure 7.11 (a) shows the same before the energy imbalance cut is applied. A MC study showed that this cut removes hardly any signal events; it removes mostly combinatorial background. The resulting peak, at 1521 $\pm$ 1 MeV, has a statistical significance of 6σ. This check gives confidence, not only in the proton-pion separation method used in the analysis, but also in the signal itself.

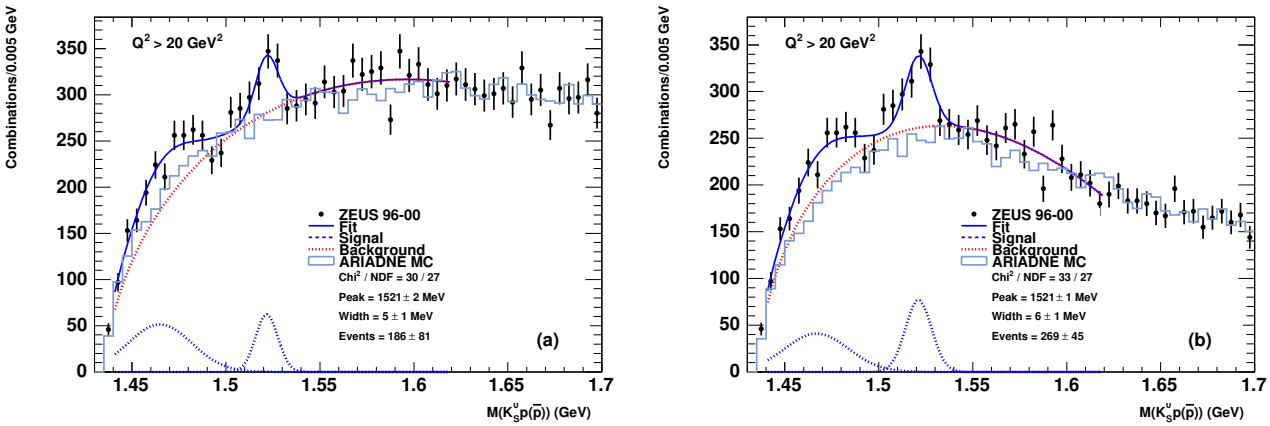

Figure 7.11: Invariant-mass spectra for the $K^0_S p(\bar{p})$ channels for cuts similar to those in fig. 7.2 minus the lower dE/dx cut plus before $E(p) > E(K^0_S)$ requirement (a) and after (b) for $Q^2 > 20$ (b) GeV^2. The solid line is the result of a fit to the data using a three-parameter background function plus two Gaussians. The dashed lines show the Gaussian components and the dotted line, the background according to this fit.

7.4.3 Energy imbalance and K^* cuts combined

Both the energy imbalance and K^* cuts serve only to illustrate, qualitatively, the robustness of the 1522 MeV peak and to verify that the lower cut on dE/dx works well to reduce pion contamination. These cuts are not used to make a quantitative assessment of either the peak's position or its significance. The reason for not using the $E(p) > E(K^0_S)$ and the K^*-rejection cuts is that the two cuts, especially in combination, lead to a complicated background shape, making the significance and the mass of the signal difficult to evaluate.

Figure 7.12 shows the events rejected by these two cuts separately. The $K^0_S p(\bar{p})$ invariant-mass spectrum with the nominal cuts, but without the $E(p) > E(K^0_S)$ and K^*-rejection cuts or the lower dE/dx cut for $Q^2 > 2$, is shown by the solid circles. The squares represent events that are rejected by the K^*-cut and the triangles represent the events removed with the $E(p) > E(K^0_S)$ requirement. The K^*-rejection cut removes more events to the left of 1522 MeV than it does to the right. However, the crucial point here is that the energy-imbalance cut starts removing events directly at about 1520 MeV. Hence, at the very least, these cuts when applied together, can enhance the significance of the peak, making the mass measurement difficult to evaluate. On the other hand, the combination of these

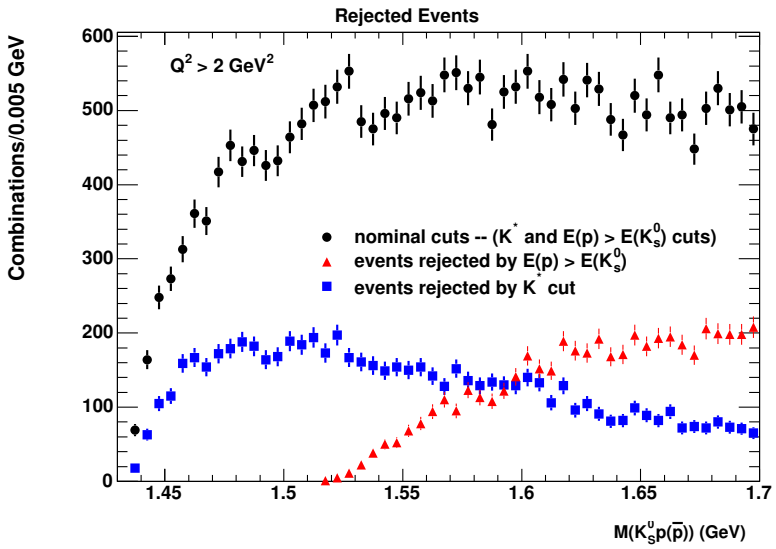

Figure 7.12: Invariant-mass spectrum for the $K^0_S p(\bar{p})$ channels for cuts similar to those in fig. 7.2 minus the lower dE/dx cut (circles), events rejected by the K^*-cut (squares) and events rejected by the $E(p) > E(K^0_S)$-cut (triangles) for $Q^2 > 2$ GeV^2.

cuts could even produce a false peak by depleting events on boths sides of the peak as is seen in figure 7.12. For these reasons, the $E(p) > E(K^0_S)$ and K^*-rejection cuts were not used to calculate the significance of the peak. Furthermore, the two cuts in combination produce a complicated background shape, which is difficult to fit. Figure 7.13, which shows the $K^0_S p(\bar{p})$ invariant mass spectrum for $Q^2 > 2$ GeV^2 obtained with the two cuts in combination with the nominal cuts, also shows the S-shaped background.

7.4.4 Pion enhancement

So far protons have been enhanced, but what happens if they are depleted? The signal, if it is coming from protons, should disappear. To check this, K^0_S candidates were combined with primary tracks in the region $dE/dx \leq$ 1.15 mips and $p \leq$ 1.5 GeV, where pions are expected to dominate over (anti)protons. The invariant mass was reconstructed using the same procedure as before, applying the proton-mass hypothesis for selected tracks. In addition, the mass distribution was calculated using the pion band of the dE/dx plot to select proton candidates. In neither of these cases was any structure seen in the mass distribution. See figures 7.14 (a) and (b), respectively. The conclusion of

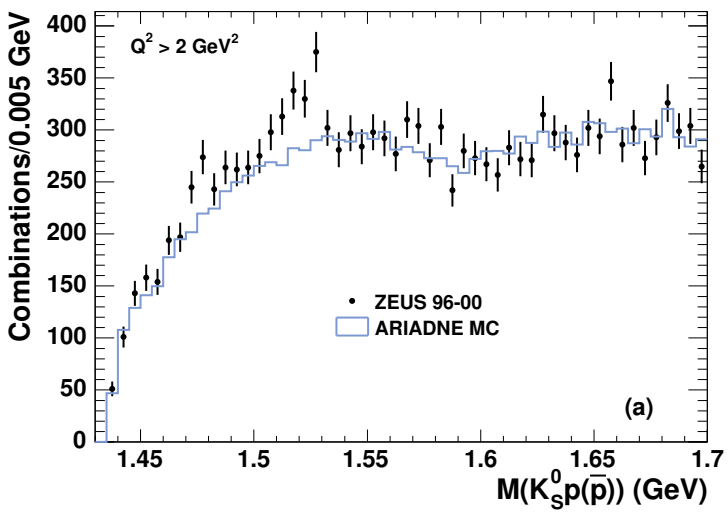

Figure 7.13: Invariant-mass spectra for the $K^0_S p(\bar{p})$ channels for cuts similar to those in fig. 7.2 minus the lower dE/dx cut, plus $E(p) > E(K^0_S)$ and K^*-rejection cuts for $Q^2 > 2$ GeV^2.

this study is that the signal is coming from protons, as opposed to pions. Once again, the confidence in the signal is enhanced.

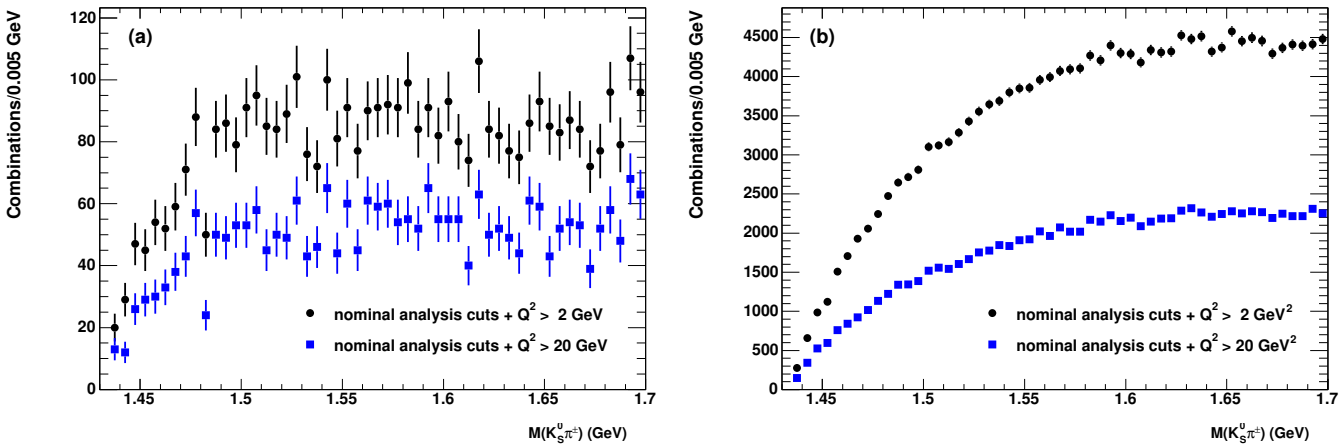

Figure 7.14: K^0_S $\pi^\pm$ invariant-mass spectra for the same cuts as those in fig. 7.2 except $dE/dx \leq 1.15$ mips and proton momentum $p \leq 1.5$ GeV with primary tracks from (a) proton band and (b) pion band for $Q^2 > 2$ and $Q^2 > 20$ GeV^2.

7.5 Checks: kaon contamination

Another possible reflection that can occur is if a kaon is misidentified as a proton. Heavy-flavor particles can contribute to the invariant mass $K^0_S\ K^\pm$ (for example, $D_S \to (K^\pm + \text{anything})$ or $(K^0, \bar{K^0} + \text{anything})$). In order to investigate whether D_S decays contribute to the signal, the $K^0_S\ K^\pm$ invariant mass was reconstructed using the $K^\pm$ mass hypothesis for proton candidates. See figure 7.15. Since charmed mesons are heavier than 1800 MeV, it is clear from the figure that heavy-flavor hadrons cannot contribute to the $K^0_S p(\bar{p})$ invariant mass spectrum as long as $M(K^0_S p(\bar{p})) \lesssim 1800$ MeV. Hence the signal is not some reflection originating from charm decays.

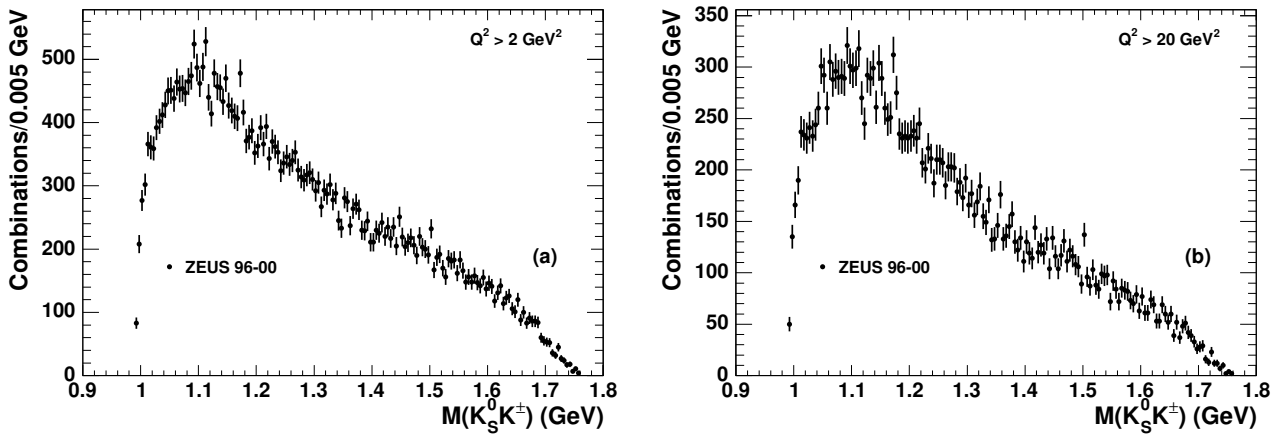

Figure 7.15: $K^0_S\ K^\pm$ invariant-mass spectra for the same cuts as those in fig. 7.2 for $Q^2 > 2$ (a) and $Q^2 > 20$ (b) GeV^2.

7.6 More checks...

If the proton and K^0_S candidates are chosen randomly from different events, one would not expect to see a signal. Hence the $K^0_S p(\bar{p})$ invariant mass was reconstructed with protons and K^0_S's selected from different events. No structure was seen in the mass distribution, giving credence to the peak at 1522 MeV. See figure 7.16.

One further check was to test the probability of a random fluctuation leading to a signal with 3.9σ significance or more in the mass range 1500–1560

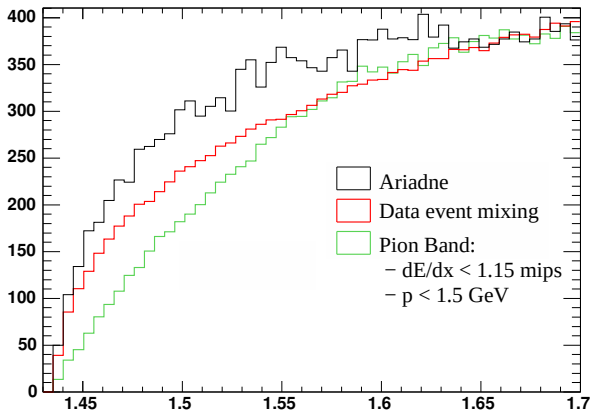

Figure 7.16: Comparison between ARIADNE, $K^0_S p(\bar{p})$ invariant-mass spectrum with randomly selected K^0_S's and protons for the same cuts as those in fig. 7.2 for $Q^2 > 5$ GeV^2.

MeV and with a Gaussian width in the range 1.5–12 MeV. Hence a number of MC experiments were carried out, using the background fit with zero gaussians as a starting distribution and generating random data using Poisson statistics. The probability of such a fluctuation was found to be 6×10^{-5}. The same exercise was carried out using the background plus the 1465 MeV Gaussian as the starting distribution, and the probability was found to be about a factor of ten lower. The results of both tests suggest that the 1522 MeV peak may not be a random fluctuation.

Lastly, the robustness of the peak was also checked by varying the event and track selections. The maximum momentum for the proton candidates was changed in a wide range from 1.2 GeV to 4.0 GeV. The dE/dx cut was varied between 1.1 and 1.3 mips. No change was seen in the peak position. The systematic uncertainties arising from these variations are given in section 7.8.

Summary of checks

Below is a short summary of the checks performed and described in the above sections.
Pion contamination:

- K^* cut: enhances the significance of the peak slightly ($2.7\sigma \rightarrow 3.3\sigma$); peak

position and width are unchanged. Message: signal is not a reflection from K^*;

- Energy imbalance cut: enhances the significance of the peak ($2.3\sigma \rightarrow 6\sigma$); peak position and width are unchanged. Validates the method used to separate protons and pions;
- Proton selection from proton band with $p \leq 1.5$ GeV, $dE/dx \leq 1.15$ mips: no peak is seen. Message: signal is not from pions;
- Proton selection from pion band: no peak is seen. Message: signal is not from pions.

Kaon contamination:

- Assume protons are kaons and reconstruct $K^0_S K^{\pm}$ mass: no enhancement is seen. Message: signal is not a reflection originating from charm decays.

Other checks:

- Random selection of protons and K^0_S's: no peak is seen;
- Vary event and track selection: peak position and width are unchanged;
- Check if peak is a random fluctuation: probability was found to be 6 x 10^{-5}.

7.7 Θ^+ production properties

All the tests conducted above suggest that the peak at 1522 MeV is robust. Hence the next step is to assume that the Θ^+ state is real and to study its production properties. For example, in what region of the detector or pseudorapity is it produced or whether it is an isotensor. The first can be done by looking at the $K^0_S p(\bar{p})$ invariant-mass distrubutions in different regions of the detector, and the second can be checked by investigating the double charge kaon-proton combinations. The latter check also provides a way to understand the efficiencies and resolutions.

7.7.1 η dependence of Θ^+ production

As has been mentioned above, assuming the Θ^+ is produced in fragmentation, one would expect an equal number of pentaquarks and their antiparticles. However, if the production of Θ^+ is somehow related to the proton remnant and the net baryon number from the proton beam, the Θ^+ should be best seen in the forward region of the detector and the signal from $\bar{\Theta}^-$ should be suppressed compared to that from Θ^+ [109]. Hence it is clear that the $K^0_S p$ and $K^0_S \bar{p}$ invariant-mass spectra should be investigated separately and in different regions of pseudorapidity.

The fit results of the $K^0_S p$ and $K^0_S \bar{p}$ invariant-mass spectra are shown again in figure 7.17, but this time in different regions of pseudorapidity. For the upper figures (a,b), η is required to be greater than zero and for the bottom figures (c,d), less than zero. This time, for all four spectra, both the peak position and width of the Gaussian describing the signal at 1521.5 MeV are fixed to the values obtained from the fit to the entire data sample: 1521.5 and 6.9 MeV. All other parameters are left free.

As can be seen, the signal is seen predominantly in the $K^0_S p$ channel in the central-to-forward region of the detector (figure (a)). Furthermore, the statistical significance of the signal has increased from 4.8σ to 5.6σ.

As for the $K^0_S \bar{p}$ channel, even though the fit yields 49 signal events, one can argue that the fit to the background undershoots the data, thereby overestimating the number of signal events and hence the significance, which is about 2σ. In any case, this result is compatible with the one for the same channel in the entire data sample.

Finally, these results, while not conclusive, are interesting because they show that Θ^+ seems to be produced in the forward direction. Whether this has something to do with the proton, needs to been seen. To this end, more statistics and studies are needed.

7.7.2 Θ^+: isotensor?

If an isotensor state is responsible for the 1522 MeV signal, its isotensor partner, the Θ^{++}, might be expected in the $K^+ p$ spectrum [111]. Hence, the presence of a peak in the like-sign spectrum would favor the isotensor interpretation of the Θ^+ state.

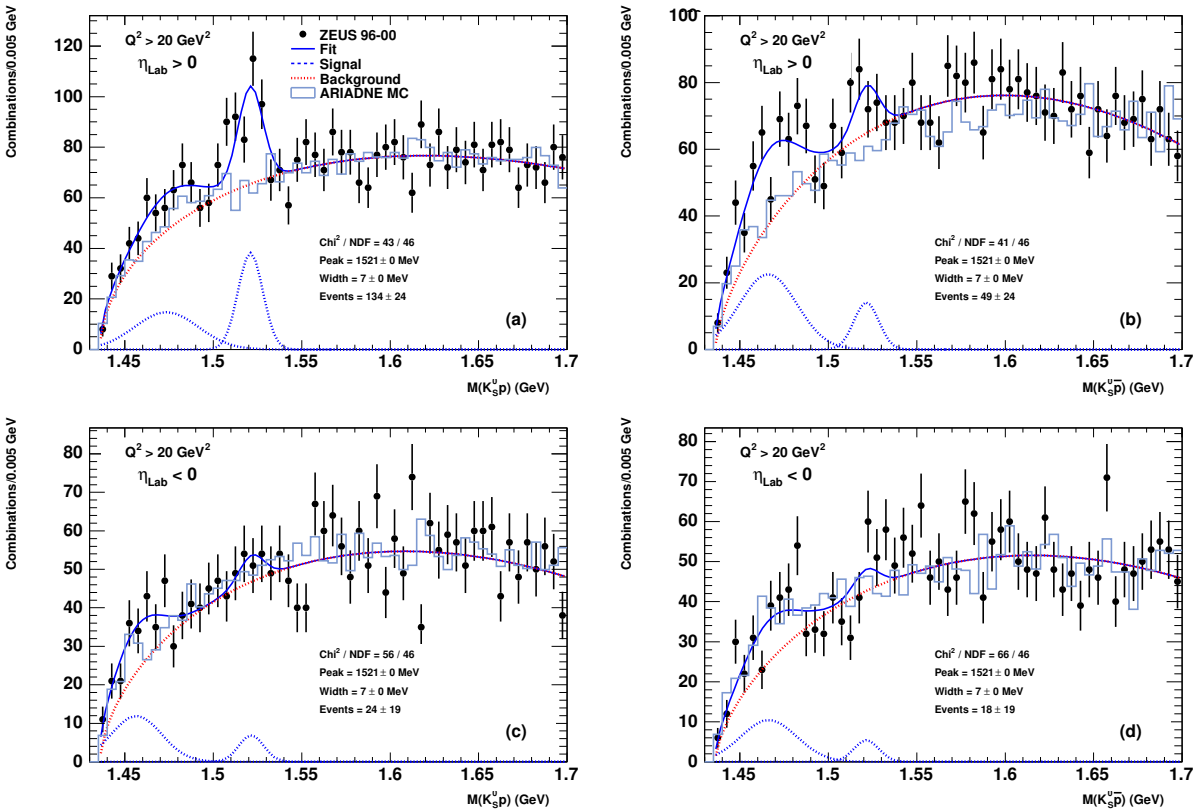

Figure 7.17: Invariant-mass spectra for the $K^0_S p$ (left) and $K^0_S \bar{p}$ (right) channels for the cuts as in fig. 7.2 for $Q^2 > 20$ GeV^2. The solid line is the result of a fit to the data using a three-parameter background function plus two Gaussians for positive η (a,b) and negative η (c,d). The dashed lines show the Gaussian components and the dotted line the background according to this fit. Both histograms show the prediction of the ARIADNE MC simulation normalized to the data in the mass region above 1650 MeV.

Furthermore, previous studies on K^0_S and Λ production in DIS [101] enhance the confidence in the K^0_S reconstruction and selection procedure, and allow cross-checks of proton identification. For example, events with two K^0_S's have been successfully used to study resonances decaying into K^0_S pairs [112]. Hence another advantage of reconstructing the Kp invariant mass is that it allows the usage of the well established $\Lambda(1520)D_{03}$-meson in this decay mode to check the efficiencies and resolutions.

For the above reasons, the $K^{\pm}p(K^{\pm}\bar{p})$ invariant mass spectra were investigated for $Q^2 > 1$ GeV^2, identifying proton and charged kaon candidates using

dE/dx in a kinematic region similar to that used in the $K^0_S p(\bar{p})$ analysis. Proton tracks were selected requiring $f < dE/dx < F$, where f and F were the same functions as before. This time, however, dE/dx was required to exceed 1.8 mips. The kaons were required to be within the functions described in equation 7.2 and to have a dE/dx measurement of above 1.4 mips. The above cuts are illustrated in figure 7.18.

$$f = \frac{0.1}{p^2} + 0.8 \qquad F = \frac{.25}{p^2} + 1.1 \tag{7.2}$$

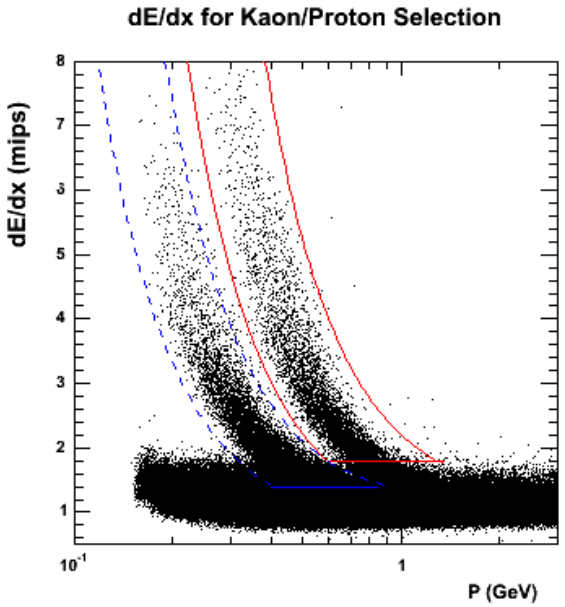

Figure 7.18: Proton and kaon selection with dE/dx. The solid(dashed) lines indicate proton(kaon) selection requirements.

The $K^{\pm}p$ spectra are shown in figure 7.19. No peak was observed near 1522 MeV in the K^+p spectrum. However, a clean signal was observed in the K^-p spectrum at 1518.5 ± 0.6(stat.) MeV, corresponding to the $\Lambda(1520)D_{03}$ for $Q^2 > 1$ GeV^2. A fit using a Gaussian convoluted with a Breit-Wigner, with the Gaussian width fixed to the detector resolution, yields an intrinsic width of 13.7 ± 2.1(stat.) MeV, consistent with the PDG value of 15.6 ± 1.0 MeV [44]. The fact that both the mass and width measurements agree with the PDG values verifies that there are no significant reconstruction biases in the pentaquark mass range. Furthermore, the absence of a signal in the K^+p channel disfavors the isotensor interpretation of the Θ^+.

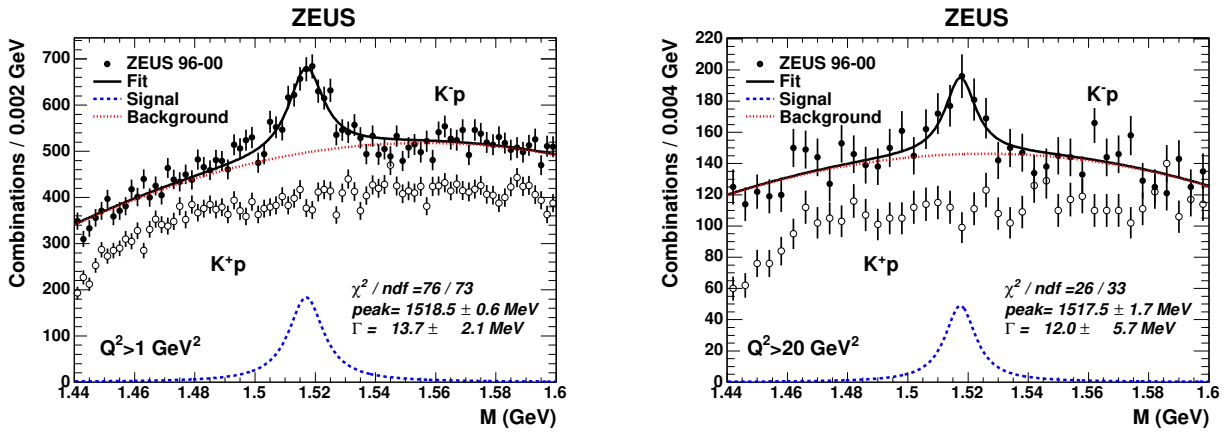

Figure 7.19: Invariant-mass spectra for the $K^{\pm}p$ and $K^{\pm}\bar{p}$ channels for $Q^2 > 1$ (a) and $Q^2 > 20$ (b). (See text for more on cuts). The solid line is the result of a fit to the data using a three-parameter background function plus one Gaussian. The dashed lines show the Gaussian components and the dotted line, the background according to this fit.

7.8 Systematic uncertainties

In order to estimate the sensitivity of the measurement to changes in the selection criteria, several systematic checks were performed. The systematic uncertainties on the peak position and the width, determined from the fit shown in Fig. 7.5, were evaluated by changing the selection cuts and the fitting procedure. The uncertainties on the peak position and the Gaussian width for each check are given in parentheses (Mass, Width) in MeV. The following systematic studies have been evaluated:

- the 40-hit requirement for the proton candidates was not used (0.4, 0.0). The variations of the cuts on the tracks in the laboratory frame were found to have a negligible effect on the peak;
- the dE/dx cut was increased to 1.3 mips (-1.6, +1.8). The maximum momentum of protons was varied within 1.3 GeV (+0.7, 0.0) to 4.0 GeV (-0.2,0.0);
- the bin size was raised (lowered) by 1 MeV -0.7,+1.2 (0.0,+0.5); the log-likelihood method was used for the fitting procedure instead of the χ^2 method (0.0, 0.1);

- the fit was made using only a single Gaussian (-1.2, -2.0), or with three Gaussians (-0.6, $+0.8$); the background function was changed to a third-order polynomial ($+0.6$, 0.0);
- the CTD momentum calibration uncertainty on the peak position was calculated from the mass measurements of K^0_S, Λ and the Λ_c reconstructed in the $K^0_S p(\bar{p})$ decay channel ($^{+1.7}_{-1.4}$).
- the DIS cuts were raised and lowered by about 10% from their nominal values and were found to have minute to no effect on the Gaussian width. The variation on the peak position obtained by raising and lowering the cuts by about 10% from their nominal values is listed in table 7.2.

Quantity	Increased	Decreased
	Mass,Width (MeV)	Mass,Width (MeV)
$y_{\rm JB}$	$+0.1,\ 0.0$	$+0.1,\ 0.0$
$y_{\rm el}$	$0.0,\ 0.0$	$-0.1,\ 0.0$
$\rm E_{el}$	$+0.5,\ 0.0$	$0.0,\ 0.0$
$\rm E - p_z$	$+0.4,\ 0.0$	$+0.1,\ 0.0$
$\rm \lvert Z_{vtx}\rvert$	$+0.1,\ 0.0$	$+0.2,\ 0.0$

Table 7.2: Sensitivity of the $K^0_S p(\bar{p})$ mass and width measurements to changes in selection criteria for fit results for $Q^2 > 20$ GeV^2.

The overall systematic uncertainties on the peak position and the width of $^{+2.1}_{-2.6}$ MeV and $^{+2.4}_{-2.0}$ MeV were determined by adding the above uncertainties in quadrature. The largest contribution on the uncertainty arose from varying the assumption of the shape of the background.

7.9 Summary

A peak is seen at about 1522 MeV in the $K^0_S p(\bar{p})$ invariant-mass spectrum in the kinematic region of $Q^2 > 20$ GeV^2. The peak position, determined from a fit to the mass distribution is 1521.5 ± 1.6(stat.) $^{+2.1}_{-2.6}$(syst.) MeV, and the measured Gaussian width of $\sigma = 6.9 \pm 1.4$(stat.) $^{+2.4}_{-2.0}$(syst.) MeV is above, but consistent with, the experimental resolution of 2.7 ± 0.1 MeV. The number of events ascribed

to the signal by this fit is 217 ± 45. The statistical significance, estimated from the number of events assigned to the signal by the fit, varies between 3.5σ and 4.8σ, depending on the assumption of the background.

An enhancement was also seen in the $K^0_S\bar{p}$ channel. The number of signal events in the $K^0_S\bar{p}$ channel is 75 ± 40. If the K^0_Sp signal is interpreted as a pentaquark, then the enhancement in the $K^0_S\bar{p}$ channel may correspond to its antiparticle, the $\bar{\Theta}^-$. This would be the first evidence of $\bar{\Theta}^-$.

Several cross checks were made in order to validate the particle identification, to study possible reflections from known states and to verify the robustness of the peak. The 1522 MeV peak passes all the checks. Furthermore, the probability of a similar signal anywhere in the range 1500–1560 MeV arising from fluctuations of the background was found to be below 6×10^{-5}.

Lastly, the signal was observed to come predominantly from protons in the forward region, thereby raising the question whether the Θ^+ production might have some connection with the proton-remnant, despite the particle/antipraticle symmetry observed, for example, in Λ production. Whether this is the case, needs to be seen. To this end, more statistics are needed.

Chapter 8

Θ^+ cross section

Chapter 7 provided a description of the reconstruction of the $K^0_S p(\bar{p})$ final state and the studies conducted on the $K^0_S p(\bar{p})$ invariant-mass spectrum and their results. A peak is seen at about 1522 MeV for $Q^2 > 20$ GeV^2. The measured Gaussian width, determined from a fit to the mass distribution, is about 6.9 MeV and is above, but consistent, with the experimental resolution. The number of events ascribed to the signal by the same fit is 217 ± 45, yielding a statistical significance of 4.8σ. The significance varies depending on the assumption of the background shape. Furthermore, several studies were conducted in order to validate the particle identification, to investigate possible reflections from known states and to verify the robustness of the peak.

Be it a new particle or a fluctuation, the peak survives this cross examination. Hence the next question that begs to be asked is: what is its production rate? Or, better yet, how often is it produced in comparison to a better understood baryon, such as the $\Lambda(1116)$. The answers to these questions can shed light on the production mechanism of the Θ^+ candidate, especially since at ZEUS, it can only be produced in a kinematic region dominated by fragmentation of quarks and gluons, produced in high-energy colliding experiments.

Additionally, cross-section measurements allow quantitative comparisons with theoretical predictions and with signals and/or limits from other experiments, for example, the recent limits from H1 [28]. At present, this inter-experimental comparison is imperative in order to elucidate the peak at 1522 MeV.

8.1 Cross-section definition

The cross section, σ, is a Lorentz-invariant measure of the probability of interactions. It can be visualized as the geometrical overlap of the target and the projectile or the area presented by the target particle, which must be hit by the point-like projectile for an interaction to occur. Hence σ has the dimension of area. The cross section differential in variable x is given by,

$$\frac{d\sigma_i}{dx} = \frac{N_i(x)}{\mathcal{L}^{int} \cdot \Delta x_i \cdot A \cdot BR} \,. \tag{8.1}$$

$N_i(x)$ is the number of observed events having passed all cuts in a bin i of width, Δx. $\mathcal{L}^{int} = \int L dt$ is the integrated luminosity of the total data sample, A is the detector acceptance and BR is the branching ratio for the decay channels investigated. The detector acceptance is defined as the ratio of the number of reconstructed events in a certain bin to the number of generated events from the decay channel being investigated in the same bin. The cross-section definition has to account for the acceptance since the measured distributions generally do not coincide with the true (MC generator-level) distributions. This is due to reconstruction and trigger inefficiencies and a finite detector resolution.

For the present measurement, $N_i(x)$ is the number of observed Θ^+ or Λ-baryon candidates and is determined from the fits described before.

8.2 Reminder: data sample and selection cuts

Before moving on to the cross-section extraction, a brief summary of the data sample and selection cuts is provided here as a reminder. They have already been described in detail in the previous chapters.

8.2.1 DIS event selection

The entire data-sample, collected by the ZEUS detector between 1996-2000, is used for the cross-section measurement. This sample corresponds to $\mathcal{L} = 121\pm$ 2 pb^{-1}, at $\sqrt{s}$ = 300 and 318 GeV. While for the $K^0_S p(\bar{p})$ invariant-mass reconstruction, DIS events measured with $Q^2 > 2$ GeV^2 were used, for the cross-section measurement, events with $Q^2 > 20$ GeV^2 are used. This is because, as was seen in chapter 7, there is no significant signal below Q^2 of 20 GeV^2. The following cuts were used to select the DIS events:

- $E_{e'} \geq 10$ GeV;
- $0.04 \leq\ y \leq\ 0.95$;
- $38\ \leq\ \delta\ \leq\ 60$ GeV;
- a primary vertex position in the range $\mid Z_{vertex} \mid \leq\ 50$ cm;
- $Q^2_e \geq\ 20$ GeV^2 ;
- at least one secondary vertex in the event.

8.2.2 Track selection

Events that passed the above selection cuts were further filtered by imposing several tracking related cuts, restricting the study to a region where the CTD track acceptance and resolution is high:

- $p_T \geq 0.15$ GeV;
- $|\eta| \leq 1.75$.

8.2.3 Electron selection

The same requirements are made on the scattered electron as before save one. For reasons that are explained in section 8.4 below, the SRTD cut has been increased to $R > 25$ cm. This cut on the electron position in the RCAL is to remove events with electrons near the beam-pipe region, where a bad reconstruction of the electron may occur.

8.2.4 Θ^+ reconstruction

A brief summary is provided here on K^0_S and proton selection.

K^0_S selection

K^0_S-mesons, identified by their decay mode, $K^0_S \rightarrow \pi^+\pi^-$, were required to meet the following criteria:

- $p_T(K^0_S) \geq 0.3$ GeV;

- $|\eta(K^0_S)| \leq 1.5$;
- $483 \leq \mathrm{M}(\pi^+\pi^-) \leq 513$ MeV;
- a proton-pion mass hypothesis was imposed on tracks satisfying the above cuts. Those with $\mathrm{M}(\mathrm{p}\,\pi) < 1121$ MeV, were rejected in order to reduce contamination from $\Lambda(\bar{\Lambda})$.

Proton selection

The $K^0_S p(\bar{p})$ invariant mass distribution was obtained by combining the K^0_S candidates with (anti)proton candidates, the selection of which was done using information on the energy-loss, dE/dx, in the CTD. Tracks were required to:

- originate from the primary-vertex;
- have more than 40 CTD hits per track;
- be in the dE/dx bands described in section 6.5;
- have $p < 1.5$ GeV and $dE/dx > 1.15$ mips in order to remove contamination from pions.

8.2.5 Λ reconstruction

The Θ^+ production rate is compared to that of $\Lambda(1116)$. The reasons for choosing $\Lambda(1116)$ were iterated in chapter 6, an important one being that it can be reconstructed with both the dE/dx and V0 methods. With the dE/dx method, Λ's can be selected in exactly the same way as Θ^+'s. This means that the uncertainties in the Monte Carlo simulation of the dE/dx cancel in the ratio $\sigma(\Theta^+ \rightarrow K^0 p)/\sigma(\Lambda \rightarrow p\pi)$. Furthermore, in the event that Monte Carlo simulation might not adequately reproduce the energy-loss measurement in the CTD, a comparison of the Λ cross section obtained using the secondary-vertex method can be used to estimate systematic uncertainties due to the dE/dx method in the Θ^+ cross-section evaluation. Lastly, the V0 method also provides a measure of the uncertainty on the K^0_S reconstruction.

Λ (dE/dx method)

Λ-baryons were selected in the decay mode $\Lambda \rightarrow p\pi$. All tracks were required to have more than 40 CTD hits per track. Furthermore, the proton candidates were selected in much the same way as they were for the Θ^+ state. All tracks were required to:

- be in the dE/dx bands described in section 6.5;
- have $p < 1.5$ GeV and $dE/dx > 1.15$ mips in order to remove contamination from pions.

All tracks *excluded* by the proton dE/dx bands were accepted as pion candidate tracks. Lastly, for the Θ^+ state, proton candidate tracks were selected by requiring that they originate from the primary vertex. For the simple reason that Λ-baryons are not expected to decay at the primary vertex, this requirement was not made here. Furthermore, *no* vertexing information is required for these tracks as the idea is to separate the two means of Λ reconstruction as much as possible.

Λ (V0 method)

Λ selection with the secondary vertex method has been described in much detail in section 6.3 and will not be repeated here.

8.3 Monte Carlo revisited

A detailed description of the Monte Carlo simulation used in this analysis was provided in chapter 3 and summarized in table 3.1. The acceptance for Θ^+ production was calculated using the RAPGAP model, whereby Σ^+-baryons were assumed to have the same production and decay characteristics as the Θ^+-baryons. The modified Σ^+-baryons were assumed to have a zero natural-width and a mass of 1522 MeV, and were forced to decay, with 100% branching ratio, to the $K^0 p(\bar{p})$ final state. Hence it is important to bear in mind, that the usage of the above MC for the detector acceptance and cross-section extraction for the Θ^+ particle means that the results have to be treated with caution. These results are valid as long as the assumption that Θ^+ is similar to Σ-baryons holds.

For the Λ-baryons, the ARIADNE model for fully inclusive DIS was used.

8.4 Trigger revisited

For the cross-section measurement, the trigger selection used thus far and described in chapter 5, has been slightly modified for reasons that are explained here.

For the signal extraction, an OR between the low-Q^2 (DIS01) and medium-Q^2 (DIS03) inclusive triggers was used. Now only DIS03 is required, and no conditions are placed on DIS01. This change was motivated by two reasons. One is that Q^2 and the scattering angle or the radius of the electron are correlated and since the signal is seen above Q^2 of 20 GeV^2, the smaller radius trigger of the two is not needed. The other reason is that it simplifies the treatment of the data which was taken with changing prescale values and box cut or radius requirements. The simulation of the DIS01 prescales in conjunction with that of the varying DIS03 radius/box cut, both summarized in table 5.2, is a task best suited for Sisyphus as not much is gained in this analysis by doing so.

Since the RAPGAP MC was generated with the 1998 detector configuration, the offline SRTD radius of the scattered-electron position is required to be, R $>$ 25 cm. Furthermore, because of the varying box/radius cut (i.e. Q^2), not all events have the same weight. The events are weighted corresponding to the ratio of luminosity with the respective radius cut as follows:

- BC $>$ 14 x 14 cm^2: 7.39 pb^{-1}/120.65 pb^{-1} = 0.0162;
- R $>$ 25 cm: 7.39 + 47.95 pb^{-1}/120.65 pb^{-1} = 0.4587;
- R $>$ 35 cm: (7.39 + 47.95 + 65.31) pb^{-1}/120.65 pb^{-1} = 1.0.

8.5 Θ^+ acceptance and cross section

The cross section for $\Theta^+(\bar{\Theta}^-) \rightarrow K^0 p(\bar{p})$ was measured in the kinematic region $p_T > 0.5$ GeV, $|\eta| < 1.5$ and $0.04 < y < 0.95$ for (a) $20 < Q^2 < 40$ GeV^2, (b) $40 < Q^2 < 80$ GeV^2 and (c) $80 < Q^2 < 160$ GeV^2. The binning was chosen such that the statistics were distributed evenly over the three bins. The upper limit on the last bin is chosen because there are almost no events above Q^2 of 160 GeV^2. (It also makes the plotting of the acceptance and the cross section value in the last bin easier, especially for the Θ^+/Λ ratio.)

Figure 8.1 shows the $K^0_S p(\bar{p})$ invariant-mass in the three Q^2 bins in data on the left and in MC on the right. For data, as before, the number of reconstructed Θ^+ events was determined via a fit with a three-parameter background function plus two Gaussians. All parameters were left free. In chapter 7 it was shown that this fit provides the best χ^2 by numbers of degrees of freedom. The solid line is the result of this fit and the dashed lines show the Gaussian components and the dotted line, the background according to this fit. The histogram shows the prediction of the ARIADNE MC simulation normalized to the data in the mass region above 1650 MeV.

In the MC, the number of reconstructed Θ^+ events were determined via a fit with a second-order polynomial function plus one Gaussian. Once again, the solid line in the figure is the result of this fit and the dashed, the background according to this fit.

Figure 8.2 shows the acceptance on the top and cross section on the bottom for $\Theta^+(\bar{\Theta}^-) \to K^0 p(\bar{p})$ for the three different Q^2 regions. The branching ratios for $K^0 \to K^0_S \to \pi^+\pi^-$ of 50% and 68.6%, respectively, were taken from the PDG [44]. The results are plotted at the bin centers and the horizontal bars in the figure represent the binwidths.

The acceptance for Θ^+ varies between 3.3% and 4.8%, the lowest value being in the first Q^2 bin. The cross-section values are listed in table 8.2 in section 8.8. Furthermore, the overall acceptance and cross section for $Q^2 > 20$ GeV^2 were found to be 4% and 130.0 $\pm$ 26.9(stat.) pb, respectively.

8.5.1 Low Θ^+ acceptance

The detector acceptance for $\Theta^+(\bar{\Theta}^-) \to K^0 p(\bar{p})$ is rather low, especially for the lowest Q^2 bin (20-40 GeV^2). To investigate whether the acceptance is even lower for $Q^2 < 20$ GeV^2, which would explain the lack of a visible signal in that region, the acceptance was calculated for Q^2 between 2 and 20 GeV^2.

Θ^+ acceptance: $2 < Q^2 < 20$ GeV^2

For $Q^2 < 20$ GeV^2, the medium-Q^2 trigger, DIS03, can no longer be used. There is essentially no acceptance in this kinematic region since DIS03 utilizes a cut of R > 25 cm for most of the data taken with it on (see section 8.4). Hence, the trigger requirement was changed to the low-Q^2 trigger or DIS01. Furthermore, the DIS01 prescale, as described in chapter 5, was simulated as well.

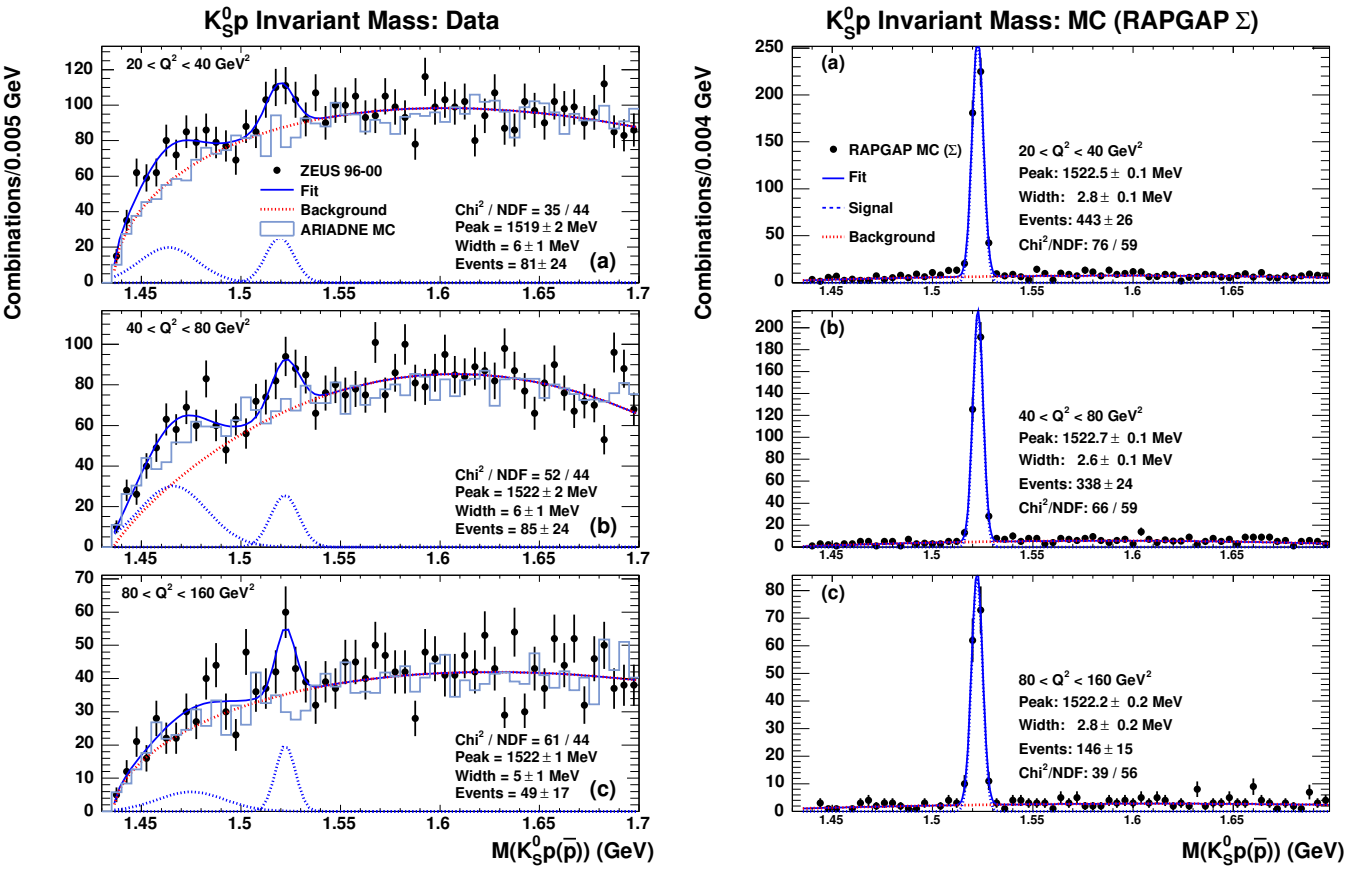

Figure 8.1: Invariant-mass spectra for $K^0_S p(\bar{p})$ channel in data (left) and in RAPGAP MC (right) for (a) $20 < Q^2 < 40$ GeV^2, (b) $40 < Q^2 < 80$ GeV^2 and (c) $80 < Q^2 < 160$ GeV^2. The solid line is the result of the fit to the data and MC. The dashed line shows the background component of the fits. (See text).

The detector acceptance for Q^2 between 2 to 20 GeV^2, not shown here, was found to be 0.5±0.03%, which is quite low compared to 4%, on average, for the other three bins. This rather low acceptance means that there is low sensitivity in the low Q^2 region. Hence a Θ^+ signal cannot be excluded in this region. However, it is possible that the suppression of the signal may also be related to its unknown production mechanism.

For the rest of the discussion, only the region above Q^2 of 20 GeV^2 is considered. The region below Q^2 of 20 GeV^2 will be revisited in section 8.7, where the production rates of Θ^+ to Λ are compared.

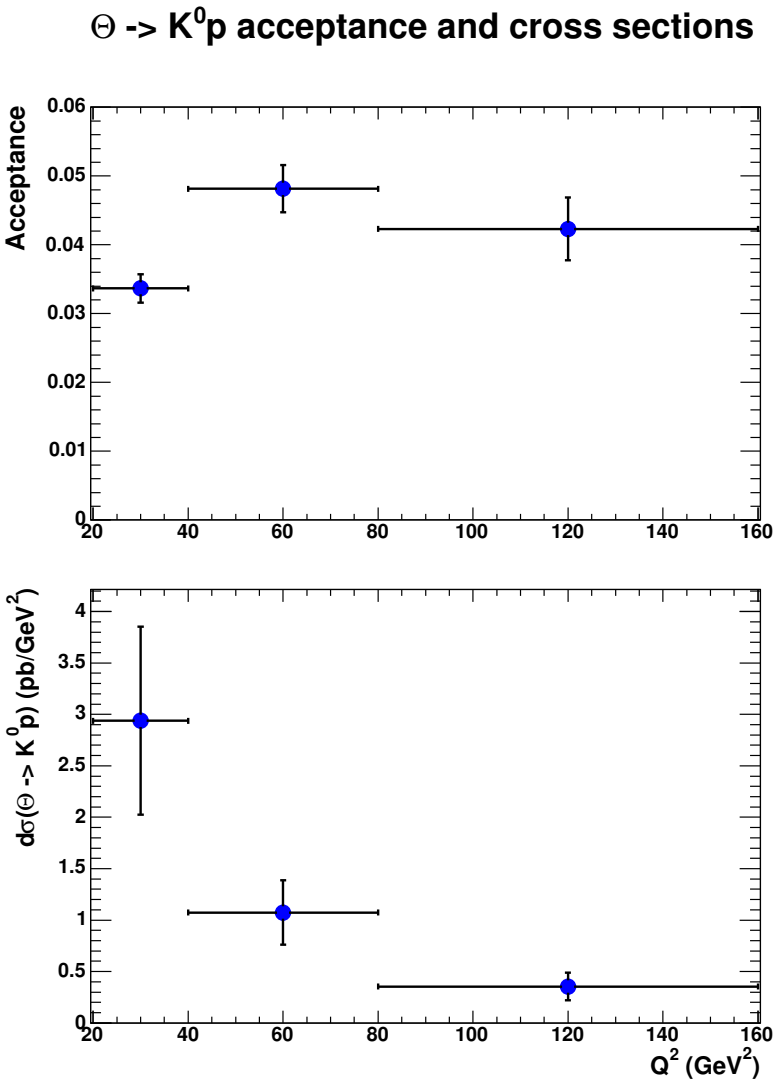

Figure 8.2: Acceptance (top) and cross section (bottom) for $\Theta^+(\bar{\Theta}^-) \rightarrow K^0 p(\bar{p})$ measured in the kinematic region given by $0.04 < y < 0.95$, $p_{\mathrm{T}} > 0.5$ GeV and $|\eta| < 1.5$ for bins of $20 < Q^2 < 40$ GeV^2, $40 < Q^2 < 80$ GeV^2 and $80 < Q^2 < 160$ GeV^2. The horizontal bars in the figure represent the binwidths.

8.6 Λ acceptance and cross section

dE/dx method

The cross section for $\Lambda \rightarrow p\pi$ (and their antiparticles) was measured in the same kinematic region of $p_T > 0.5$ GeV, $|\eta| < 1.5$ and $0.04 < y < 0.95$ for (a) 20

$< Q^2 < 40$ GeV^2, (b) $40 < Q^2 < 80$ GeV^2 and (c) $80 < Q^2 < 160$ GeV^2.

Figure 8.3 shows the $p\pi$ invariant-mass in the three Q^2 bins in data on the left and in MC on the right. For both data and MC, a single-Gaussian fit was used with a second-order polynomial function for the description of the background. The solid line is the result of this fit and the dotted line, the background according to this fit. The background is large, since *no* vertexing information is required for these tracks as the idea is to separate the two means of Λ reconstruction as much as possible.

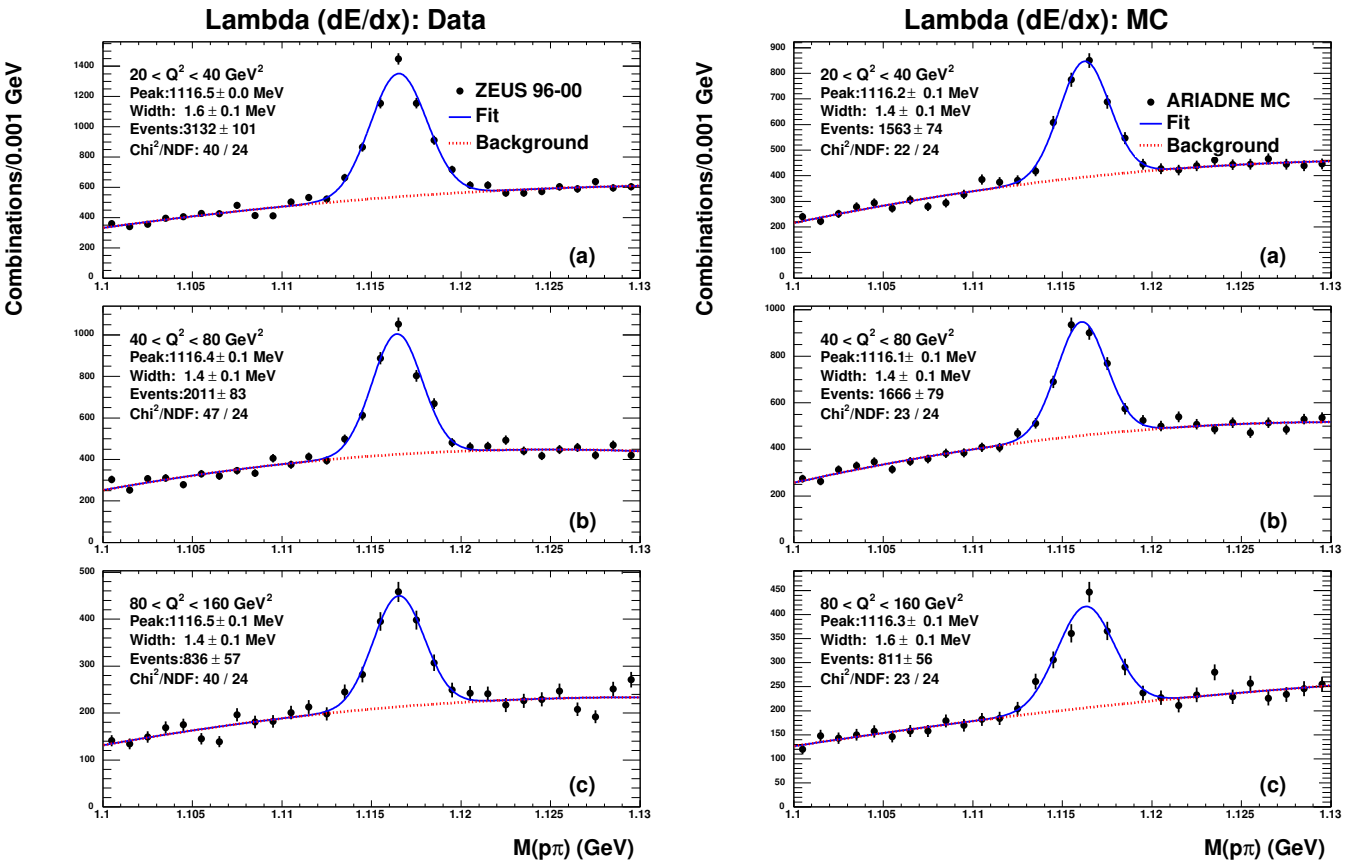

Figure 8.3: Invariant-mass spectra for pπ using dE/dx information in data (left) and in ARIADNE MC (right) for (a) $20 < Q^2 < 40$ GeV^2, (b) $40 < Q^2 < 80$ GeV^2 and (c) $80 < Q^2 < 160$ GeV^2. The solid line is the result of the fit to the data and MC. The dashed line shows the background component of the fits. (See text).

V0 method

The Λ acceptance and cross section for the same kinematic region are obtained again, but this time using the secondary-vertex information.

Figure 8.4 shows the $p\pi$ invariant-mass in the three Q^2 bins in data on the left and in MC on the right. For both data and MC, a single-Gaussian fit was used with a second-order polynomial function for the description of the background. The solid line is the result of this fit and the dotted line, the background according to this fit. The background is much lower compared to that obtained using the dE/dx method.

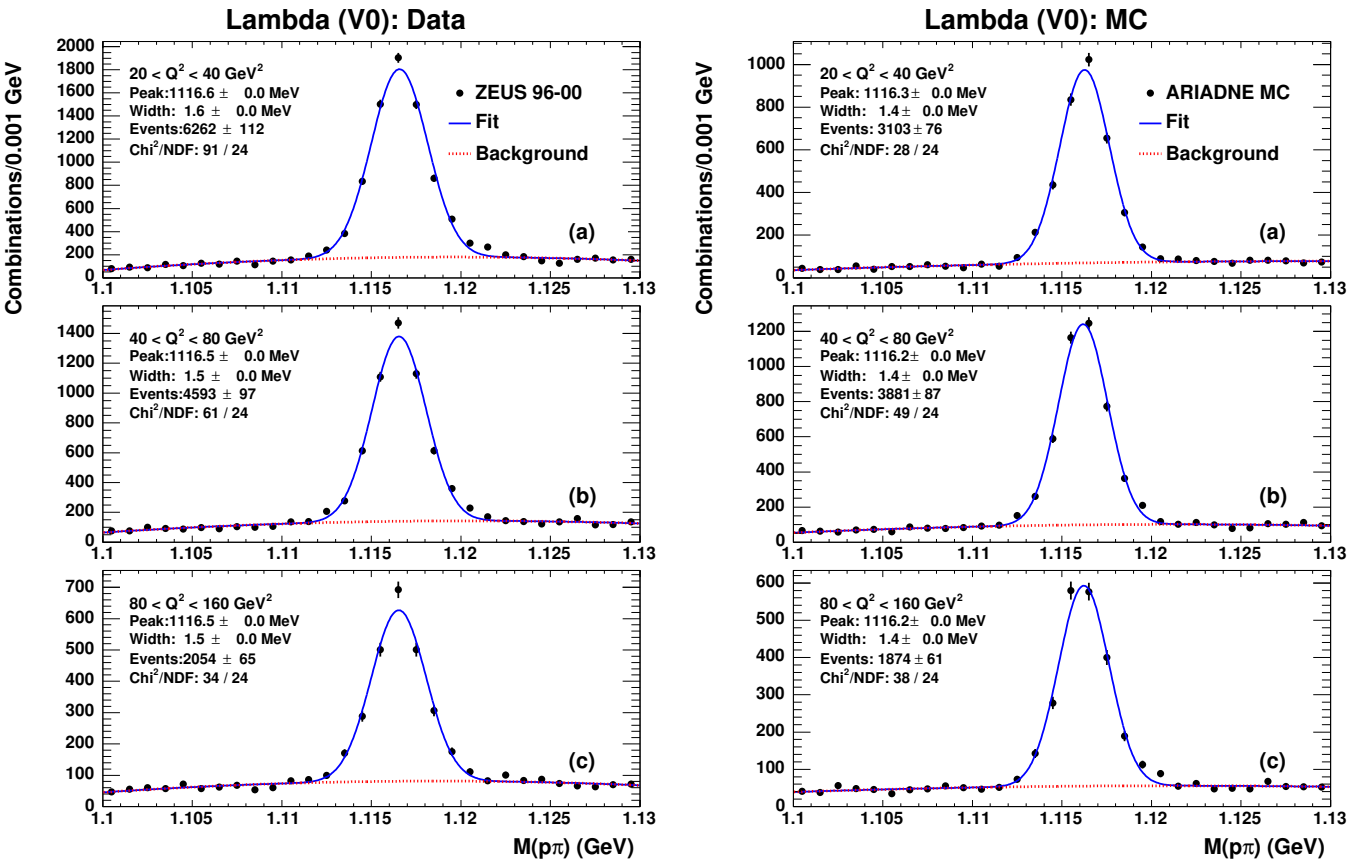

Figure 8.4: Invariant-mass spectra for pπ using V0's in data (left) and in ARIADNE MC (right) for (a) $20 < Q^2 < 40$ GeV^2, (b) $40 < Q^2 < 80$ GeV^2 and (c) $80 < Q^2 < 160$ GeV^2. The solid line is the result of the fit to the data and MC. The dashed line shows the background component of the fits. (See text).

Comparison between dE/dx and V0 Λ

The top part of figure 8.5 shows the detector acceptances and the bottom figure, the cross sections for Λ-baryons with both the dE/dx and the V0 methods. Once again, the results are plotted at the bin centers and the horizontal bars in the figure represent the binwidths. The cross sections, listed in table 8.1, agree within 6% and this difference will be used in the estimation of the systematic uncertainty on the K^0_S reconstruction with the secondary-vertex information, since an independent check is not possible for K^0_S. For the calculation of the detector acceptance, the branching ratio of 63.9% was taken from the PDG.

The acceptance for Λ with the dE/dx (V0) method varies from 2% (4%) in the first bin to about 4% (9%) in the second two bins. In general, the detector acceptance is higher for V0 Λ's than it is for the dE/dx Λ's, on average, by about 72%. This can be understood by revisiting the definition of the acceptance. In this analysis, the detector acceptance is defined by the number of particles reconstructed in a given bin of Q^2, divided by those generated in the same bin. Since the two methods of Λ reconstruction use the same MC, the number of generated Λ's is the same for both. However, this is not the case for the number of reconstructed Λ's. The right side of figure 8.3 shows the number of Λ-baryons reconstructed with the dE/dx method, while the right side of figure 8.4 shows the same with the V0 method. The number of Λ-baryons reconstructed with the dE/dx method is less by about 60% than it is for the V0 Λ's, which, by definition, yields a lower acceptance.

The reason for reconstructing a lower number of Λ's with the dE/dx method is due to a combination of the lower cut on dE/dx and the upper cut on proton momentum for proton selection. These two cuts restrict the analysis to low-momentum protons, which the V0 method does not.

8.7 Θ^+/Λ cross-section ratio

The purpose of obtaining the Λ cross section was to compare Θ^+ production rate to that of an established baryon containing strangeness.

Figure 8.6 shows the ratio of the Θ^+ to the Λ cross sections for the same three bins in Q^2, plus the one for Q^2 of 2 to 20 GeV^2. The ratio, defined in the same kinematic region as above is:

$$\text{ratio} = \frac{\sigma(e^{\pm}p \to e^{\pm}\,\Theta^+ X \to e^{\pm}\,K^0 p(\bar{p})\,X)}{\sigma(e^{\pm}p \to e^{\pm}\Lambda X \to e^{\pm}p\pi X)}.$$

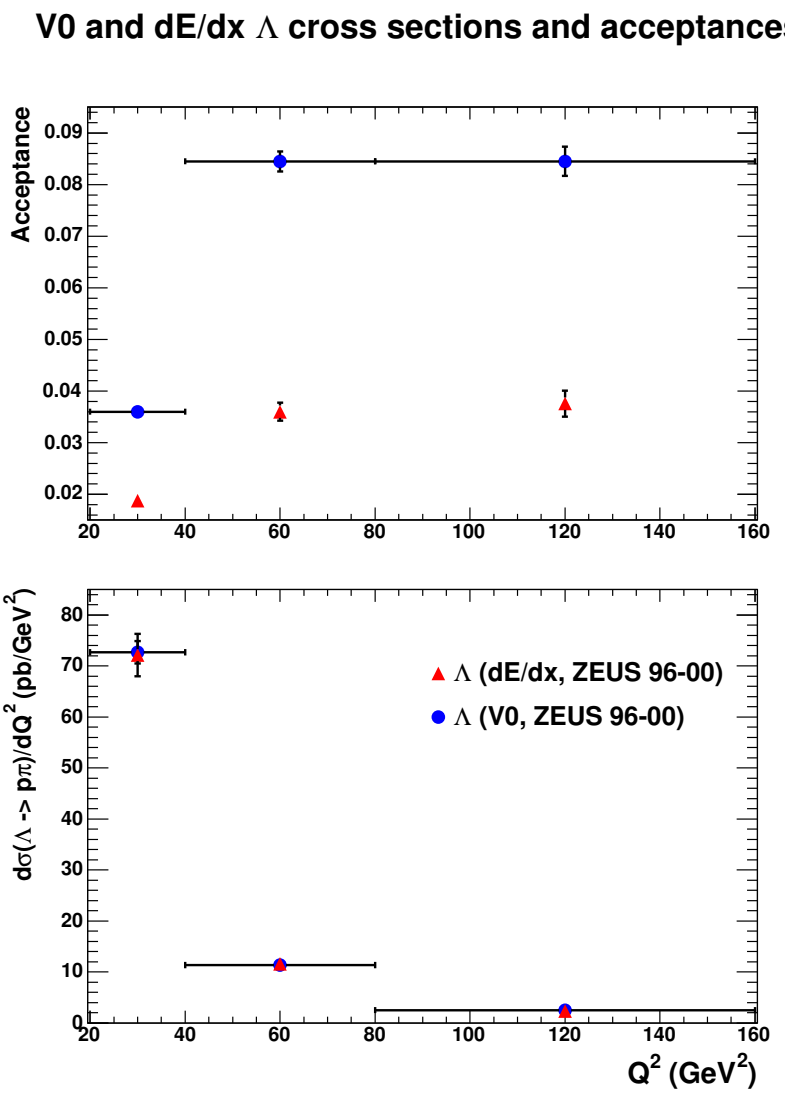

Figure 8.5: Acceptance (top) and cross-section (bottom) comparison for $\Lambda \to p\pi$ using V0's (circles) and dE/dx information (triangles). All measurements are in the kinematic region given by $0.04 < y < 0.95$, $p_{\mathrm{T}} > 0.5$ GeV and $|\eta| < 1.5$ for bins of $20 < Q^2 < 40$ GeV^2, $40 < Q^2 < 80$ GeV^2 and $80 < Q^2 < 160$ GeV^2. The horizontal bars in the figure represent the binwidths.

For the lowest bin in Q^2, the ratio is about $7 \pm 7\%$, consistent with zero. Additionally, within the large statistical errors, the distribution of the ratio seems

	Q^2 (GeV^2)	$\sigma(\Lambda \rightarrow p\pi)$ (pb/GeV^2)	Stat. Err.
dE/dx	20 - 40	72.146	$\pm$ 4.175
	40 - 80	11.578	$\pm$ 0.734
	80 - 160	2.363	$\pm$ 0.230
	$>$ 20	3192.9	$\pm$ 119.2
V0	20 - 40	72.683	$\pm$ 2.225
	40 - 80	11.349	$\pm$ 0.354
	80 - 160	2.512	$\pm$ 0.116
	$>$ 20	3383.8	$\pm$ 64.5

Table 8.1: Cross sections for Λ-baryons.

to be consistent with a constant, but a linearly rising function would fit it just as well. However higher statistical precision is needed to draw a definitive conclusion. Since the Θ^+ has another decay channel in addition to $\Theta^+(\bar{\Theta}^-) \rightarrow K^0 p(\bar{p})$, this ratio sets a lower limit on the production rate of the Θ^+ to that of the Λ-baryon. The same ratio, for $Q^2 > 20$ GeV^2, is 4.1 ± 0.9(stat.)%.

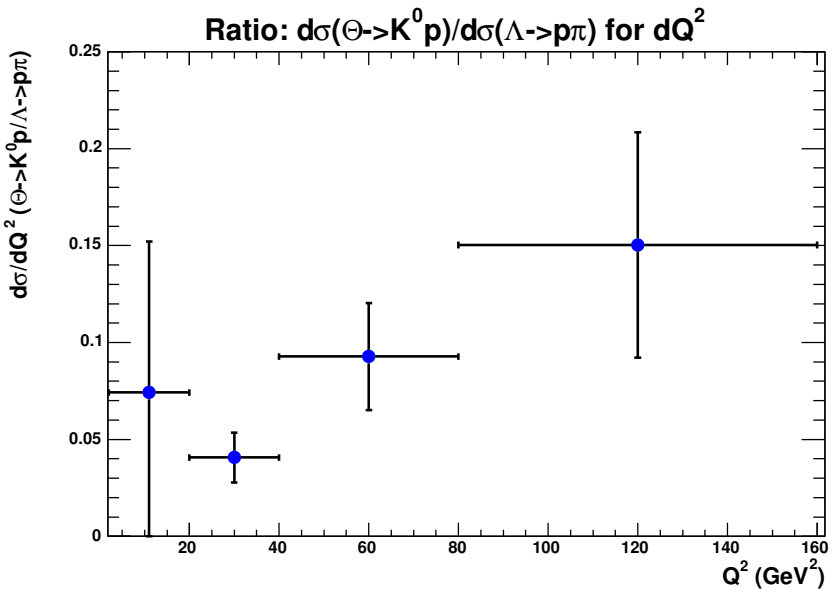

Figure 8.6: Ratio of the cross section for $\Theta^+ \rightarrow K^0 p$ to $\Lambda \rightarrow p\pi$ using dE/dx information, measured in the kinematic region given by $0.04 < y < 0.95$, $p_{\mathrm{T}} > 0.5$ GeV and $|\eta| < 1.5$ for bins of $2 < Q^2 < 20$ GeV^2, $20 < Q^2 < 40$ GeV^2, $40 < Q^2 < 80$ GeV^2 and $80 < Q^2 < 160$ GeV^2.

8.8 Systematic uncertainties

The nominal cross section, defined earlier, has been calculated using the detector-level event-selection criteria described in section 8.2. In order to estimate the sensitivity of the measured cross section and cross-section ratio to changes in the selection criteria and the method used to extract the cross section, to migrations across the kinematic boundaries and to the modelling of the data, several systematic checks and additional consistency checks have been performed.

The systematic uncertainties in this analysis can be divided into three categories:

- Uncertainties in the event selection, which should affect both the Θ^+ and Λ cross sections identically -

  e.g.: DIS cuts;

- Uncertainties in Θ^+ or Λ reconstruction, which may or may not affect their respective cross sections identically, but should partially cancel in the ratio of the cross sections -

  e.g.: dE/dx and proton momentum cuts;

- Uncertainties in Θ^+ reconstruction and signal extraction, affecting the Θ^+ cross section only -

  e.g.: secondary vertexing for K^0_S; the assumption of the background shape and of the width of the signal.

Below is a list of the systematic uncertainties on the measured cross section calculated for the three different bins in Q^2. The systematic uncertainty for the lowest bin, for Q^2 of 2 to 20 GeV^2 is not calculated since within the sizable statistical uncertainty, no signal is observed. The uncertainties were determined by changing the selection cuts as described above. The range in the uncertainty over the three bins is given in parentheses:

- Uncertainties in the event selection: the DIS-selection requirements ($y_{\rm JB}$, $y_{\rm el}$, $E_{\rm el}$, δ and the vertex position) were raised and lowered by about 10% from their nominal values and were found to have a negligible effect on the final cross sections for both Θ^+ and Λ;

- Uncertainties related to both Θ^+ and Λ reconstruction: The dE/dx cut was increased to 1.2 mips (Θ^+: $-19\% \rightarrow +11\%$, Λ: $+3\% \rightarrow +8\%$). The maximum momentum of protons was increased to 1.7 GeV (Θ^+: $-10\% \rightarrow +4.9\%$, Λ:$+7\% \rightarrow +10\%$).

- Uncertainties related to the Θ^+ reconstruction: The width of the Gaussian distribution was fixed ($-1\% \rightarrow -4\%$). The double Gaussian fit was replaced by a single Gaussian fit ($-26 \rightarrow -49\%$). The Λ cross section was reconstructed using the secondary vertex algorithm. The difference between Λ cross sections obtained using the dE/dx and the secondary-vertex methods was included in the Θ^+ cross section ($-2\% \rightarrow 6\%$).

Lastly, as a check on the reconstruction of Q^2, the electron method was replaced by the double angle method ($-4\% \rightarrow -14\%$).

As can be expected, the most significant errors arise from the assumption of the background shape for the Θ^+ (i.e. changing the fit to include one Gaussian versus two). All the other errors in addition are insignificant in comparison. It is for this reason that the normalization uncertainties due to the luminosity measurement error, and those due to the Λ and K^0_S decay branching ratios were not included in the systematic uncertainties. Also not included is the systematic uncertainty on the reconstruction of Q^2 as that test served more as check.

Since the exact correlation between the errors has not been evaluated here, they are assumed to be uncorrelated. Hence the above uncertainties are added in quadrature. While this is the safer approach, it can, however, over-estimate the error. Figure 8.7 shows the cross section for Θ^+ and associated uncertainties. The thicker bars in the figure indicate the systematic uncertainty and the thinner, the total error. Table 8.2 summarizes the Θ^+ cross sections for the different values of Q^2. Finally, figure 8.8 shows the ratio of the two cross sections and its associated

Q^2 (GeV^2)	$\sigma(\Theta^+(\bar{\Theta}^-) \rightarrow K^0 p(\bar{p}))$ (pb/GeV^2)	Stat. Err.	Syst. Err
20 - 40	2.938	$\pm$0.913	+0.221, -0.960
40 - 80	1.074	$\pm$0.313	+0.015, -0.574
80 - 160	0.355	$\pm$0.133	+0.075, -0.121
> 20	130.0	$\pm$ 26.9	

Table 8.2: Cross sections for Θ^+-baryons and associated uncertainties.

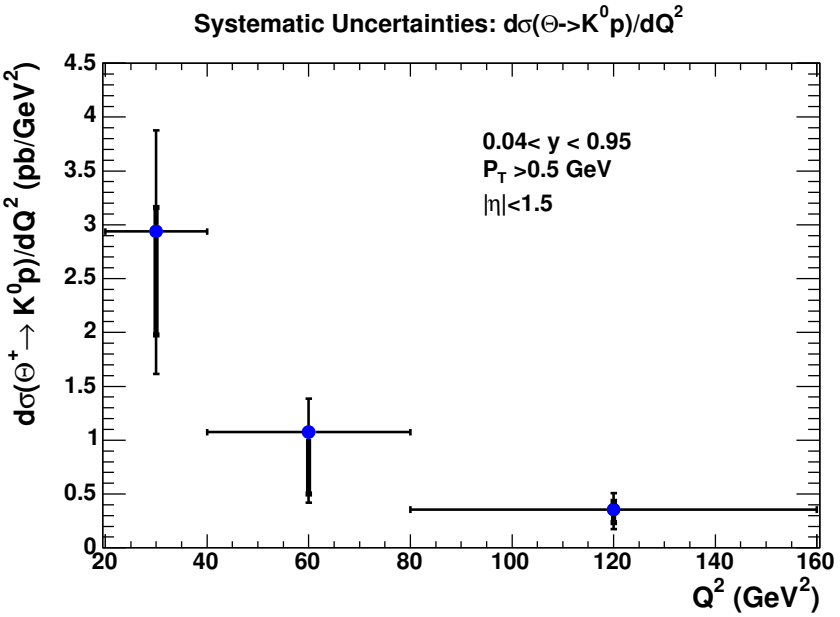

Figure 8.7: The cross section for $\Theta^+(\bar{\Theta}^-) \to K^0 p(\bar{p})$ and associated uncertainty, measured in the kinematic region given by $0.04 < y < 0.95$, $p_{\mathrm{T}} > 0.5$ GeV and $|\eta| < 1.5$ for (a) $20 < Q^2 < 40$ GeV^2, (b) $40 < Q^2 < 80$ GeV^2 and (c) $80 < Q^2 < 160$ GeV^2.

uncertainty. The thicker bars indicate the systematic error. The thinner, the total error.

Once again, the dominant error arises from the assumption of the background shape for the 1522 MeV signal.

8.9 Summary

The total and differential cross sections for the Θ^+-baryons and their antiparticles were measured and are listed in table 8.2. The kinematic region for this measurement is given by $0.04 < y < 0.95$, $p_T > 0.5$ GeV and $|\eta| < 1.5$ with (a) $20 < Q^2 < 40$ GeV^2, (b) $40 < Q^2 < 80$ GeV^2 and (c) $80 < Q^2 < 160$ GeV^2. The acceptance for Θ^+ varies between 3 - 5%, the lowest value being in the first Q^2 bin.

The total and differential cross sections for the Λ-baryons and their antiparticles were also measured in the same kinematic range via both the secondary vertexing and dE/dx information and are given in table 8.1. The

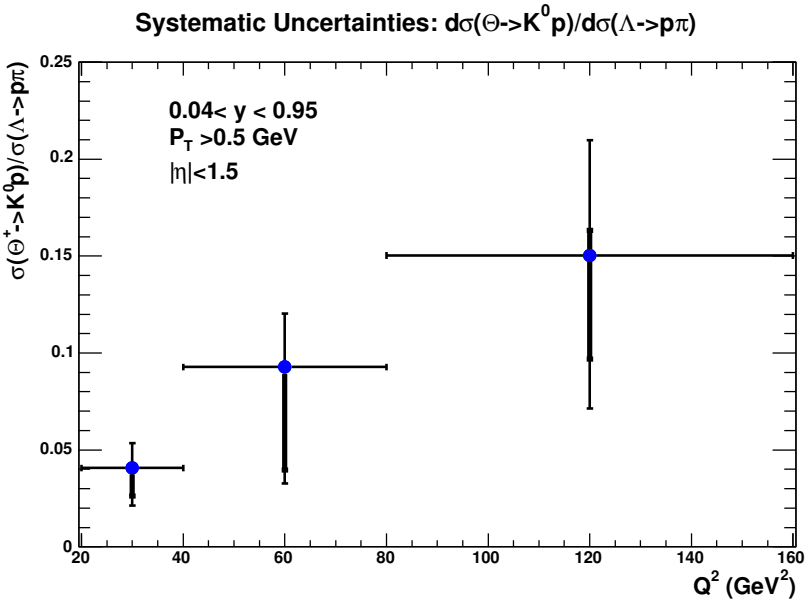

Figure 8.8: Ratio of the cross section for $\Theta^+ \to K^0 p$ to $\Lambda \to p\pi$ and associated uncertainty, measured in the kinematic region given by $0.04 < y < 0.95$, $p_{\mathrm{T}} > 0.5$ GeV and $|\eta| < 1.5$ for bins of $20 < Q^2 < 40$ GeV^2, $40 < Q^2 < 80$ GeV^2 and $80 < Q^2 < 160$ GeV^2.

two methods yield cross section results that are within about 6% of each other, however the detector acceptance with the two methods is not equal. On average, the acceptance is about 72% lower for the dE/dx method than it is for the V0 method. The number of reconstructed lambdas is lower by about 60% with the dE/dx method as compared to the V0 method. The potential reasons for this difference are explained in section 8.6.

The ratio of the Θ^+ to the Λ cross section for the same three bins in Q^2 is shown in figure 8.8. The ratio varies between 4% (lowest Q^2 bin) to 15% (highest Q^2 bin). The ratio for $Q^2 < 20$ GeV^2 is about 7 ± 7%, consistent with zero. Within the large uncertainties, the distribution of the ratio seems to be consistent with a constant; however, the ratio could also be rising with Q^2. In order to draw a definitive conclusion, higher statistical precision is needed. The overall ratio for $Q^2 > 20$ GeV^2 is about 4.1 ± 0.8 (stat.)%.

Since the Θ^+ has another decay channel in addition to $\Theta^+ \to K^0 p$, namely that of $\Theta^+ \to nK^+$, the above ratio sets a lower limit on the production rate of the Θ^+ to that of the Λ-baryon. If the branching ratios for the two channels are

assumed to be equal, then the total Θ^+ cross-section ratio is doubled.

Finally, the detector acceptance for Θ^+ for $Q^2 < 20$ GeV^2 is only $0.5 \pm .03\%$ compared to 4% for $Q^2 > 20$ GeV^2. This rather low acceptance means that there is low sensitivity in the low Q^2 region. Hence a Θ^+ signal cannot be excluded in this region. However, it is possible that the suppression of the signal may also be related to the unknown production mechanism of the signal.

Summary and discussion

Interest in light-hadron spectroscopy has been revived recently by the observation of baryonic resonances compatible with the theoretical prediction of pentaquarks, i.e. a bound state of four quarks and an antiquark. Although almost all known hadrons can be interpreted in terms of baryons or mesons or bound states of qqq or $q\bar{q}$, respectively, the theory of Quantum Chromodynamics does not exclude the existence of other color-neutral quark combinations such as tetraquarks ($qq\bar{q}\bar{q}$), pentaquarks ($qqqq\bar{q}$), etc., or states including gluons such as glueballs (gg) or hybrids ($q\bar{q}g$).

While several models allowing such multi-quark bound states exist on the market, it was the work of Diakonov, Petrov and Polyakov, in which they provide quantitative predictions for the Θ^+, a bound state of $uudd\bar{s}$, that has generated all the recent interest [46].

A narrow baryonic state decaying to $K^0_S p(\bar{p})$

This thesis has presented a search for such a resonant state in the $K^0_S p(\bar{p})$ invariant-mass spectrum. The data was collected with the ZEUS detector at HERA and correspond to an integrated luminosity of 121 pb^{-1}. The analysis was performed in the central rapidity region of inclusive deep inelastic scattering at an ep center-of-mass energy of 300-318 GeV for exchanged photon virtuality, $Q^2 > 2$ GeV^2.

The charged tracks were selected in the CTD with $p_T > 0.15$ GeV and $|\eta| < 1.75$, restricting this study to a region where the CTD track acceptance and resolution are high. The K^0_S and Λ[1] hadrons were identified by their charged decay modes $K^0_S \to \pi^+\pi^-$ and $\Lambda(\bar{\Lambda}) \to p\pi^-(\bar{p}\pi^+)$. Pairs of oppositely charged tracks, measured by the CTD and assigned to a displaced secondary vertex, were

[1]The nominal Λ sample includes $\bar{\Lambda}$.

combined to form $K^0_S(\Lambda)$ candidates and the tracks were assigned the mass of the charged pion (charged pion and proton). The number of K^0_S with $p_T(K^0_S)$ > 0.3 GeV and $|\eta(K^0_S)| < 1.5$ was 270K. Λ's were reconstructed so that the Θ^+ production rate could be compared to that of the Λ, which is a well-established baryon containing strangeness.

The (anti)proton-candidates were selected via the energy-loss measurement, dE/dx, in the CTD. The $K^0_S p(\bar{p})$ invariant mass was obtained by combining K^0_S candidates with candidates from the $p(\bar{p})$ dE/dx band. The CTD resolution for the $K^0_S p(\bar{p})$ invariant-mass, near 1530 MeV, was estimated from Monte-Carlo simulations to be 2.7 ± 0.1 MeV for both the $K^0_S p$ and the $K^0_S \bar{p}$ channels.

Peak parameters

The results presented in this thesis support the existence of the Θ^+ state. A narrow resonance is seen in the $K^0_S p(\bar{p})$ invariant-mass spectrum in the kinematic region of $Q^2 > 20$ GeV^2. The peak position, determined from a fit to the mass distribution, is 1521.5 ± 1.6(stat.) $^{+2.1}_{-2.6}$(syst.) MeV. It agrees well with the measurements by SVD, HERMES and COSY-TOF for the same decay channel [10–12], but is lower than the mass measurements from experiments reconstructing the K^+n decay channel [4–7].

The measured Gaussian width is $\sigma = 6.9 \pm 1.4$(stat.) $^{+2.4}_{-2.0}$(syst.) MeV, which is slightly above, but consistent with the experimental resolution. If the width of the Gaussian is fixed to this experimental resolution, the extracted Breit-Wigner width is $\Gamma = 4.1 \pm 3.2$(stat.) MeV. The number of events ascribed to the signal by the same fit is 217 ± 45. The statistical significance, estimated from the number of events assigned to the signal by the fit, varies between 3.5σ and 4.8σ, depending on the assumption of the background shape. An enhancement near 1465 MeV, which can be described by a second Gaussian function, can either be attributed to another, broader resonance such as $\Sigma(1480)$ [44], or can be regarded as the empirical parametrization of a more complicated background shape. A fit where the second Gaussian is excluded yields almost identical results, indicating robustness of the peak against the choice of background function. However this fit yields a slightly worse χ^2/NDF.

Several cross checks were made in order to validate the particle identification, to study possible reflections from known states and to verify the robustness of the peak. The 1522 MeV peak passes all the checks.

$\bar{\Theta}^-$: Antipentaquark?

The first Θ^+ observations were made by fixed-target experiments at low center-of-mass energies where valence quarks from the target nucleons can easily take part in the pentaquark final state. The analysis presented in this thesis investigates Θ^+ production at a much higher center-of-mass energy of 300–318 GeV. In this kinematic region, hadrons are mainly produced from the fragmentation of a sea quark or antiquark in the proton struck by the photon. Hence, hadrons and their antiparticles are produced in approximately equal proportions as was seen from the Λ studies presented in this thesis. Therefore, in addition to the uudd$\bar{\text{s}}$ states seen by fixed-target experiments, ZEUS is also able to search for the $\bar{\Theta}^-$ state with quark content $\bar{\text{u}}\bar{\text{u}}\bar{\text{d}}\bar{\text{d}}$s. To this end, the invariant-mass spectra of $K^0_S p$ and $K^0_S \bar{p}$ were searched independently. An enhancement was also seen in the $K^0_S \bar{p}$ channel. The number of events ascribed to the signal by the same fit described above is 75 ± 40. If the $K^0_S p$ signal is interpreted as a pentaquark, then the measurement of the slight enhancement in the $K^0_S \bar{p}$ channel may be the first evidence for its antiparticle, the $\bar{\Theta}^-$. (The number of $K^0_S p$ events ascribed to the signal by the fit is 149 ± 38).

Θ^+: Isotensor?

If an isotensor state is responsible for the Θ^+ signal, its isotensor partner, the Θ^{++}, might be expected in the $K^+ p$ spectrum. Furthermore, a way to check the efficiencies and resolutions is via the reconstruction of the well-established $\Lambda(1520)D_{03}$ meson in its charged Kp decay mode. To this end, the $K^{\mp} p$ and $K^{\pm}\bar{p}$ invariant-mass spectra were investigated for $Q^2 > 1$ GeV^2. The proton and charged kaon candidates were identified using the dE/dx information as before. No peak is observed near 1522 MeV in the $K^+ p(K^- \bar{p})$ spectra, while a clean signal is seen in the $K^- p(K^+ \bar{\text{p}})$ channel at 1518.5 ± 0.6(stat.) MeV, corresponding to the $\Lambda(1520)D_{03}$ state. The fact that both mass and width are in good agreement with the PDG values verifies that there are no significant reconstruction biases in the pentaquark mass range. Also, the absence of a peak in the like-sign spectrum disfavors the isotensor interpretation of the Θ^+ state [111].

η dependence of Θ^+ production

Assuming the Θ^+ is produced in fragmentation, one would expect an equal number of pentaquarks and their antiparticles. However, if the production of

Θ^+ is somehow related to the proton-remnant and the net baryon number from the proton beam, the Θ^+ should be best seen in the forward region of the detector and the signal from $\bar{\Theta}^-$ should be suppressed compared to that from Θ^+ [109]. Hence the $K^0_S p$ and $K^0_S \bar{p}$ invariant-mass spectra were investigated separately and in different regions of pseudorapidity. The Θ^+ signal was observed to come predominantly from protons in the forward region, which does not support the assumption that the production is via fragmentation of sea quarks. Instead it raises the question whether Θ^+ production might have some connection with the valence quarks or the proton-remnant. However, higher statistical precision is necessary in order to draw a stronger conclusion.

Θ^+ acceptance and cross section

Also reported in this thesis are cross-section measurements for Θ^+ production and decay. With the assumption that the signal is real, the cross section for $\Theta^+(\bar{\Theta}^-)$ $\rightarrow K^0 p(\bar{p})$ was measured in the kinematic region, defined by $0.04 < y < 0.95$, $p_T > 0.5$ GeV and $|\eta| < 1.5$. The branching ratio for $K^0 \rightarrow K^0_S \rightarrow \pi^+\pi^-$ was taken from the PDG. The number of reconstructed Θ^+ events was determined using the fit described above.

The acceptance for Θ^+ was calculated using the RAPGAP model, whereby Σ^+-baryons were assumed to have the same production and decay characteristics as the Θ^+-baryons. The modified Σ^+-baryons were assumed to have a zero natural-width and a mass of 1522 MeV and were forced to decay, with 100% branching ratio, to the $K^0 p(\bar{p})$ final state. Hence it is important to bear in mind, that the usage of the above MC for the detector acceptance and cross-section extraction for the Θ^+ particle means that the results have to be treated with caution. These results are valid as long as the assumption that Θ^+ is similar to Σ-baryons holds.

For $Q^2 > 20$ GeV^2, the acceptance for the Θ^+ was found to be about 4% and the overall cross section, $e^\pm p \rightarrow e^\pm \Theta^+ X \rightarrow e^\pm K^0 p X = 130 \pm 26.9(\text{stat.})$ pb. Lastly, the differential cross section, $d\sigma/dQ^2$, for $Q^2 > 20$ GeV^2 was presented and can be found in chapter 8.

Low Θ^+ acceptance for $Q^2 < 20$ GeV^2

For Q^2 below 20 GeV^2, the acceptance for the Θ^+ was found to be 0.5%, compared to 4% for Q^2 above the same value. This rather low acceptance means that there is low sensitivity in the low Q^2 region. Hence a Θ^+ signal cannot be excluded in this region. However, it is possible that the suppression of the signal may also be related to its unknown production mechanism.

Θ^+/Λ cross section ratio

The $\Theta^+(\bar{\Theta}^-) \rightarrow K^0 p(\bar{p})$ cross section was compared to that of $\Lambda \rightarrow p\pi$, where the Λ-baryons were reconstructed via both the dE/dx and the secondary vertexing information. The latter method provides a cross check on the detector acceptance with the dE/dx method and a measure of the uncertainty on the K^0_S reconstruction. The number of reconstructed Λ-events was determined using a fit with one Gaussian and a second-order polynomial background function. The branching ratio for $\Lambda\rightarrow p\pi$ was taken from the PDG. For the acceptance for Λ-baryons, the ARIADNE model for fully inclusive DIS was used. The resulting values were 10% for the V0 method and 4% for the dE/dx method. The two methods yield cross section results that are within 6% of each other. This difference is taken into account in the calculation of the systematic uncertainty, which is presented in detail in the thesis.

The ratio of Θ^+/Λ production cross section, defined in the same kinematic region as above, is:

$$\text{ratio} = \frac{\sigma(e^{\pm}p \rightarrow e^{\pm}\,\Theta^+\,X \rightarrow e^{\pm}\,K^0 p\,X)}{\sigma(e^{\pm}p \rightarrow e^{\pm}\Lambda X)}.$$

For $Q^2 > 20$ GeV^2, this ratio varies between 4% and 15% as a function of Q^2. For $Q^2 < 20$ GeV^2, the same ratio is 7 ± 7%, which is consistent with zero.

Since the Θ^+ has another decay channel in addition to $\Theta^+ \rightarrow K^0 p$, namely that of $\Theta^+ \rightarrow nK^+$, the above ratio sets a lower limit on the production rate of the Θ^+ to that of the Λ-baryon. If the branching ratios for the two channels are assumed to be equal, then the total Θ^+ cross-section ratio is doubled.

Discussion and Outlook

More negative results for the Θ^+ have emerged during the writing of this thesis. The new results from the CLAS collaboration do not provide evidence for a Θ^+ signal in the $\gamma p \to nK^+K^0_S$ channel and are in direct contradiction to the SAPHIR result [7]. The H1 collaboration has also searched for a $\Theta^+(\bar{\Theta}^-)$ signal in the $K^0_S p(\bar{p})$ channel in a similar kinematic region to the analysis presented in this thesis. They set an upper limit on the cross section in the mass range of 1.48 to 1.7 GeV [28]. Interestingly, their base limit of about 45 pb becomes less stringent and rises to 75 - 120 pb by a positive fluctuation in the mass window of interest (1.52 - 1.54 GeV). This is not in contradiction with the results presented here. (It has to be noted that the H1 analysis utilizes an integrated luminosity of about 75 pb^{-1}, as compared to 121 pb^{-1} used in this analysis).

Low vs high-energy experiments...

Regarding the results presented in this thesis, several puzzles remain. Firstly, with the exception of the ZEUS result, all the positive results for Θ^+ are at relatively low energies, suggesting that exotic baryons may have production mechanisms that are different from those of conventional baryons, i.e. perhaps they are not produced in fragmentation?

The high-energy experiments that do not see the signal can be divided into two categories, e^+e^- and high-energy hadron-beam experiments. In the former reaction, the initial state has zero quark content. Θ^+ production requires 4 quarks and one antiquark, which means there need to be at least 5 quarks and 5 antiquarks in the final state. In e^+e^- collisions, the first $q\bar{q}$ pair is produced via e^+e^- annihilation, while the rest would have to be produced in fragmenation. A theoretical estimate by Y. Azimov [113] suggests that, for this reason, the BES result [19] is not likely to be sensitive enough to search for the Θ^+ from e^+e^- collisions. Also the BABAR collaboration see no evidence of the Θ^+ [21]. Furthermore, in spite of the large statistical precision, they see *no structure at all* in the $K^0_S p$ channel. Since the strangeness is unknown in this channel, some Σ^{*+} resonances are expected, for example the $\Sigma(1670)$, which has an estimated width of 60 MeV [44].

The same criticism applies for the high-energy hadron-beam experiments. For example, the HERA-B [25] experiment does not see evidence for the Θ^+ in the

reaction, $pC \to X(K^0_S\ p)$. However, they see no structure in the entire spectrum. Regarding the $p\bar{p}$ experiments, the main concern is the high track multiplicity resulting in a high combinatorial background.

Fluctuation?

So what is different about ZEUS? There are two possible answers. One is that the enhancement at 1522 MeV is a fluctuation. To this end, a number of MC experiments were carried out to ascertain the probability of the peak being a fluctuation. Depending on the assumption of the background shape, i.e, with or without the Gaussian function to describe the enhancement at 1465 MeV, the resulting probabilities were 6×10^{-6} and 6×10^{-5}, respectively. While the probability that the 1522 MeV peak is a random fluctuation is low, it is, however, not zero.

New Σ^{*+} resonance?

The other possibility is that the ZEUS result, presented in this thesis, could be a new resonance. Since the $K^0_S p(\bar{p})$ decay channel, analyzed here, cannot determine the strangeness of the state, there remains the possibility that the signal could be a new Σ^{*+} resonance. The low mass obtained by ZEUS is another puzzle. For the experiments that do see a Θ^+ signal, figure 2 in the introduction of this thesis shows the world average for peak positions. Intriguingly, the mass of the Θ^+ measured in the K^+n channel tends to be larger than that measured in the $K^0_S p$ channel. However, the ZEUS mass is significantly lower than all the rest. This raises the question as to whether ZEUS and the other experiments are measuring the same object.

To that end, the strangeness can perhaps be ascertained by requiring an additional $K^{\pm}$ in the final state. Since the initial ep state contains no strangeness, at least one more strange particle should be produced along with the Θ^+ in the final state in order to conserve strangeness. The knowledge of the strangeness of the accompanying particle would shed light on the strangeness of the K^0_S, and in turn, that of the Θ^+. However, in order to perform such a study, higher statistical precision is required.

In addition, higher statistics would also allow studies of the angular distributions which would shed light on the spin of this resonance.

HERA II

This analysis will benefit in the future from the high-luminosity running currently underway. So far, an integrated luminosity of over 160 pb^{-1} has been delivered during the HERA II data-taking period, already surpassing the HERA I dataset. In addition, the ZEUS detector has been upgraded with a new Silicon Microvertex Detector (MVD), which will provide improvements in vertex and tracking resolutions. According to one study [114], the primary vertex resolution with the MVD is improved by a factor of about 4 in x, 3 in y and 10 in z. These improved resolutions will reduce the uncertainties on the track positions close to the primary vertex. Furthermore, advances in the understanding of the dE/dx measurement and particle identification using the calorimeter should also improve the analysis in the future.

The experimental results on Θ^+ are controversial. There are about as many negative results as positive for its existence. As for the positive results, while a kinematic reflection or a cusp effect could affect one reaction channel, it would be difficult to find a mechanism that could create a false peak in all cases. And if the Θ^+ exists, no reasonable theoretical prediction is available for the probability of its production. None of the models are able to convincingly explain, simultaneously, its low mass, narrow width and its production mechanism. Hence the proof of its existence is an experimental issue, requiring high-statistics experiments. Finally, if the Θ^+ is confirmed, then a new landscape of multi-quark hadrons will have emerged. Hence the search is indeed worth the effort!

Appendix A

ZEUS vertex reconstruction

A.1 Primary vertex reconstruction

The vertex fit mathematics employed in VCTRAK is detailed in reference [90]. As has been mentioned in chapter 4, VCTRAK provides two methods of fitting a set of N tracks to a vertex.

A.1.1 Simple vertex fit

This method is crude and does not solve for the track parameters refitted to the vertex, just the 3 parameters of the vertex position $\vec{V} = (V_x, V_y, V_z)$. The simple vertex fit can be considered as a "vertex pattern recognition tool", whose output can be used a in full vertex fit.

A.1.2 Full vertex fit

The full vertex fit solves for the $3+3N$ parameters consisting of the vertex position $\vec{V}$ and 3 parameters for each track, θ, ϕ and Q/R calculated at the vertex.

A.2 Secondary vertex reconstruction

The VCTRAK output track helices can be used directly to identify secondary vertices. The multiple vertex mode implemented in VCTRAK is significantly more complicated than the so-called VFIND method, however the two methods are similar in many aspects and achieve the same results [100]. Hence a brief outline of the VFIND algorithm is described here.

A.2.1 VFIND

The VCTRAK output track helices can be used directly to identify secondary vertices. The simplest method involves testing each pair of tracks and testing for intersection in the $x-y$ plane, then checking the separation in z at this point. Given two tracks (labelled 1 and 2) as parameterized in chapter 4, the center of curvature of each track can be calculated according to:

$$X_{C_i} = (R_i + D_{H_i})\ sin\phi_{H_i} \quad (A.1)$$
$$Y_{C_i} = -(R_i + D_{H_i})\ cos\phi_{H_i}\ , \quad (A.2)$$

where the subscript i indicates track 1 or 2. The distance (D) and the angle (β_i) between the two track centers can be simply calculated from the previous equation. Two tracks in the $x-y$ plane do not intersect if:

$$D > R_1 + R_2 \quad (A.3)$$
$$R_1 > D + R_2 \quad (A.4)$$
$$R_2 > D + R_1\ , \quad (A.5)$$

and so can quickly be rejected. Figure A.1 shows an example where the two tracks do intersect in the $x-y$ plane and $D \neq R_1 + R_2$ (so there are two distinct solutions.) The angle subtended by half of the chord joining the two track intersection candidates (α_i) is given by

$$sin\alpha_i = \frac{(R_1 + R_2 + D)(R_1 + R_2 - D)(R_2 + D - R_1)(R_1 + R_2 + D)}{(2DR_i)^2}\ . \quad (A.6)$$

The position of the secondary vertex candidates in the $x-y$ plane are then given by

$$X_{V_i} = X_{C_i} + R_i\ cos(\beta_i \pm \alpha_i) \quad (A.7)$$
$$Y_{V_i} = Y_{C_i} + R_i\ sin(\beta_i \pm \alpha_i)\ . \quad (A.8)$$

The azimuthal angle of the tangents to each track at the candidate vertices are

$$\phi_{i,1} = \beta_i \pm \alpha_i - 3\pi/2 \quad (A.9)$$
$$\phi_{i,2} = \beta_i \pm \alpha_i - \pi/2\ , \quad (A.10)$$

where the second subscript now corresponds to the track at vertex candidate i. The z position of the tracks at the candidate intersection point can be determined by the track path length in the x y plane given by

$$s_{i,j} = s(\phi_{i,j}) = -QR_j(\phi_{i,j} - \phi_{H_j}) \ , \tag{A.11}$$

and then using

$$Z_{V_{i,j}} = \frac{Z_{H_j} + s_i}{tan\ \theta_j} \ . \tag{A.12}$$

The difference between the Z_V position of two tracks at their apparent intersection ($\delta z_i = Z_{V_{i,1}} - Z_{V_{i,2}}$) in the $x - y$ plane can then be used to select events with good secondary vertex candidates. Intersections with δz below some cut (< 3 cm) are then considered two track secondary vertices.

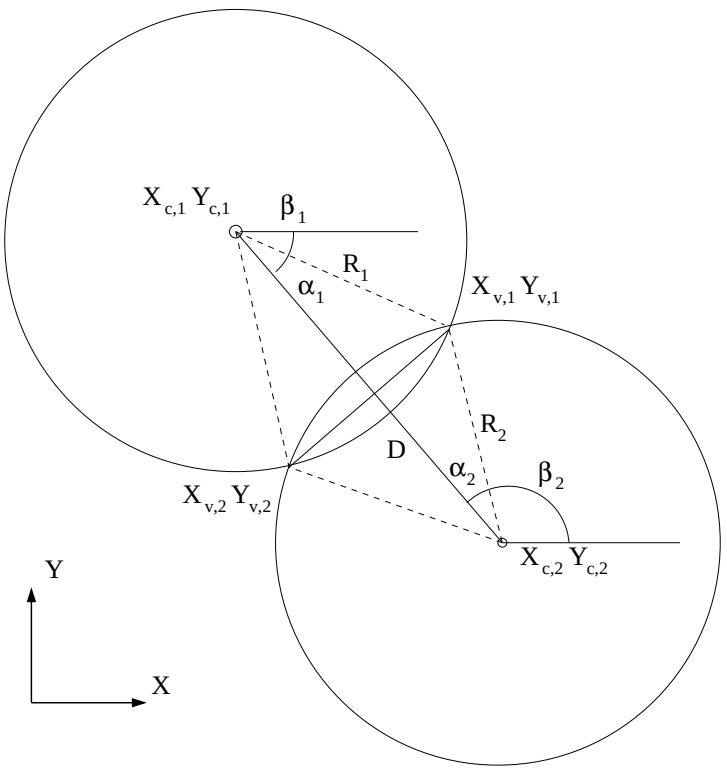

Figure A.1: Intersecting helical tracks in $x - y$ plane.

A.2.2 VCTRAK multivertex mode

The multiple vertex mode implemented in VCTRAK is significantly more complicated than the VFIND method described above, hence only a brief outline of the algorithm is described here

- Pairs of tracks are tested for intersection in $x-y$ plane and are kept if they pass loose cuts on δz and δr (the closest distance in the transverse plane), in much the same way as described for VFIND.
- The pairs of tracks are passed to the "simple vertex" fit to obtain a crude vertex position and χ^2 for the secondary vertex.
- The resulting simple two track vertices are then used as cluster sites for multiple vertex finding. The subsequent algorithm for assigning tracks to clusters is highly complicated and a keen reader is referred to [89]. Once tracks have been assigned (or not) to a cluster site, the full vertex fit is performed for all vertices.

Bibliography

[1] M. Peskin and D. Schroeder, *An Introduction of Quantum Field Theory*, Addison-Wesley (1995).

[2] www-zeus.desy.de/physics/sfew/PUBLIC/sfew_results/preliminary/moriond04/zeush1.php.

[3] J. Dudek, *Phenomenology of exotic hadrons - hybrid mesons and pentaquarks*, Ph.D. thesis, Univ. of Oxford (2004).

[4] LEPS Collaboration, T. Nakano *et al.*, Phys. Rev. Lett. **91**, 012002 (2003).

[5] CLAS Collaboration, V. Kubarovsky *et al.*, Phys. Rev. Lett. **91**, 252001 (2003).

[6] CLAS Collaboration, V. Kubarovsky *et al.*, Phys. Rev. Lett. **92**, 032001 (2004). Erratum; ibid, 049902.

[7] SAPHIR Collaboration, J. Barth *et al.*, Phys. Lett. **B572**, 127 (2003).

[8] DIANA Collaboration, V.V. Barmin *et al.*, Phys. Atom. Nucl. **66**, 1715 (2003).

[9] A.E. Asratyan, A.G. Dolgolenko and M.A. Kubantsev, Phys. Atom. Nucl. **67**, 682 (2004); Yad. Fiz. **67**, 704 (2004); hep-ex/0309042.

[10] SVD Collaboration, A. Aleev *et al.*, Submitted to Yad. Fiz. (2004); hep-ex/0401024.

[11] HERMES Collaboration, A. Airapetian *et al.*, Phys. Lett. **B585**, 213 (2004).

[12] COSY-TOF Collaboration, M. Abdel-Bary *et al.*, Phys. Lett. **B595**, 127 (2004).

[13] COSY-TOF Collaboration, P. Aslanyan, V. Emelyanenko and G. Rikhkvitzkaya, hep-ex/0403044 (2004).

[14] ZEUS Collaboration, S. Chekanov *et al.*, Phys. Lett. **B591**, 7 (2004).

[15] NA49 Collaboration, C. Alt *et al.*, Phys. Rev. Lett. **B92**, 042003 (2004).

[16] H1 Collaboration, A. Aktas *et al.*, Phys. Lett. **B588**, 17 (2004).

[17] Belle Collaboration, S.K. Choi *et al.*, Phys. Rev. Lett. **91**, 262001 (2003); CDF Collaboration, D. Acosta *et al.*, Phys. Rev. Lett. **93**, 072001 (2004); Babar Collaboration, B. Aubert *et al.*, Phys. Rev. Lett. **93**, 041801 (2004); D0 Collaboration, V.M. Abazov *et al.*, Phys. Rev. Lett. **93**, 162002 (2004).

[18] Selex Collaboration, A.V. Evdokimov *et al.*, Phys. Rev. Lett. **93**, 242001 (2004).

[19] BES Collaboration, J. Z. Bai *et al.*, Phys. Rev. **D70**, 012004 (2004); hep-ex/0402012.

[20] BELLE Collaboration, K. Abe *et al.*, *Study of the baryon-antibaryon low-mass enhancements in charmless three-body baryonic B decays*, Contributed paper to 32nd International Conference on High-Energy Physics, Beijing (2004); hep-ex/0409010.

[21] BABAR Collaboration, B. Aubert *et al.*, *Search for strange pentaquark production in e^+e^- annihilations at S**(1/2) = 10.58-GeV and in Upsilon(4S) decays*, Contributed paper to 32nd International Conference on High-Energy Physics, Beijing (2004); hep-ex/0408064.

[22] ALEPH Collaboration, S. Schael *et al.*, Phys. Lett. **B599**, 1 (2004).

[23] I. Kravchenko on behalf of the CDF Collaboration, *Pentaquarks and the X(3872) results from CDF*, Contributed paper to the 32nd International Conference on High-Energy Physics, Beijing (2004).

[24] HyperCP Collaboration, M. J. Longo *et al.*, Phys. Rev. **D70**, 111101 (2004); hep-ex/0410027.

[25] HERA-B Collaboration, I. Abt *et al.*, Phys. Rev. Lett. **93**, 212003 (2004).

[26] C. Pinkenburg for the PHENIX Collaboration, J. Phys. **G30**, S1201 (2004); nucl-ex/0404001.

[27] R. De Vita, CLAS Collaboration, *Search for pentaquark at CLAS in photoproduction from proton*, American Physical Society Meeting, Florida, U.S.A. (2005)

[28] C. Risler, *H1 Search for a narrow baryonic resonance decaying to* $K^0_S p(\bar{p})$, XIII International Workshop on Deep Inelastic Scattering, Wisconsin, U.S.A. (2005).

[29] J. Ellis, Summary of the 32nd International Conference on High-Energy Physics, Beijing (2004); hep-ph/0409360.

[30] S. Chekanov *et al.*, ZEUS Collaboration, Phys. Lett. **B610**, 212-224 (2005).

[31] ZEUS Collaboration, S. Chekanov *et al.*, Eur. Phys. J. **C38**, 29-41 (2004); hep-ex/0409033.

[32] F. Halzen and A.D. Martin, *Quarks & Leptons*, J. Wiley and Sons (1984).

[33] M.Gell-Mann, Phys. Lett **8**, 214 (1964);
G.Zweig, CERN Rep. 8182/TH 401.

[34] For example, F.Halzen and A.D.Martin, *Quarks and Leptons*, Wiley (1984); D.Griffiths, *Introduction to Elementary Particles*, Wiley (1987).

[35] C.G. Callan and D. Gross, Phys. Rev. Lett. **22**, 156 (1969).

[36] T. Eichen *et al.*, Phys. Lett. **B46**, 274 (1973).

[37] TASSO Collaboration, R. Bradelik *et al.*, Phys. Lett. **B86**, 243 (1979).

[38] Y.L. Dokshitzer, Sov. Phys. JETP **46**, 641 (1977);
V.N. Gribov and L.N. Lipatov, Sov. J. Nucl. Phys. **15**, 438 (1972);
G. Altarelli and G. Parisi, Nucl. Phys. **B126**, 298 (1977).

[39] L.N. Lipatov, Sov. J. Nucl. Phys. **23**, 338 (1976);
E.A. Kuraev, L.N. Lipatov and V.S. Fadin, Sov. Phys. JETP **45**, 199 (1977);
Y.Y. Balitskii and L.N. Lipatov, Sov. J. Nucl. Phys. **28**, 822 (1978).

[40] M. Corradi, Summary of the Heavy Flavour Working Group, DIS, Wisconsin, U.S.A., 2005.

[41] B. Andersson, G. Gustafson, G. Ingelman and T. Sjöstrand, *Parton fragmentation and string dynamics*, Phys. Rep. **97**, 31 (1983).

[42] R.D. Field and S. Wolfram, A QCD model for e^+e^- annihilation, Nucl. Phys. **B213**, 65 (1983);
B.R. Webber, *A QCD model for jet fragmentation including soft gluon interference*, Nucl. Phys. **B238**, 492 (1984).

[43] Y. Azimov *et al.*, *The string effect and QCD coherence*, Phy. Lett. **B165**, 147 (1985);
G. Gustafson and U. Petterson, *Dipole formation of QCD cascades*, Nucl. Phys. **B306**, 746 (1988);
B. Andersson *et al*, *Coherence effects in deep inelastic scttering*, Z. Phys. **C 43**, 625 (1989).

[44] Particle Data Group, K. Hagiwara *et al.*, Phys. Rev. **D66**, 010001 (2002);
Particle Data Group, S.Eidelman *et al.*, Phys. Lett. **B592**, 1 (2004).

[45] R.L. Jaffe, Proc. Topical Conference on Baryon Resonances, Oxford, July 1976, SLAC-PUB-1774.

[46] D. Diakonov, V. Petrov, M.V. Polyakov, Z. Phys. **A359**, 305 (1997).

[47] R. Jaffe and F. Wilczek, Phys. Rev. Lett. **91**, 232003 (2003); hep-ph/0312369.

[48] F. Stancu and D. O. Riska, hep-ph/0307010;
A. Hosaka, hep-ph/0307232;
C. E. Carlson *et al.*, hep-ph/0312325;
Y. X. Liu, J. S. Li and C.G. Bao, hep-ph/0401197.

[49] M. Karliner, H.J. Lipkin, Phys. Lett. **B575**, 249 (2003); hep-ph/0307243.

[50] T. W. Chiu and T. H. Hsieh; hep-ph/0403020.

[51] Shi-Lin Zhu, Phys. Rev. Lett. **91**, 232002 (2003);
R. D. Matheus *et al.*, hep-ph/0309001;
J. Sugiyama *et al.*, hep-ph/0309271.

[52] F. Csikor *et al.*, hep-lat/0309090;
S. Sasaki, hep-lat/0310014.

[53] D. Diakonov, *From pions to pentaquarks*, hep-ph/0406043;
D. Diakonov, *Chiral symmetry and pentaquarks*, hep-ph/0412272;
D. Diakonov, *Chiral quark soliton model*, hep-ph/9802298.

[54] E. Klempt, Lectures given at 18th Annual Hampton University Graduate Studies (HUGS at JLab), Newport News, Virginia, hep-ph/0404270 and references therein (2003).

[55] M. Oka, Theoretical Overview of the Pentaquark Baryons, Prog. Theor. Phys. **112**, 1 (2004); hep-ph/0406211.

[56] Shi-Lin Zhu, AAPPS Bulletin **14N3**, 14 (2004).

[57] M. Chemtob, Nucl. Phys. **B256**, 600 (1985);
W. Walliser, Nucl. Phys. **A548**, 649 (1992).

[58] T.H.R. Skyrme, *A nonlinear field theory*, Proc. Roy. Soc. Lond. **A260**, 127 (1961).

[59] A. V. Manohar, Nucl. Phys. **B248**, 19 (1984).

[60] M. Praszalowicz, in *Skyrmions and Anomalies*, Eds. M. Jezabek, M. Praszalowicz, World Scientific (1987).

[61] R.L. Jaffe, Eur. Phys. J. **C35**, 221 (2004); hep-ph/0401187.

[62] D. Diakonov, V. Petrov, M.V. Polyakov, JLAB-THY-04-12, hep-ph/0404212 (2004).

[63] J. R. Ellis, M. Karliner and M. Praszalowicz, JHEP **0405**, 002 (2004); hep-ph/0401127.

[64] B. Jennings and K. Maltman, Phys. Rev. **D69**, 094020 (2004);
F.E. Close and J.J. Dudek, Phys. Lett. **B586**, 75-82 (2004);
D. Melikhov, S. Simula and B. Stech, Phys. Lett. **B594**, 265 (2004); hep-ph/0405037;
M. Karliner and H. J. Lipkin, Phys. Lett. **B586**, 303 (2004); hep-ph/0401072.

[65] *HERA: A Proposal for a large electron-proton colliding beam facility at DESY*, DESY-HERA-81/10, Hamburg (1981).

[66] *Proceedings of the 1995/96 Workshop on 'Future Physics at HERA'*, Eds. G. Ingelman, A. De Roeck, R. Klanner (1996);
The HERA Luminosity Upgrade, DESY-HERA-98/05, Ed. U. Schneekloth (1998).

[67] ZEUS Collaboration, *The ZEUS detector, Status Report 1993*; U. Holm ed. (1993).

[68] A. Andresen *et al.* (ZEUS calorimeter group), Nucl. Instr. and Meth. **A 309**, 101 (1991).

[69] M. Derrick *et al.*, Nucl. Instr. and Meth. **A309**, 77 (1991).

[70] A. Bernstein *et al.*, Nucl. Instr. and Meth. **A336**, 23 (1993).

[71] B. Foster *et al.*, Nucl. Instr. and Meth. **A338**, 254 (1994).

[72] B. West, *Charm and Virtual Photon at HERA and a Global Tracking Trigger for ZEUS*, Ph.D. thesis, Univ. College London (2001).

[73] R. Hall-Wilton *et al.*, Internal ZEUS-Note 99-024 (1999).

[74] A. Bamberger *et al.*, Nucl. Instr. and Meth. **A401**, 63-80 (1997).

[75] ZEUS Collaboration, J. Breitweg *et al.*, Phys. Lett. **B481**, 213 (2000);
ZEUS Collaboration, J. Breitweg *et al.*, Eur. Phys. J. **C18**, 625 (2001).

[76] H. Bethe and W. Heitler, Proc. Roy. Soc. **A146**, 83 (1934).

[77] K. Piorzkowski and M. Zachara, Internal ZEUS-Note 94-167 (1994).

[78] R.Brun; GEANT 3.13, CERN DD/EE/84-1 (1987).

[79] H. Spiesberger, *HERACLES and DJANGOH: Event generation for ep interactions at HERA including radiative processes* (1998), Available on WWW:http://www.desy.de/∼hspiesb/djangoh.html;
H. Spiesberger, *DJANGO6 version 2.4 - A Monte Carlo generator for deep inelastic lepton-proton scattering including QED and QCD radiative effects* (1996), Available on http://www.desy.de/∼hspiesb/django6.html.

[80] H. Spiesberger, *HERACLES. An event generator for ep interactions at HERA including radiative processes: version 4.6*, Available on http://www.desy.de/∼hspiesb/heracles.html;
A. Kwiatkowski, H. Spiesberger and H.-J. Möhring, *Comp. Phys. Commun.* **69**, 155 (1992).

[81] G. Ingelman, A. Edin and J. Rathsman, Comp. Phys. Commun. **101**, 108 (1997).

[82] L. Lönnblad, Comp. Phys. Commun. **71**, 15 (1992).

[83] T. Sjöstrand, Comp. Phys. Commun. **82**, 74 (1994).

[84] G. Marchesini, B. R. Webber, G. Abbiendi, I. G. Knowles, M. H. Seymour and L. Stanco, *HERWIG: A Monte Carlo event generator for simulating hadron emission reactions with interfering gluons - Version 5.1*, April 1991, Comput. Phys. Commun. 67 (1992) 465;
G. Corcella *et al.*, *HERWIG 6: An event generator for hadron emission reactions with interfering gluons (including supersymmetric processes)*, JHEP **0101**, 010 (2001).

[85] P. de Jung, *Status of the Uranium Calorimeter Reconstruction Software*, Internal ZEUS-Note 92-019 (1992).

[86] CTEQ Collaboration, H.L. Lai *et al.*, Eur. Phys. J. **C12**, 375 (2000).

[87] H. Jung, Comp. Phys. Comm. **86**, 147 (1995).

[88] H. Jung, *The RAPGAP Monte Carlo for Deep Inelastic Scattering version 2.08*, Available on http://www.quark.lu.se/∼hannes/rapgap.html.

[89] G.F. Hartner, *VCTRAK(3.07/04): Offine Output Information*, Internal ZEUS-Note 97-064 (1997);
G. F. Hartner, *VCTRAK Briefing: Program and Math*, Internal ZEUS-Note 98-058 (1998).

[90] P. Billoir and S. Qian, Nucl. Inst. Meth. **A311** (1992).

[91] P.S. Bailey, B. Foster, G.P. Heath *et al.*, The design and perfomance of the ZEUS central tracking detector z-by-Timing system. Nucl. Instrum. Methods **A396**, 320 (1997).

[92] A. Savin, *Study of calorimeter noise in the 1996 data*, Internal ZEUS-Note 98-07 (1998);
M. Martinez, *Calorimeter noisy cell study for 1998-2000 ZEUS Data*, Internal ZEUS-Note 00-016 (2000).

[93] H. Abramowicz, A. Caldwell and R. Sinkus, Nucl. Inst. Meth. **A365**, 508 (1995).

[94] N. Tuning, *ZUFOs: Hadronic Final State Reconstruction with Calorimeter, Tracking and Backsplash Correction*, Internal ZEUS-Note 01-021 (2001).

[95] H. Abramowicz, A. Caldwell and R. Sinkus, *Nucl. Instr. and Meth.*, **A365**, 508 (1995);
R. Sinkus and T. Voss, *Nucl. Instr. and Meth.*, **A391**, 360 (1997).

[96] S. Bentvelsen, J. Engelen and P. Kooijman, *HERA Workshop 1991, Vol. 1*, 23 (1991).

[97] F. Jacquet and A. Blondel, *Proc. of the study of an ep facility for Europe*, ed. U. Amaldi, DESY 79-48, 393 (1979).

[98] S. Schlenstedt, *Luminosity Calculation and EVTAKE*, 1992-1999.

[99] M. Wodarczyk, *Measurement of the proton structure function of the proton at HERA from 1996 and 1997 ZEUS Data*, Ph.D. thesis, Univ. of Wisconsin (1999);
R. Deffner, *Measurement of the F_2 structure function F_2 at HERA using the 1996 and 1997 ZEUS Data*, Ph.D. thesis, Univ. of Bonn (1999).

[100] S. Boogert, *Photoproduction of K^0_S mesons and Λ baryons in electron proton collisions at ZEUS Data*, Ph.D. thesis, Univ. of Oxford (2002).

[101] A. Raval on behalf of the ZEUS Collaboration, *Measurement of Strange Particle Production in Deep Inelastic $e^+p \to e^+X$ Scattering at HERA*, To appear in the proceedings of the XI International Conference on Deep Inelastic Scattering, St. Petersburg, Russia, 2003.

[102] A. Ziegler, *Investigation of the Scintillating Fiber SCSF-38M for the 6m-Tagger and Measurement of Inclusive K^0_S meson and Λ baryon Production in Neutral Current Deep Inelastic Scattering at HERA*, Ph.D. thesis, Universität Hamburg (2003).

[103] C. Risler, *Produktion seltsamer neutraler Teilchen in tiefinelastischer Streuung bein HERA* , Ph.D. thesis, Universität Hamburg (2004).

[104] Private communication with Gerd Hartner, Mark Sutton, Alex Tapper and Richard Hall-Wilton.

[105] A. Cottrell, www-pnp.physics.ox.ac.uk/∼cottrell/.

[106] R.Cahn and G. Trilling, Phys. Rev. **D69**, 011501 (2004).

[107] R. Arndt, I. Strakovsky and R. Workman, Phys. Rev. **C68**, 042201(R) (2003).

[108] A. Geiser on behalf of the ZEUS Collaboration, *Recent spectroscopy results from ZEUS*, To appear in the proceedings of 39th Rencontres de Moriond on QCD and High-Energy Hadronic Interactions, La Thuile, Italy, 2004; hep-ex/0406046.

[109] S. Chekanov, *Pentaquarks in high-energy colliding experiments: perspectives from HERA*, Submitted to Phys. Lett. **B**, hep-ph/0502098 (2005).

[110] B. Levchenko, *Kinematic selection criteria in a new resonance searches: Application of pentaquark states*, hep-ph/0401122 (2004).

[111] S. Capstick, P.R. Page and W. Roberts, Phys. Lett. **B570**, 185 (2003).

[112] ZEUS Collaboration, S. Chekanov *et al.*, Phys. Lett. **B578**, 33 (2004).

[113] Y. I. Azimov and I.I.Strakovsky, Phys. Rev. **C70**, 035210 (2004).

[114] J. J. Velthuis, *Radiation hardness of the ZEUS MVD frontend chip and Strangeness production in ep scattering at HERA*, Ph.D. thesis, Universiteit van Amsterdam (2003).

Erklärung

Hiermit versichere ich, die vorliegende Dissertation unter Angabe aller Quellen und Hilfsmittel selbständig angefertigt zu haben.

Hamburg, den 26. Mai 2005

(Amita Raval)

Acknowledgements

This result would not have been possible without the combined efforts of many. To those who gave me help, support and encouragement, I owe a great deal of gratitude.

First and foremost, I thank Prof. Robert Klanner for not only making this thesis possible, but for also providing comments on the thesis that were both astute and valuable. Thanks also go to Wolfram Zeuner for facilitating my move to the Hamburg University/DESY group, and for all his sound advise and support - financial or otherwise. I'd also like to thank Jim Whitmore for money during the last month of my Ph.D.

Achim Geiser, I thank for the many, long and interesting discussions, for his dedication, energy and support. His enthusiasm and curiosity for Physics are remarkable! I thank Sergei Chekanov for his patience, generosity and determination. He made the pentaquark search a fun adventure!

Of the many people who work very hard to ensure that the ZEUS collaboration has data to analyze, Alessandro Polini and Chris Youngman come to mind. I am simply in awe of Polini's incredible dedication to the experiment. I would like to take this opportunity to thank them both and others like Krzysztof Wrona whose efforts allow the rest of us to conduct analyses.

For all things "strange", the top honor goes to Mark Sutton. Thank-you, Mark, for all your help with the analysis and CTD-related issues, which you continue to provide even after your departure from Hamburg. Three strange co-conspirators, I would like to thank, are Andy Ziegler, Andrew Cottrell, Zhenhai Ren - Andy, for helping me get started and Andrew and Zhenhai, for the inumerable discussions.

I thank Jon Butterworth, Massimo Corradi, Uri Karshon and Rik Yoshida for taking a keen interest in this analysis and for providing many useful suggestions along the way. Also for reading and commenting on parts of this thesis, I thank Elisabetta Gallo, Claudia Glasman, Alessandro Polini, Christiane Risler and Alex Tapper. Thank-you Alex for reading the whole thing twice!

Then there is the Hamburg University gang, which I thank for providing all sorts of help and creating a convivial working atmosphere. Thanks to Sonja Hillert, Liz Nuncio-Quiroz, Raquel Santamarta, Volker Adler, Ingo Bloch, Nicola Coppola (honorary member), Dominik Dannheim, Oliver Gutsche, Benjamin Kahle, Damir Lelas and Chi-Nhan Nguyen. Thanks to all of you, it was fun being a student again. Thanks especially to Chi-Nhan and Volker for putting up with me, day in, day out, for the last three years. You two make it difficult for me to leave that office - so I won't.

John ‘JLo’ Loizides, I’d like to thank for that infectious chuckle and twinkle in the eye. Thanks for the much needed silliness and mischief, John! Richard Hall-Wilton and Uwe Schneekloth, I am grateful to for all their support and help, especially when I was a beginner here.

I would also like to thank Prof. Bob Orr and Jean-Francois Arguin at the University of Toronto. Bob, thank-you for teaching me the tricks of the EHEP trade (don’t know if you succeeded!). And Jean-Francois, thanks to your friendship, my experience of Toronto (and Montreal) was richer. Also without you, those field theory homeworks would have been unbearable!

I have to thank ‘The H1-HERMES-ZEUS Ladies’ for providing a wonderful support system by being there for me in times of need, be it professional or personal... and for all those ‘ladies nights out’, which were sheer fun! Thank-you Elisabetta Gallo, Raquel Santamarta, Christiane Risler, Jo Cole, Monica Turcato, Heuijin Lim, Katarzyna Klimek, Liz Nuncio-Quiroz, Elke Aschenauer, Kathy Farrow and Alessia Bruni.

The absence of my family was eased by my Italian friends, some of whom are, in fact, like family. I owe them a sincere, heartfelt gratitude for taking me under their vast and gracious umbrella: Alessandro Polini, Andrea Longhin, Elisabetta Gallo, Massimo Corradi, Monica Turcato, Enrico Tassi and Roberto Carlin. Grazie a tutti! Andrea, thank-you for being my first friend in Hamburg.

I would like to thank close friends who gave me courage and inspiration during the more disheartening times. Randy Boyter, ye of exceptional compassion, intelligence and wit, thank-you for being the wonderful friend that you are. Tapper, thank-you for all your help, patience and understanding. I have much to gain from your erudition and gentility (and your minimalist aestheticism). Polini, I thank you for, well, for just about everything. Your joi de vivre and grand generosity have sustained me.

Carolyn Adams, my friend and sister, no amount of gratitude is enough for the encouraging words and emotional support you’ve provided over the course of my study. Thank-you for your thoughtfulness, sensitivity and generosity. Our long cross-Atlantic conversations have kept me anchored.

I’d like to thank my brother, Aseem, for his sensitivity, warmth, humor and wisdom (doled out often in Yoda-speak). Thank-you Aseem for helping me maintain a sense of balance and mirth. Finally, I thank my Mom and Dad, who have given me the courage to question and the freedom to explore. I thank you for teaching me to keep an open, balanced mind and for providing me with an example of how to live.

Lastly, I would like to dedicate this work to Ba. I don’t know a more exceptional human being.